NASA Technical Memorandum 102208

Euler and Potential Experiment/CFD Correlations for a Transport and Two Delta-Wing Configurations

R. M. Hicks, S. E. Cliff, J. E. Melton, R. G. Langhi, A. M. Goodsell, D. D. Robertson, and S. A. Moyer

August 1990

NASA
National Aeronautics and
Space Administration

Euler and Potential Experiment/CFD Correlations for a Transport and Two Delta-Wing Configurations

R. M. Hicks, S. E. Cliff, J. E. Melton, R. G. Langhi, A. M. Goodsell, D. D. Robertson, and S. A. Moyer, Ames Research Center, Moffett Field, California

ORIGINAL CONTAINS
COLOR ILLUSTRATIONS

August 1990

NASA

National Aeronautics and
Space Administration

Ames Research Center
Moffett Field, California 94035-1000

EULER AND POTENTIAL EXPERIMENT/CFD CORRELATIONS FOR A TRANSPORT AND TWO DELTA-WING CONFIGURATIONS

R. M. Hicks, S. E. Cliff, J. E. Melton, R. G. Langhi,
A. M. Goodsell, D. D. Robertson, and S. A. Moyer
Ames Research Center

INTRODUCTION

The development of Computational Fluid Dynamics(CFD) has passed through two phases over the past 30 years. The initial phase, lasting from the late '50s to the early '70s, was a period of exploration and slow growth. Expectations for the future of CFD were modest and wind tunnel testing dominated the design process. The second phase, which lasted until the early '80s, was a period of rapid growth in algorithm and grid topological complexity. This was a period of great expectation for the future of CFD and a time when the imminent demise of wind tunnels was predicted. A third phase has been entered in which CFD limitations are more apparent and code advancement has been substantially replaced by code refinement. Many wind tunnels are being refurbished and a few new tunnels are being planned or built.

Most of the computational results presented at technical symposia and in the technical literature during the early phase of development described the flow about two-dimensional (2-D) or axisymmetric configurations with attached flow. This was a period when panel codes and finite-difference approximations of the potential equation were state of the art. Modest claims were made for the value of CFD as a design tool. The second phase was a time when exaggerated claims for the capabilities of CFD were made and technical presentations often contained flow-field calculations for separated flows about simple geometries or attached flow for complete aircraft. Finite-volume approximations to the full potential, Euler, and Navier-Stokes equations began to appear and finite-difference approximations became less popular. The majority of the experiment/CFD correlations presented were good, with the calculations sometimes appearing to be a fairing of the experimental data. Flow-field computations for complete aircraft were presented by code developers after many months of code manipulation. Such calculations show the ultimate value of CFD, but tend to give false hope to the aircraft designer who is led to believe that such codes can be used to design arbitrary aircraft configurations. When an engineer attempts to use these codes to design a configuration different from the one used to demonstrate the code, the idiosyncrasies and limitations of the code become apparent. The Euler and Navier-Stokes codes are not as robust as potential-flow codes and require a level of user skill beyond that of most design engineers. The use of such codes often requires frequent consultation with the author of the code because the numerical methods used to solve the fluid dynamic equations contain many parameters which must be adjusted to fit each aerodynamic configuration and/or flow condition. Many aircraft designers are specialists in aerodynamics but have little training in numerical analysis and fluid dynamics, making the application of Euler and Navier-Stokes codes to practical design problems difficult at best. Knowledge of numerical analysis is not sufficient to guarantee successful code application if the user is not also the code developer since most CFD codes use little structured programming and include little documentation, making reprogramming during the design process nearly impossible. The Euler and Navier-Stokes codes require more computer memory and more CPU time than potential-flow

codes. These are the primary reasons that the use of the Euler and Navier-Stokes codes in aircraft design has been limited to a class of problems which are dominated by vortical flow.

Before one attempts a design problem, the flow-field characteristics and flight conditions should be examined to determine the least complicated fluid dynamic equations which will describe the flow about the configuration being considered. If the potential equation is deemed adequate, there is little justification for using the Euler equations. A commercial transport wing flow field is adequately described by the full potential equation for the transonic cruise condition. The aerodynamic characteristics of highly swept wings are more accurately described by the Euler or Navier-Stokes equations because of the presence of rotational flow. Separated flows not initiated by abrupt geometric change (e.g., a sharp leading edge) are not predicted accurately by the most advanced CFD codes, even in two dimensions. The Navier-Stokes equations are valid for separated flow, but the numerical models used to solve the equations do not, in general, calculate separation correctly. The maximum lift coefficient for an arbitrary airfoil section is no closer to predictability today than it was 10 years ago. The absolute level of drag is another quantity which cannot be determined accurately for an arbitrary aircraft configuration.

In spite of the limitations and inaccuracies of current CFD codes, the aircraft designer can eliminate many hours of wind tunnel testing by judiciously using CFD during the design process. The designer should calibrate the code against data for configurations which are similar to the one being designed, to ascertain whether the code is capable of calculating the absolute level of the aerodynamic forces and moments or can merely produce the correct trends with variation in flow condition and/or geometry. CFD can be used to enhance the utility of an experiment in many ways (e.g., the placement of pressure taps on a wind tunnel model can be made less arbitrary by calculating the regions with large pressure gradients prior to model design).

The examples presented in this chapter will address a selection of successes and failures of CFD. Experiment/CFD correlations involving full potential and Euler computations of the aerodynamic characteristics of four commercial transport wings; and two low-aspect-ratio, delta-wing configurations will be shown. The examples will consist of experiment/CFD comparisons for aerodynamic forces, moments, and pressures. Navier-Stokes calculations will not be considered in this report. The computational results discussed in the following sections are representative of the level of accuracy which can be obtained without reprogramming the codes used in this study. Coding changes would require the active participation of the code authors and therefore would not be indicative of the level of accuracy which can be obtained from advanced CFD codes by a typical aircraft designer. An effort was made to determine optimum values for grid density, grid distribution, artificial dissipation, CFL (Courant, Friedrichs, Lewy) number, enthalpy damping, and multigrid scheme for each flow condition and configuration analyzed during this study.

NOMENCLATURE

C   chord
C_D drag coefficient
C_{D_o} drag at zero lift
C_L lift coefficient
C_M pitching-moment coefficient
C_P pressure coefficient
M   Mach number
Re   Reynolds number
X   chordwise distance
α angle of attack
η span station in fractions of span
Subscripts
∞ free-stream conditions
th   theoretical

SECTION 1
COMMERCIAL TRANSPORT WING/BODY CONFIGURATIONS
MODEL AND TEST DESCRIPTION

A planform view of the large semispan model with the dimensions indicated in inches is shown in Fig. 1. This model was tested in the Ames Research Center 11-Foot Transonic Wind Tunnel. The model was mounted approximately 6 inches above the tunnel floor, which brought the wingtip to a position only 2 feet from the tunnel ceiling. The model was manufactured from stainless steel and had eight chordwise rows of pressure taps. Each row had 23 upper-surface and 12 lower-surface orifices, giving a total of 280 surface pressure measurements on the wing. An installation photograph showing a rear quartering view of the model is shown in Fig. 2. Pressure rails (clearly visible in Fig. 2) were attached to both walls in an effort to assess the wall interference of the large semispan model, which had 2.8% blockage. The test was conducted over a Mach number range from 0.4 to 0.86. The Reynolds numbers, based on mean aerodynamic chord, varied from 1.4 to 5.1 million at Mach 0.40 and 2.3 to 8.5 million at Mach 0.86. Transition was fixed at 5% chord on the upper surface and 10% chord on the lower surface for most test conditions. Limited transition-free runs were also included. Four wings were tested on a common body with identical planforms but different airfoil sections and twist distributions.

EXPERIMENT/CFD CORRELATIONS

The primary purpose of this study was to evaluate an inviscid Euler code for the design and analysis of commercial transport wings. In actual practice there is little justification for using Euler solvers in transport wing design since the flight regime of primary interest is transonic cruise and experience has shown that the full potential equation with a simple quasi-three-dimensional (3-D) integral boundary layer correction is adequate for this purpose.[1] However, Euler flow solvers have proliferated in recent years, driven by academic competition, so it is of interest to the aircraft designer to determine the range of applicability of such codes. This section will evaluate an Euler code with C-H- and H-O-grid topologies for transport wing design. (Two later sections of this report will evaluate the same code with the H-O-grid topology for design of low-aspect-ratio delta wings.) This section will also include limited computational results from a fully conservative potential-flow code and a nonconservative potential-flow solver. The conservative code is coupled to a 3-D, finite-difference, boundary layer code and the nonconservative code includes a quasi-3-D, integral boundary layer correction. The Euler code used for this study was originally developed by Jameson[2] and was subsequently modified by personnel of the Lockheed Georgia Co. The code, designated FLO57, will be evaluated by addressing two issues. The first is the code's capability of determining quantitative aerodynamic forces, moments, and pressures; and the second is the code's capability of ordering the four transport wings correctly with respect to drag level. The latter capability is the best that can be expected from most CFD codes.

The common planform showing the distribution of defining sections is shown in Fig. 3. Each of the four wings had 23 defining stations from root to tip. The most inboard section shown in the figure is inside the body and was obtained by extrapolating the sections toward the centerline. This was done to evaluate two different techniques of describing the wing to the C-H grid-generation code. Experience has shown that some grid generators give smoother cell distribution near the wing/fuselage intersection if a defining section inside the body is included in the wing definition.

4

The results of this study showed that little difference could be detected in the computational results from including the additional section inside the body. Hence, all results presented were obtained from grids generated from the 23 defining stations begining at the wing root rather than the 24 defining stations shown in the figure. The wing sections for the four wings analyzed during this study are shown in Fig. 4. Note the difference in lower-surface contours between Wing A and Wings B, C, and D from $\eta = 0.147$ to $\eta = 0.501$. Beyond $\eta = 0.501$ the wing sections become similar with minor differences in thickness.

Two different grid topologies were evaluated with FLO57. The majority of the computational results shown in this section were obtained from an elliptic grid generator which produced C-contours in the wraparound streamwise direction and H-contours in the spanwise direction. This grid-generation code was developed by personnel at the Lockheed Georgia Co. The distribution of cells on the wing surface is uniform in the spanwise direction and is clustered near the leading and trailing edges (Fig. 5). The grid had 151 points in the wraparound streamwise direction, with 121 points on the surfaces of the wing. The cell distribution in the plane of the wing is shown in Fig. 6. Note that the cells are skewed along the nose of the body—a well-known deficiency with C-H grids for long forebodies. The spacing between grid lines beyond the tip increases more rapidly than desired for optimum computational results. Also note the large grid cells adjacent to the centerplane upstream of the nose. These large cells, along with the skewed cells along the nose, could give questionable aerodynamic quantities on the nose of the body. The C-H grid has 31 points in the spanwise and vertical directions, with 25 points on the wing and body. The cell distribution on the centerplane, including the half-body, is shown in Fig. 7. The large cells adjacent to the aft section of the fuselage and the high-aspect-ratio cells along the aft body are another reason for inaccurate body forces. The outer boundary is fairly close to the body, resulting in further uncertainties in the computational results. A limited amount of time was available to conduct this study; therefore, different outer-boundary locations were not examined.

An algebraic grid generator was used to produce the H-O grid topology evaluated during this study.[3] The H- and O-contours are in the streamwise and spanwise directions, respectively. The H-O wing-surface grid has clustering near the root and tip, with fewer points on the surface than the C-H grid has (compare Figs. 5 and 8). Note that the C-H grid has greater leading- and trailing-edge clustering than the H-O grid does. The grid cell distribution and shape in the plane of the wing adjacent to the body is more regular for the H-O grid than for the C-H grid (compare Figs. 6 and 9). The outer boundary of the H-O grid is considerably farther from the body than that of the C-H grid. The H-O grid also has more clustering near the nose of the body than the C-H grid does, resulting in better definition of the nose flow field. The H-O-grid distribution on the centerplane has more clustering and more uniform cell shape than the C-H grid (compare Figs. 7 and 10). Both grid topologies have regions of cell distortion which are largely unavoidable. An H-H grid topology avoids most of the problems associated with H-O and C-H grids, but requires substantial clustering near blunt leading edges for accurate prediction of pressure peaks. The computational results will show that in spite of the large differences between the H-O and C-H grid topologies the predicted surface pressures are similar.

The experimental and theoretical surface pressure distributions for Wing A are shown in Fig. 11. The theoretical pressures were obtained from FLO57 with the C-H grid topology (designated

FLO57C in the figures). Results will be shown for Mach numbers of 0.40, 0.70, and 0.80 and theoretical angles of attack of $-2°$, $0°$, $2°$, and $4°$, except as noted. (The phrase "theoretical angle of attack or $\alpha_{th} = -X°$" refers to the angle of attack associated with the computational results.) The computational results are the best solutions obtainable from FLO57 after several grid densities and distributions are examined. The experimental and theoretical pressure distributions are compared for closely matched lift coefficients and Mach numbers in this section. Pressure comparisons will be shown at eight spanwise stations from 15% to 95% semispan. Note the self-scaling vertical axis when comparing pressure distribution plots. The experiment/CFD comparisons for $M_\infty = 0.40$ and $\alpha_{th} = -2°$ are shown in Fig. 11(a). The experimental upper and lower surface pressures are depicted by circular and square symbols, respectively. The computational and experimental pressures correlate fairly well at most span stations, except the lower surface pressures near the leading edge show small differences. The overall correlation is somewhat better near the root ($\eta = 0.15$) than near the tip ($\eta = 0.95$). The aft loading is predicted accurately by FLO57 at all span stations because of moderate adverse pressure gradients, thin boundary layers, and attached flows. The experimental and theoretical pressures correlate fairly well at all span stations for $\alpha_{th} = 0°$, showing that boundary-layer effects are negligible (Fig. 11(b)). The experiment/CFD correlation for $\alpha_{th} = 2°$ is slightly worse than at lower angles of attack particularly near the leading edge on the upper surface of the outboard section of the wing (Fig. 11(c)). The trend of poorer experiment/CFD correlation with increasing angle of attack observed in Figs. 11(a) - 11(c) did not continue at $\alpha_{th} = 4°$, where excellent correlation is observed at all span stations (Fig. 11(d)).

The experiment/CFD pressure comparisons for Wing A at Mach 0.70 are shown in Figs. 11(e) - 11(h). Again, the correlation is good at all angles of attack with the exception of the tip region at $\alpha_{th} = 4°$ (Fig. 11(h)). The shock position and strength are calculated accurately at most span stations. The shocks are weak, and good trailing-edge pressure recovery is observed at this Mach number, thus the inviscid approximation is valid. The experiment/CFD pressure comparisons for Mach 0.80 are shown in Figs. 11(i) - 11(l). The fact that an upper-surface shock wave near midspan is predicted to be too far aft with too much strength at $\alpha_{th} = 0°$ indicates that a boundary layer displacement surface should be included in the calculation (Fig. 11(j)). The pressure recovery at the trailing edge indicates attached flow at all span stations at $\alpha_{th} = 2°$, but the shock wave has sufficient strength to cause a thick turbulent boundary layer over the aft region of the wing. The decambering effect of a displacement surface would result in a weaker shock with a more forward position and better experiment/CFD correlation. Separated flow is present near midspan at $\alpha_{th} = 4°$ and the experiment/CFD correlation is poor, as would be expected (Fig. 11(l)). The limits of applicability of FLO57 have clearly been exceeded for separated flow on transport wings.

Wing A pressure distributions calculated by FLO57 with C-H- and H-O-grid topologies are compared for matched angle of attack at Mach 0.80 in Fig. 12 (FLO57 with the H-O-grid topology is designated FLO57O in the figures). The C-H and H-O grids have 145,111 and 131,805 points, respectively. The shape of the pressure distributions calculated by the two grid topologies exhibit minor differences. For example, shock strength and position are different at some angles of attack over the inboard region of the wing (Fig. 12(c)). The computational results from the two grids show greater differences over the inboard region of the wing where the difference in grid cell distribution between the two topologies is largest (e.g., Fig. 12(d)). The span station nearest the tip might be expected to show large grid effects since this region of the wing is difficult computationally. The

effect of grid topology on wing pressures is shown for only one Mach number since the differences were small.

A single calculation using an H-H-grid topology was generated for Wing A by using the fast multigrid, isolated-wing, Euler code FLO60. H-H grids use upper and lower blocks, and therefore require more computer memory than C-H and H-O grids. A grid with dimensions of 96x16x16 was chosen for efficient use of the Cray XMP-48. Additional computations were not performed because body and boundary layer effects were not included in the solutions, and the experiment/CFD correlation obtained is worse than for FLO57 (compare Figs. 11 and 13). Note that the theoretical shock positions predicted by FLO60 are too far forward at $\eta = 0.225$ and $\eta = 0.305$, and the upper-surface computational pressures are substantially different from the test data at most span stations. The poor experiment/CFD correlation found with FLO60 has many possible causes. The total number of mesh points was only 24,576 compared with 145,111 and 131,805 for the C-H and H-O grids used with FLO57, and thus the surface definition was poor, particularly around the blunt leading edge where H-H grids are notoriously bad. Aeroelastic, boundary layer, wind tunnel wall and numerical errors are additional possible reasons for the poor experiment/CFD correlation.

An attempt was made to determine the relative importance of viscous and body effects by conducting experiment/CFD correlations with an isolated-wing code with a boundary layer correction. The code chosen for this part of the study was FLO22NM: a full-potential code with an integral boundary layer subroutine and a C-H-grid topology with 192 streamwise, 24 vertical, and 32 spanwise points. FLO22NM was originally developed by Jameson[4] and was subsequently modified by McDonnell Douglas Aircraft to include a boundary layer correction. The boundary layer displacement surface is computed iteratively along with the potential solution and is added strip-wise to the wing surfaces. The boundary layer displacement surface was updated five times during convergence. Computational pressures obtained from FLO22NM are compared with test pressure distributions in Figs. 14 and 15 for Mach numbers of 0.40 and 0.80, respectively. Comparisons are shown for theoretical angles of attack ranging from 0° to 4° and 0° to 5° at Mach 0.40 and 0.80, respectively. The experimental and theoretical pressures are compared for closely matched lift coefficient, Mach number and Reynolds number. The experiment/CFD comparisons for Mach 0.40 are good at all test conditions (Fig. 14). The shapes of the pressure distributions including the aft loading are predicted accurately by FLO22NM at Mach 0.40. The experiment/CFD correlation for FLO22NM is slightly better than that for FLO57 at low lift coefficients and substantially better at higher lift coefficients. The angle of attack required for a given lift coefficient is greater for FLO22NM than that for FLO57 because FLO22NM neglects the body and includes viscosity whereas FLO57 includes the body and neglects viscosity. FLO22NM predicts pressures more accurately near the tip than FLO57 does at Mach 0.40 (compare Figs. 11(c) and 14(e)). The FLO22NM experiment/CFD correlation is better than that for FLO57 at Mach 0.80 (e.g., compare Figs. 11(k) and 14(i)). The shock strength and location are predicted more accurately by FLO22NM at most test conditions. The only test condition where FLO22NM shows poor experiment/CFD correlation is at Mach 0.80 and $\alpha_{th} = 5°$, where the experimental trailing-edge pressure recovery on the upper surface shows flow separation at $\eta = 0.70$. It appears that an isolated-wing potential-flow code with a quasi-3-D boundary layer gives more accurate predictions of transport wing pressures with less computer resources than does a wing-body Euler code.

7

The Wing A experimental aerodynamic force and moment coefficients are compared with computational coefficients obtained from FLO57 with the C-H grid in Fig. 15. The FLO57 lift-curve slope is greater than the experimental slope at all Mach numbers because of neglected viscous effects. The inviscid drag prediction is less than the experimental drag but the difference is less than expected because of inaccurate integration of surface pressures. The only favorable comment that can be made regarding the drag predictions is that the shape of the polar at Mach 0.70 appears to be correct—a result which may be fortuitous. The pitching moment curves predicted by FLO57 exhibit more static stability than do the test results at all Mach numbers, which is consistent with the pressure distributions shown earlier. The irregularities in the theoretical pitching moment curve for Mach 0.40 will be explained after the computational results for Wings B and C have been discussed. The explanation will be more convincing when additional data have been presented. The smoother cell distribution of the H-O grid compared with the C-H grid results in a more regular pitching moment curve at Mach 0.40 (Fig. 16).

The FLO22NM force and pitching moment computations are compared with test data and FLO57 computations for Wing A at Mach 0.40 and 0.80 in Fig. 17. The FLO22NM computational lift-curve slopes are less than the experimental and FLO57 computational slopes at both Mach numbers, which is consistent with the missing body lift and the decambering of the wing caused by the boundary layer displacement surface. The drag predicted by FLO22NM is lower than that of FLO57 because of inaccurate integration of surface pressures for the latter; but the polar shapes using FLO22NM are in better agreement with the test data, which indicates that its shock and induced-drag calculations are more accurate. The FLO22NM pitching moments are more negative than those of FLO57 and experiment because the destabilizing body moments are neglected.

Pressure distributions computed by FLO57 are compared with experimental pressures for Wing B in Fig. 18. The lower-surface pressure contours for Wing B differ from those for Wing A because of greater lower-surface thickness over most of the span (compare Fig. 11(a) with Fig. 18(a)). The increased flow acceleration along the lower surface is evident at the four inboard span stations and is predicted accurately by FLO57 (Fig. 18). The experiment/CFD correlation is good at all angles of attack at Mach 0.40. The computational pressures are more positive than the experimental pressures over the forward region of the wing near the tip at Mach 0.70 and $\alpha_{th} = 4°$. The experiment/CFD correlation is acceptable at all span stations for the other three angles of attack at Mach 0.70. The experiment/CFD correlation is unacceptable when shock waves are present on the wing at Mach 0.80. The theoretical shock strength and position is usually greater than the experimental values because viscous effects are neglected. The computational and experimental lift coefficients are poorly matched at the highest angle of attack at Mach 0.80, so the correlation is questionable (Fig. 18(l)). However, the poor experimental pressure recovery over the aft portion of the upper surface indicates separated flow and hence inviscid calculations are meaningless.

The effect of grid topology on the pressure distributions for Wing B was examined at 2° angle of attack for Mach numbers of 0.40 and 0.70. The results are shown in Fig. 19. The computed pressures from the two topologies are similar except for minor differences near the leading edge at most span stations. The effect of grid topology appears to be smaller for Wing B than for Wing A (compare Figs. 12 and 19). However, the Mach number for the Wing A grid comparison was

higher, resulting in strong shock waves and more difficult computations. In summary, it appears that the effects of grid topology on wing pressures are small for both Wing A and Wing B.

The Wing B experimental and computational force and moment coefficients are compared in Fig. 20. The degree of correlation of experiment with theory is similar to that shown for Wing A (compare Figs. 15 and 20). The irregular shapes of the force and moment curves noted for Wing A was also observed for Wing B. In particular, the pitching moment curve for Wing B at Mach 0.40 exhibits irregularities similar to those shown for Wing A. The wing forces and moments in the presence of the body, and the body forces and moments in the presence of the wing, were analyzed independently in an effort to explain the poor pitching moment results. The wing forces and moments in the presence of the body were smooth with no irregularities. However, the fact that the body forces and moments exhibited a break in the curves showed that the body is responsible for the irregular force and moment curves (Fig. 21). The irregular moment curves for Wing A and Wing B will be shown to correlate with variations in code convergence level when Wing C is discussed.

The effect of grid topology on the forces and moments for Wing B at Mach numbers of 0.70 and 0.80 is shown in Fig. 22. The computational lift and pitching moment curves from the two grids agree well in slope and magnitude. The drag polars are similar in shape, but the C-H grid gives a larger value of drag at all test conditions because of inaccurate surface pressure integrations. The fact that neither grid topology gives good correlation with the test data shows that the inviscid Euler equations are of questionable value for design and analysis of commercial-transport wings.

The experimental and theoretical pressure distributions for Wing C are shown in Fig. 23. The wing-section contours for Wing C are similar to those for Wing B, hence the experiment/CFD correlations for the two wings should be comparable. A minor difference between Wings B and C is that the upper-surface pressure distribution for Wing C exhibits a reflex near the 55% chord station at $\eta = 0.15$ for $\alpha_{th} = 4°$; this reflex is predicted accurately by FLO57 (compare Figs. 18(d) and 23(d)). The predicted shock strength and position appear to be slightly better at some test conditions for Wing C than for Wing B (compare Figs. 18(k) and 23(k)).

The computational and experimental aerodynamic forces and moments for Wing C are compared in Fig. 24. The experiment/CFD correlation is comparable to that for Wings A and B except that the Wing C theoretical results are more regular at Mach 0.40. In particular, the pitching-moment curve for Wing C does not have the sinusoidal shape of the curves for Wings A and B. The body and wing planform is identical for all four wings, so it is unlikely that the unusual pitching moment characteristics are due to geometric differences between the wings. Examination of the convergence trends for Wings A, B and C provides a plausible explanation for the unusual moment curves. The initial and final average residuals for the computational results obtained from FLO57 with the C-H grid are shown in Table 1. The numbers shown in parentheses are the total number of iterations for each solution. The order-of-magnitude reduction in average residual for each solution is shown in Table 2. Note that the convergence level as a function of angle of attack exhibits a wave pattern similar to the pitching-moment wave pattern for Wing A at Mach 0.40 (Fig. 15(a)). Also note that the more fully converged solutions give pitching-moment coefficients which are nearest to the test data (Figs 15(a) and 20(a)). The pitching-moment and convergence wave patterns for

Wing B are reversed from those of Wing A, and the trends are consistent for each wing. The convergence levels for Wing C at Mach 0.40 show less waviness, which is consistent with the shape of the pitching-moment curve (Fig. 24(a)). The order-of-magnitude reduction in values shown in Table 2 for Mach 0.70 and 0.80 show little variation with angle of attack, which is consistent with the pitching-moment curves for these test conditions. It appears that the irregular pitching-moment curves are related to varying levels of convergence for the computational results. All attempts to improve convergence for the cases in question by varying input parameters and running additional iterations were unsuccessful.

The effect of grid topology on the aerodynamic force and moment coefficients for Wing C is shown in Fig. 25. The H-O-grid lift curves correlate somewhat better with the test data than those of the C-H grid at Mach 0.40 and 0.70. The opposite is true at Mach 0.80. The C-H-grid pitching moments correlate somewhat better with the experimental data than the H-O-grid moments, but neither prediction is acceptable. The H-O-grid drag coefficients are less than those of the C-H grid, primarily because of inaccurate surface pressure integrations for the latter. In summary, the drag and moment predictions for Wing C are poor and the lift-curve calculation is acceptable. However, accurate lift-curve prediction can be achieved by far simpler methods than a 3-D Euler code.

Experimental and theoretical pressure distributions for Wing D are compared in Fig. 26. The Wing D experimental pressures near the leading edge over the outboard section of the wing are slightly more negative than those of Wing C (compare Figs. 23(c) and 26(c)). These pressures were not predicted accurately by FLO57, so the experiment/CFD correlation was somewhat poorer for Wing D than for Wing C. However, the differences are small and the trends and conclusions remain the same as for the three wings discussed earlier. Note that the difference in shock strength between Wings C and D is predicted correctly by FLO57 for Mach 0.70 and 2° angle of attack (compare Figs. 23(g) with 26(g)). The experiment/CFD correlation for Wing D at Mach 0.80 and $\alpha_{th} = 2°$ is worse than for Wing C at the same flow conditions (compare Fig. 23(k) with 26(k)). Note that the predicted shock position is less accurate for Wing D over the outboard region of the wing at this Mach number. The experimental data show that Wing D has less drag than Wing C for most lift coefficients at Mach 0.70 and 0.80, while FLO57 predicts lower drag for Wing C. Such results indicate that FLO57 has limited value for transport-wing design when used with the grid generators discussed in this chapter. The experiment/CFD correlation for Wing D at the highest angle of attack at Mach 0.80 is better than for the other three wings, because Wing D has a lower lift coefficient and less flow separation.

The experimental pressure distributions for Wing D are compared with computational pressures from FLO22NM in Fig. 27. The experiment/CFD correlation for Wing D is similar to that shown for Wing A at Mach 0.40 (compare Figs. 14 (a-e) with 27 (a-e)). The pressure distribution predictions for the two wings, including the effects of small geometric differences in the leading edge region, are acceptable. The experimental and theoretical lift coefficients are more closely matched for Wing A than for Wing D at higher angles of attack, so the experiment/CFD correlation appears better for Wing A (compare Figs. 14(j) and 27(j)). The Wing D experiment/CFD correlation appears worse at $\alpha_{th} = 5°$ than at the lower angles of attack because of a greater mismatch in computational and experimental lift coefficients (Fig. 27(k)). The experimental data indicate

10

flow separation at $\alpha_{th} = 5°$ and $\eta = 0.7$ and 0.85, which contributes to the poor experiment/CFD correlation.

The aerodynamic force and moment coefficients predicted by FLO57 are compared with experimental quantities for Wing D in Fig. 28. The theoretical lift-curve slope is greater than the experimental slope at all Mach numbers because of neglected boundary-layer effects. The computational drag is clearly too large near zero lift, where the flow is shock-free at Mach 0.40 and 0.70 primarily because of inaccurate surface pressure integrations. The computational pitching-moment coefficients show excessive static stability consistent with an inviscid theory. The body forces, in the presence of the wing, for Mach 0.40 show that the irregular shape of the wing/body pitching-moment curve is caused by inaccurate body forces (Fig. 29). However, the pitching-moment curve for Wing D is more regular than those for Wings A and B (Figs. 15 and 20). Note that the shape of the moment curve for Wing D corresponds to the trend in convergence level with angle of attack shown in Table 2. This provides more evidence to support the hypothesis that the irregular moment curves are related to convergence-level variations.

The influence of grid topology on the experiment/CFD correlation for Wing D at Mach numbers of 0.70 and 0.80 is shown in Fig. 30. The lift-curve slopes computed by use of the H-O and C-H grids are greater than the experimental slopes at both Mach numbers. The pitching moments calculated by use of the C-H grid correlate more closely with experiment than those of the H-O grid for Wing D, while the reverse is true for Wing A (compare Figs. 16 and 30). The pitching moment predictions from both grid topologies are poor for the two wings, giving further evidence that the Euler computational methods described in this chapter have limited use in transport-wing design and analysis.

The experimental forces and moments for Wing D are compared with computations from FLO22NM and FLO57 with the C-H grid for Mach 0.40 and 0.80 in Fig. 31. The lift-curve slope predicted by FLO22NM is less than experiment for Mach 0.40 because FLO22NM neglects body lift and includes viscous decambering of the wing, while the FLO57 lift-curve slope is too high because FLO57 neglects viscosity. The agreement between experimental and theoretical lift curves for FLO22NM at Mach 0.80 is fortuitous. The shape of the FLO22NM drag polars correlate somewhat better with experiment than those of FLO57, which indicates better shock and induced-drag prediction for the latter. The FLO22NM pitching moment curve exhibits excess static stability consistent with an isolated-wing calculation. When the body forces and moments calculated by FLO57 are added to the isolated-wing forces and moments from FLO22NM, the experiment/CFD correlation improves as shown in Fig. 32. This correlation is the best obtained for the four transport wings evaluated during this study. It is apparent that both viscosity and body effects should be included in the computations to obtain acceptable force and moment predictions. Even a quasi-3-D boundary layer correction appears adequate for attached-flow conditions.

Experimental pressure distributions are compared with FLO28BL pressure distributions for Wing D at Mach 0.80 and $C_L = 0.55$ in Fig. 33. FLO28BL is a fully conservative wing-body potential-flow code[5] coupled with a 3-D finite-difference boundary layer program. The experiment/CFD correlation is acceptable at all span stations. Small discrepancies are observed at the outboard stations, particularly near the tip. Note that the FLO28BL and FLO22NM experiment/CFD

correlations are similar, indicating that acceptable pressure predictions can be achieved for flight conditions with attached shockless or weak-shock flow without including body effects (compare Figs. 27(i) and 32). The C-H grid used with FLO28BL has dimensions of 217x25x33, giving a total of 179,025 points. The cell distribution on the center plane is shown in Fig. 34. Note that the cells are more uniformly distributed and more regular in shape than those of the C-H grid used with FLO57 (compare Figs. 7 and 34). The outer boundary of the FLO28BL grid is considerably farther from the body than that of the FLO57 with the C-H grid.

An important part of this code evaluation was to determine whether FLO57 can predict (1) which of the four wings has the lowest drag and (2) the order of the wings with respect to drag. A CFD code which cannot predict drag increments resulting from small geometric changes has limited use in aerodynamic design. Experimental drag polars for the four wings at Mach 0.80 are shown in Fig. 35. The range of lift coefficients shown is appropriate for commercial transports operating at or near the transonic cruise condition. The experimentally determined order of the wings with respect to drag is fairly constant with lift coefficient, Wing A having the lowest drag and Wing C the highest. The theoretical drag polars show that the wing with lowest drag is lift-coefficient dependent, and Wing A does not have the lowest drag at any lift coefficient, in contrast to the experimental results (Fig. 36). These drag comparisons show that FLO57 with the C-H grid described here may not be capable of predicting drag as a function of small geometric change and hence may be unacceptable for transport-wing design. An assessment of the ability of the full-potential code FLO22NM to predict the correct order of Wings A and D with respect to drag is shown in Fig. 37. Both experiment and theory show that Wing A has lower drag than Wing D has. However, the drag differences are small, and only two wings were considered, so it is difficult to draw meaningful conclusions from this part of the study.

CONCLUDING REMARKS

1. Experiment/CFD pressure correlations for a wing/body Euler code were acceptable for attached subsonic flow and transonic flow with weak shocks on a commercial-transport wing.

2. Experiment/CFD pressure correlations for a wing/body Euler code were unacceptable for transonic flow with shock waves of moderate strength on a commercial-transport wing.

3. Experiment/CFD force and moment correlations for a wing/body Euler code were unacceptable for subsonic or transonic flight conditions with attached flow for commercial-transport wings.

4. The wing/body Euler code was not capable of predicting the order of the four commercial-transport wings with respect to drag level.

5. Computed Euler results were little effected by changing from a C-H- to an H-O-grid topology.

6. A nonconservative, isolated-wing, full-potential code with a quasi-3-D integral boundary layer correction was found to give better correlation with experimental pressures than a wing/body Euler code does.

7. A full-potential wing-body code coupled to a 3-D finite-difference, boundary layer program gave satisfactory agreement with experimental pressures for a typical transonic cruise condition of a commercial transport.

SECTION 2
GENERIC FIGHTER

EXPERIMENTAL WORK

In an effort to increase the understanding of vortical flows at transonic speeds, Erickson and Rogers[6] conducted a series of experimental investigations into the behavior of a generic fighter model at transonic conditions. The model has a cropped delta wing with a leading-edge sweep of 55°, an aspect ratio of 1.8, and a taper ratio of 0.2. The wing sections were modified NACA 65A005 airfoils with sharp leading edges. A chine with wedge cross section was added to the forebody 0.5 inches above the wing. A planform view, a side view, and two cross-sectional views of the model are shown in Fig. 38. The model has a total of 80 upper-surface static-pressure taps located at 30%, 40%, 50%, 62.5%, and 75% of the distance along the wing centerline chord, as depicted in Fig. 38. The wing was mounted on a generic fuselage that accommodated a four-module Scanivalve and a six-component balance.

The model was tested in the 7- by 10-Foot Transonic Wind Tunnel of the David Taylor Naval Ship Research and Development Center, at Mach numbers between 0.40 and 0.95 and at angles of attack between 0° and 22°. The effects of Mach number, angle of attack, and leading-edge flap deflection on the wing-upper-surface pressure distributions were studied. The model was also tested in the 6- by 6-foot wind tunnel of NASA Ames Research Center at Mach numbers between 0.40 and 1.8 and at angles of attack from 0° to 24°. The purpose of the Ames test was to determine the flow-field changes over the wing resulting from placing a chine at various locations on the forebody.[7]

COMPUTATIONAL WORK

The grid generated about the generic fighter has an H-O topology which allows good leading-edge resolution. The grid was generated using an elliptic solver written by Melton.[3] This code solves the Laplace equation in two dimensions in order to smoothly wrap a grid around the body at specific longitudinal locations. This grid is then algebraically redistributed in the direction normal to the wing surface to provide clustering specified by the user near the wing surface, and also to provide a smooth transition between grid planes in the streamwise direction.

The grid used in the computations has a total of 426,790 points. There are 134 points in the streamwise direction; 94 of which are on the body. There are 49 points from the surface to the outer boundary, and 65 points circumferentially around the wing/body configuration. The grid extends 6.5 centerline chordlengths upstream and 6.5 centerline chordlengths downstream of the body, and 7 semispanlengths radially to the outer boundary. Examples of the grid for the wing/body model are given in Figs. 39(a) and 39(b). The chine was modeled as a flat plate. A grid plane at the chine trailing edge is shown in Fig. 39(c).

RESULTS AND DISCUSSION

FLO57 solutions were obtained at Mach numbers of 0.60 and 0.80 for both the wing/body and wing/body/chine configurations. Table 3 contains the computational run schedule. A minimum of 1200 iterations were run at the low angles of attack and 3000 to 3500 iterations at higher angles to

achieve a reduction of at least three orders of magnitude in the average residual. The lift, drag, and moment histories generally show convergence after about 1000 iterations while the residuals are still decreasing. All solutions were obtained on the Cray-2 at NASA Ames Research Center. The memory requirement was approximately 16 MW and the CPU time required for 1,000 iterations was approximately 10,300 seconds resulting in 4 to 10 hours for each solution. Computed pressure lift, drag, and pitching-moment coefficients for each Mach/alpha combination were compared to experimental results at 30%, 40%, 50%, 62.5%, and 75% chord stations. A discussion of the results for each combination of Mach number and configuration will be presented below.

Mach = 0.60, Wing/Body

The flow is attached with no leading-edge vortex at $\alpha = 4°$. FLO57 pressure distributions compare well with experimental results (Figs. 40(a)-40(d)).

The experimental results show that a vortex has begun to form near the leading edge at $\alpha = 8°$. The computational results correlate poorly with experimental results as shown in Figs. 41(a)-41(d). The Euler results show the formation of a weaker vortex inboard of the experimental vortex. Since the vortex is in the formative stage, the Euler solution may be sensitive to grid density and leading-edge resolution.

The vortex strength increases and the location moves inboard at $\alpha = 12°$ (Figs. 42(a)-42(d)). The Euler results predict the strength and position of the primary vortex accurately at 40% chord. The secondary separation and other viscous effects can be seen in the experimental pressure distributions further aft on the wing. The secondary separation moves the primary vortex inboard and creates a low pressure region extending outboard from the core of the primary vortex. These flow characteristics cannot be modeled with the Euler equations. FLO57 predicts a stronger primary vortex that lies outboard of the experimental vortex at 50% and 62.5% chord. At 75% chord the Euler results show a flattening of the vortex core, which suggests that the vortex may be bursting. Further evidence of vortex breakdown was given by numerical simulations of particle paths showing recirculation within the core.

Vortex bursting is apparent in both computational and experimental pressure distributions at $\alpha = 16°$ and $\alpha = 20°$. The vortex structure is no longer maintained and the pressure distributions become unsteady aft of the breakdown position (Figs. 43(a)-43(d) and 44(a)-44(d)). Numerical behavior believed associated with vortex bursting is depicted by the unstable and oscillatory moment coefficient histories shown in Fig. 45. FLO57 predicts the burst location ahead of the experimental position at both angles of attack. The comparison between Euler and experimental results improves at stations where experiment and computations indicate that breakdown has occurred. The existence of a cross-flow shock is shown in the experimental pressure distributions, but not in the FLO57 results (Fig. 43).

Comparisons between the experimental and computational force coefficients show that FLO57 predictions are accurate until approximately $\alpha = 16°$, where the vortex appears to burst over a large portion of the wing (Fig. 46). Moment predictions do not compare well with experiment above $\alpha = 8°$. However, the angle at which the moment-curve slope changes is accurately predicted by FLO57.

14

Mach = 0.60, Wing/Body/Chine

The comparisons between computational and experimental results improved for the wing/body/chine configuration. The pressure distributions for all angles of attack are shown in Figs. 47-51. The flow over the forebody without the chine is strongly affected by viscous separations which cannot be modeled in an Euler simulation. The dominant vortex from the chine is captured by the Euler code, allowing a more representative computational model of the forebody flow field approaching the apex of the main wing.

Both Euler and experimental results show that the chine delays the onset of instabilities which lead to vortex breakdown. This is clearly evident by comparing the moment histories in Fig. 52 with those from the wing/body configuration shown in Fig. 45. The location of vortex breakdown given by the computational pressure distributions is ahead of that shown by the experimental data. FLO57 does not predict the strengthening of the cross-flow shock by the chine. Increased grid resolution may be required to capture the shock.

The lift, drag, and moment curves are given in Fig. 53. The Euler code overpredicts the increment in lift due to the chine. The drag differences at low-lift conditions and the change in slope of the moment curve were accurately predicted.

Mach = 0.80, Wing/Body

The experiment/CFD correlations at $M_\infty = 0.80$ are similar to those at $M_\infty = 0.60$. The pressure distributions for $M_\infty = 0.80$ are shown in Figs. 54-58. The experimental and computational pressure distributions agree well at $\alpha = 5°$ over the entire wing since the flow is fully attached. The computational pressure distributions are in poor agreement with the wind tunnel data when the vortex begins to form near the leading edge at $\alpha = 8°$. An increase in Mach number causes the vortex burst location to move forward on the wing above $\alpha = 12°$. The Euler simulation predicts bursting prematurely, as observed at $M_\infty = 0.60$. The Euler solutions show poor agreement with experimental results at both $\alpha = 16°$ and $\alpha = 20°$. The FLO57 results do not show a distinct vortex at either angle of attack and have flat spanwise pressure distributions. The moment histories show random behavior for both angles of attack with a large increase in nose-down pitching moment (Fig. 59). The computational lift, drag, and moment curves show good agreement with test data for angles of attack below approximately 12° (Fig. 60). The Euler predictions become less accurate when vortex bursting becomes more extensive.

Mach = 0.80, Wing/Body/Chine

Placing the chine on the forebody above the wing surface improves the correlation of experiment with CFD and delays the onset of vortex burst. The pressure distributions are shown in Figs. 61-64. The moment histories given in Fig. 65 are smoother than those from the wing/body. The increase in lift and the decrease in drag are overpredicted by FLO57 (Fig. 66). The shape of the moment curve was accurately predicted by the Euler code.

CONCLUDING REMARKS

The Euler code FLO57 has been used to calculate transonic flow over two configurations of a generic fighter model. Results were computed at Mach numbers of 0.60 and 0.80 for selected angles of attack between 4° and 20°.

The Euler code predicts the aerodynamic quantities accurately for attached flow conditions but less accurately when the leading-edge vortex is forming. This may be due to the sensitivity of FLO57 to grid resolution and geometry modeling near the leading edge. However, after the vortex is established, the Euler results show good agreement with experimental data until vortex breakdown occurs in the computations. The Euler code appears to predict bursting prematurely. The reason for this is unknown. When the experimental results indicate vortex bursting, the experiment/CFD correlation improves.

The effect of adding the chine to the forebody is to delay the onset of vortex breakdown both numerically and experimentally, and to improve Euler predictions. The decoupled chine vortex interacts favorably with the main wing flow field, increasing the effective leading-edge sweep.[8] The experiment/CFD correlations improve with the addition of the chine which may result from fixed forebody separation at the chine, providing a dominant flow feature for the Euler code to capture. Without the chine, the Euler code has difficulty modeling the unsteady flow separations on the forebody, especially at high angles of attack.

STUDY OBJECTIVES AND MODEL GEOMETRY

Wind tunnel testing requirements for instrumentation, propulsion-simulation hardware, and support systems are often in conflict for physical space inside a wind tunnel model. As a result, forces and moments are sometimes derived from integrated experimental pressure data. This method is usually suspect because of the relatively small number of pressure measurements available over complex 3-D surfaces. The first part of this section presents a comparison between CFD predictions and wind tunnel data for surface pressure distributions and longitudinal forces and moments. The effects of numerical discretization were explored by using three computational grids of varying density. The large number of wind tunnel pressure taps available on this model allowed for colored surface pressure contour comparisons between the experimental and computational results. This technique was found to be useful for highlighting small discrepancies in wing pressure distributions that were sometimes overlooked when viewing traditional pressure distribution plots. The second part of this section investigates the feasibility of integrating experimental pressures to determine the forces and moments acting on a wind tunnel model. An integrated approach for determining forces and moments using wind tunnel data and CFD predictions is described.

The wind tunnel model was a full-span delta wing with $62.5°$ leading-edge sweep. A plan view showing pressure-tap locations is given in Fig. 67. The simple geometry and large number of pressure taps (287) made it ideal for both CFD code validation and surface-pressure integration. To accommodate other test requirements, the model was supported near the wingtips. As a result, there was a fairly large gap between the tenth and eleventh chordwise rows of pressure taps. In addition, a few geometric modifications were made to the wind tunnel model prior to the present test to assist in the pressure-integration study and to assure tunnel compatibility. The shroud required for sting mounting also covered a small portion of the upper surface and some of the associated pressure taps. Outside of these regions, the model had an excellent pressure-tap distribution on both the upper and lower surfaces. The geometry used for the CFD analysis and post-test pressure integrations was obtained in a panel-code-type input format. It consisted of three networks containing the forward wing region, the aft wing region, and the sting shroud. There were a total of 12 span stations, with 27 chord points used to define each airfoil. This definition was assumed to accurately duplicate the contours of the wind tunnel model, although some inaccuracies were known to exist.

WIND TUNNEL TEST

The model was tested in the Ames 11- by 11-Foot Transonic Wind Tunnel over a wide range of Mach numbers and model attitudes. This section will present only the longitudinal data obtained at $M_\infty = 0.8$, Re/ft = 2.5 million; $M_\infty = 0.7$, Re/ft = 2.5 million; and $M_\infty = 0.4$, Re/ft = 2.0 million.

CFD ANALYSIS

Grid Generation. An H-O-grid topology was chosen for this study because it can handle wings with low taper ratios or pointed tips, and provides for an efficient clustering of points along

the leading edge. The grid-generation process can be broken down into three steps. In the first step, a commercial CAD/CAM system was used to generate cross sections of the model at specified longitudinal locations.[9] These cross sections were then redistributed in order to provide grid clustering in regions of high curvature. Finally, the surface grid at each cross section was extended into the 3-D space surrounding the body. In order to produce a smooth grid, a 2-D elliptic grid-generation routine was used to create each grid plane. A cross-sectional view of one of the fine grid planes is shown in Fig. 68. Since the grids are created at successive longitudinal stations, the sting can be easily incorporated. Three grids of varying density were used to investigate the sensitivity of the computations to different discretizations. The three model upper-surface grids are shown in Fig. 69. The grid crossover that occurs near the trailing edge in these planform views is not a true crossover, but a wrapping of grid lines around the double-valued sting surface. Information about the three grids is given in Table 4.

Flow Solver. The FLO57 CFD code integrates the Euler equations using Jameson's four-stage explicit Runge-Kutta algorithm.[2] The original program used in this study had been modified by numerous authors; further modifications were necessary to incorporate the H-O-grid topology. Details of the Euler solution strategy and arguments for the applicability of Euler codes to delta wing configurations are given in Refs. 10 and 11.

CFD COMPARISONS

The extensive pressure instrumentation allowed detailed surface-pressure comparisons to be made over the entire span of the model. The lift, drag, and moment coefficients were also compared to the experimental data. Three grids of varying density were used to provide an estimate of the effect of grid density on solution characteristics. All solutions were run to a minimum of three orders of magnitude convergence in the density residual. Lift, drag, moment, and the number of supersonic points versus iteration were also monitored to ensure converged results. Table 4 provides information about the computational resources required for the FLO57 analysis. The computational run schedule is given in Table 5. The predicted and experimental surface pressure comparisons are shown in Figs. 70-72, and the resulting force and moment data are presented in Figs. 73-75. Included with the experimental data and FLO57 predictions are the results of an analysis using a panel code.[12] The agreement between the FLO57 computations and wind tunnel pressure distributions is generally good except in regions where significant viscous effects were present. The pressure distributions of Figs. 70-72 show the ability of the Euler code to predict the details of the inboard pressure distributions, including the magnitude and extent of the leading-edge expansion spikes. At the trailing edge, FLO57 overestimates the amount of pressure recovery. The wind tunnel pressure distributions do not recover to the same level as FLO57 because of boundary layer displacement effects and trailing-edge separation.

The detailed mechanics of the leading-edge vortex formation and the secondary separations of the boundary layer caused by resulting adverse spanwise pressure gradients are also incorrectly modeled by the inviscid Euler code. The effect of these modeling differences on the pressure distributions becomes significant as the vortex strength increases along the leading edge. These vortex/boundary layer interactions result in an increasingly poorer C_p comparison toward the tip. The result of neglecting the physics involved in these important flowfield interactions is clearly seen in the outboard pressure distributions of Figs. 70(d), 71(d), and 72(c). Increasing the angle

18

of attack strengthens the vortex and increases its interaction with the boundary layer. Although the overall pressure agreements between the computations and wind tunnel tests were very good, the slope and sign of the moment curves predicted by FLO57 did not correlate well for any of the three Mach numbers investigated, as seen in Figs. 73-75. However, these correlations are better than those shown in section 1 for commercial transport wings. The origin of the difference between the wind tunnel moment curve and the FLO57 and PANAIR predictions was difficult to identify. The fact that this difference persisted even at low lift conditions was especially troubling, because the effects of incorrect vortex modeling, viscosity, and shock waves were not expected to be large for small angles of attack. Studying individual chordwise pressure distributions did not yield any obvious explanations. In order to study the decambering effect of the boundary layer, a turbulent displacement thickness was calculated and added to the upper and lower surfaces for the medium grid, but it did not appreciably change the FLO57 moment slope. A thorough check of the wind tunnel data-reduction system was also made.

The origin of the difference between the FLO57 and wind tunnel moment curves was eventually discovered by comparing the overall computed and experimental pressure distributions. This was accomplished by preparing colored planform views of the model which combined experimental and computational predictions. One half of each surface of the wing was colored with the experimental pressures, and the other half by the predicted computational pressures.[13] Each wind tunnel pressure tap was assigned a surrounding area on the wing, and these areas were colored by the C_p measured at the tap. Each surface cell in the FLO57 grid was similarly colored by the pressure predicted at its center, making a direct comparison between the experiment and computations possible. Although these colored planform comparisons are more qualitative than the traditional chordwise plots, they tend to accentuate overall trend differences. This can be seen by studying Figs. 76-77, which correspond to α sweeps at $M_\infty = 0.40$ and 0.80. Upon close review, it can be seen that the upper-surface pressure distributions predicted by FLO57 tend to have a slightly lower pressure extending further aft on the wing. This additional aft loading, when integrated over the entire span, produces a more negative pitching moment and exists even at low lift conditions. Further review of the plots of individual chordwise pressure distributions shows this difference to be small, but to extend over the entire span. It would appear that geometrical inaccuracies in the wing geometry network files, and not viscous effects, are the major source of the computational moment discrepancy. The effect of the grid density on surface C_p distributions did not appear to be very large, but did increase somewhat near the wingtips. The lift, drag, and moment were also little affected by grid size. Additional expensive, large-grid solutions were not obtained at $M_\infty = 0.4$ and 0.7 since the three grids gave similar results at $M_\infty = 0.8$

EXPERIMENTAL PRESSURE INTEGRATION

The experimental pressure-integration scheme used the simple midpoint rule, where an area and unit normal vector were associated with each tap location. In order to compare the resulting integrated data with the balance data, a skin-friction estimate was added to the drag computations. Tap areas were determined by placing a panel around each pressure tap. Sides of these panels were positioned at the midpoint between adjacent taps. The unit normal vectors assigned to each area were the unit normals to the surface calculated at the centroid of each panel. These centroids were generally close to the tap locations. Since the sting shroud was not pressure instrumented, it was not modeled in the pressure-integration scheme. Instead, the panel areas of the closest spanwise

19

taps were extended to the model centerline (Fig. 78). The integration scheme might have been improved by determining an average unit normal vector over the surface of a panel instead of using that found at the centroid. In addition, a higher-order numerical integration method could have been used.[14] The midpoint rule was used for this study because it was straightforward and it simplified location and correction of errors in the integration scheme.

SKIN FRICTION ESTIMATION

Skin-friction increments were applied only to the drag since its effect on pitching moment was assumed to be negligible. The incompressible, flat-plate, 2-D skin-friction estimates used were:[15]

$$C_{F_{Turb}} = 0.074 / Re^{0.2}$$
$$C_{F_{Lam}} = 1.328 / \sqrt{Re}$$

Boundary layer transition was forced near the leading edges of the wings by a transition strip set 1.0 inch streamwise from the leading edge. The drag increment due to this strip was shown to be insignificant. In addition, drag sensitivity to the turbulent transition location (in case the transition strip failed to trip the boundary layer) was analyzed and found to be negligible. The above coefficients were based on the transition-strip location and mean chord.

INTEGRATED FORCE AND MOMENT COMPARISONS

Force and moment comparisons of balance, integrated pressures, and integrated pressures plus skin friction are shown in Figs. 79-81. The lift curve derived from the integrated pressures agrees well with the balance data for all three Mach numbers. This is expected, since the distribution of integration panels projected onto a plane perpendicular to the lift axis is good. The only gaps occur at the sting shroud and just inboard of the two wingtip rows. The pitching-moment data also agree quite well. There is a general trend, however, for the integrated pressures to consistently give a more positive pitching moment than the balance data. This trend becomes significant at higher angles of attack. A possible reason for this discrepancy is removal of the sting shroud from the integration scheme. The shroud extended 2.9 inches past the trailing edge. At zero angle of attack the surface of the shroud is nearly parallel to the freestream and does not contribute to the frontal area of the model. At higher angles of attack the aft end of the shroud becomes visible to the oncoming flow and exerts a nose-down moment not captured by the experimental pressure integration. The balance drag polar and the integrated-pressure drag polar do not agree as well as the lift and moment curves at the three Mach numbers. The integrated pressures overestimate the drag by a constant increment over the range of lift coefficients, but give the correct shape of the polars. Analysis of this drag shift identified a number of possible causes:

1) Inaccurate wind tunnel data.
2) Errors in the integration scheme.
3) Inaccurate skin-friction estimate.
4) Errors in geometry used in integration.
5) Inadequate number of pressures on the model surface.

These causes were analyzed, and are discussed in the following sections.

Inaccurate Wind Tunnel Data. The wind tunnel data was thoroughly examined and all data and corrections appear to be accurate within the limits of the instrumentation ($\Delta\ C_D \leq \pm 0.0003$).

Errors in the Integration Scheme. Possible errors in the integration scheme were evaluated by examining the unit normal vectors and panel areas assigned to each pressure tap. These values were compared with normal vectors and panel areas previously determined by the test engineer. The earlier values were not used for this study because the manner in which the areas around the sting shroud were computed was unclear. All the values compared very well with only a few minor differences. These differences were not large enough to explain the drag shift found in the integration.

Inaccurate Skin-Friction Estimate. The analysis of errors in the skin-friction estimate was limited to the turbulent region since only a very small portion of flow over the model's surface was laminar. The turbulent estimate is a crude incompressible value from Prandtl's 1/7th-power velocity profile.[15] This relation is the classical turbulent skin-friction estimate generally used in conceptual design. A method that incorporates compressibility was proposed by Sivells and Payne.[16] Of course, the largest difference between the two methods is found at $M_\infty = 0.80$ where $C_{F,turb} = 0.00316$ for the classical Prandtl method and 0.002926 for Sivells and Payne. Here the skin friction coefficient is reduced by 7.5%. However, a reduction in skin friction on the order of 50% would be necessary to match the balance. Also, as opposed to using a Reynolds number based on mean chord, the planform was divided into eight chordwise strips of the same width. The skin friction for each strip based on local chord was determined. The total was then derived by summing the skin friction over the strips. The error associated with this was on the order of 1%. Therefore, any error in skin friction would be due to 3-D and pressure-gradient effects which were not considered during this study.

Errors in Integration Geometry . The most obvious geometrical difference between the balance measurement and the integration scheme was the sting shroud. As mentioned earlier, there were no pressures available for integration over the surface of the shroud. Instead, the sting shroud was excluded from the surface integration and each pressure tap adjacent to the shroud was assigned an area extending to the model centerline. The balance drag includes skin friction and pressure drag, hence a method of determining the effect of removing the sting shroud from the integration can be assessed. First, the increment in skin friction due to differences in wetted area with and without the sting shroud is calculated. The difference in total drag is $C_D = 0.0002$. This is on the order of the resolution of the balance. Second, the effect of removing the shroud from the integration of pressure forces is estimated. The surface of the sting shroud has no aft-facing area and the final balance forces included base and cavity corrections. Therefore, the pressure on the sting shroud did no contribute to the final balance drag. In comparison, the geometry used for the pressure integration has an aft-facing surface area in the region occupied by the shroud. This additional aft-facing area in the integration geometry contributes to the axial force. Therefore, if the axial force due to this area is removed from the integration, a reasonable estimate of the effect of the shroud can be determined.

Another method for determining the effect of removing the shroud on the integration of pressures can be determined from computations. The FLO57 solution included the shroud, hence the surface grid can be modified so that the cells adjacent to the shroud can be extended to the model centerline as the experimental panels were; then an estimate of the drag differences with and without the shroud may be obtained. Results from both methods are presented in Fig. 82 for $M_\infty = 0.80$. Values found using the experimental pressures are combined with the data in Fig. 83. The figure

demonstrates that the shroud correction improves the correlation between the balance and integration curves, but a sizable shift in drag still remains unexplained. No other major geometric differences are present to explain this drag shift.

Inadequate Number of Pressures on the Model Surface. Accurate drag calculation by surface-pressure integration requires a large number of panels with significant leading- and trailing-edge clustering to resolve large pressure gradients. This wind tunnel model was chosen for this study because of its large number of pressure taps and its simple shape. However, the drag still could not be estimated accurately. Economic and instrumentation limitations restrict the number of pressure taps that may be incorporated into a model. Increasing the number of taps on a wind tunnel model to obtain drag by surface-pressure integration is not practical. A higher-order numerical integration or curve-fitting technique could be used. However, no curve-fitting method will capture regions without taps, such as leading-edge suction or, in this case, the sting shroud. This section demonstrates a method to correct the integrated pressures without increasing the number of taps. The pressure integration used a discrete pressure and a unit normal vector for each panel. The integration method more accurately approximates a continuous pressure field as the number of integration panels increases. The difference between the force computed from the discretized integration method and that from a continuous pressure field acting on infinitesimal areas is defined to be the discretization error. The most dense computational grid and the experimental integration panels at one location on the model are compared in Fig. 84. The FLO57 surface grid was assumed to approximate a continuous pressure field and the discretization error was quantified in the following ways:

1) The pressure at each tap location predicted by FLO57 was determined. Tap pressures were obtained by interpolating from the surrounding cell centers.

2) These interpolated pressures were combined with the experimental tap areas and unit normals, and were then integrated.

3) Drag polars from step 2 and from the original FLO57 solution quantify the discretization error as shown in Fig. 85.

Therefore, the discretization error associated with the experimental pressure integration scheme can be determined by relying on an estimate from the computational solution. The discretization error found in Fig. 85 can be expected to apply to the experimental pressure integration if FLO57 gives an accurate estimate of the flowfield. The integration results improve when this error is removed (Fig. 85). When the skin-friction estimate is added the agreement with the balance data is good (Fig. 86). It is important to note here that the discretization error described above includes the effect of the sting shroud because the FLO57 results were obtained from geometry that included the shroud. Therefore, this error-estimation method is also capable of capturing geometric differences between the integration geometry and the actual model configuration. Unfortunately, the method does not retain the same accuracy for all test conditions. The discretization error found from FLO57 at high lift coefficients does not match the increment needed to correct the experimental integration at $M_\infty = 0.40$ (Fig. 87). However, at lower angles of attack the correction works well. The deviation at high angles of attack is probably due to inaccurate computational results at those test conditions. The computational drag polars show greater drag due to lift than the experimental data do at $M_\infty = 0.40$. When the discretization error determined from the computational solution is removed from the experimental pressure integration at $M_\infty = 0.40$ as shown in Fig. 87, the final result shows an increase in drag due to lift which is too large. However, the zero-lift

22

drag coefficient matches the balance data closely. Therefore, discretization-error estimation using a computational solution is limited to conditions where the flowfield is accurately modeled by the CFD code. The discretization error found from computations is essentially the integration error due to the inability to interpolate pressures accurately between taps. The success of the method results from using the computational solution as a "higher-order" integrator. Also, the integrated experimental pressure data were easily corrected for the sting shroud since the computational geometry included the shroud.

CONCLUDING REMARKS

The Euler code FLO57 has been compared with experimental data at three Mach numbers and at several angles of attack. The code gave accurate results over the forward regions of the model but, as expected, poor experiment/CFD correlations were observed near the trailing edge because of neglected viscosity. In addition, the CFD solution was used to improve the feasibility of using experimentally measured pressures to obtain quantitative forces and moments acting on a wind tunnel model. The computational solution was used to correct the discretization error resulting from a finite number of pressure taps, thus giving improved values for drag. Experiment and CFD can be used to their mutual enhancement. Proper experimental validation of CFD codes is necessary to determine the conditions under which computations may be expected to give satisfactory results. In addition, CFD solutions may be used to assist the experimentalist before a test by improving the conceptual design, by indicating locations of high pressure gradients for improved pressure-tap placement, and by projecting the test-condition limitations resulting from balance design limits. Furthermore, as demonstrated in this study, CFD may be used after a test to improve the quality and resolution of the experimental data.

ACKNOWLEDGMENTS

23

REFERENCES

[1] Henne, P. A., and Hicks, R. M., "Wing Analysis Using a Transonic Potential Flow Computational Method," NASA TM 78464, July 1978.

[2] Jameson, A, Schmidt, W., and Turkel, E., "Numerical Solutions of the Euler Equations by Finite Volume Methods Using Runge-Kutta Time Stepping Schemes," AIAA Paper 81-1259, 1981.

[3] Melton, J. E., and Langhi, R. G., "Surface Grid Generation for Advanced Transport Configurations, Numerical Grid Generation in Computational Fluid Mechanics '88," Pineridge Press Limited, Swansea SA3 4BQ, U.K., 1988.

[4] Jameson, A., and Caughey, D. A., "Numerical Calculation of the Transonic Flow Past a Swept Wing," COO-3077-140, ERDA Math and Comput. Lab., New York Univ., June 1977.

[5] Caughey, D. A., and Jameson, A., "Numerical Calculation of Transonic Potential Flow About Wing-Fuselage Combinations," AIAA Paper 77-677, June 1977.

[6] Erickson, G. E., and Rogers, L. W., "Experimental Study of the Vortex Flow Behavior on a Generic Fighter Wing at Subsonic and Transonic Speeds," AIAA Paper 87-1262, January 1987.

[7] Erickson, G. E., Rogers, L. W., Schreiner, J. A., and Lee, D. G., "Subsonic and Transonic Vortex Aerodynamics of a Generic Forebody Strake–Cropped Delta Wing Fighter," AIAA Paper 88-2596, June 1988.

[8] Private communication with Gary Erickson.

[9] Enomoto, F., and Keller, P., "Using a Commercial CAD System for Simultaneous Input to Theoretical Aerodynamic Programs and Wind-Tunnel Model Construction," NASA CP 2272, April 1983.

[10] Goodsell, A., Madson, M., and Melton, J., "TranAir and Euler Computations of a Generic Fighter Including Comparisons with Experimental Data," AIAA Paper 89-0263, January 1989.

[11] Newsome, R. W., and Kandil, O. A., "Vortical Flow Aerodynamics – Physical Aspects and Numerical Simulation," AIAA Paper 87-0205, January 1987.

[12] Carmichael, R. L., and Erickson, L. L., "PANAIR – A Higher Order Panel Method for Predicting Subsonic or Supersonic Linear Potential Flows About Arbitrary Configurations," AIAA Paper 81-1255, 1981.

[13] Hermstad, D. L., "RAID User's Guide," Technical Note No. 33, Rev. 2, Sterling Federal Systems, Inc., Palo Alto, CA, 1989.

[14] Rice, J. R., "Numerical Methods, Software, and Analysis: IMSL Reference Edition," McGraw-Hill, Inc., 1983, pp. 186-215.

[15] Schlichting, Hermann, "Boundary-Layer Theory," McGraw-Hill, Inc., 1979, pp. 140 and 640.

[16] Sivells, James C., and Payne, Robert G., "A Method of Calculating Turbulent-Boundary-Layer Growth at Hypersonic Mach Numbers," AEDC-TR-59-3, ASTIA Doc. No. AD-208774, Arnold Eng. Dev. Center, MA, 1959.

Table 1. Initial and final residuals in ( ) iterations. (FLO57C)

Angle of attack	Mach number		
	Wing A		
	0.4	0.7	0.8
−2	0.1801 + 2	0.3189 + 2	0.3785 + 2
	0.9109 − 1 (3000)	0.9414 − 2 (3000)	0.1645 − 1 (2800)
0	0.1804 + 2	0.3182 + 2	0.3778 + 2
	0.2704 − 2 (1250)	0.1379 − 1 (3000)	0.5188 − 2 (1740)
2	0.1796 + 2	0.3180 + 2	0.3778 + 2
	0.4085 − 1 (3000)	0.8194 − 3 (3000)	0.4325 − 2 (3000)
4	0.1799 + 2	0.3184 + 2	0.3785 + 2
	0.4492 − 2 (1250)	0.2235 − 1 (3000)	0.5241 − 2 (1740)
	Wing B		
−2	0.1740 + 2	0.3072 + 2	0.3524 + 2
	0.1915 − 2 (2000)	0.1680 − 1 (3000)	0.1610 − 1 (3000)
0	0.1732 + 2	0.3057 + 2	0.3507 + 2
	0.1389 − 1 (2000)	0.9693 − 2 (3000)	0.1079 − 1 (3000)
2	0.1726 + 2	0.3047 + 2	0.3495 + 2
	0.7426 − 2 (2000)	0.9363 − 3 (3000)	0.5453 − 2 (3000)
4	0.1716 + 2	0.3043 + 2	0.3490 + 2
	0.4513 − 1 (2000)	0.7306 − 2 (3000)	0.6130 − 2 (3000)
	Wing C		
−2	0.1732 + 2	0.3054 + 2	0.3507 + 2
	0.8751 − 2 (2800)	0.1141 − 1 (2800)	0.2068 − 1 (2800)
0	0.1723 + 2	0.3045 + 2	0.3489 + 2
	0.1558 − 1 (2800)	0.3092 − 2 (2800)	0.8481 − 2 (2800)
2	0.1717 + 2	0.3034 + 2	0.3477 + 2
	0.9070 − 2 (2800)	0.2282 − 2 (2800)	0.8982 − 2 (2800)
4	0.1714 + 2	0.3029 + 2	0.3471 + 2
	0.3568 − 2 (2800)	0.3023 − 1 (2800)	0.5526 − 2 (2800)
	Wing D		
−2	0.1732 + 2	0.3073 + 2	0.3525 + 2
	0.1647 − 1 (2800)	0.1922 − 1 (2800)	0.1205 − 1 (2800)
0	0.1724 + 2	0.3057 + 2	0.3506 + 2
	0.2324 − 1 (2800)	0.1560 − 1 (2800)	0.1853 − 1 (3000)
2	0.1718 + 2	0.3046 + 2	0.3494 + 2
	0.2396 − 1 (2800)	0.1082 − 2 (2800)	0.1867 − 2 (3000)
4	0.1715 + 2		0.3488 + 2
	0.1793 − 1 (2800)		0.2026 − 2 (2800)

Table 2. Total change in the average residual in ( ) iterations in orders of magnitude. (FLO57C)

Angle of attack	Mach number		
	Wing A		
	0.4	0.7	0.8
-2	2.30 (3000)	3.53 (3000)	3.36 (2800)
0	3.82 (1250)	3.36 (3000)	3.66 (1740)
2	2.64 (3000)	4.59 (3000)	3.94 (3000)
4	3.60 (1250)	3.15 (3000)	3.86 (1740)
	Wing B		
-2	3.96 (2000)	3.26 (3000)	3.34 (3000)
0	3.10 (2000)	3.50 (3000)	3.51 (3000)
2	3.37 (2000)	4.51 (3000)	3.81 (3000)
4	2.55 (2000)	3.62 (3000)	3.75 (3000)
	Wing C		
-2	3.29 (2800)	3.43 (2800)	3.23 (2800)
0	3.04 (2800)	3.99 (2800)	3.61 (2800)
2	3.28 (2800)	4.12 (2800)	3.59 (2800)
4	3.68 (2800)	3.00 (2800)	3.80 (2800)
	Wing D		
-2	3.02 (2800)	3.20 (2800)	3.47 (2800)
0	2.87 (2800)	3.29 (2800)	3.28 (3000)
2	2.86 (2800)	4.45 (2800)	4.27 (3000)
4	2.98 (2800)		4.24 (2800)

Table 3. Computational run summary for generic fighter

Mach	α	Configuration	Iterations	CPU time (hr)
0.60	4.0	W/B	1200	3.4
	8.0		1650	4.72
	12.0		2100	6.01
	16.0		2300	6.58
	20.0		2800	8.01
0.60	4.0	W/B/C	2000	5.72
	8.0		2000	5.72
	12.0		1800	5.15
	16.0		1800	5.15
	20.0		2400	6.87
0.80	5.0	W/B	1600	4.58
	8.0		2100	6.01
	12.0		3050	8.73
	16.0		3200	9.16
	20.0		3500	10.01
0.80	8.0	W/B/C	2300	6.58
	12.0		2500	7.15
	16.0		2400	6.87
	20.0		2900	8.30

Table 4. Grid information and memory requirements for FLO57—delta wing

Grid	i dim	j dim	k dim	Surface points	Total points	Memory MW	CPU sec/case
Coarse	67	21	43	45 × 43	60,501	2	3,100
Medium	89	29	57	57 × 57	147,117	4	7,800
Fine	113	37	73	73 × 73	305,213	8	18,000

Table 5. CFD solutions—delta wing

Mach	α	Coarse	Medium	Fine	PANAIR
0.4	−4,−2,0,2,4,6,8,10	X	X		X
0.7	−4,−2,0,2,4,6,8,10	X	X		X
0.8	−4,−2,0,2,4,6,8,10	X	X	X	X

27
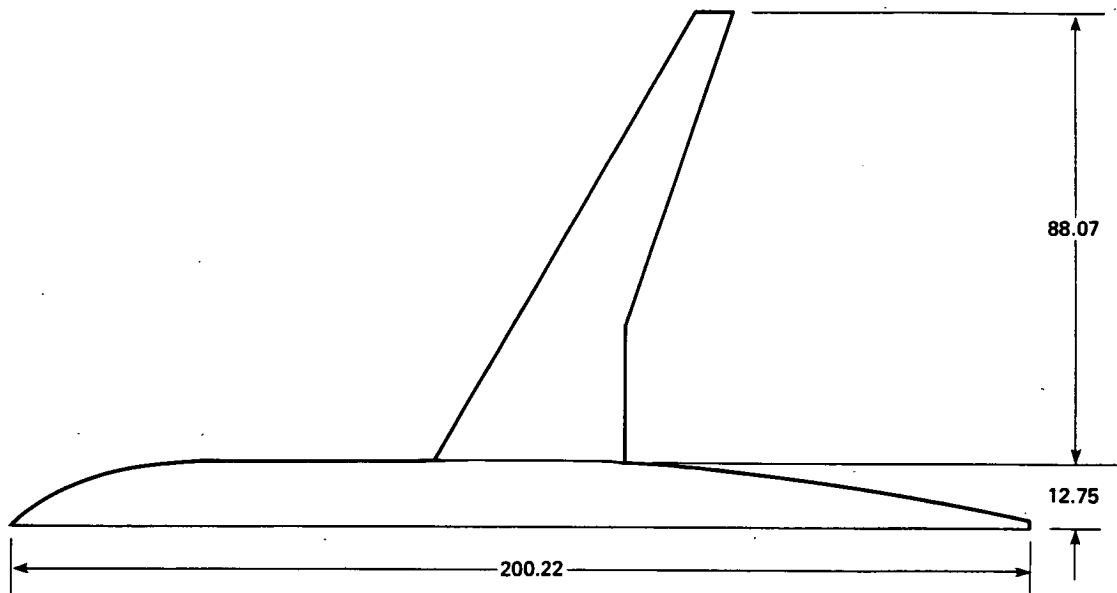
Fig. 1. Commercial transport wing/body.

Fig. 2. Semispan model in the NASA Ames 11-Foot Transonic Wind Tunnel (installation photograph).
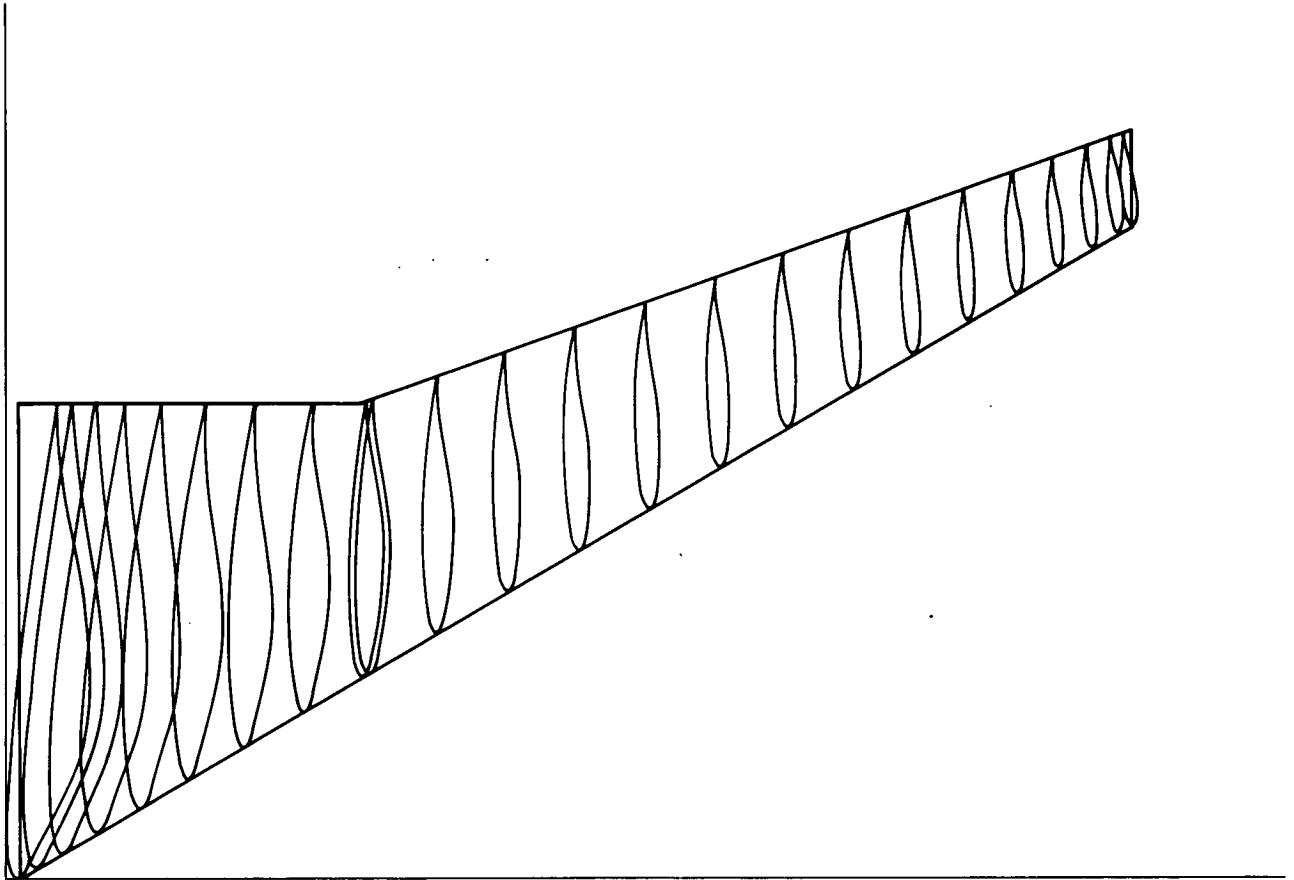
Fig. 3. Wing planform with defining sections.

Fig. 4. Wing sections.

0.777

0.825

0.869

0.908

0.941

0.968

0.990

1.000
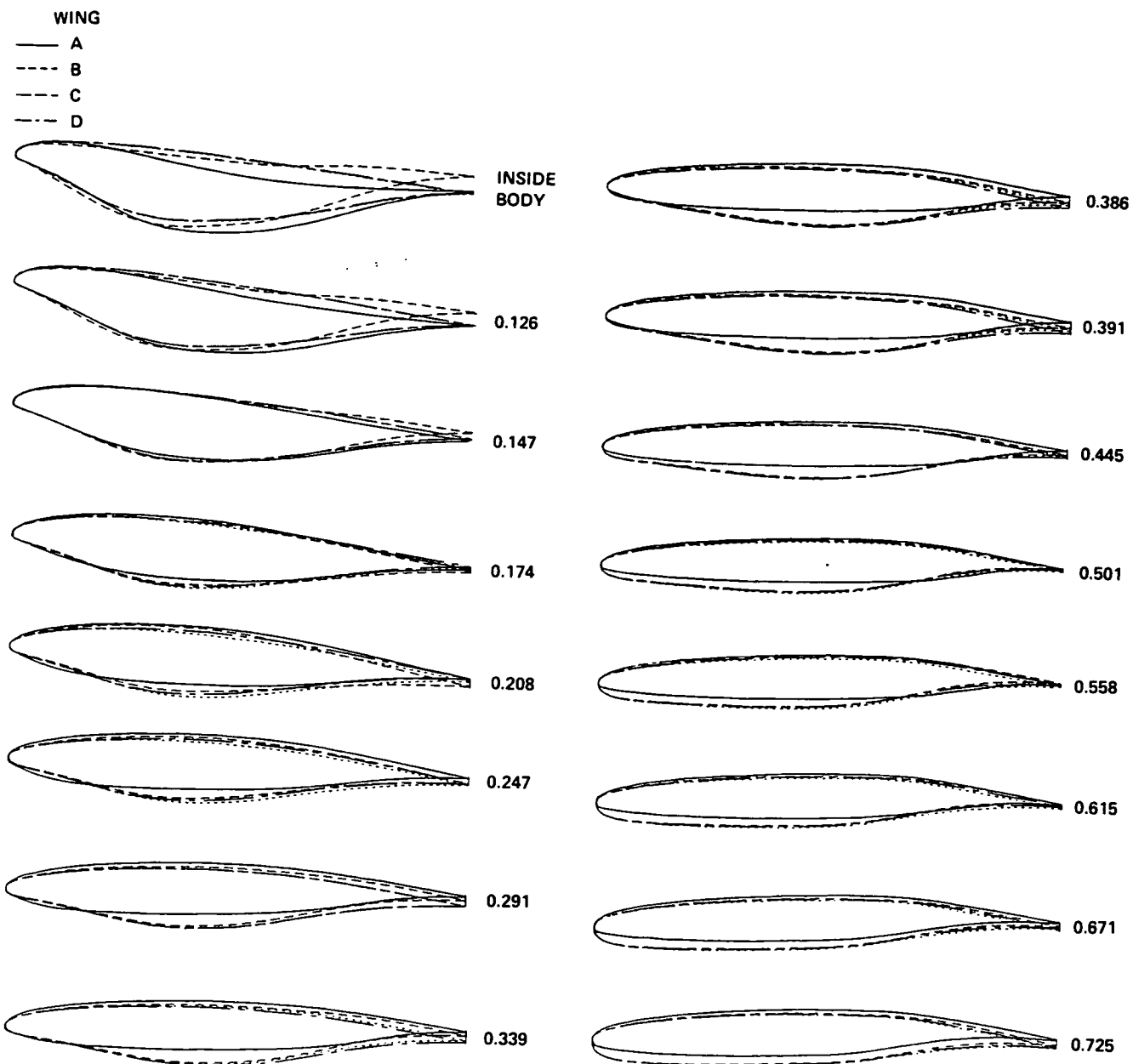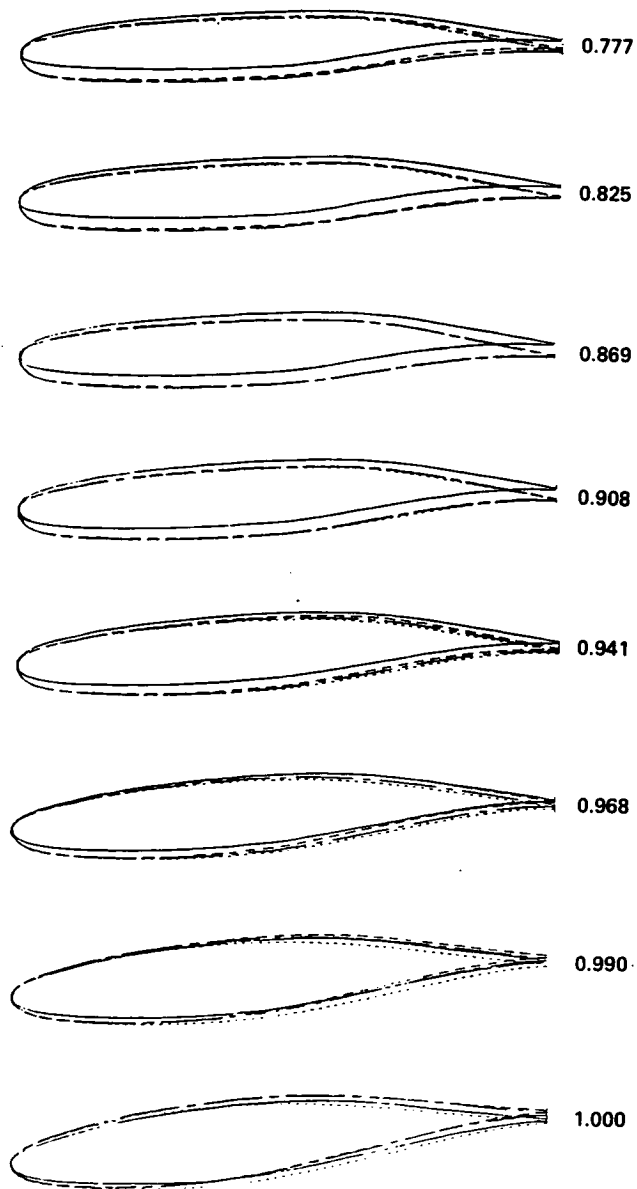
Fig. 4. Concluded.
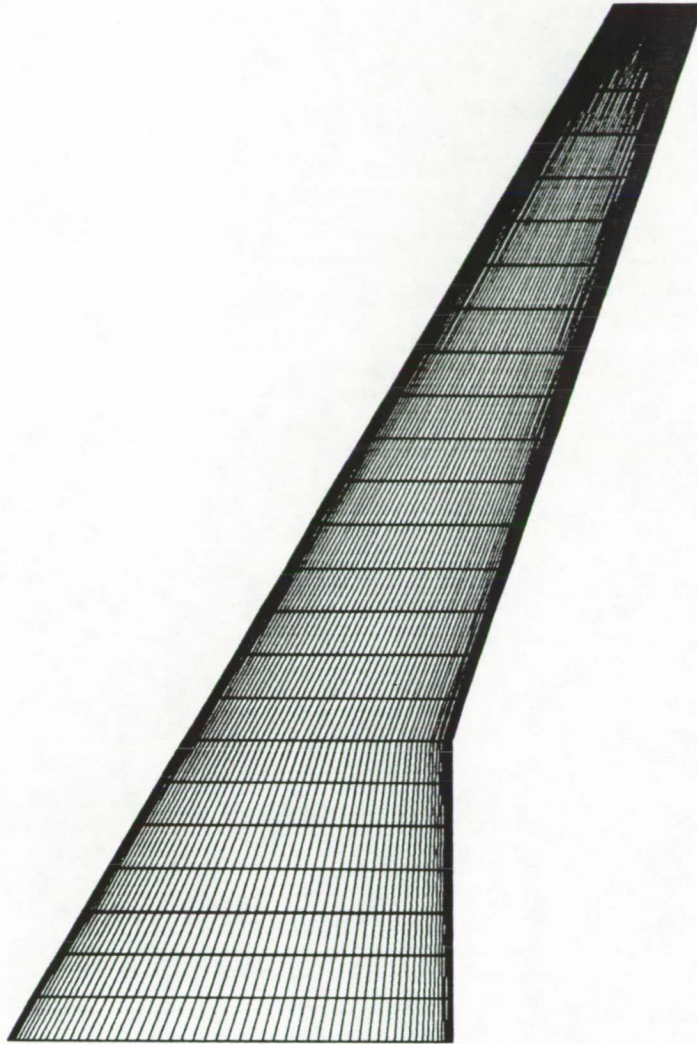
Fig. 5. C-H grid distribution on wing surface, 151 x 31 x 31 points.
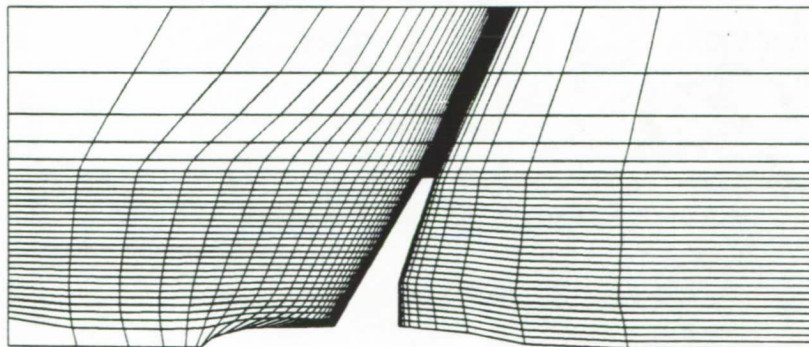
Fig. 6. C-H-grid distribution in plane of wing, 151 x 31 x 31 points.
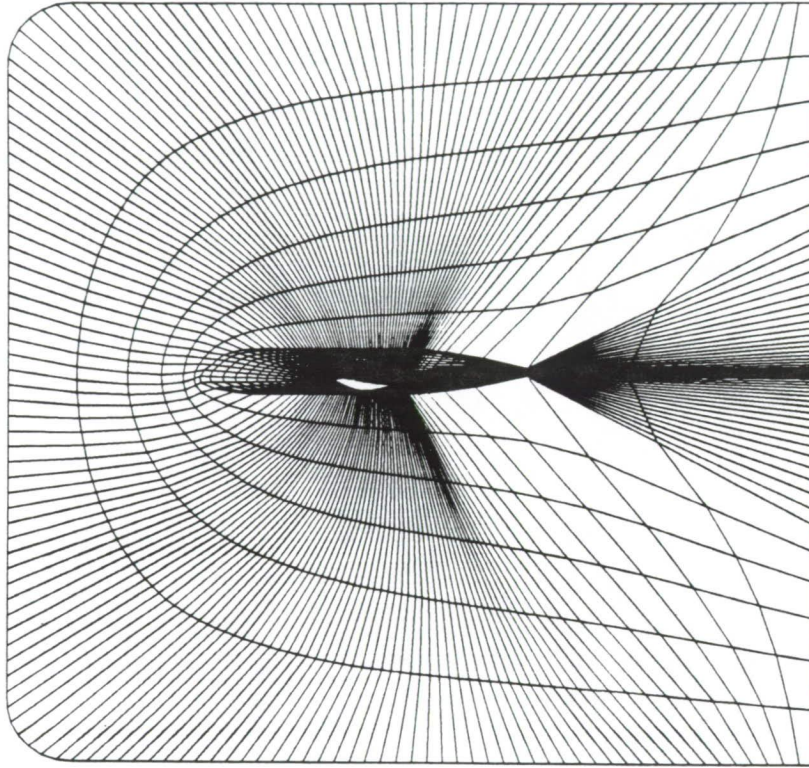
Fig. 7. C-H-grid distribution on center-plane, 151 x 31 x 31 points.
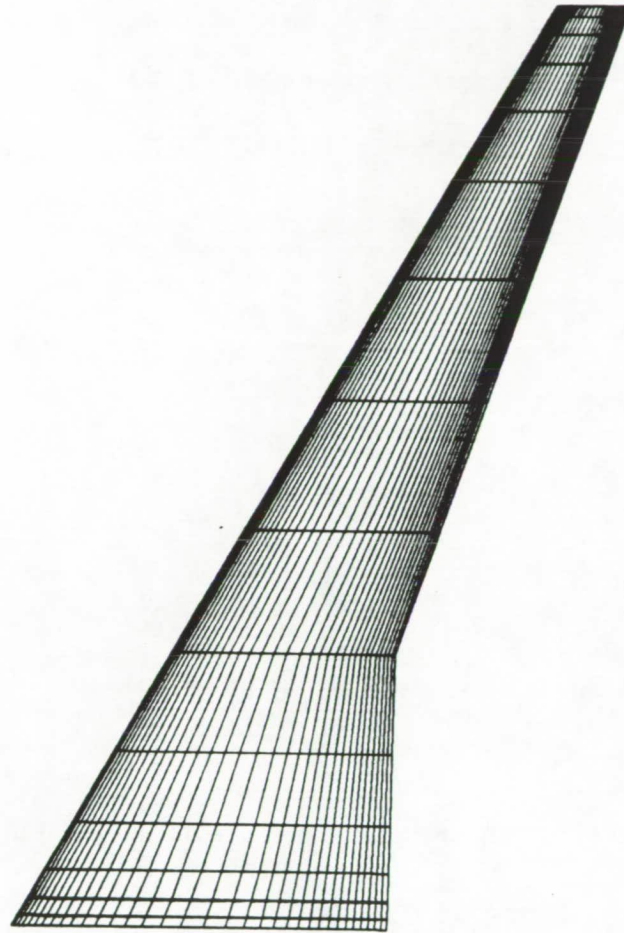
Fig. 8. H-O-grid distribution on wing surface, 101 x 29 x 45 points.
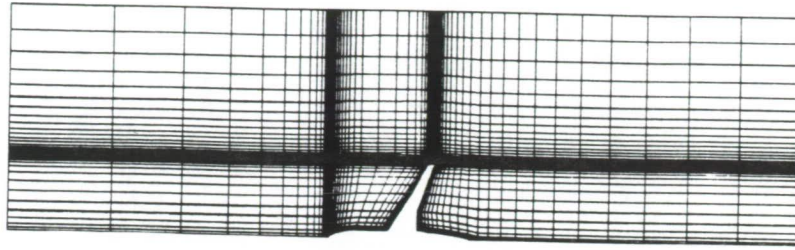
Fig. 9. H-O-grid distribution in plane of wing, 101 x 29 x 45 points.
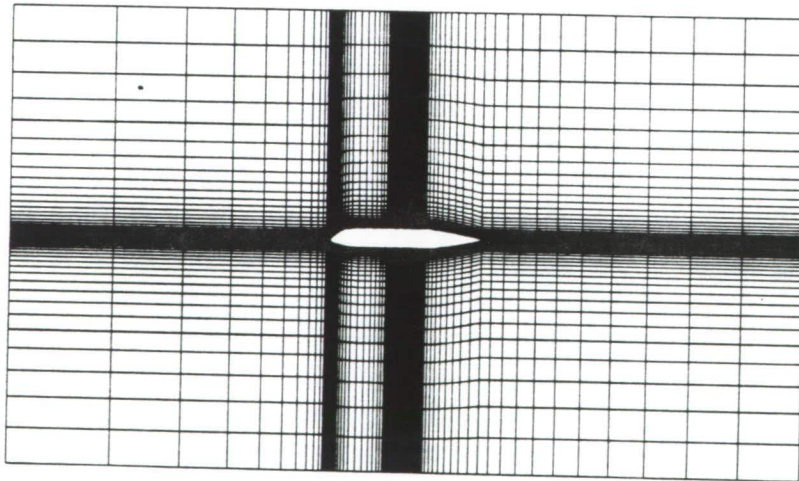
Fig. 10. H-O-grid distribution on center-plane, 101 x 29 x 45 points.

	M_∞	α	Re x 10^{-6}	C_L	C_D	C_M
O, □ EXPERIMENT	.401	-1.491	5.092	.052	.023	-.074
—— FLO57C	.400	-2.000	—	.042	.016	-.108
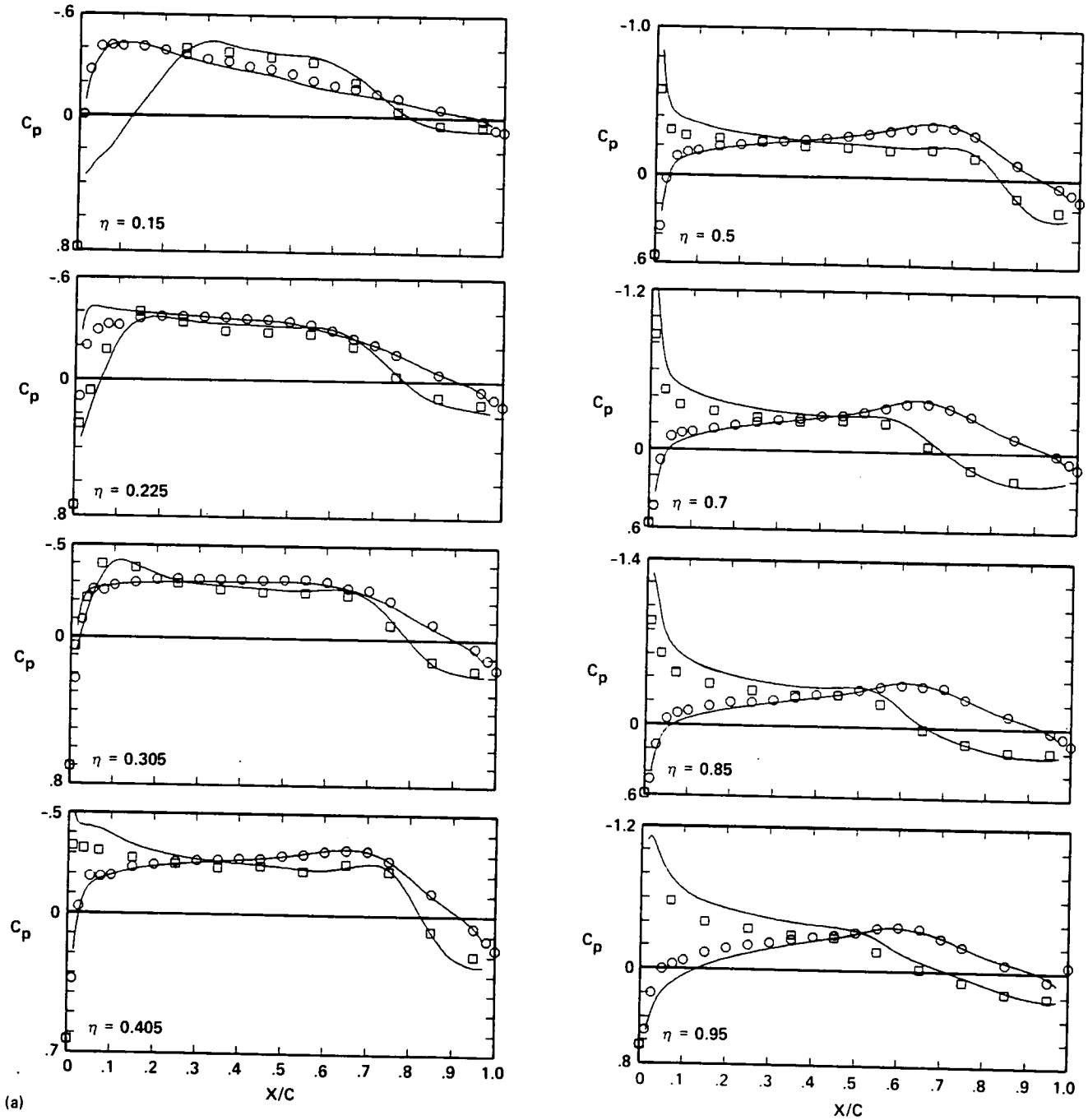
Fig. 11. Experiment-CFD pressure-distribution comparison for wing A, FLO57C.

37

	M_∞	α	Re x 10^{-6}	C_L	C_D	C_M
O, □ EXPERIMENT	.400	.488	5.082	.226	.025	-.075
— FLO57C	.400	0	—	.210	.021	-.065
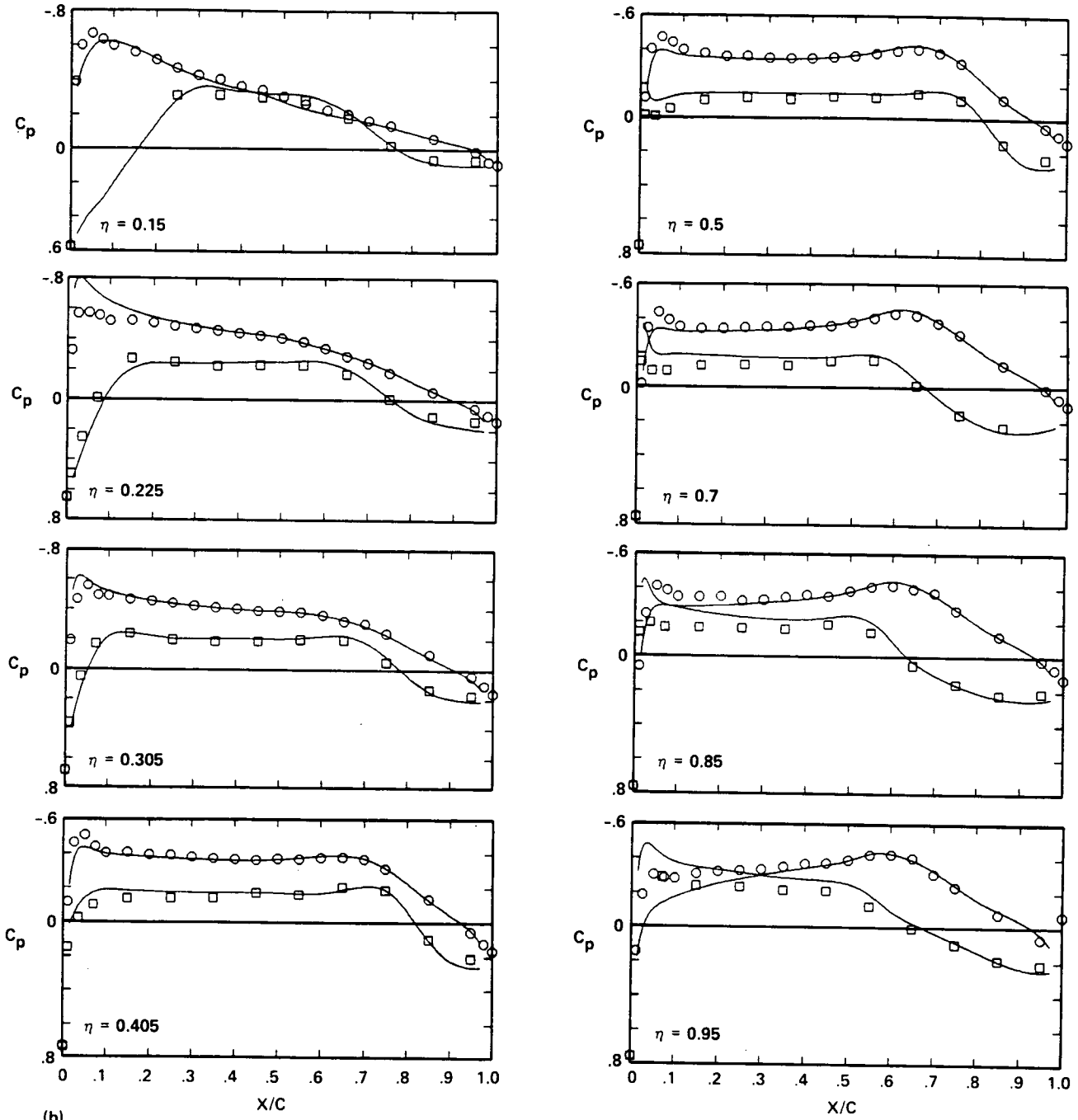
(b)

Fig. 11. Continued.

Fig. 11. Continued.

39

		M_∞	α	Re x 10^{-6}	C_L	C_D	C_M
○, □	EXPERIMENT	.400	4.470	5.081	.580	.039	-.056
—	FLO57C	.400	4.000	—	.595	.028	-.133

Fig. 11. Continued.

40
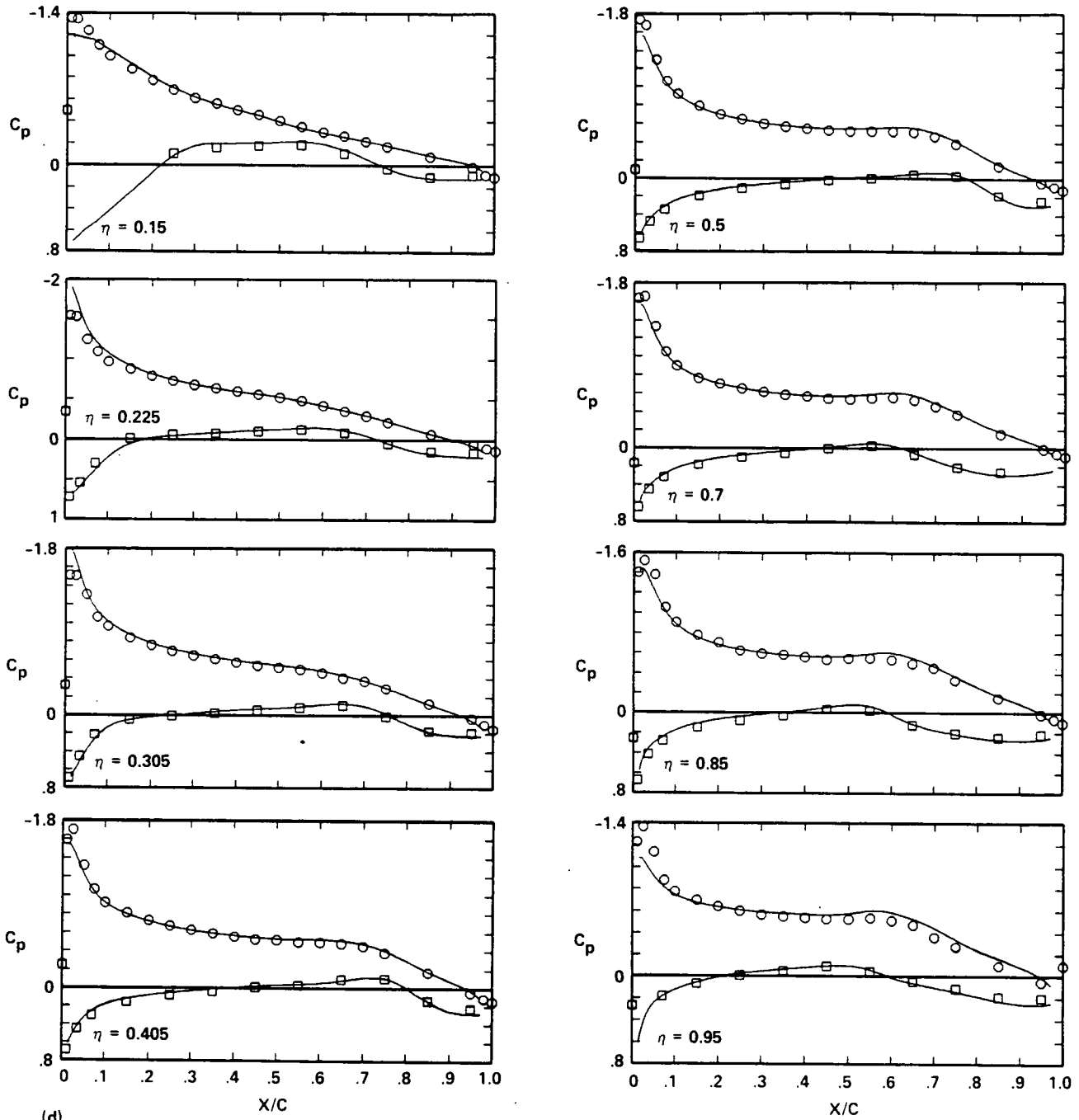
	M_∞	α	Re x 10^{-6}	C_L	C_D	C_M
O, □ EXPERIMENT	.699	-1.506	7.993	.050	.026	-.077
—— FLO57C	.700	-2.000	—	.021	.021	-.095
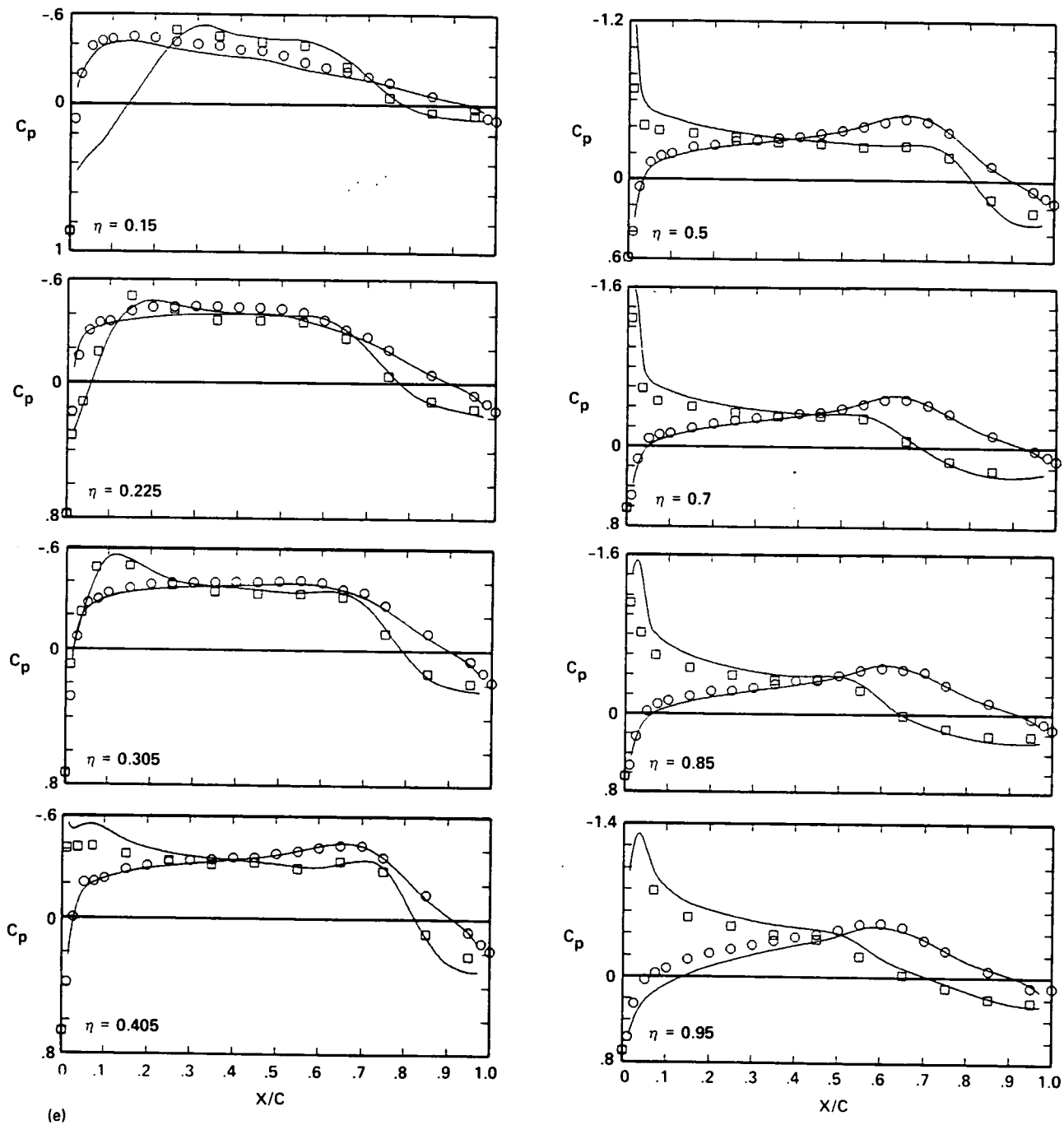
Fig. 11. Continued.

41
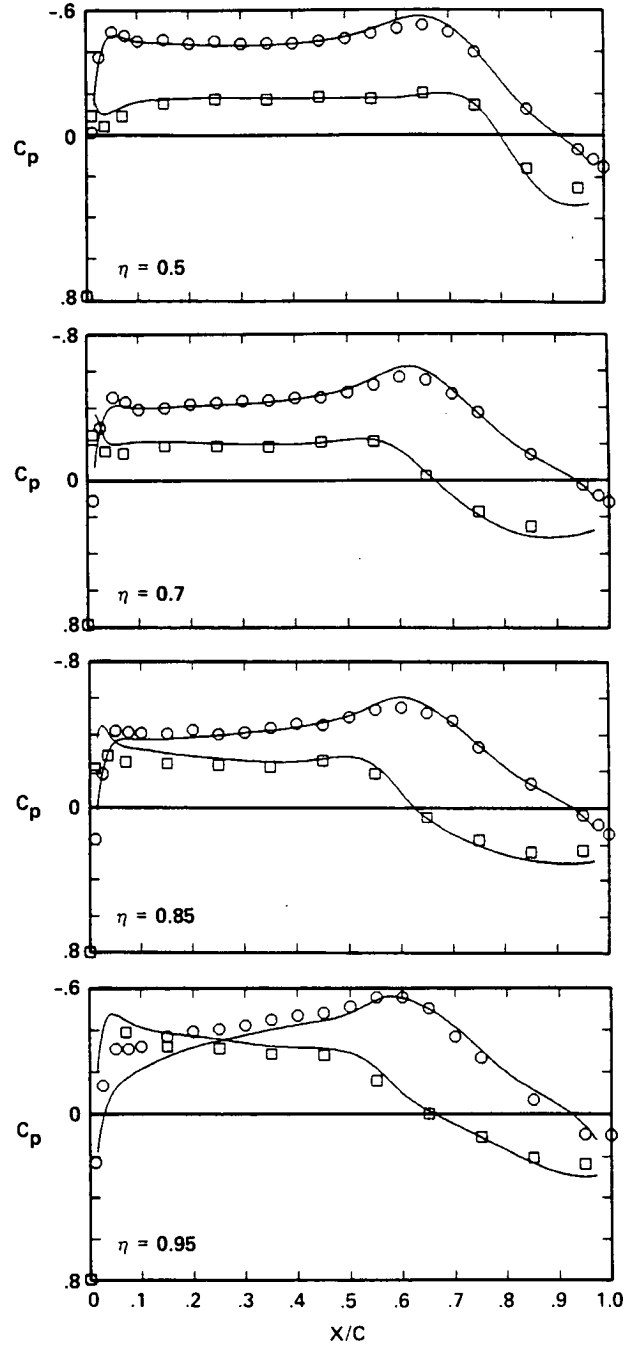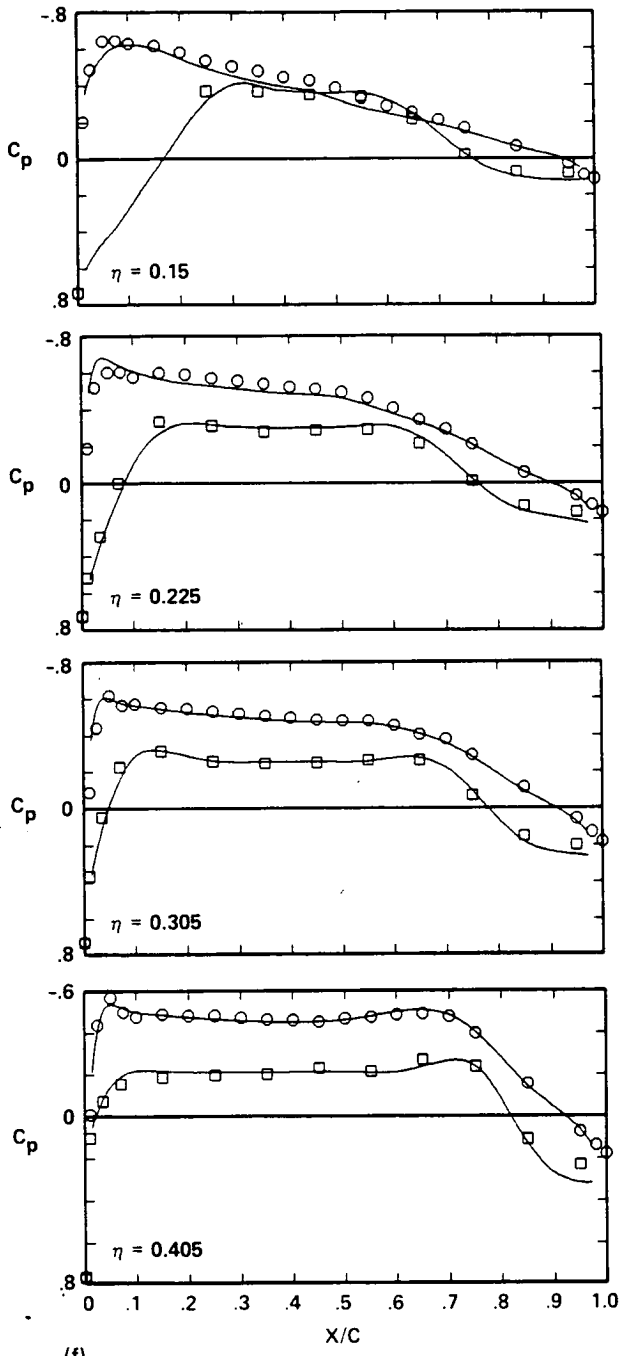
Fig. 11. Continued.

	M_∞	α	Re x 10^{-6}	C_L	C_D	C_M
O , □ EXPERIMENT	.700	2.762	7.926	.480	.037	-.084
——— FLO57C	.700	2.000	—	.480	.029	-.137

Fig. 11. Continued.

43
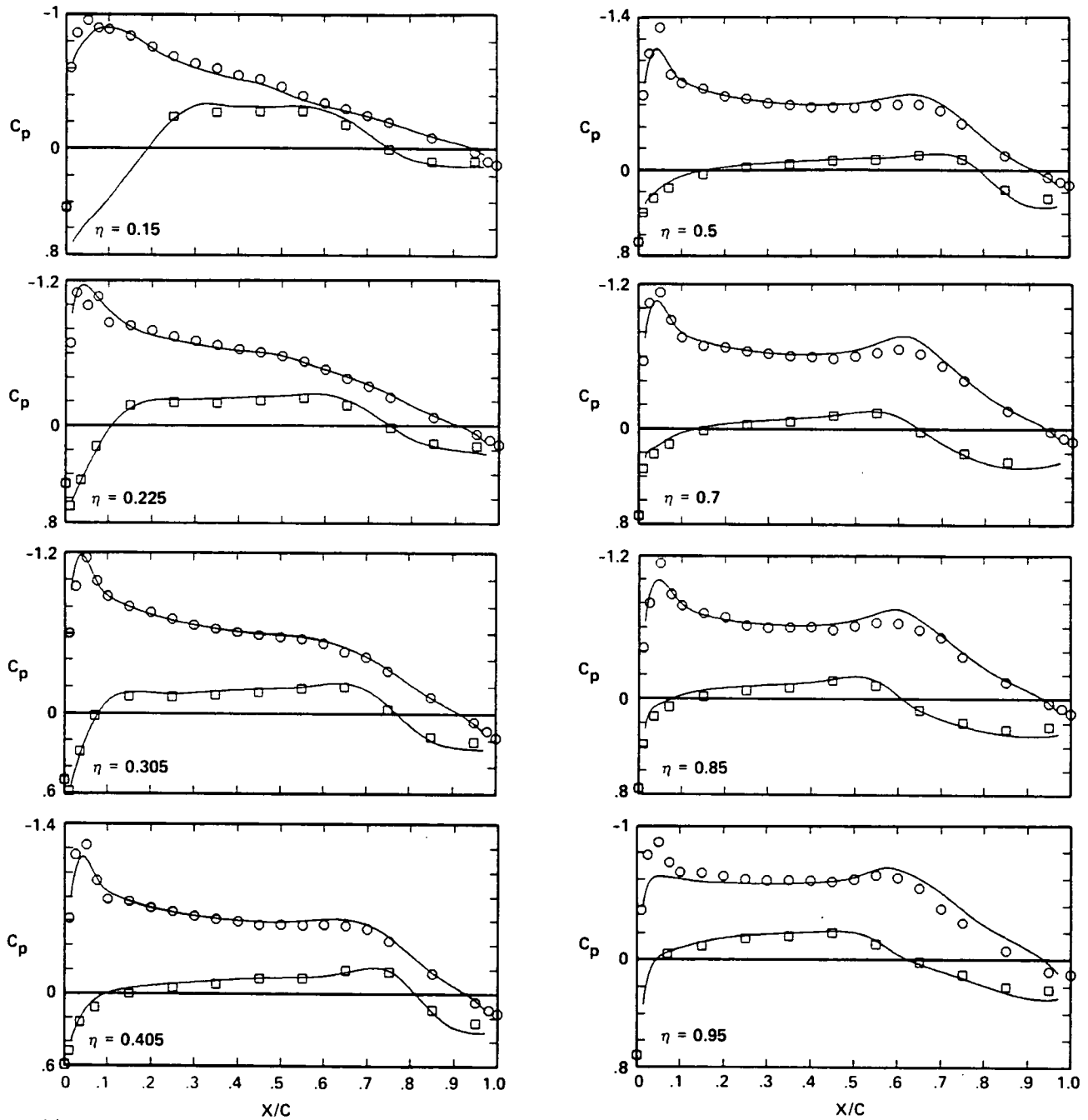
	M_∞	α	Re x 10^{-6}	C_L	C_D	C_M
O , □ EXPERIMENT	0.700	4.942	7.896	0.717	0.053	-0.076
FLO57C	0.700	4.000	—	0.715	0.041	-0.185

(h)
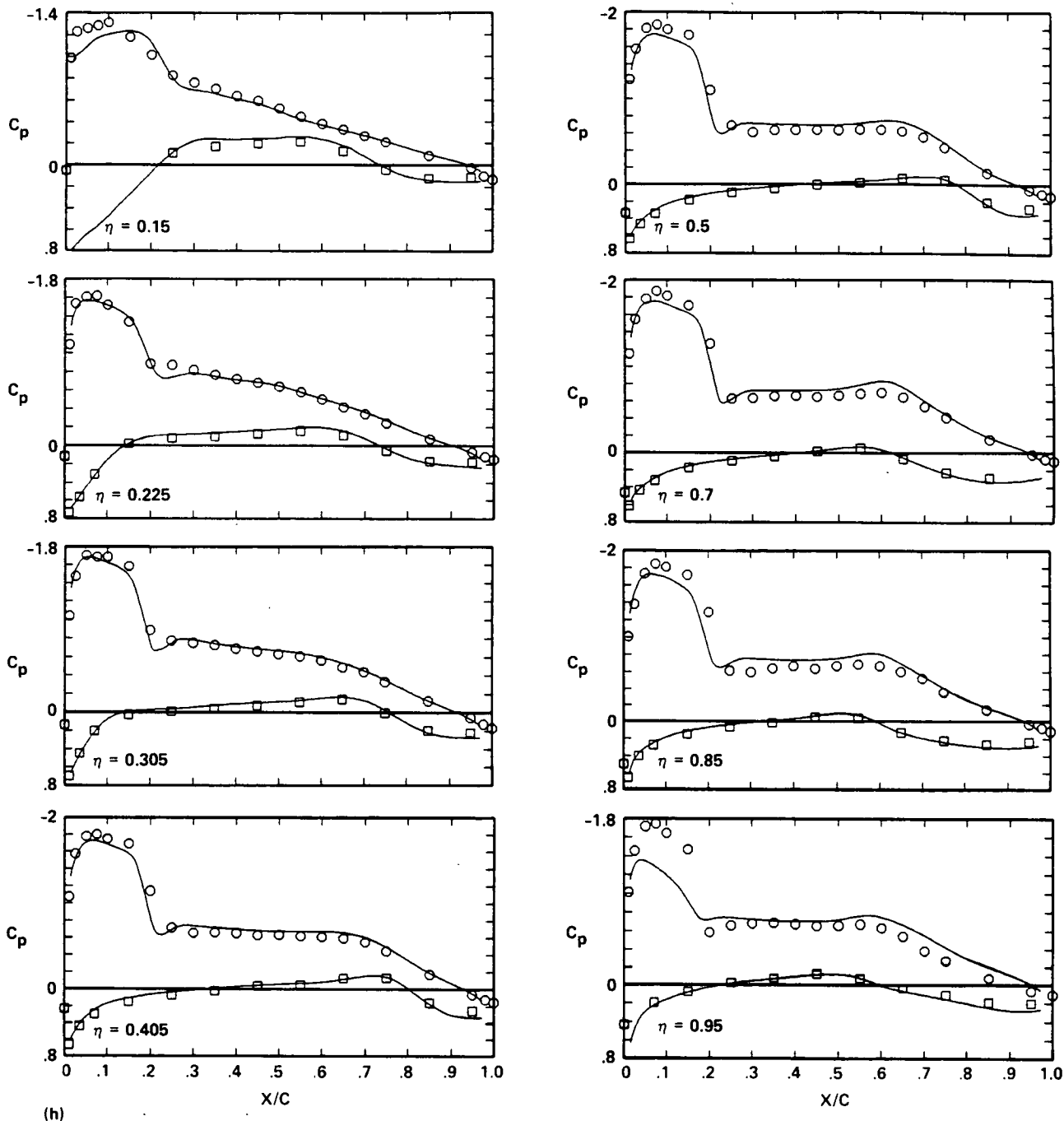
Fig. 11. Continued.

	M_∞	α	Re x 10^{-6}	C_L	C_D	C_M
O, □ EXPERIMENT	0.799	-1.530	8.286	0.047	0.029	-0.081
—— FLO57C	0.800	-2.000	—	0.017	0.028	-0.075
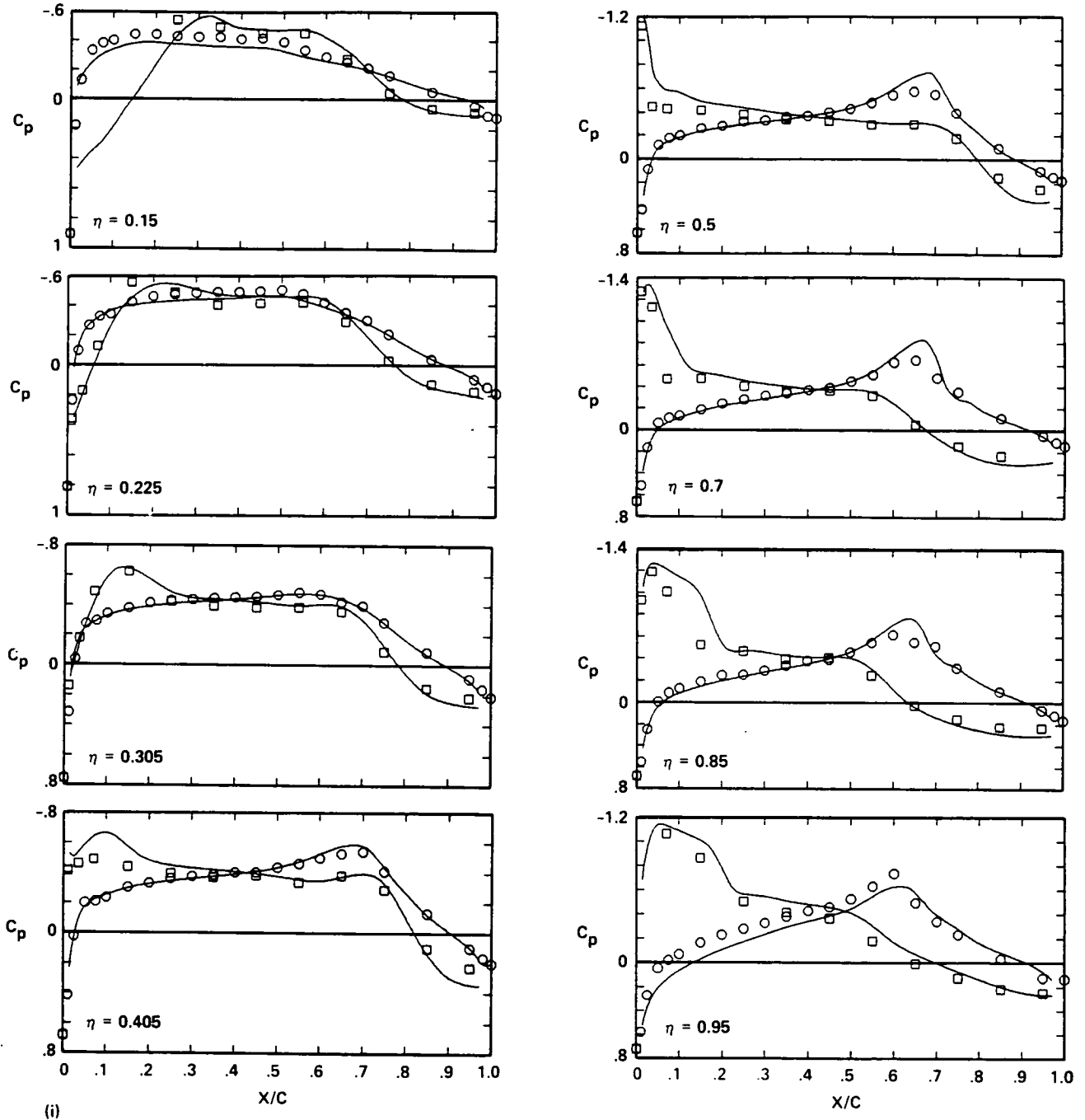
Fig. 11. Continued.

		M_∞	α	Re x 10^{-6}	C_L	C_D	C_M
O, □	EXPERIMENT	0.802	0.475	8.286	0.267	0.032	-0.099
	FLO57C	0.800	0	—	0.280	0.030	-0.121

(j)

Fig. 11. Continued.

46
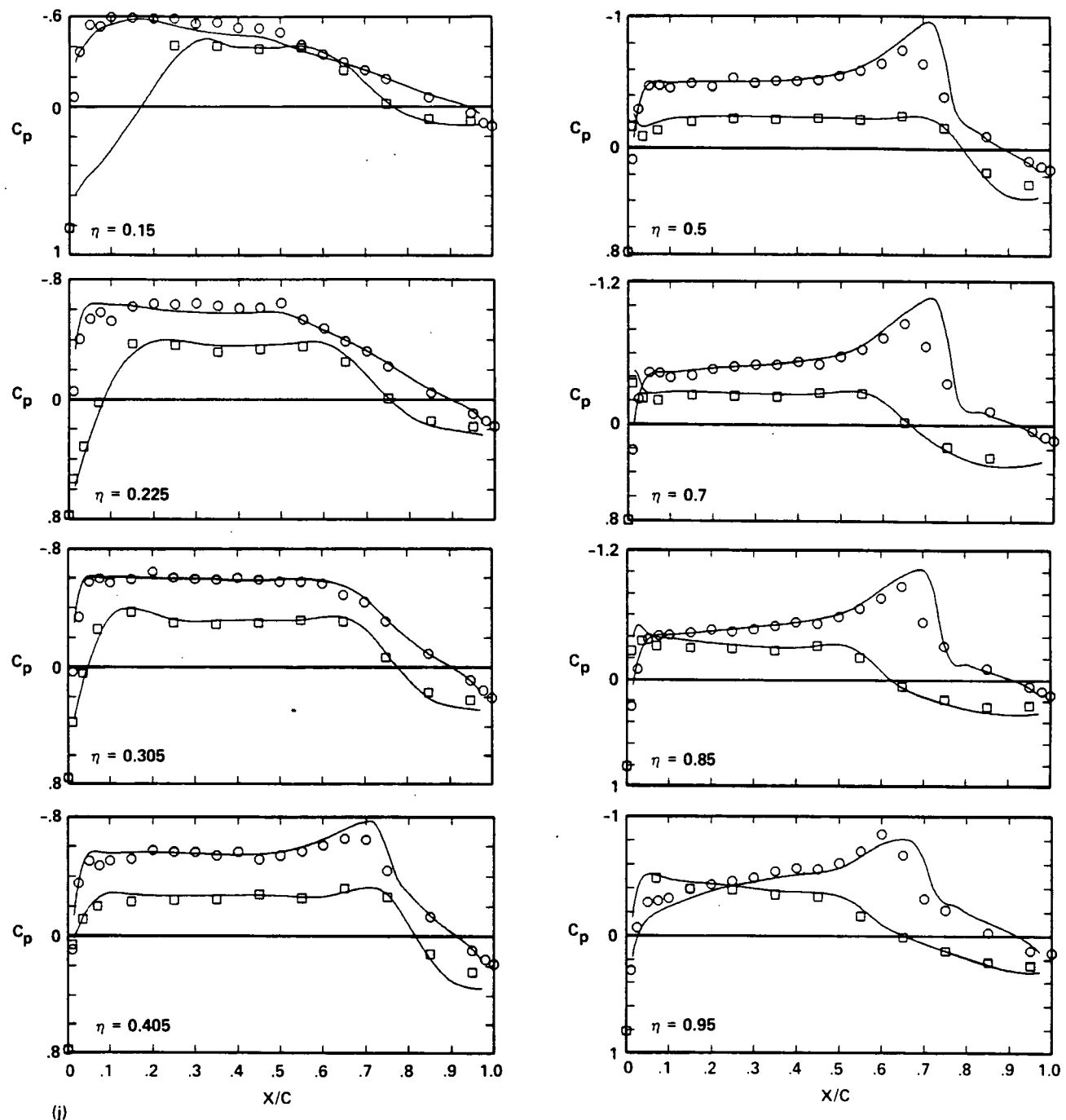
	M_∞	α	Re x 10^{-6}	C_L	C_D	C_M
○,□ EXPERIMENT	0.799	2.973	8.234	0.577	0.045	-0.117
—— FLO57C	0.800	2.000	—	0.570	0.038	-0.187
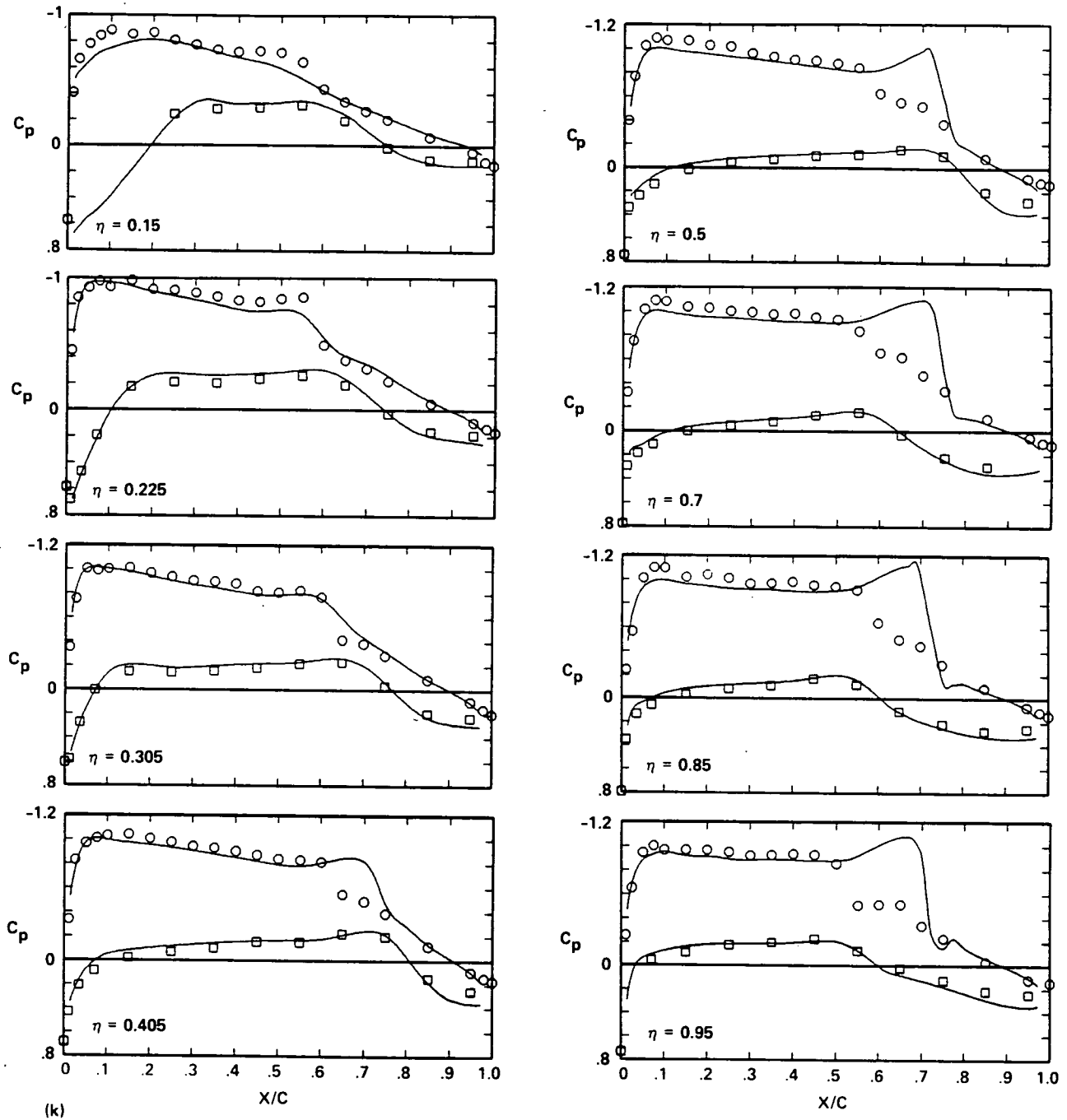
Fig. 11. Continued.

	M_∞	α	Re x 10^{-6}	C_L	C_D	C_M
○, □ EXPERIMENT	0.799	4.940	8.210	0.751	0.076	-0.088
—— FLO57C	0.800	4.000	—	0.849	0.073	-0.249
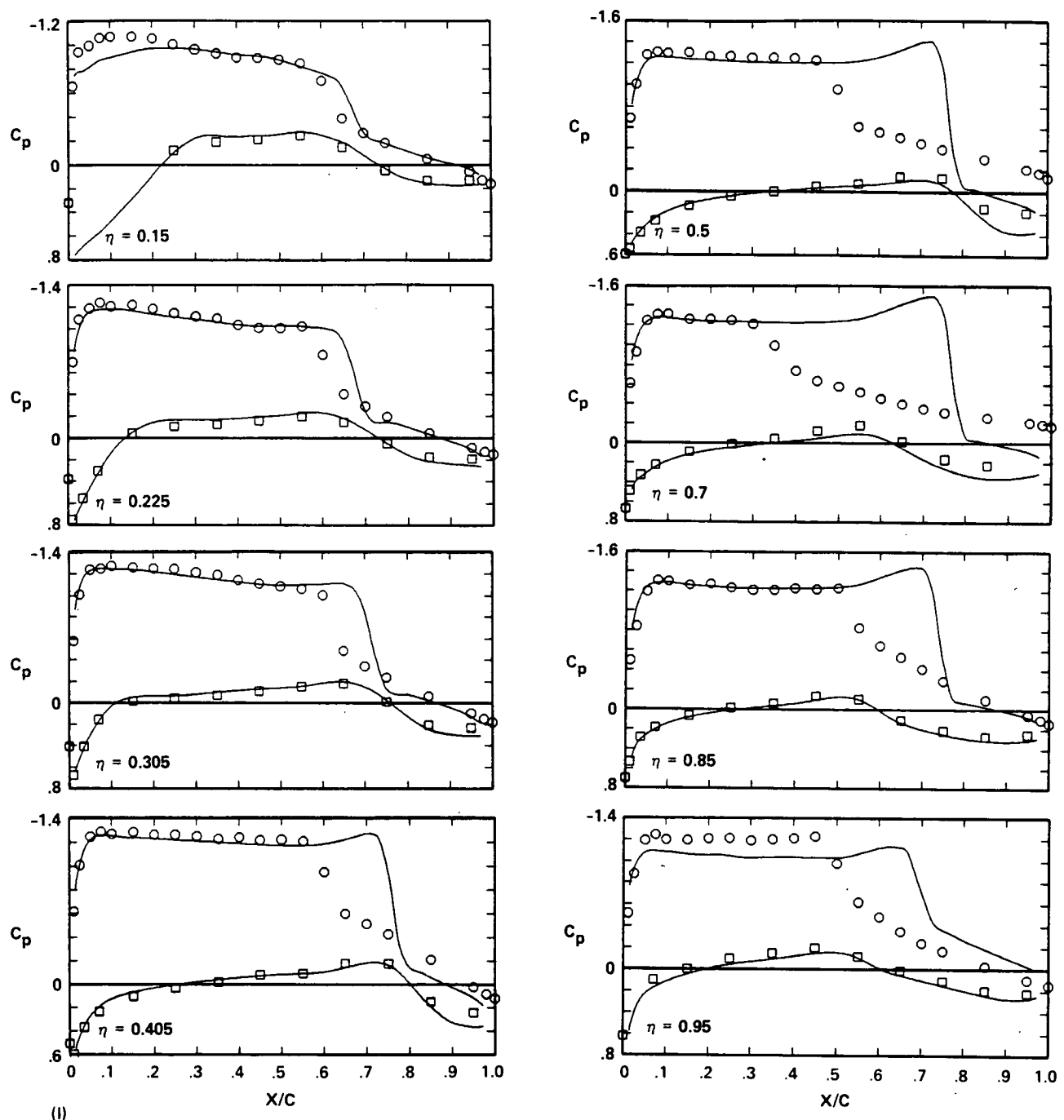
(l)

Fig. 11. Concluded.

48
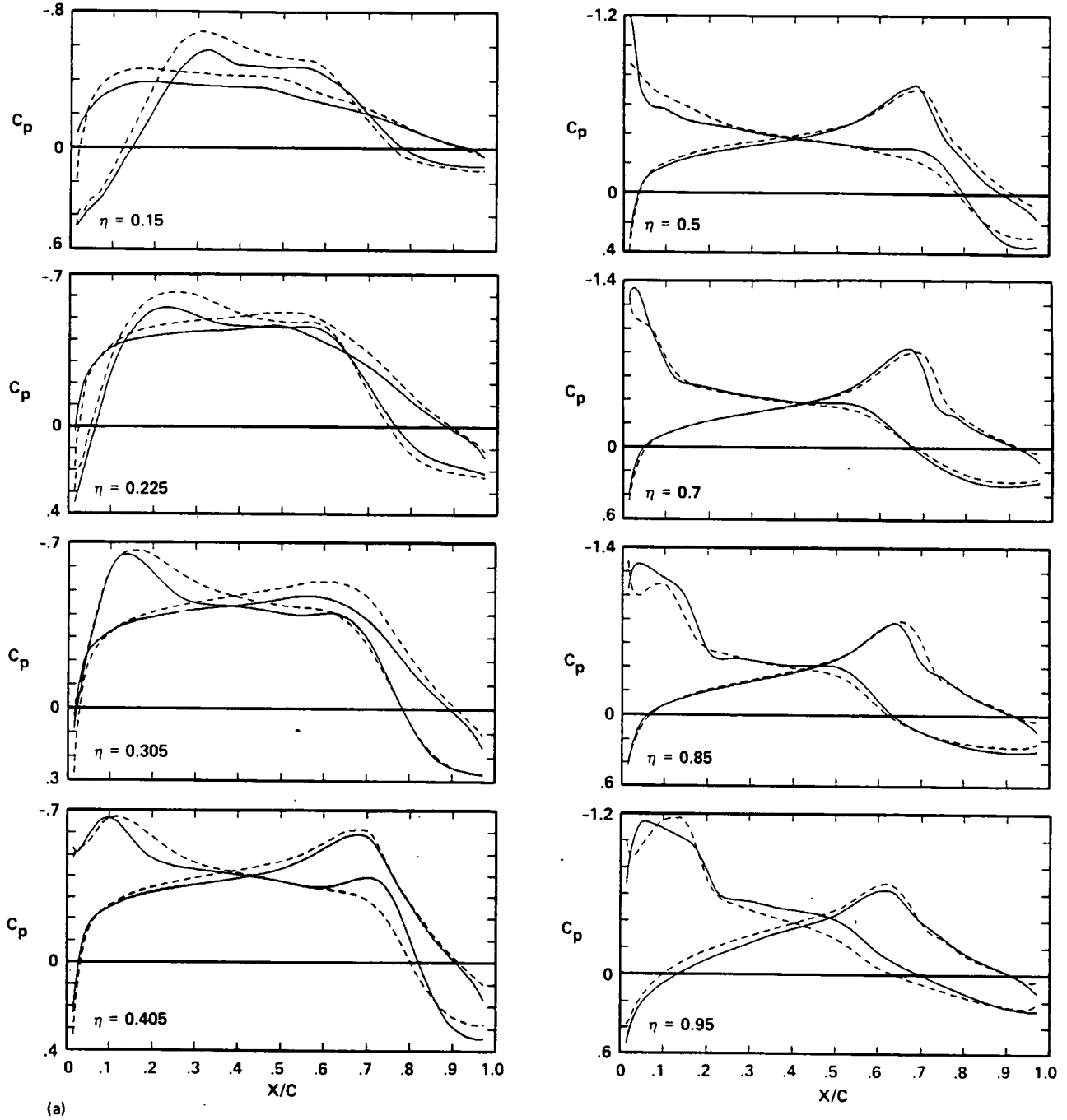
Fig. 12. Pressure-distribution comparison for Wing A, FLO57C and FLO57O.

	M_∞	α	C_L	C_D	C_M
FLO57C – 151 x 31 x 31	0.800	0	0.280	0.030	-0.121
FLO57O – 101 x 29 x 45	0.800	0	0.294	0.012	-0.129

Fig. 12. Continued.

50
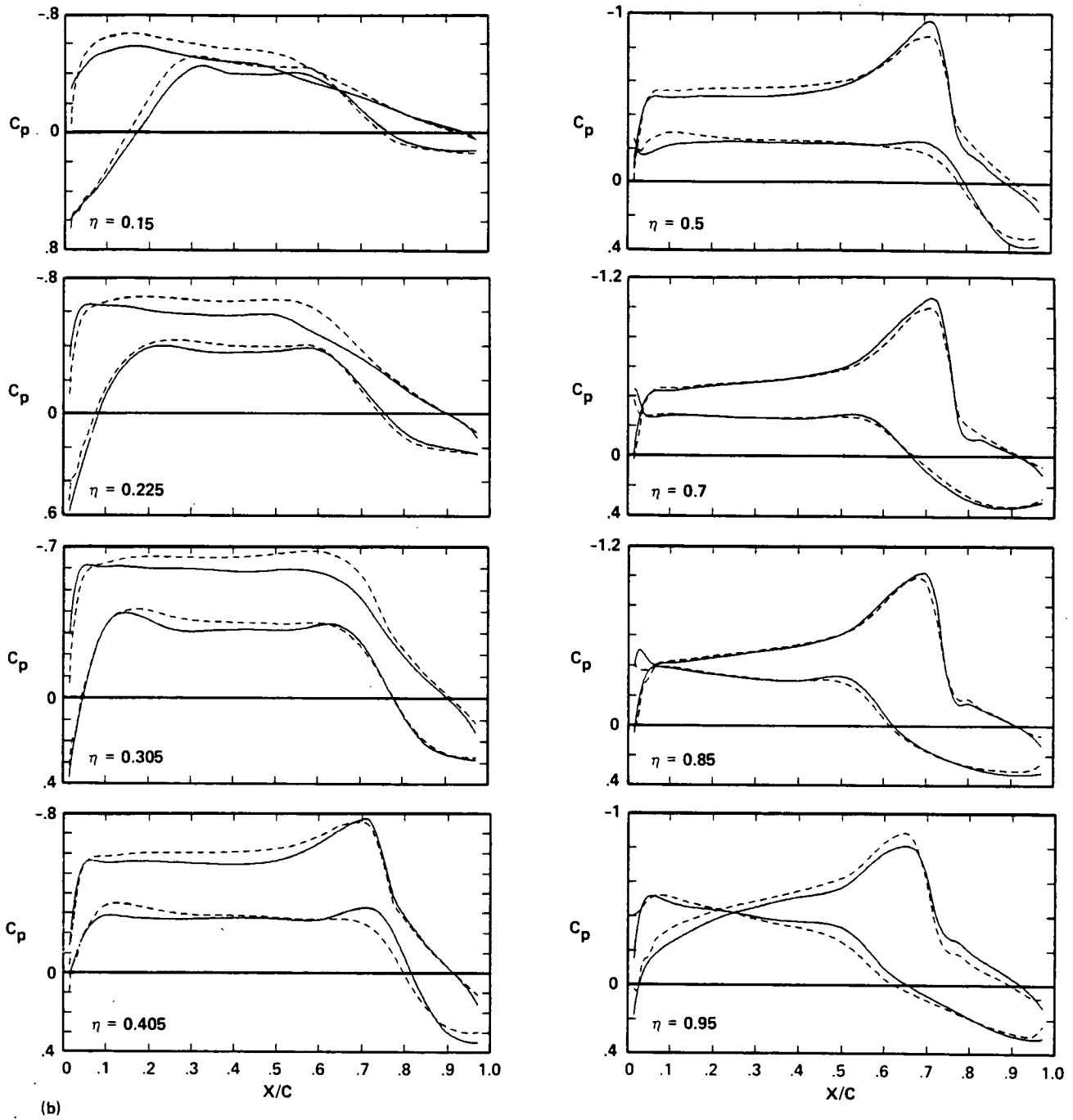
	M_∞	α	C_L	C_D	C_M
FLO57C – 151 x 31 x 31	0.800	2.000	0.570	0.038	–0.187
FLO57O – 101 x 29 x 45	0.800	2.000	0.596	0.023	–0.163
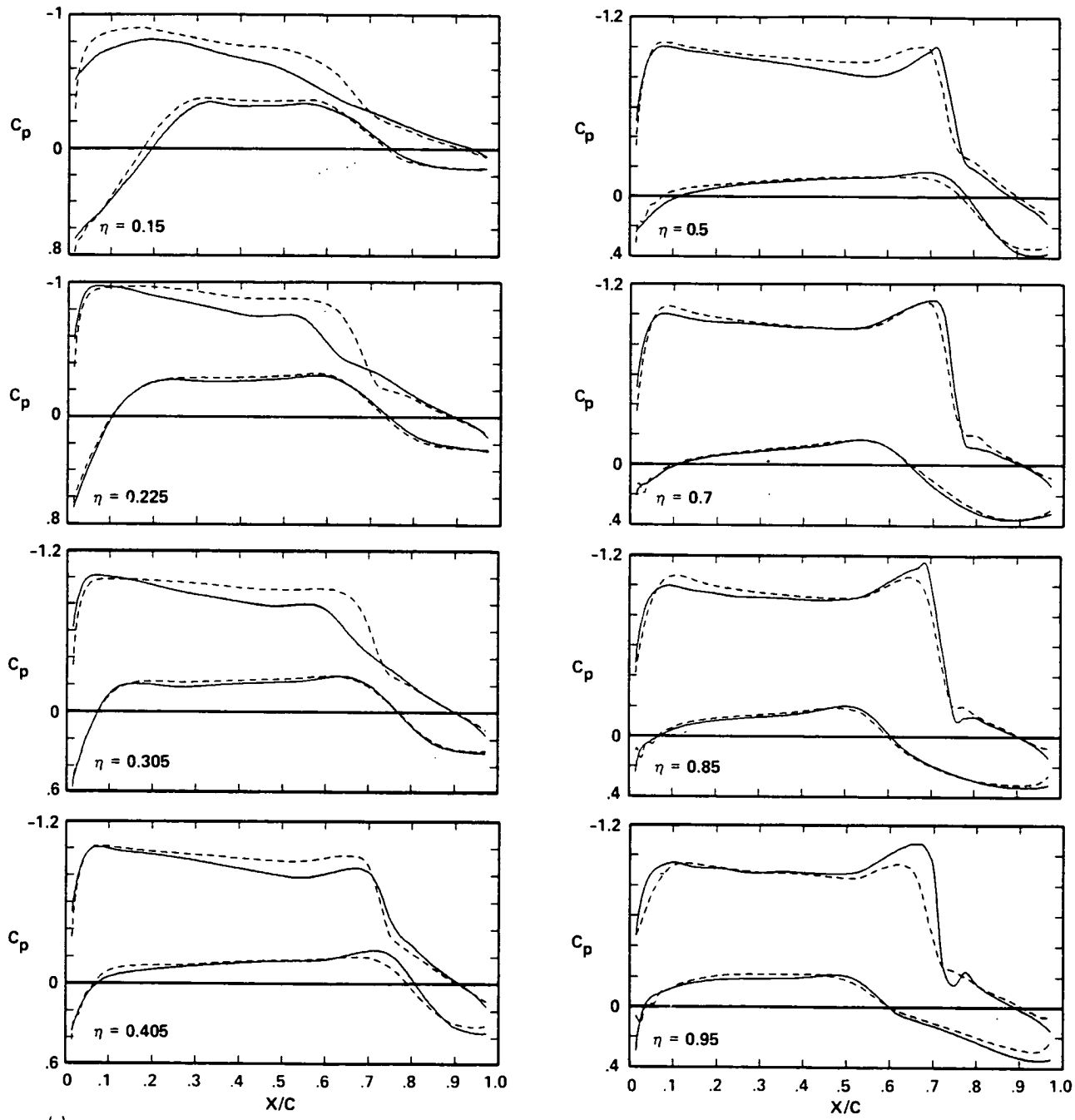
(c)

Fig. 12. Continued.
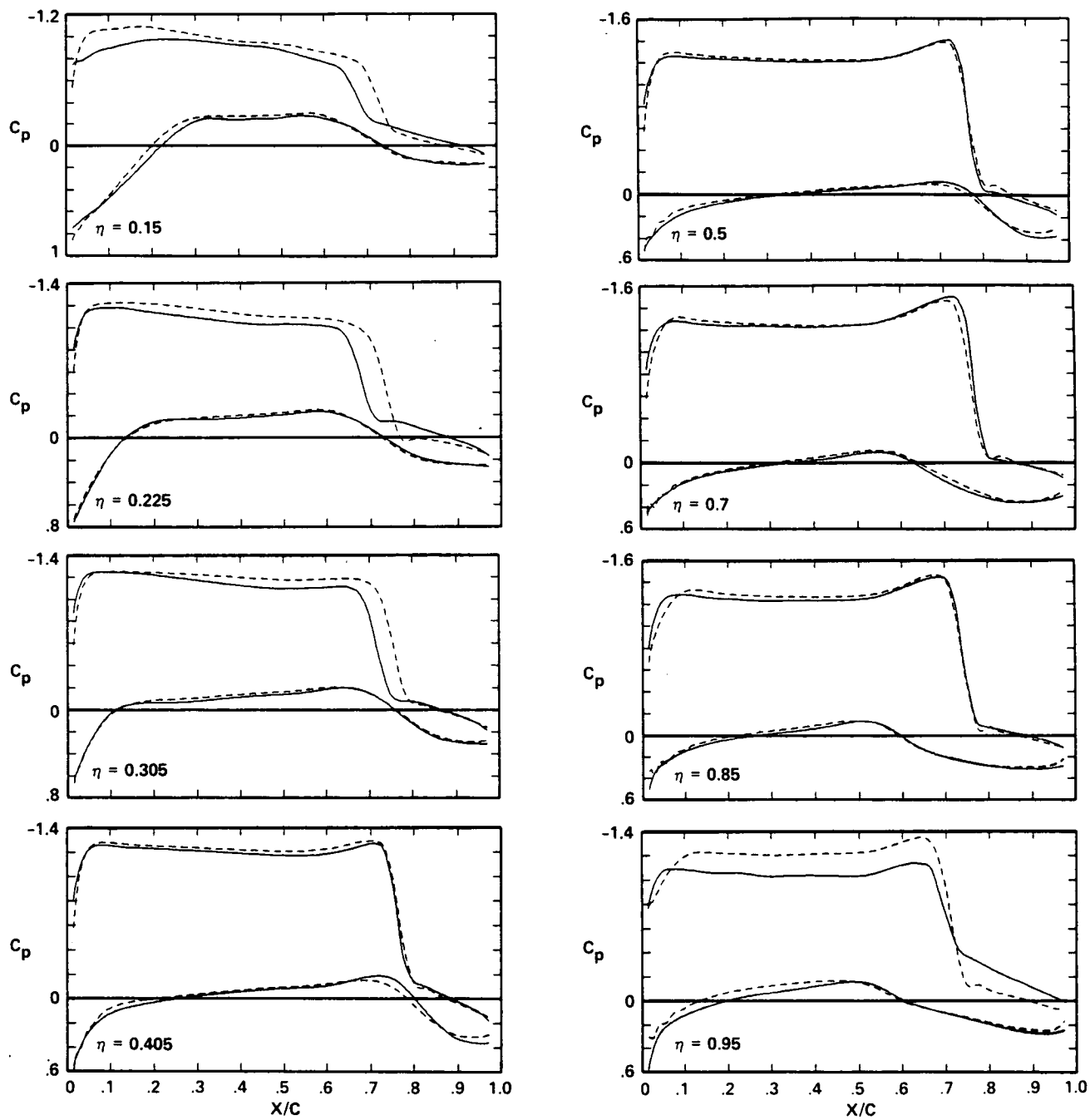
Fig. 12. Concluded.

	M_∞	α	Re x 10^{-6}	C_L	C_D	C_M
O, □ EXPERIMENT	0.801	2.023	8.280	0.443	0.039	-0.105
——— FLO60	0.800	2.000	—	0.444	0.025	-0.627
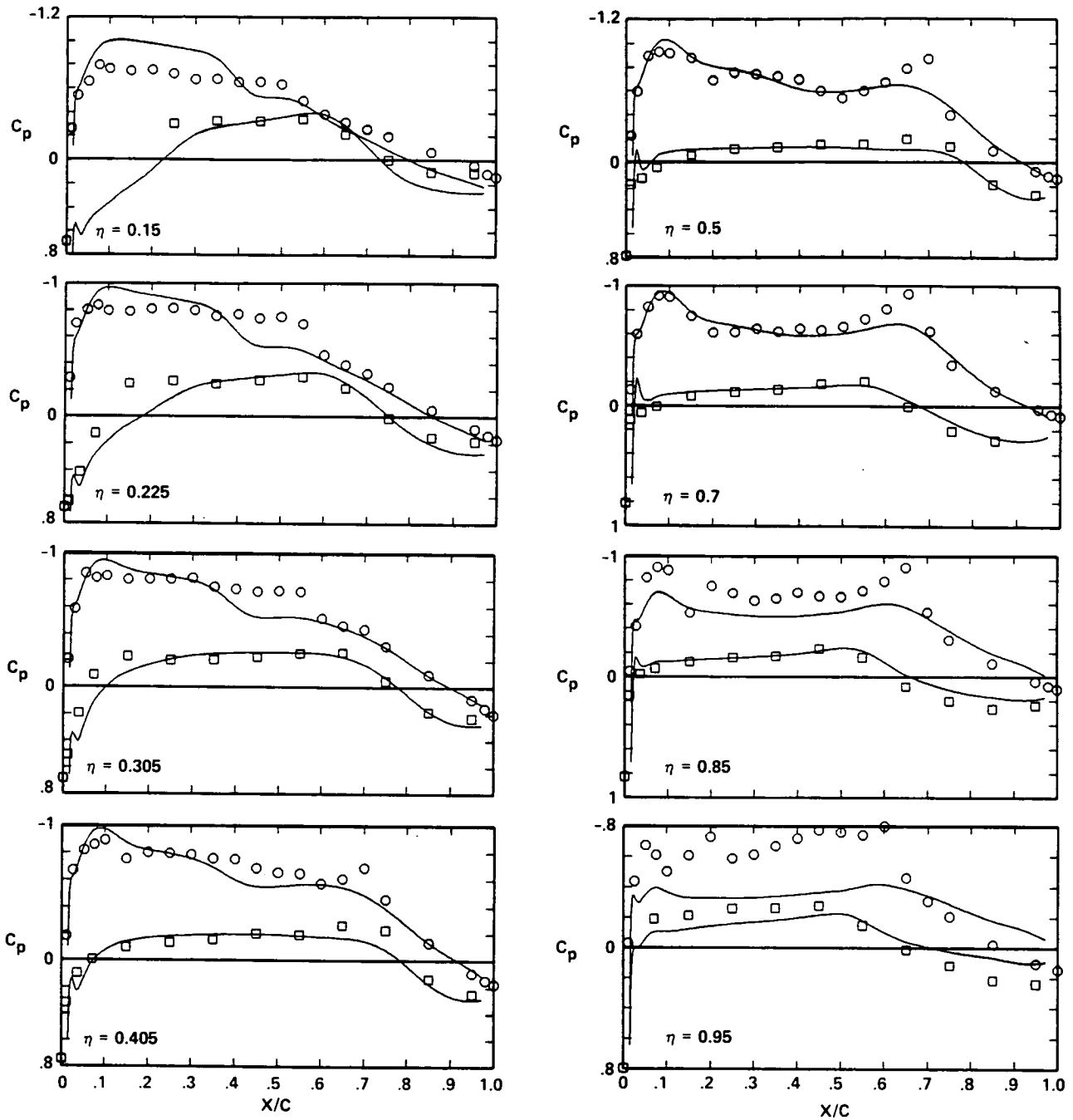
Fig. 13. Experiment–CFD pressure-distribution comparison for Wing A, FLO60.

53

	M_∞	α	Re x 10^{-6}	C_L	C_D	C_M
O, □ EXPERIMENT	0.401	-0.498	5.091	0.139	0.024	-0.077
—— FLO22NM	0.400	0	8.000	0.150	0.004	-0.057
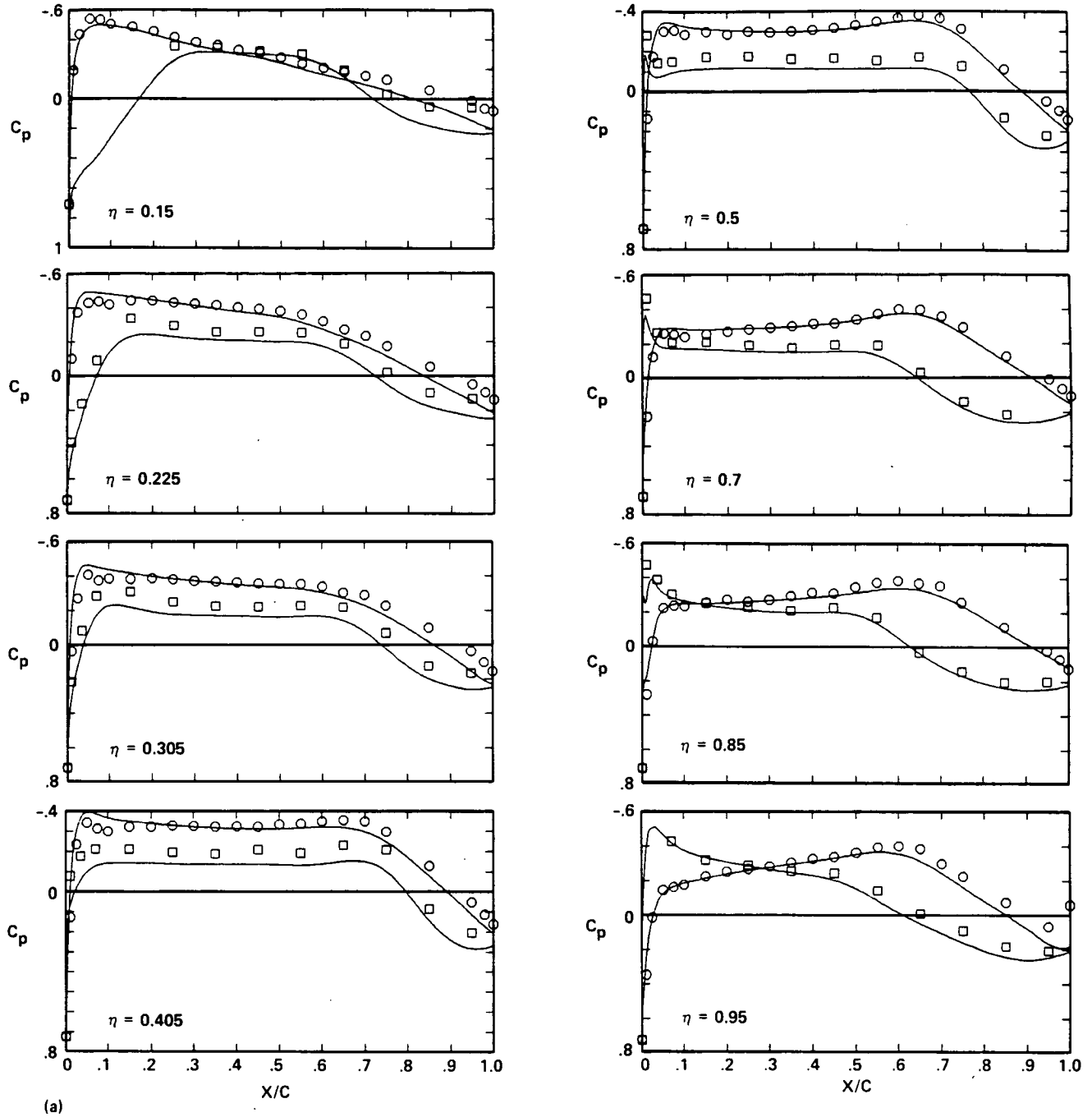
Fig. 14. Experiment–CFD pressure-distribution comparison for Wing A, FLO22NM.

	M∞	α	Re x 10⁻⁶	C_L	C_D	C_M
O , □ EXPERIMENT	0.400	0.488	5.082	0.226	0.025	-0.075
—— FLO22NM	0.400	1.000	8.000	0.222	0.005	-0.086

(b)
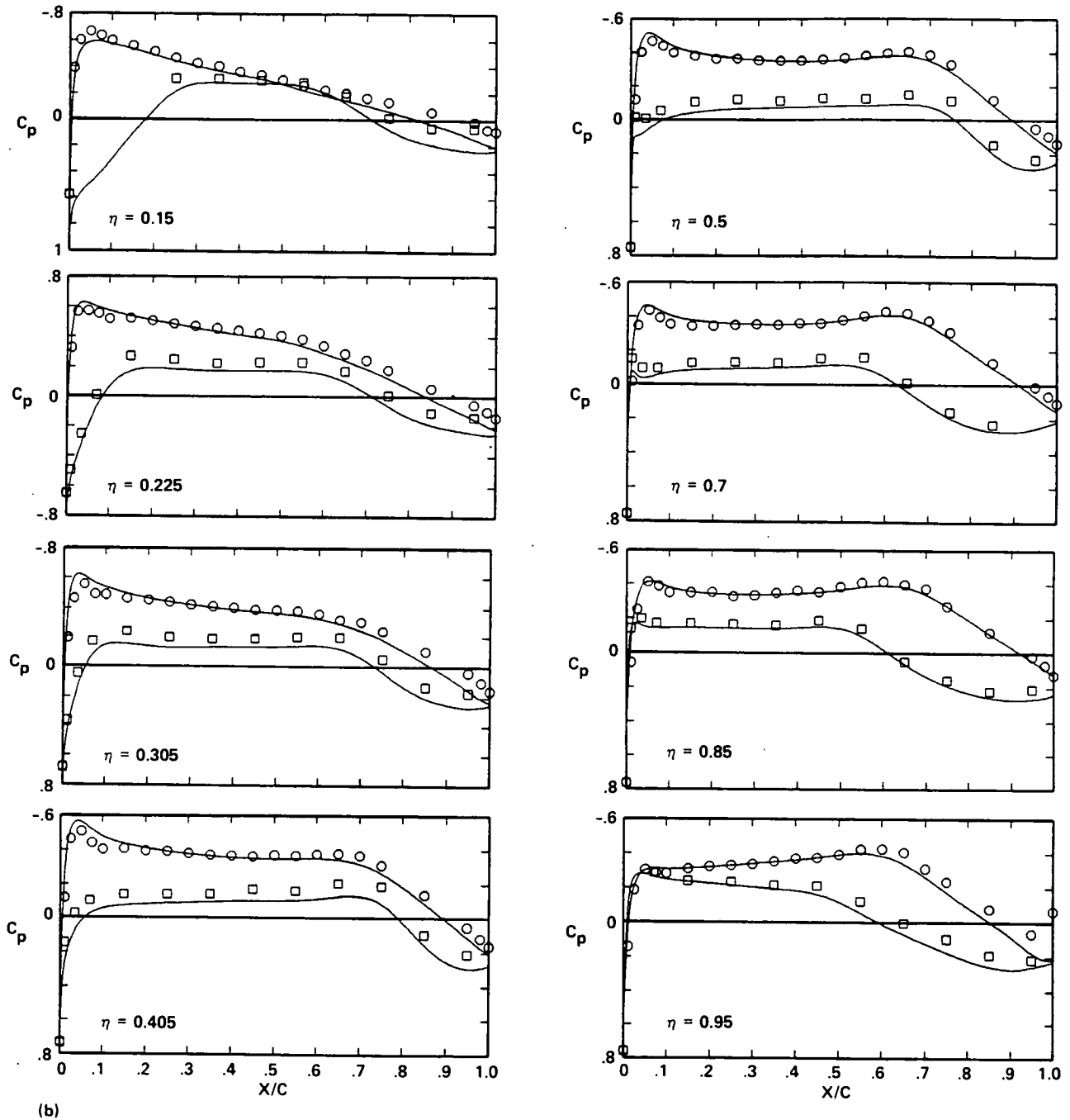
Fig. 14. Continued.

		M_∞	α	Re x 10^{-6}	C_L	C_D	C_M
$\circ$, $\square$	EXPERIMENT	0.400	1.232	5.077	0.290	0.027	-0.072
——	FLO22NM	0.400	2.000	8.000	0.292	0.006	-0.114

(c)

Fig. 14. Continued.

56
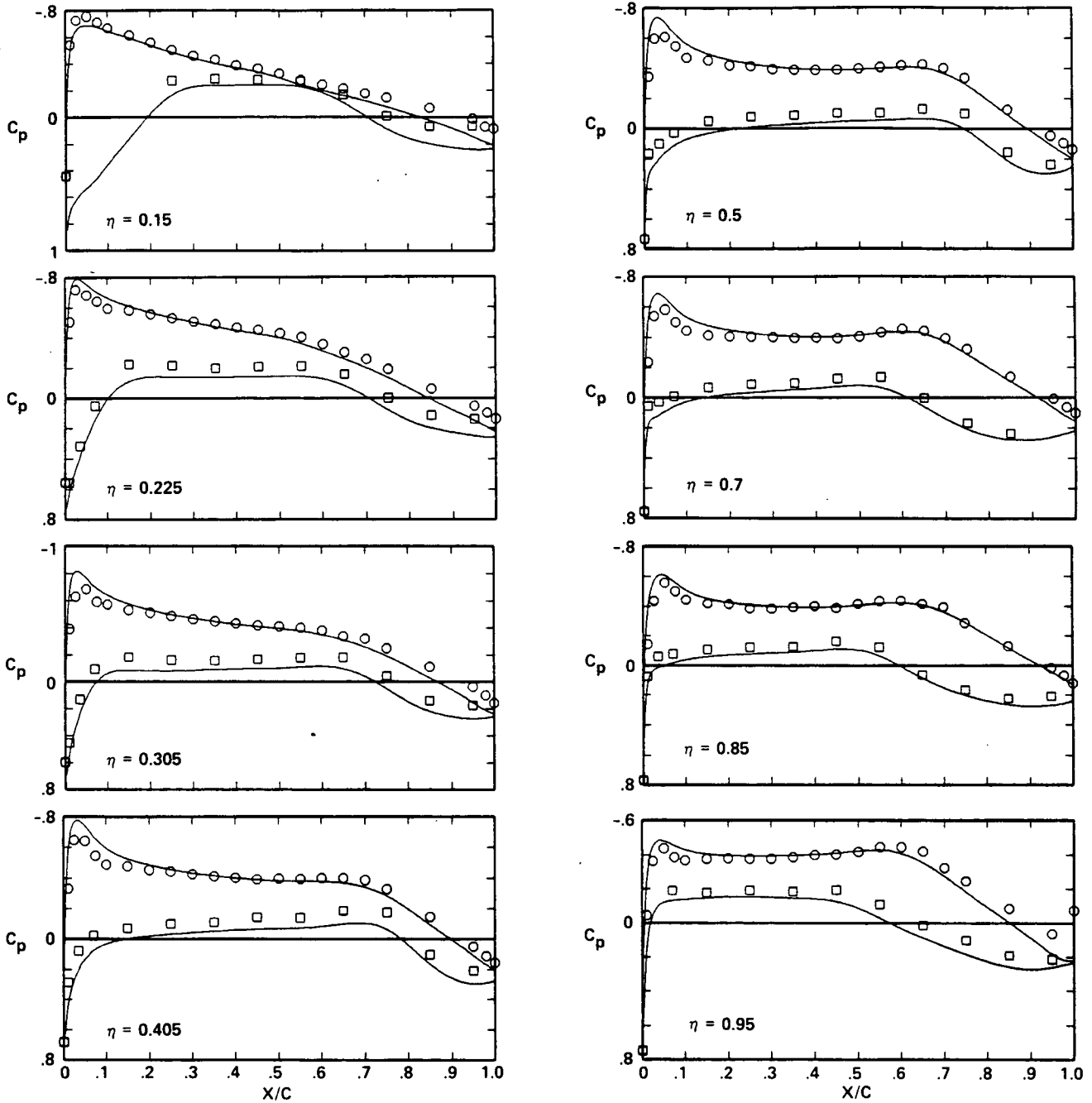
		M_∞	α	$Re \times 10^{-6}$	C_L	C_D	C_M
O , □	EXPERIMENT	0.401	1.984	5.092	0.355	0.028	-0.071
——	FLO22NM	0.400	3.000	8.000	0.362	0.008	-0.145
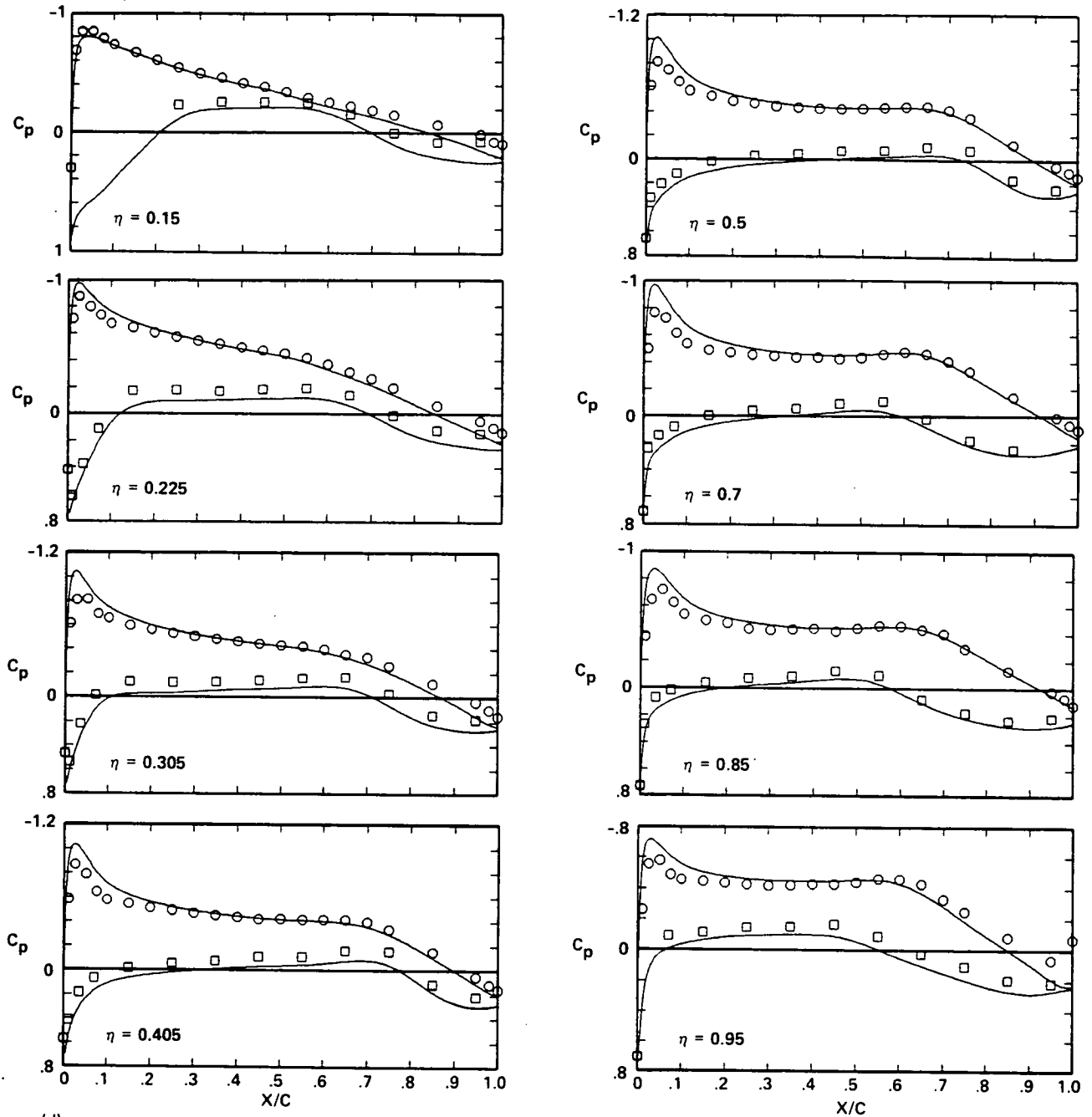
Fig. 14. Continued.

(e)

Fig. 14. Continued.

58
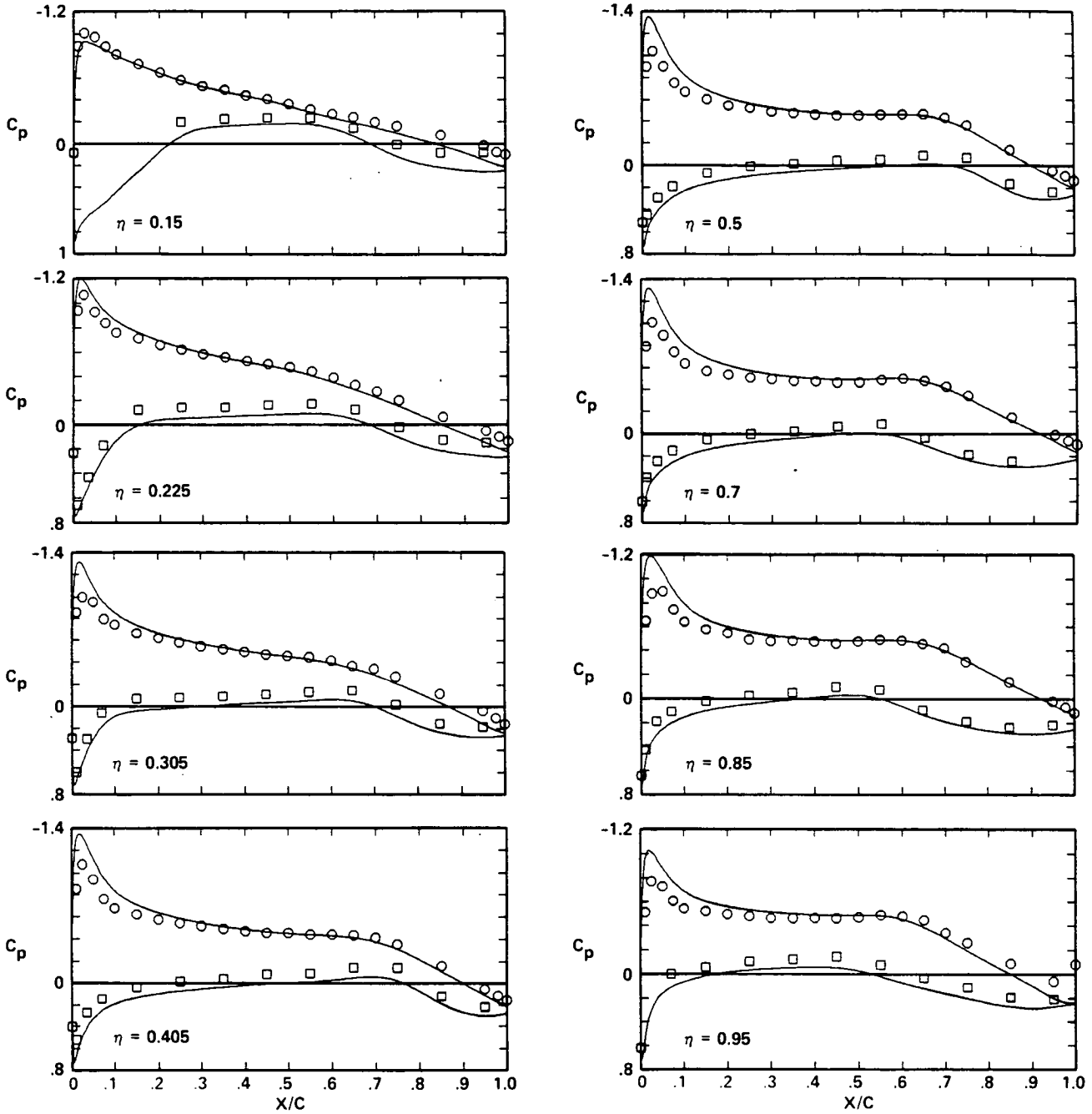
		M_∞	α	Re x 10^{-6}	C_L	C_D	C_M
O , □	EXPERIMENT	0.800	-0.043	8.280	0.209	0.031	-0.096
——	FLO22NM	0.800	0	8.000	0.216	0.004	-0.099

(f)

Fig. 14. Continued.

59
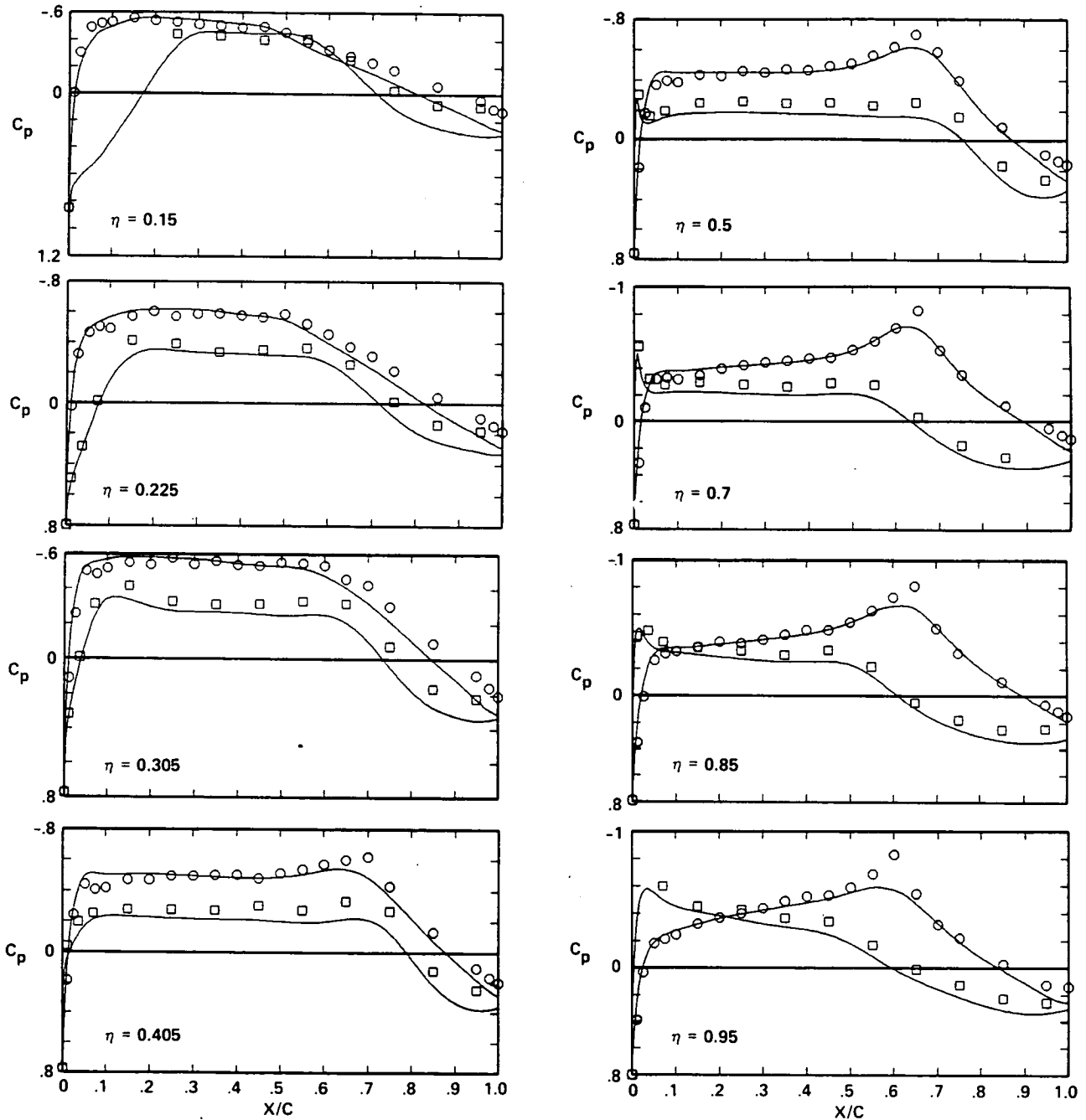
		M_∞	α	Re x 10^{-6}	C_L	c_p	C_M
O, □	EXPERIMENT	0.802	0.981	8.302	0.322	0.034	-0.100
——	FLO22NM	0.800	1.000	8.000	0.316	0.006	-0.139

(g)

Fig. 14. Continued.

60
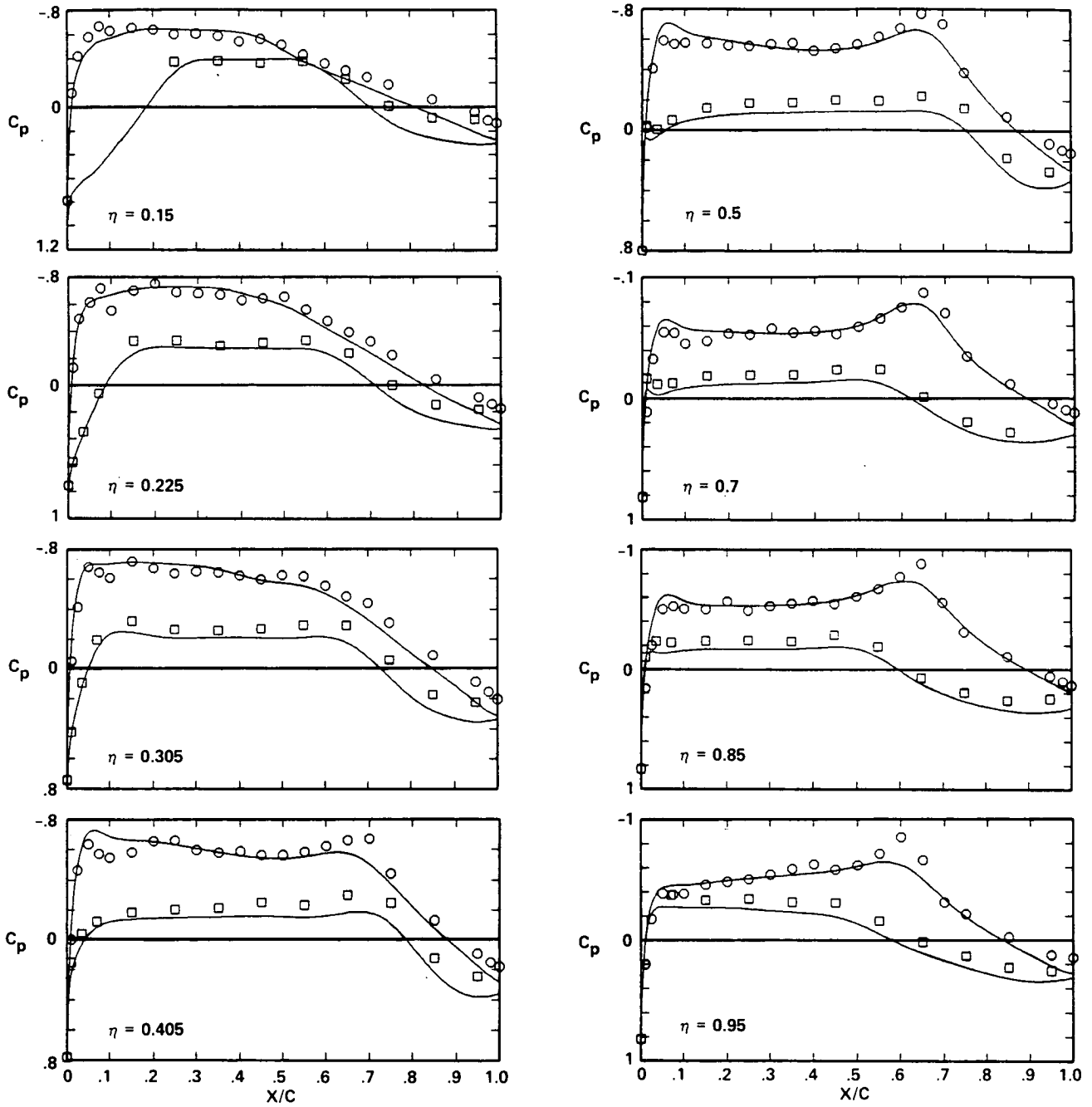
		M_∞	α	Re x 10^{-6}	C_L	C_D	C_M
O,□	EXPERIMENT	0.802	1.751	8.292	0.411	0.038	-0.103
——	FLO22NM	0.800	2.000	8.000	0.414	0.010	-0.178
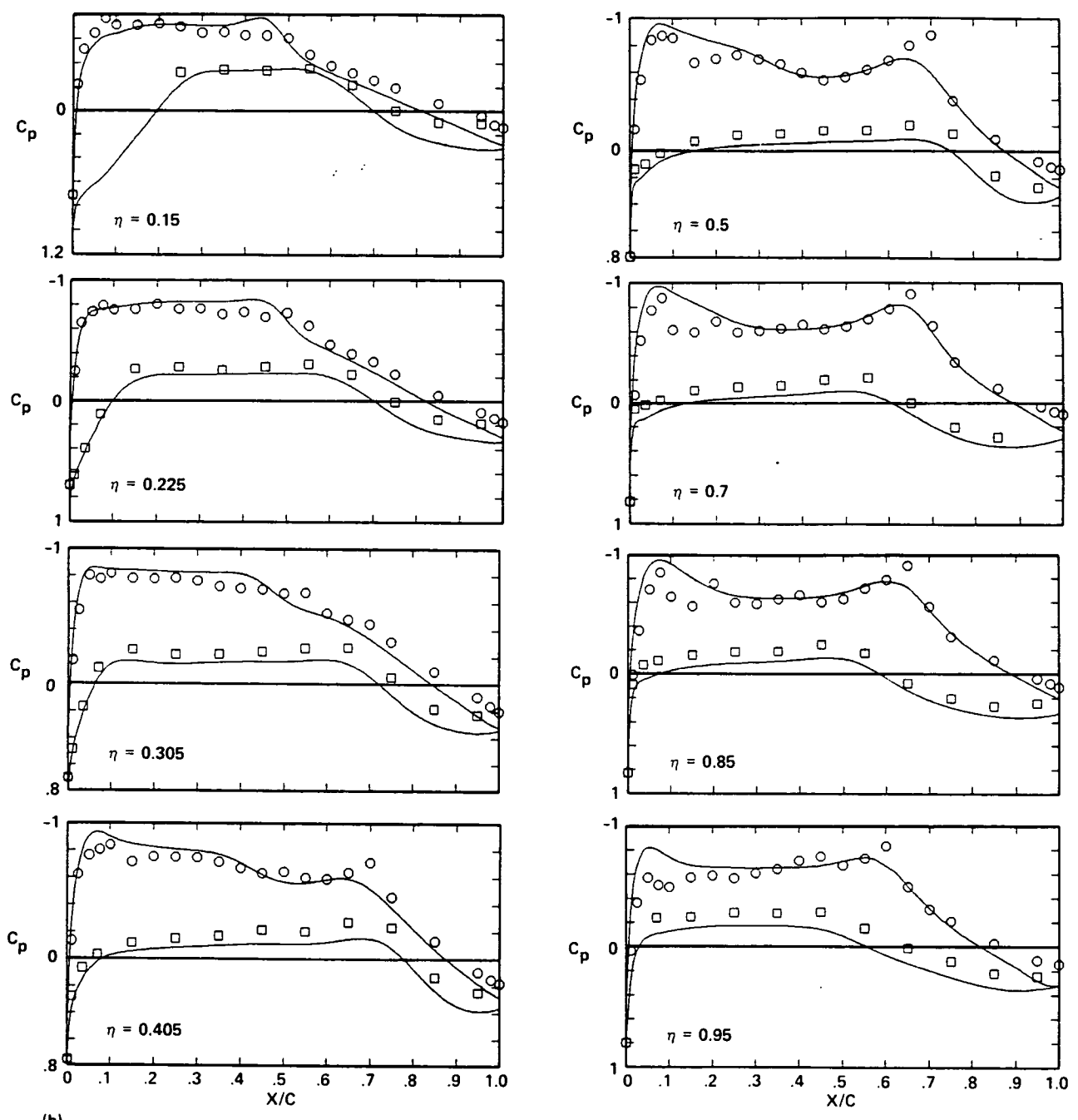
(h)
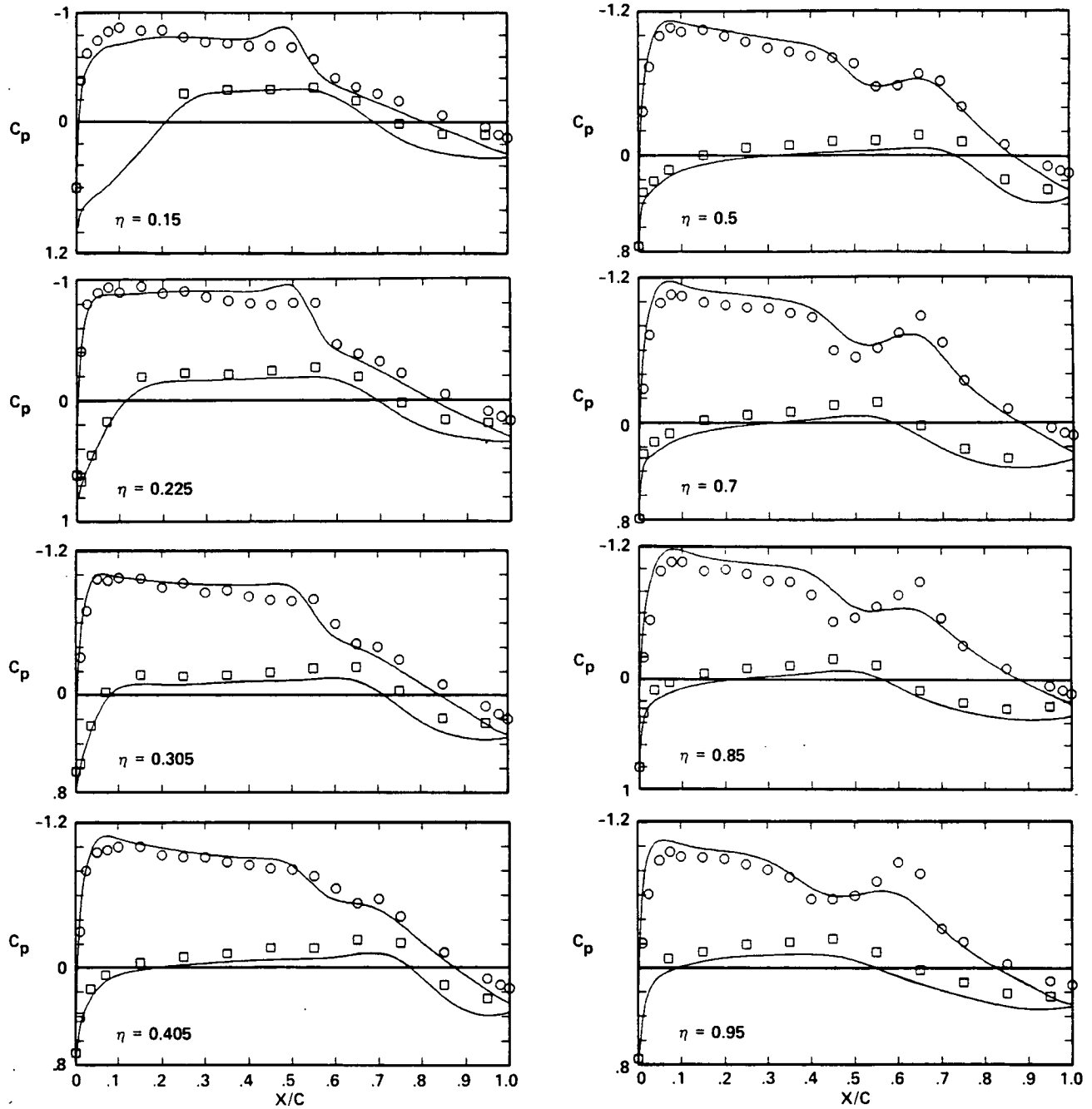
Fig. 14. Continued.

Fig. 14. Continued.

		M_∞	α	Re x 10^{-6}	C_L	C_D	C_M
○, □	EXPERIMENT	0.801	3.519	8.244	0.649	0.053	-0.123
——	FLO22NM	0.800	4.000	8.000	0.626	0.028	-0.275

(j)
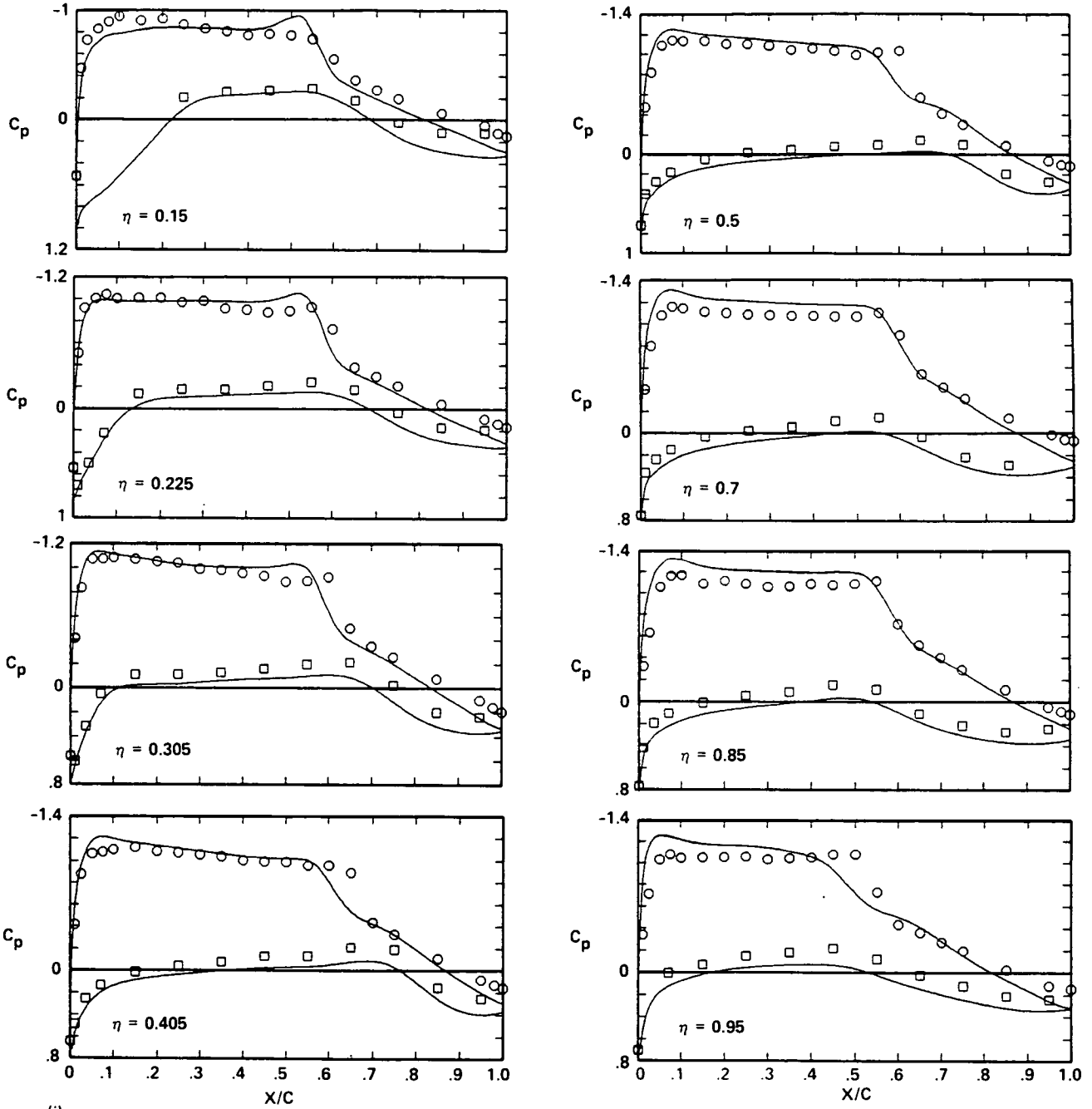
Fig. 14. Continued.

		M_∞	α	Re x 10^{-6}	C_L	C_D	C_M
O, □	EXPERIMENT	0.801	4.496	8.222	0.724	0.068	-0.100
——	FLO22NM	0.800	5.000	8.000	0.716	0.043	-0.316

(k)
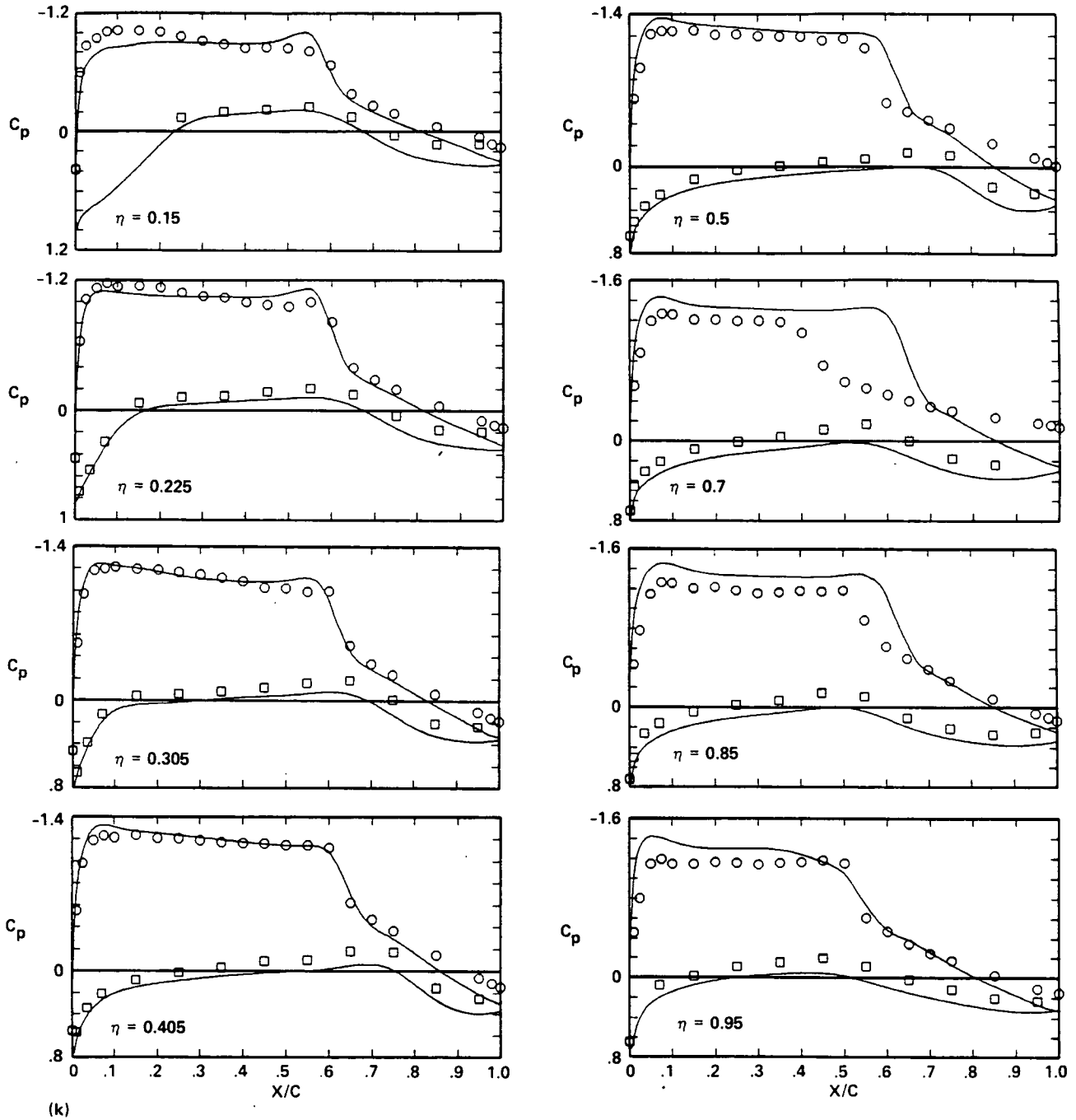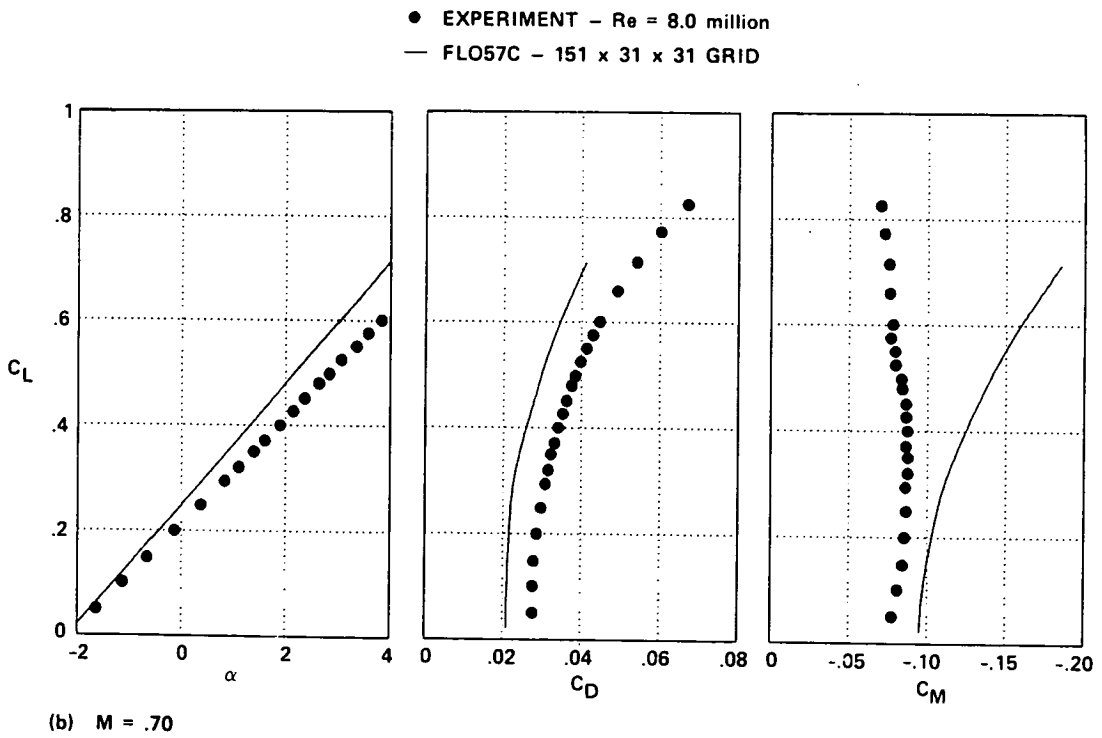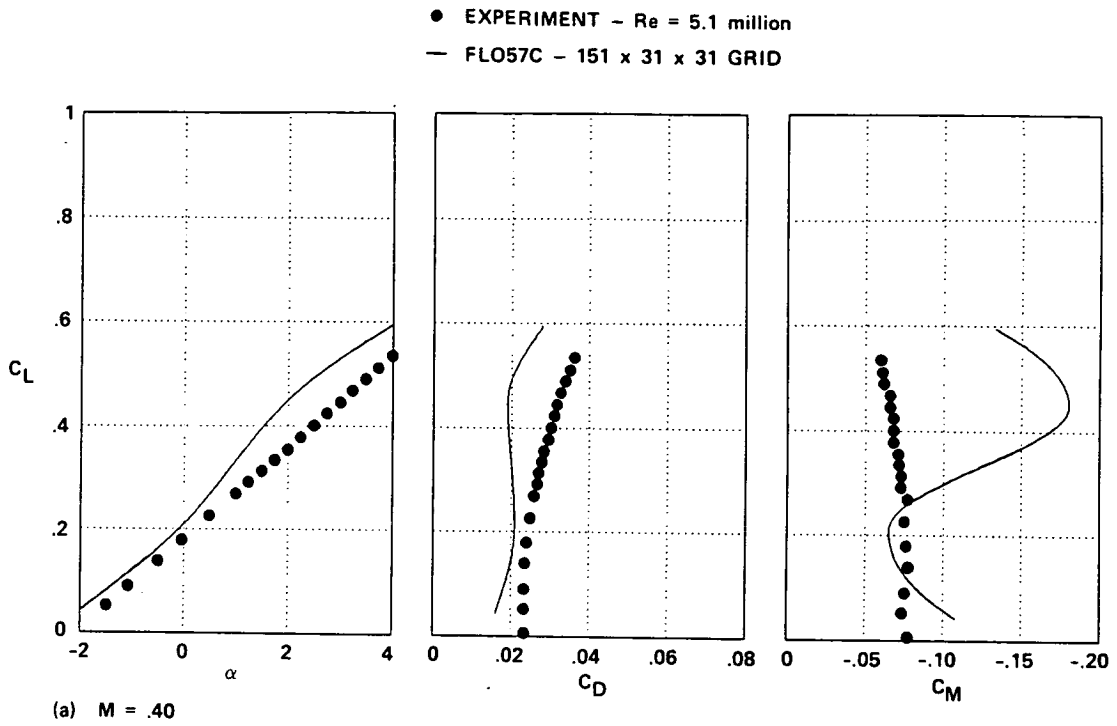
Fig. 14. Concluded.

Fig. 15. Experiment–CFD force-and-moment comparison for Wing A, FLO57C.
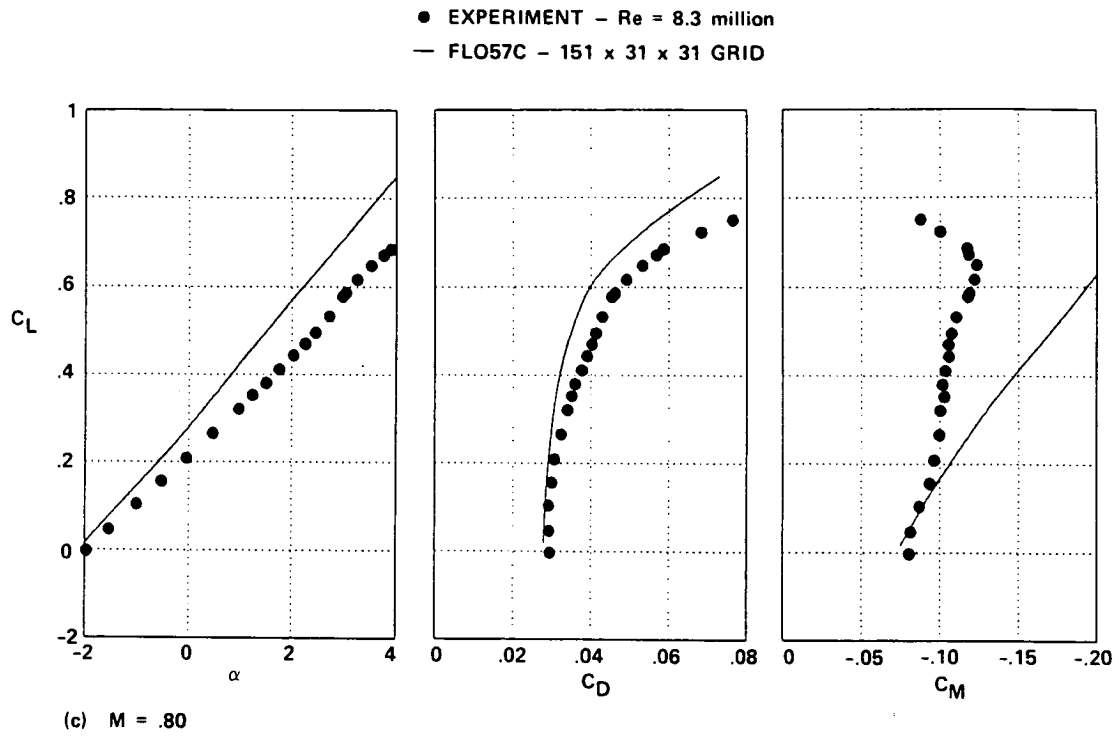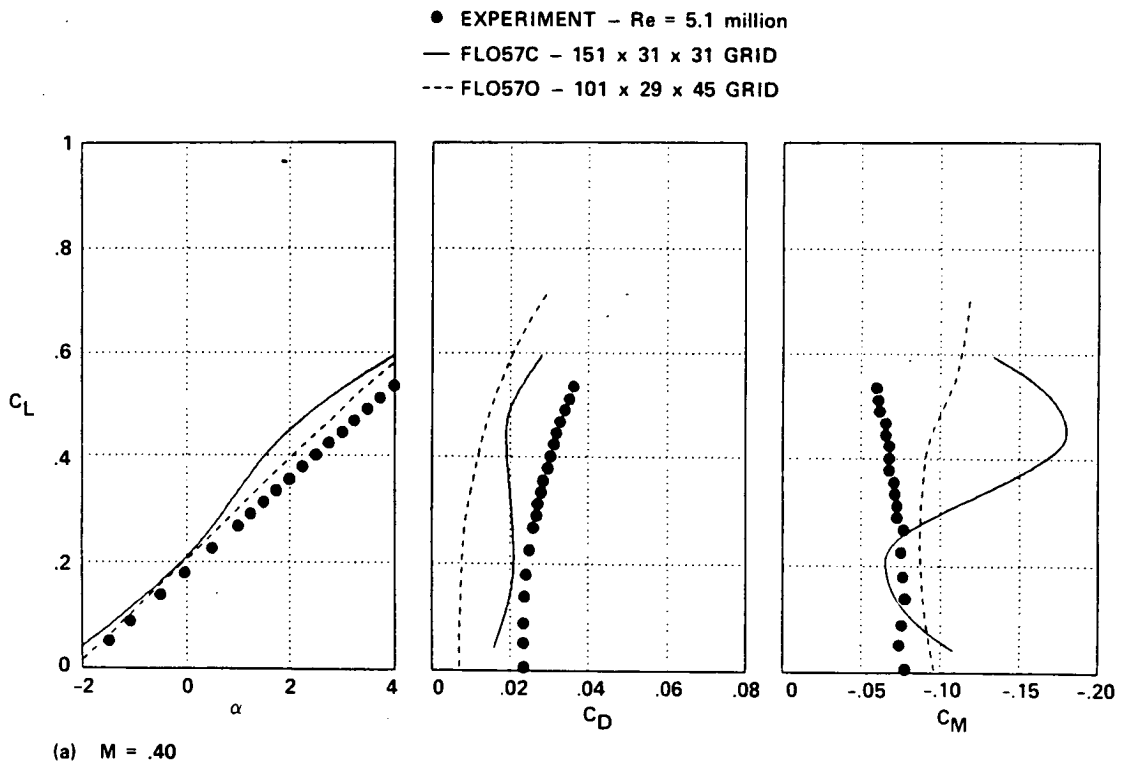
(c)   M = .80

Fig. 15. Concluded.

(a)   M = .40

Fig. 16. Experiment–CFD force-and-moment comparison for Wing A, FLO57C and FLO57O.

● EXPERIMENT – Re = 8.0 million
— FLO57C – 151 x 31 x 31 GRID
--- FLO57O – 101 x 29 x 45 GRID

(b) M = .70

● EXPERIMENT – Re = 8.3 million
— FLO57C – 151 x 31 x 31 GRID
--- FLO57O – 101 x 29 x 45 GRID

(c) M = .80

Fig. 16. Concluded.

67

(a) M = .40

(b) M = .80
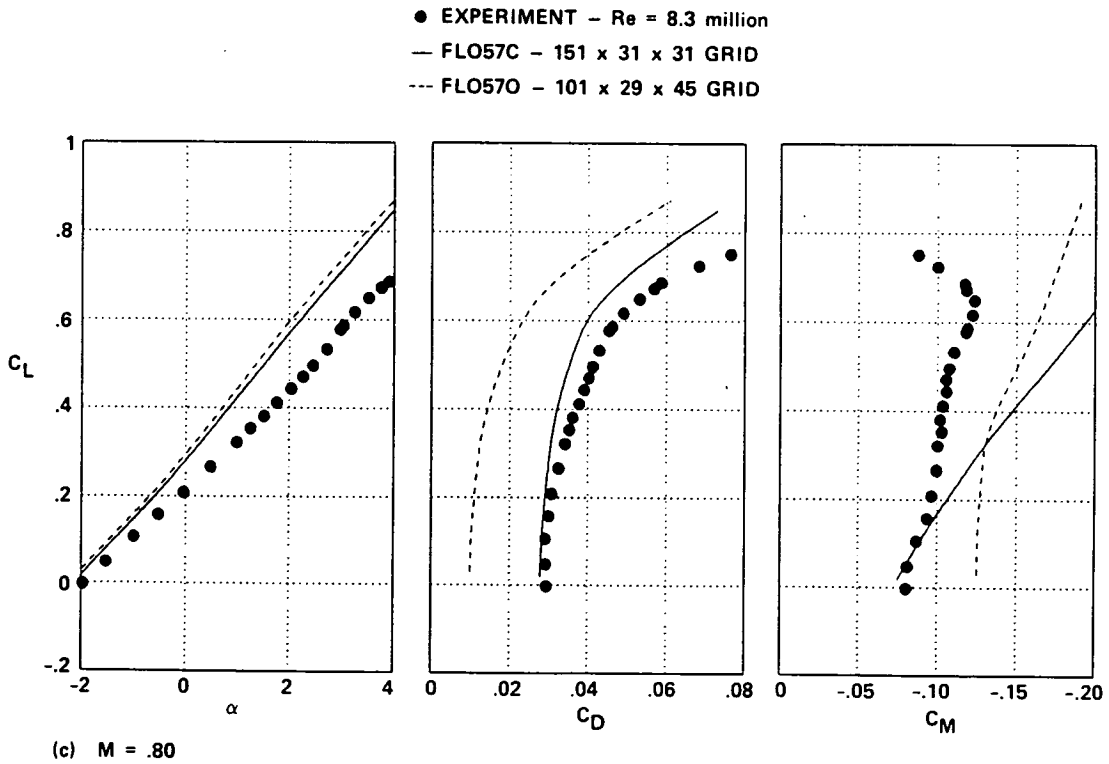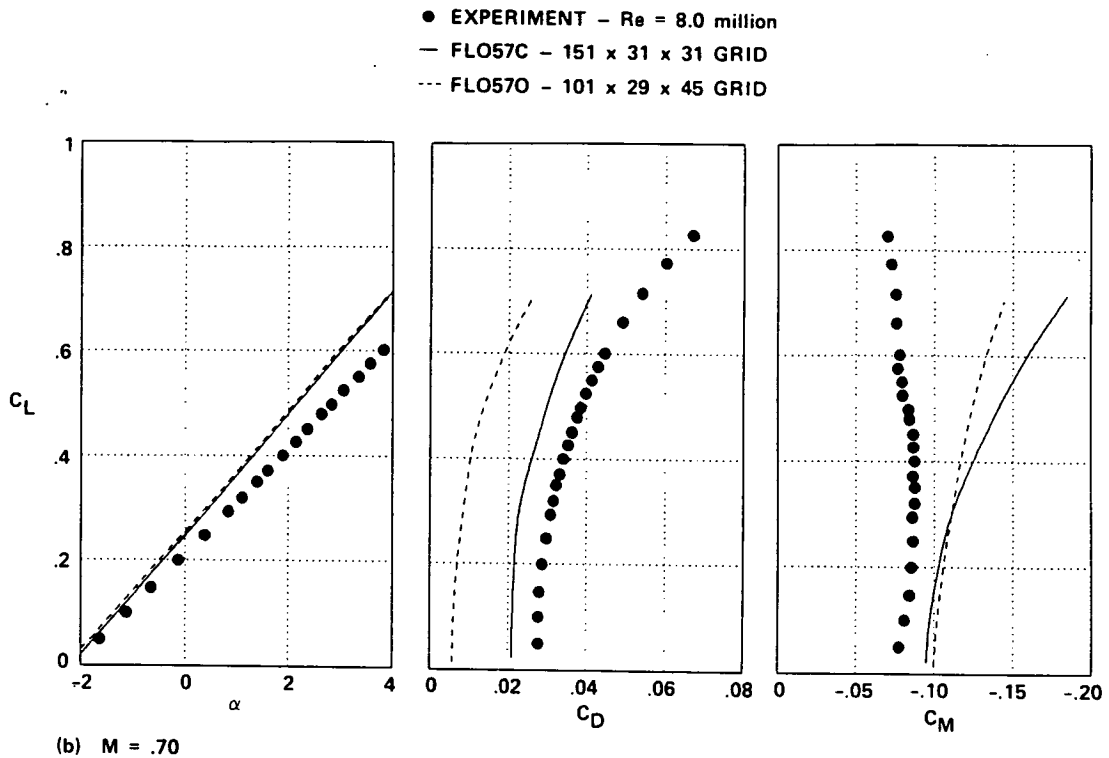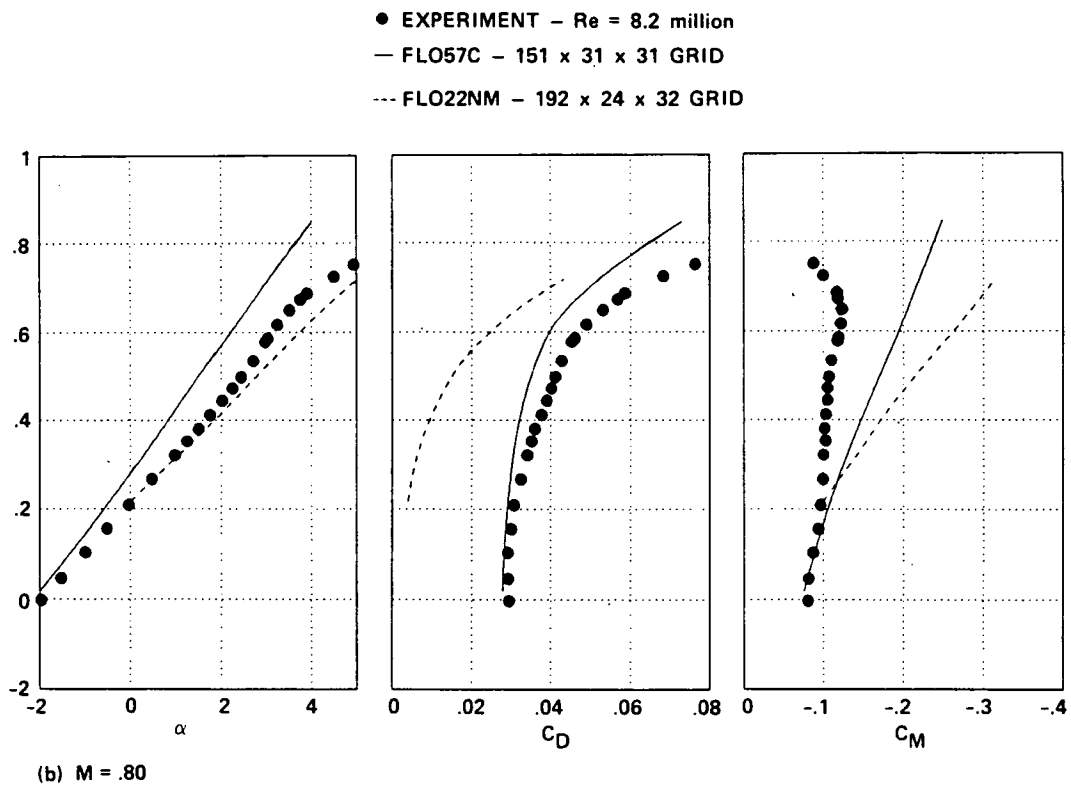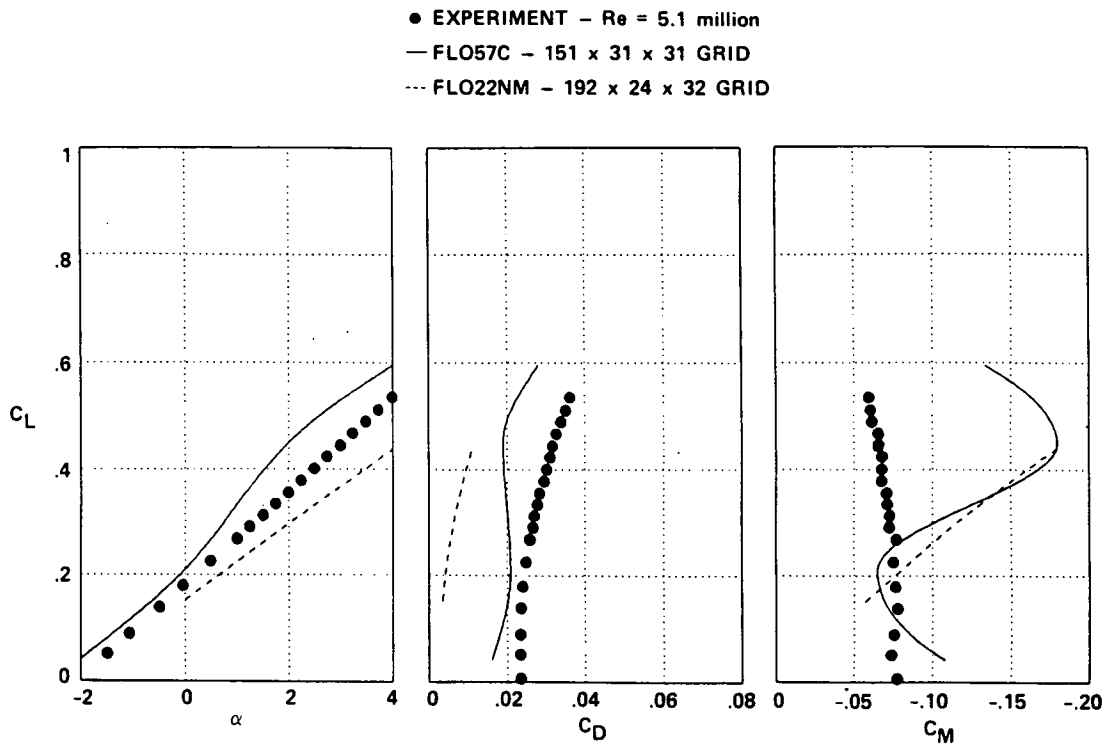
Fig. 17. Experiment–CFD force-and-moment comparison for Wing A, FLO57C and FLO22NM.

68

	M_∞	α	Re x 10^{-6}	C_L	C_D	C_M
O, □ EXPERIMENT	0.401	-1.969	5.181	0.016	.024	-0.072
—— FLO57C	0.400	-2.000	—	0.019	.021	-0.048

Fig. 18. Experiment–CFD pressure-distribution comparison for Wing B, FLO57C.
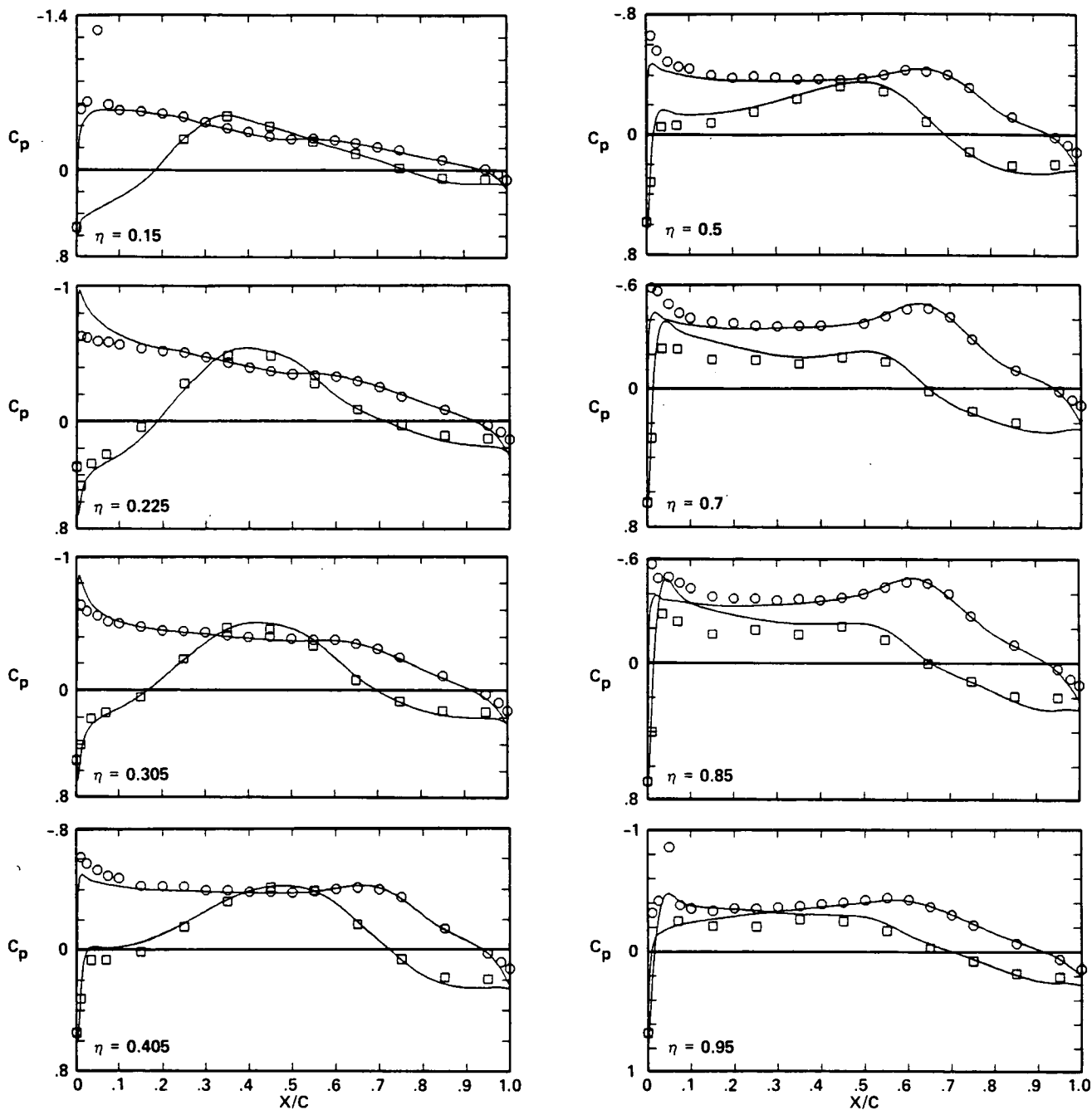
(b)

Fig. 18. Continued.

		M_∞	α	Re x 10^{-6}	C_L	C_D	C_M
O, □	EXPERIMENT	0.400	2.524	5.216	0.412	0.031	-0.067
——	FLO57C	0.400	2.000	——	0.421	0.022	-0.111
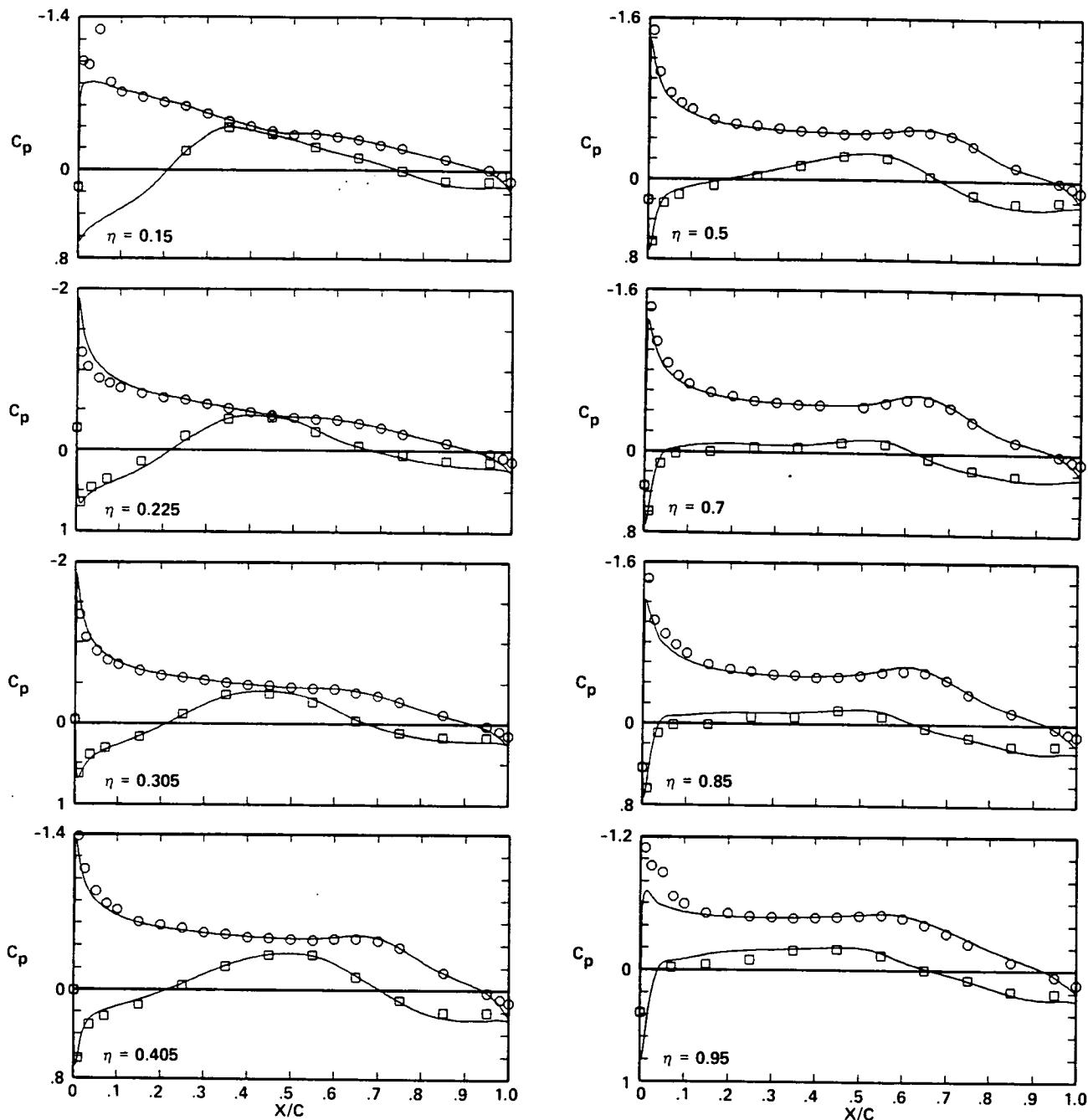
(c)

Fig. 18. Continued.

		M_∞	α	Re x 10^{-6}	C_L	C_D	C_M
○, □	EXPERIMENT	0.399	5.526	5.208	0.682	0.045	-0.048
—	FLO57C	0.400	4.000	—	0.699	0.025	-0.346

(d)
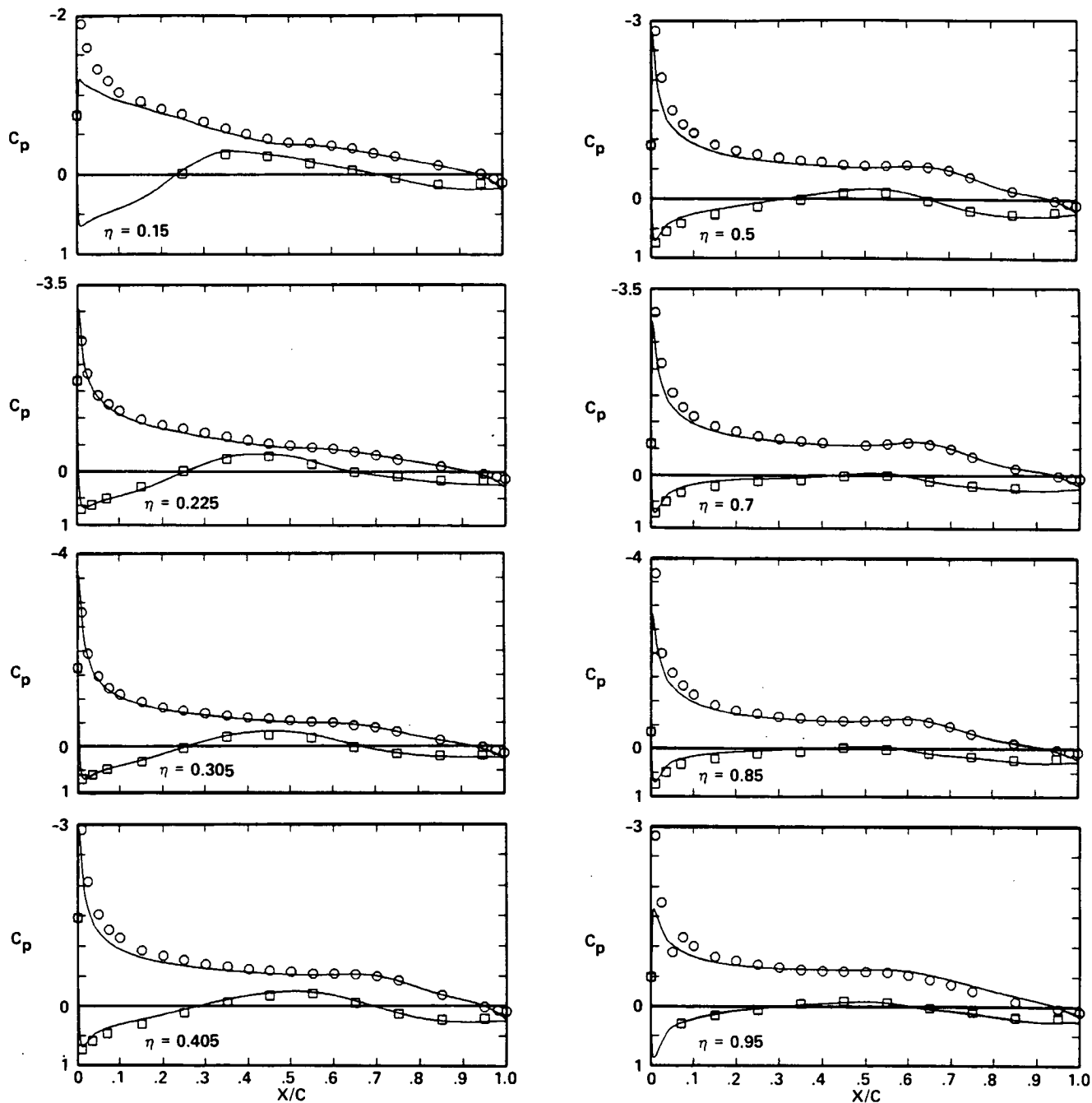
Fig. 18. Continued.

		M_∞	α	Re x 10^{-6}	C_L	C_D	C_M
○, □	EXPERIMENT	0.700	-1.450	8.055	0.061	0.026	-0.078
—	FLO57C	0.700	-2.000	—	0.026	0.023	-0.081

(e)
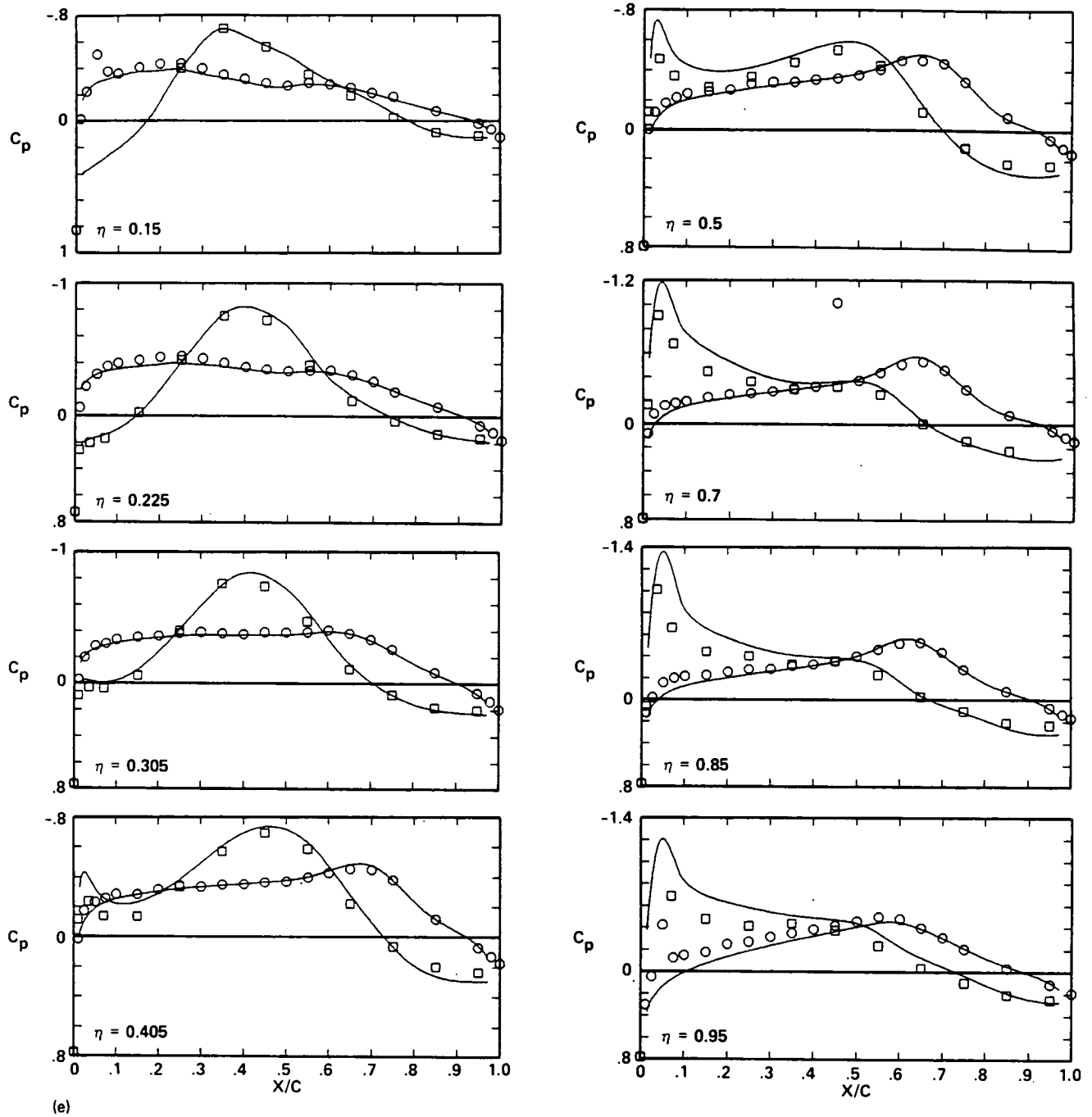
Fig. 18. Continued.

		M_∞	α	Re x 10^{-6}	C_L	C_D	C_M
$\bigcirc, \square$	EXPERIMENT	0.700	0.545	8.039	0.262	0.029	-0.088
——	FLO57C	0.700	0	——	0.256	0.024	-0.110
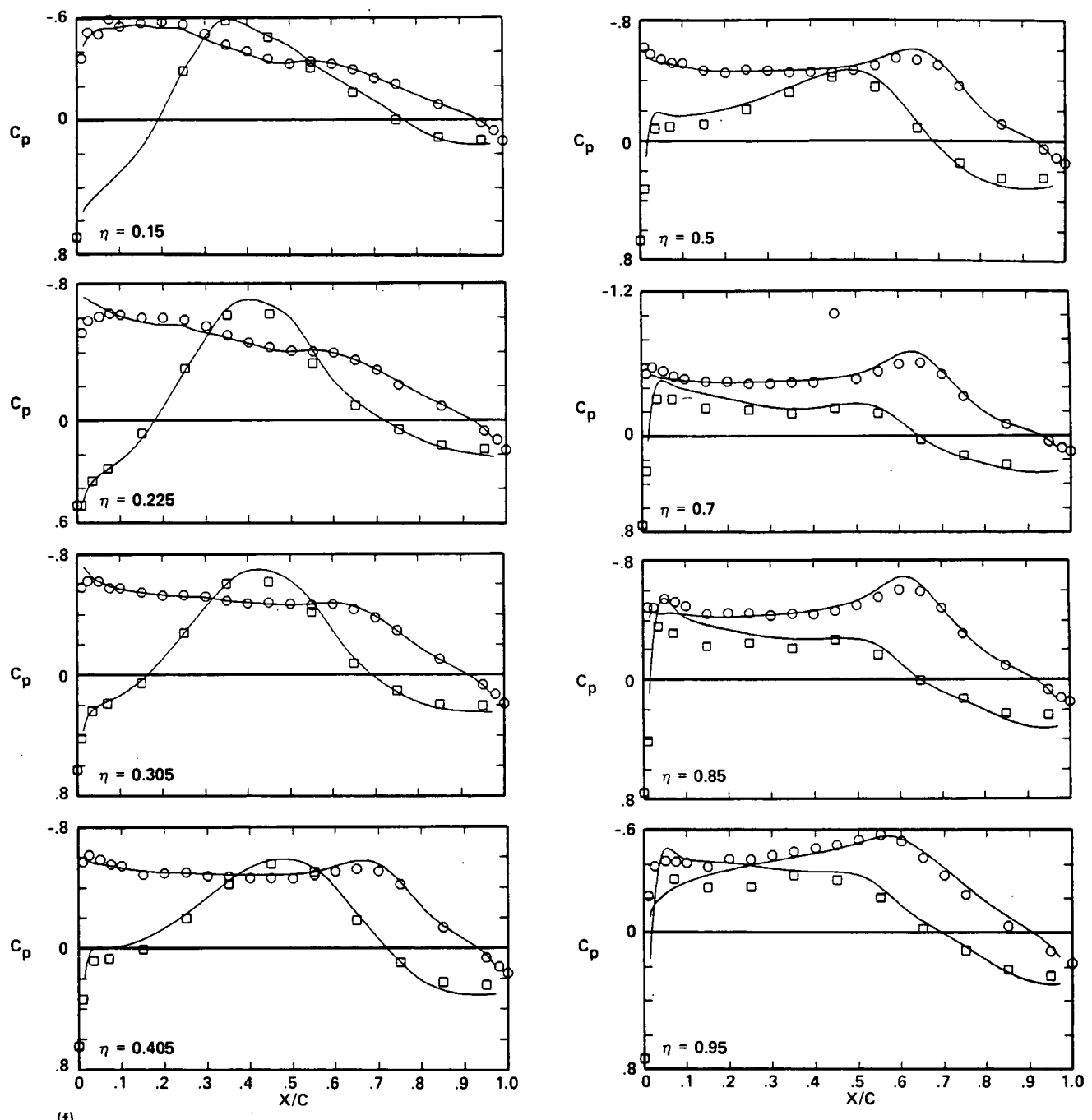
(f)

Fig. 18. Continued.

	M_∞	α	Re x 10^{-6}	C_L	C_D	C_M
○, □ EXPERIMENT	0.702	2.794	8.017	0.493	0.037	-0.084
— FLO57C	0.700	2.000	—	0.486	0.030	-0.134
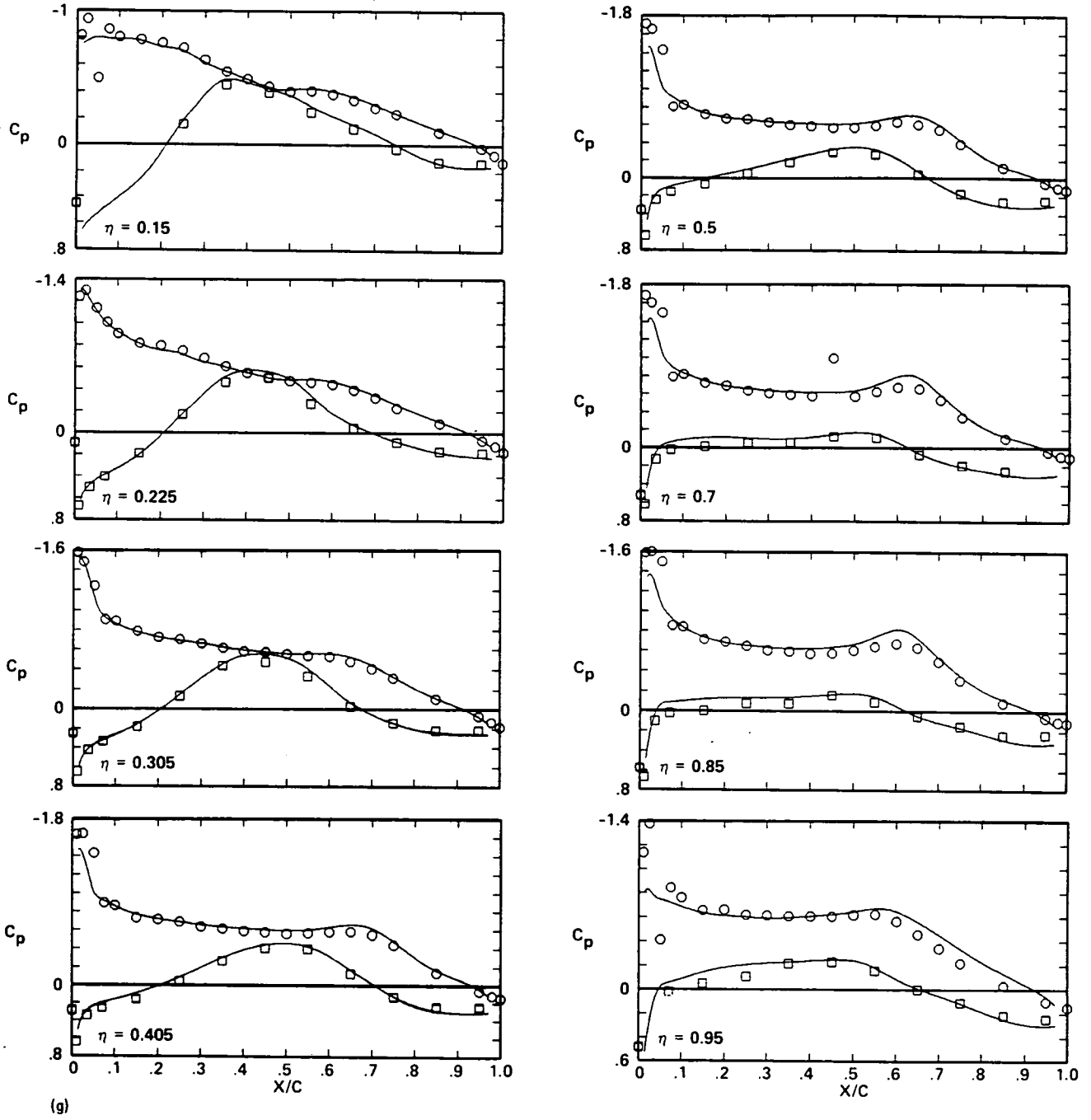
Fig. 18. Continued.
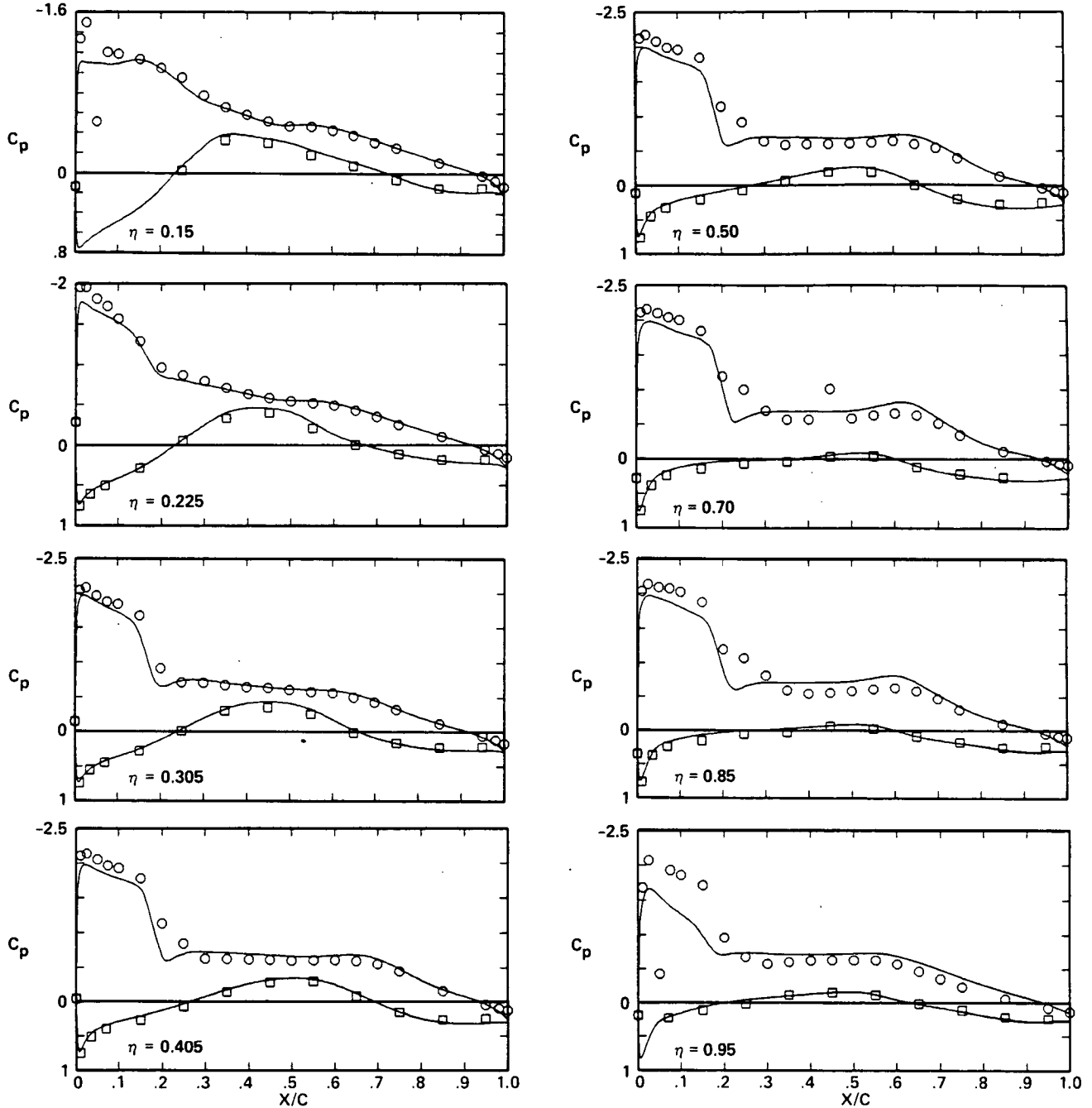
Fig. 18. Continued.

		M_∞	α	Re x 10^{-6}	C_L	C_D	C_M
○,□	EXPERIMENT	0.802	-1.957	8.275	0.013	0.034	-0.074
——	FLO57C	0.800	-2.000	——	0.020	0.029	-0.073

(i)

Fig. 18. Continued.

77
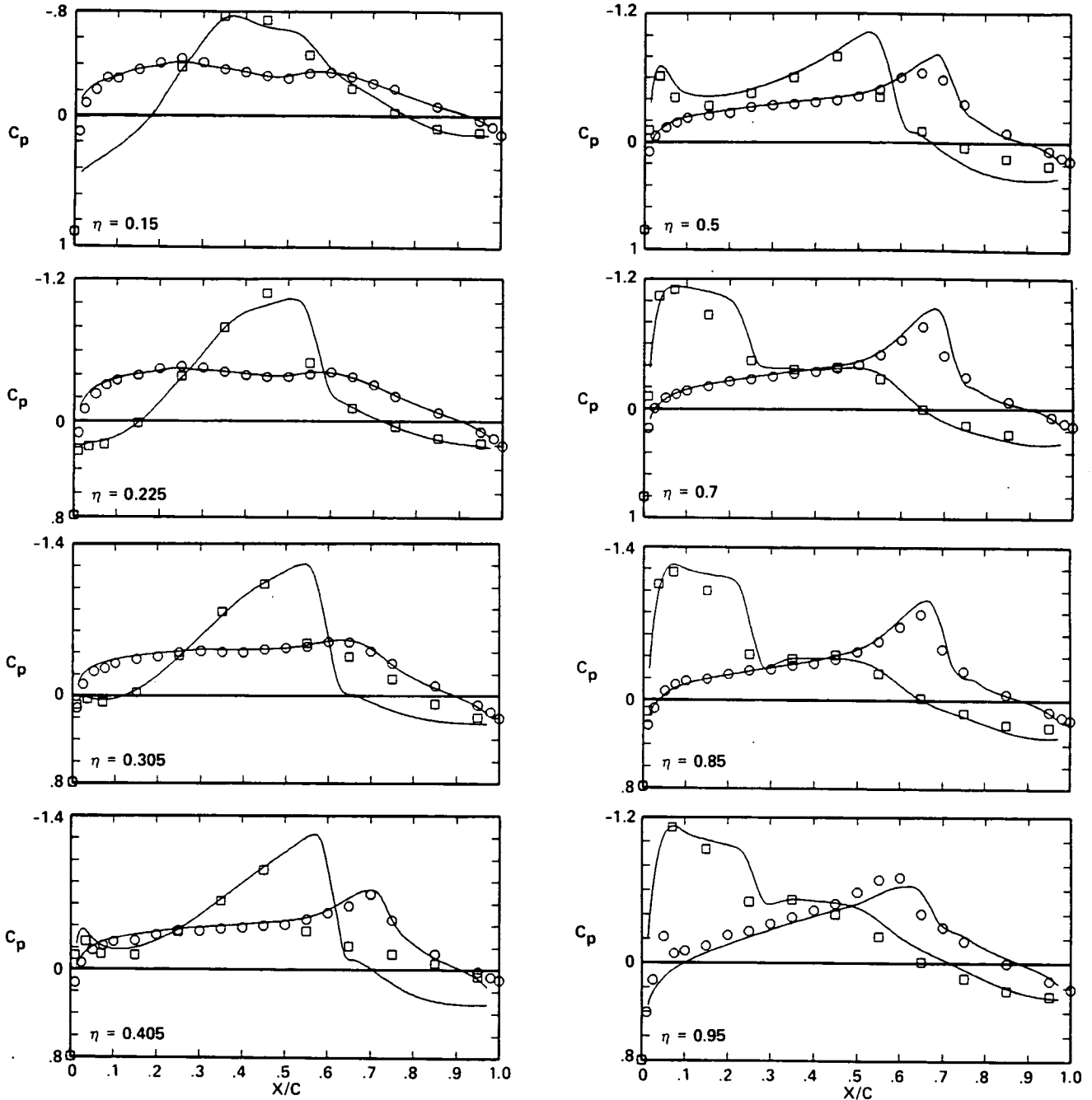
	M_∞	α	Re x 10^{-6}	C_L	C_D	C_M
○ □ EXPERIMENT	0.800	0.541	8.302	0.278	0.034	-0.095
—— FLO57C	0.800	0	——	0.291	0.030	-0.130
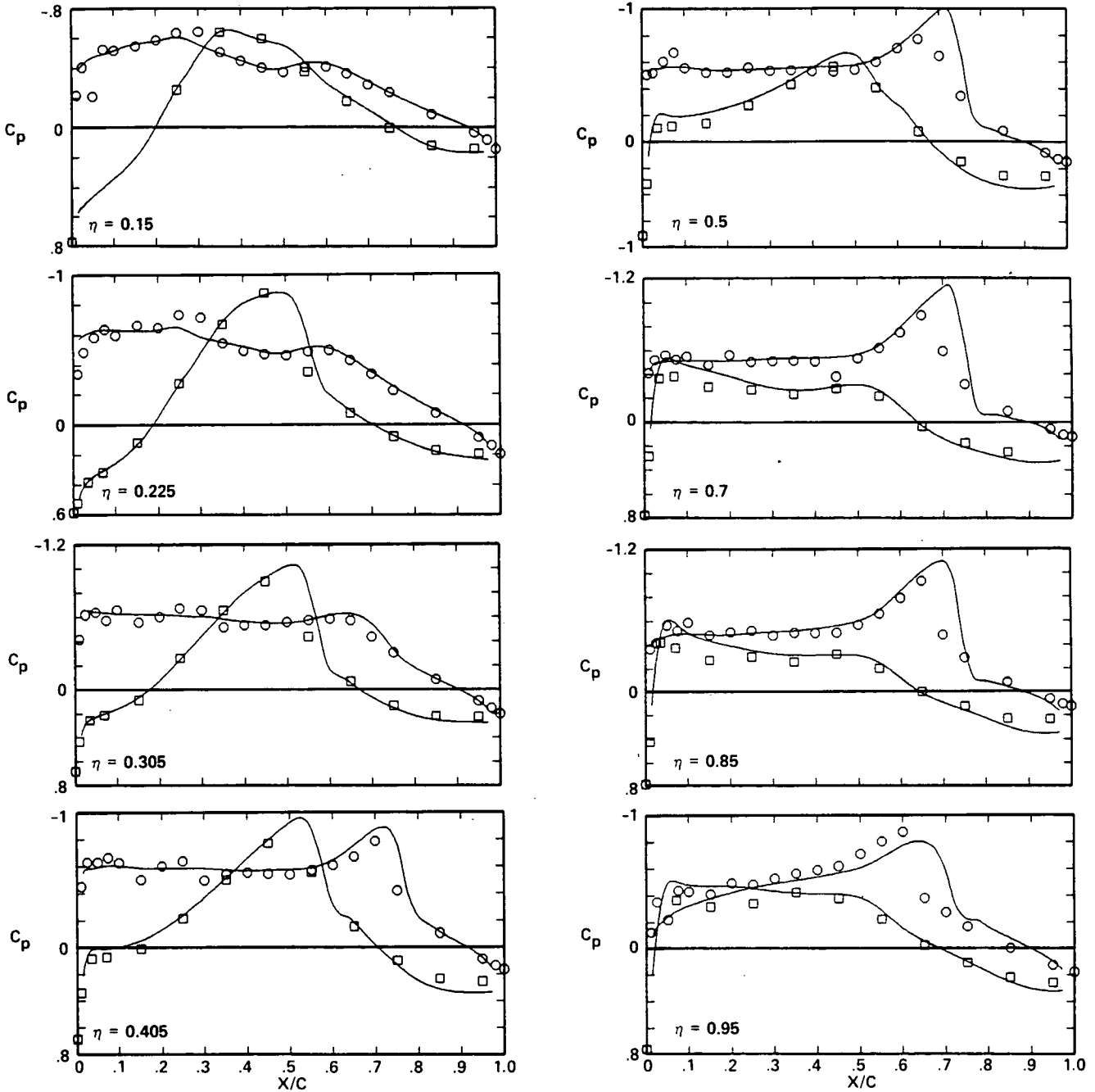
(j)

Fig. 18. Continued.

	M_∞	α	Re x 10^{-6}	C_L	C_D	C_M
○, □ EXPERIMENT	0.800	3.033	8.269	0.598	0.048	-0.117
—— FLO57C	0.800	2.000	——	0.587	0.039	-0.189

Fig. 18. Continued.

79
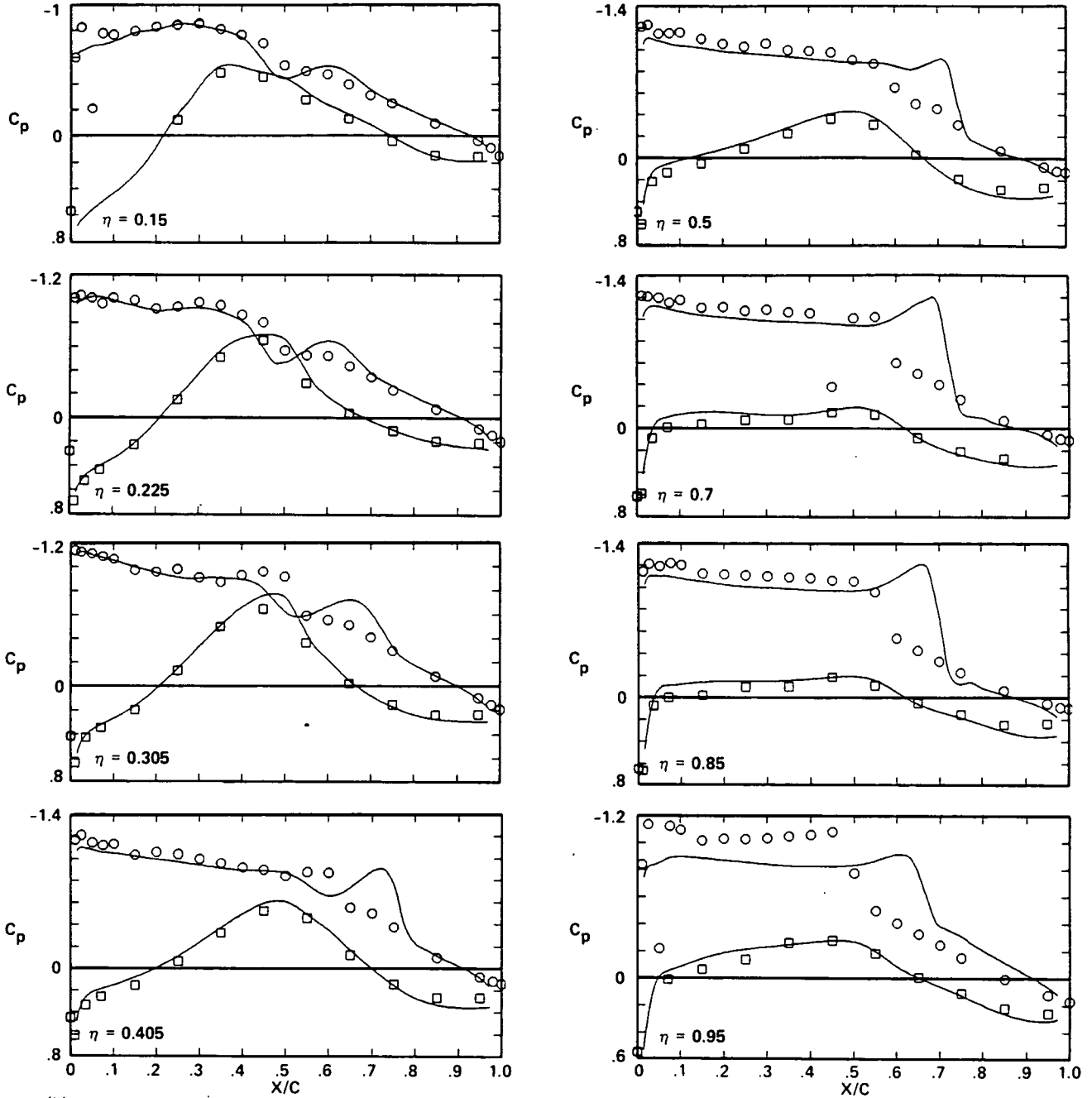
	M_∞	α	Re x 10^{-6}	C_L	C_D	C_M
O, □ EXPERIMENT	0.800	5.002	8.264	0.738	0.082	-0.051
—— FLO57C	0.800	4.000	—	0.869	0.077	-0.238

(l)

Fig. 18. Concluded.

80
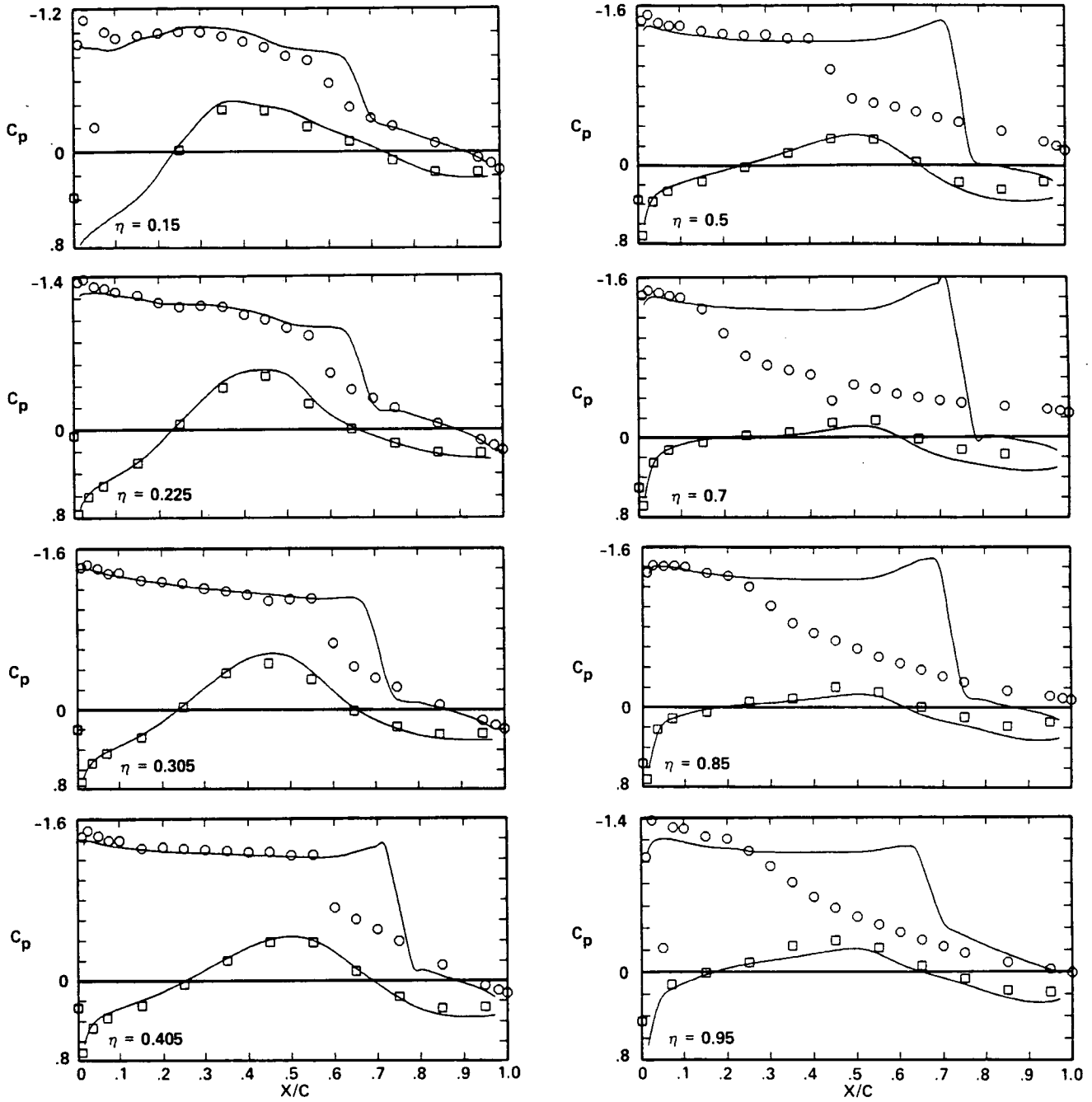
		M_∞	α	$Re \times 10^{-6}$	C_L	C_D	C_M
——	FLO57C – 151 x 31 x 31	0.400	2.000	—	0.421	0.022	-0.111
- - -	FLO57O – 101 x 29 x 45	0.400	2.163	—	0.429	0.011	-0.116
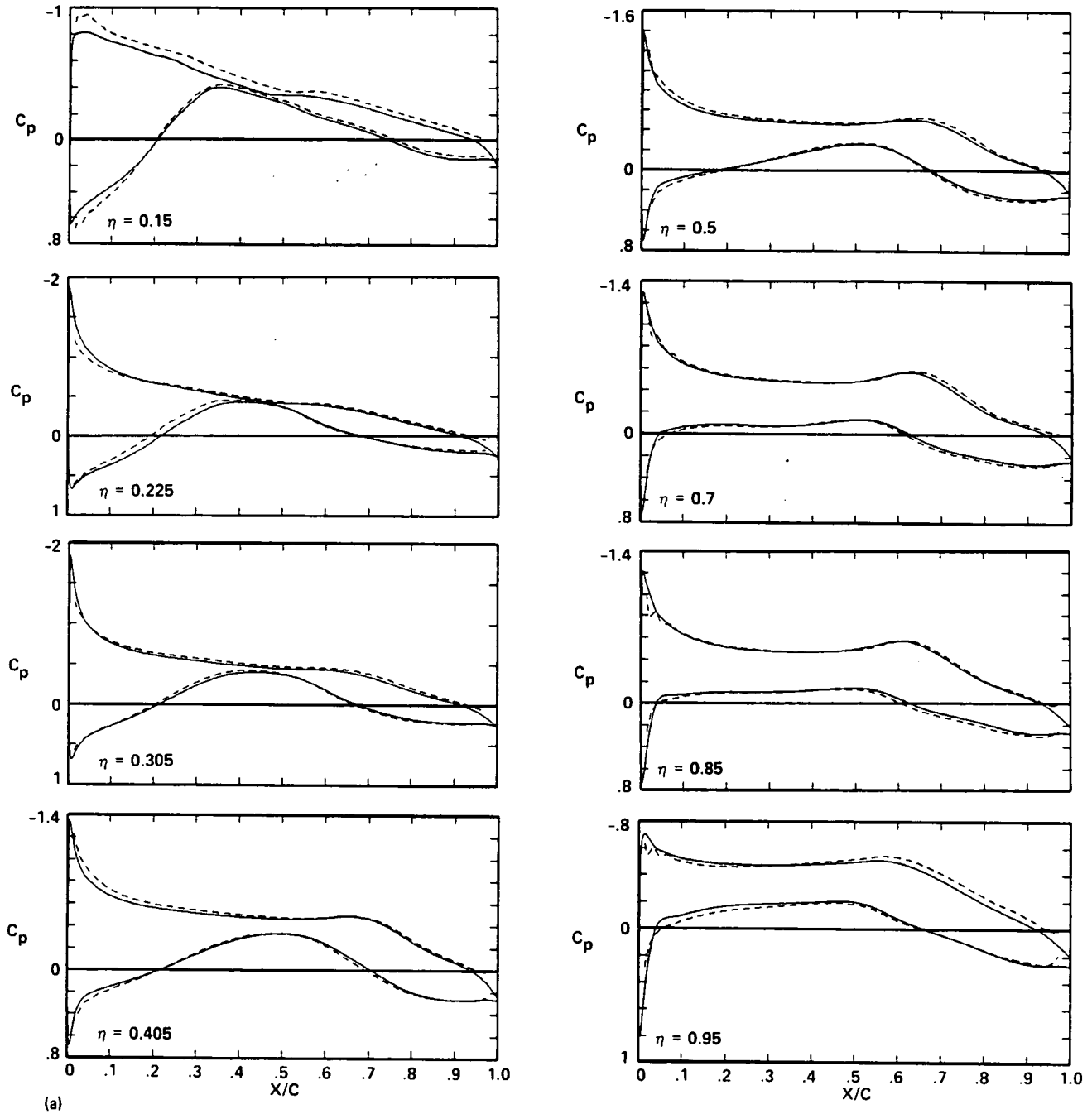
Fig. 19. Pressure-distribution comparison for Wing B, FLO57C and FLO57O.

	M_∞	α	Re x 10^{-6}	C_L	C_D	C_M
—— FLO57C – 151 x 31 x 31	0.700	2.000	—	0.486	0.030	-0.134
---- FLO57O – 101 x 29 x 45	0.700	2.110	—	0.510	0.016	-0.146

(b)

Fig. 19. Concluded.

● EXPERIMENT – Re = 5.2 million
— FLO57C – 151 x 31 x 31 GRID

(a) M = .40

● EXPERIMENT – Re = 8.0 million
— FLO57C – 151 x 31 x 31 GRID

(b) M = .70
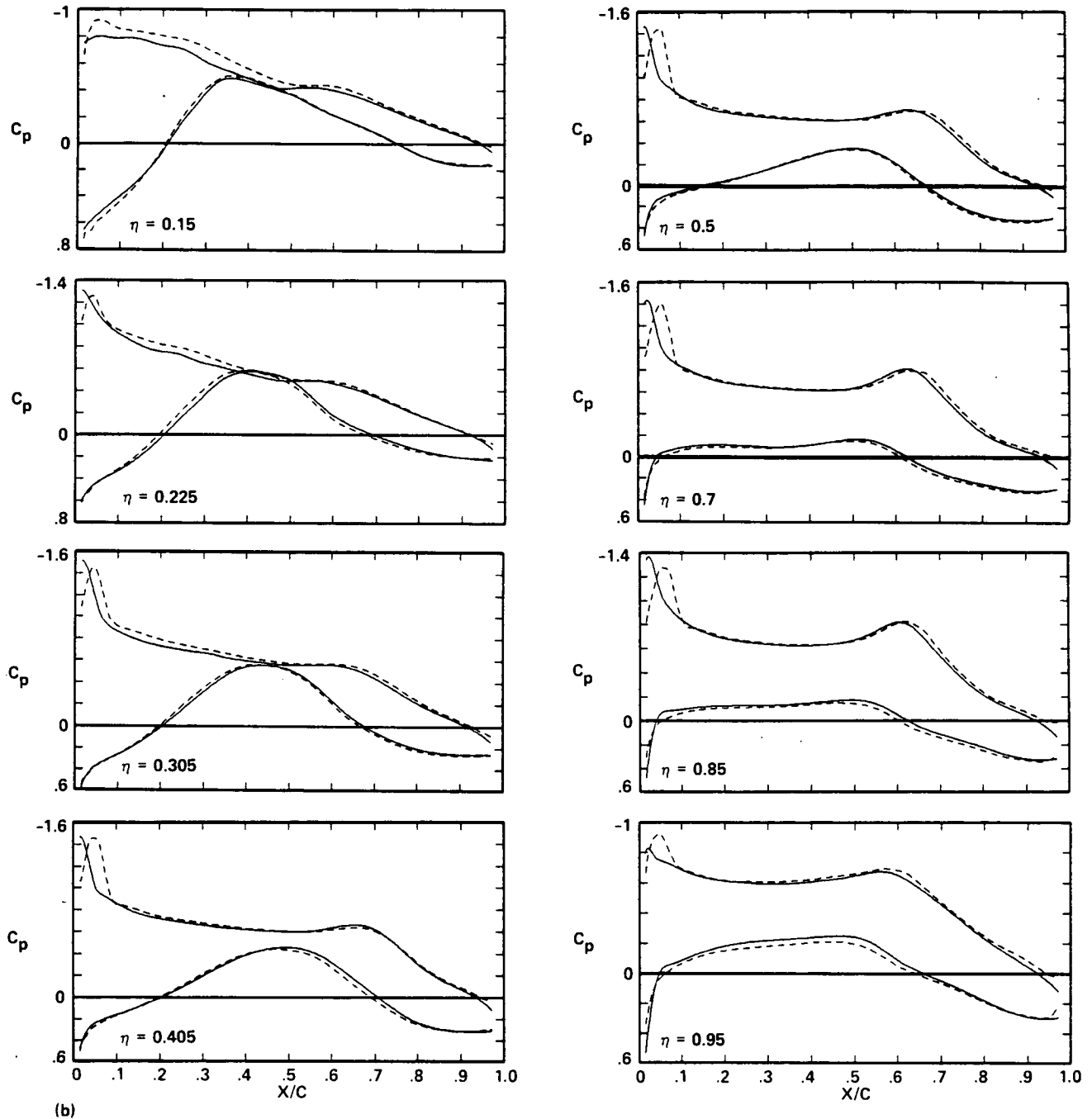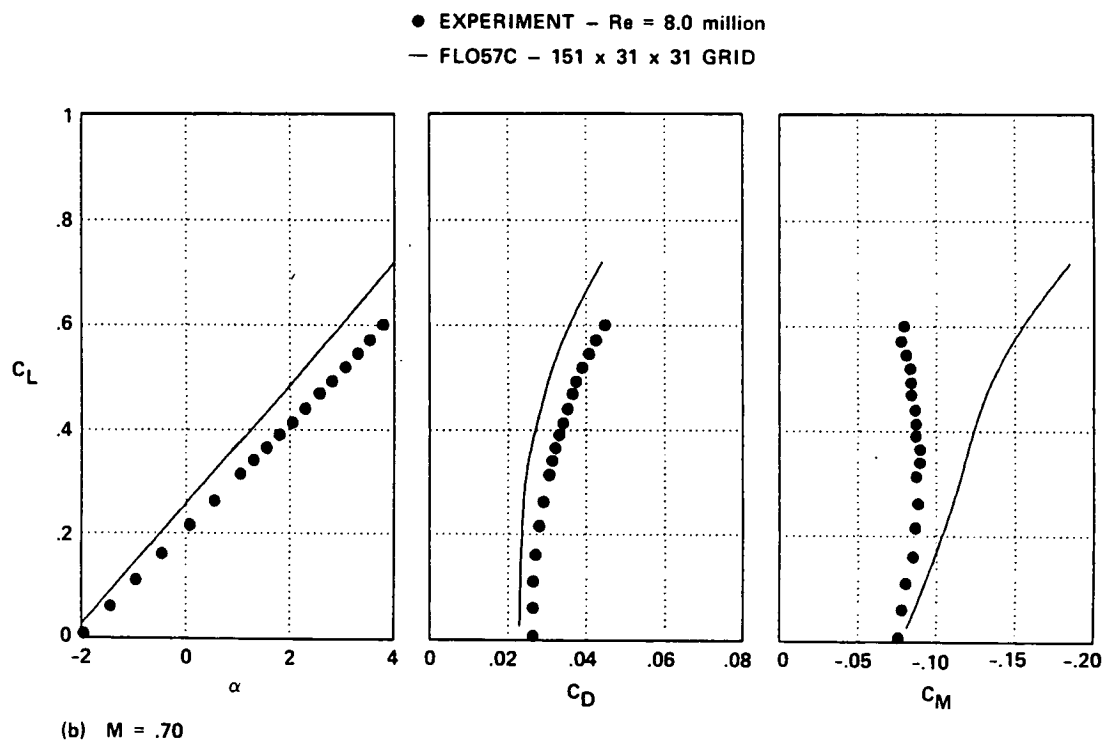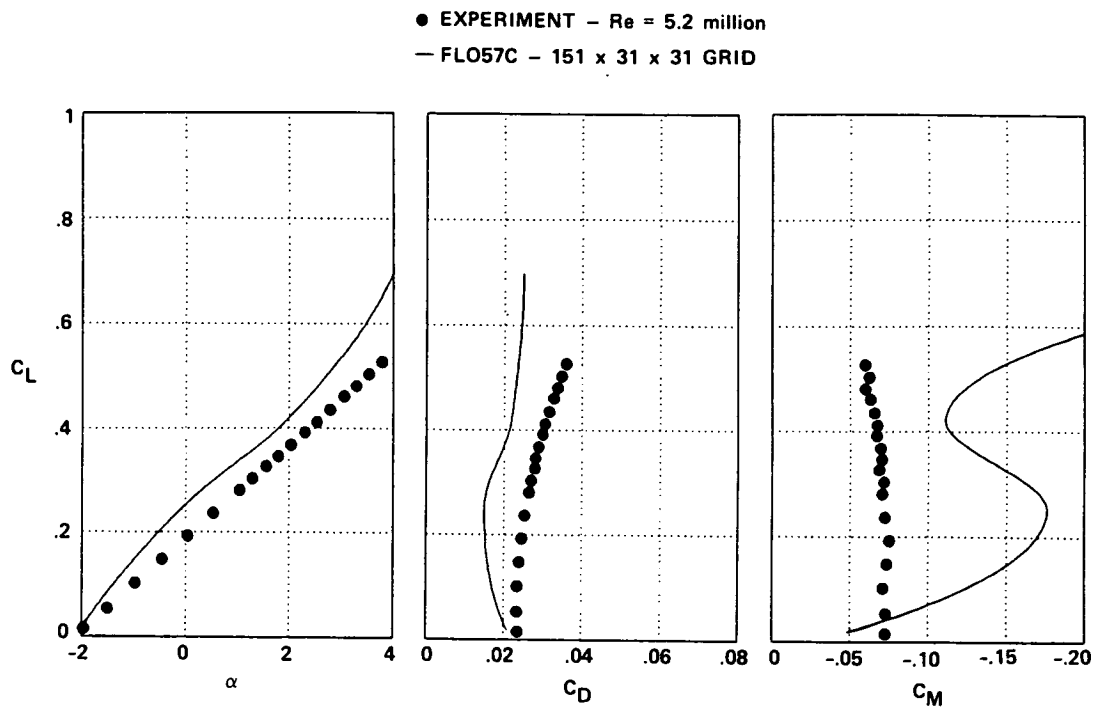
Fig. 20. Experiment–CFD force-and-moment comparison for Wing B, FLO57C.

(c)   M = .80

Fig. 20. Concluded.

——— M = .4
– – – M = .7
.... M = .8
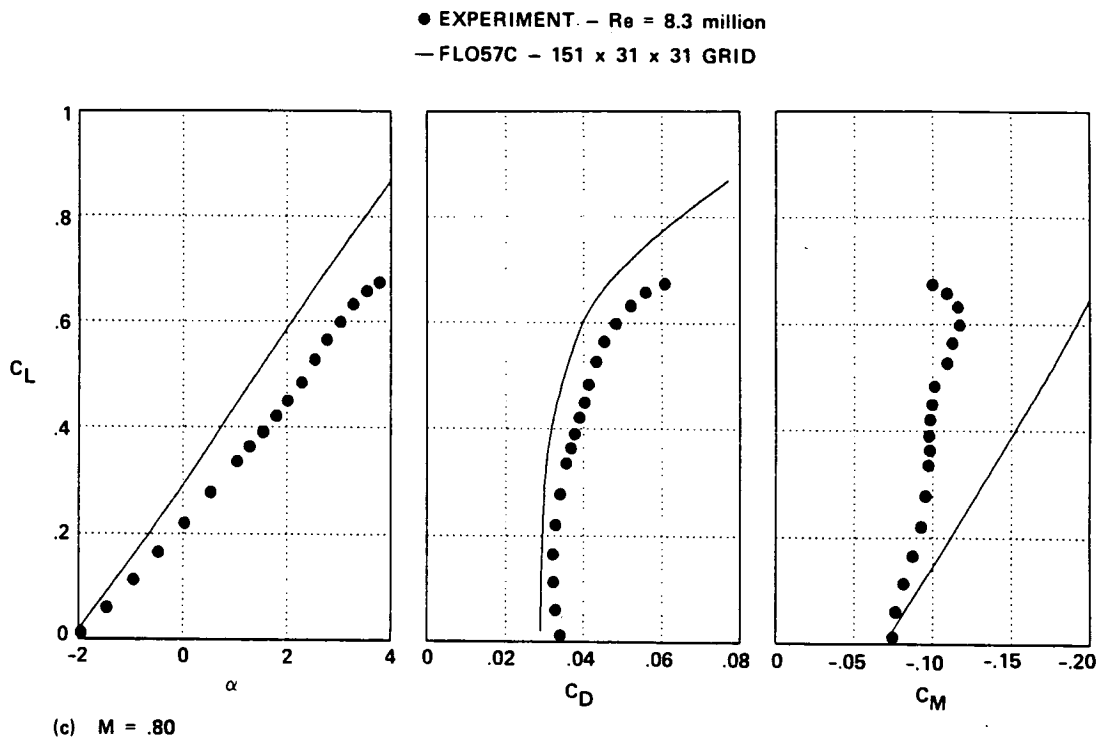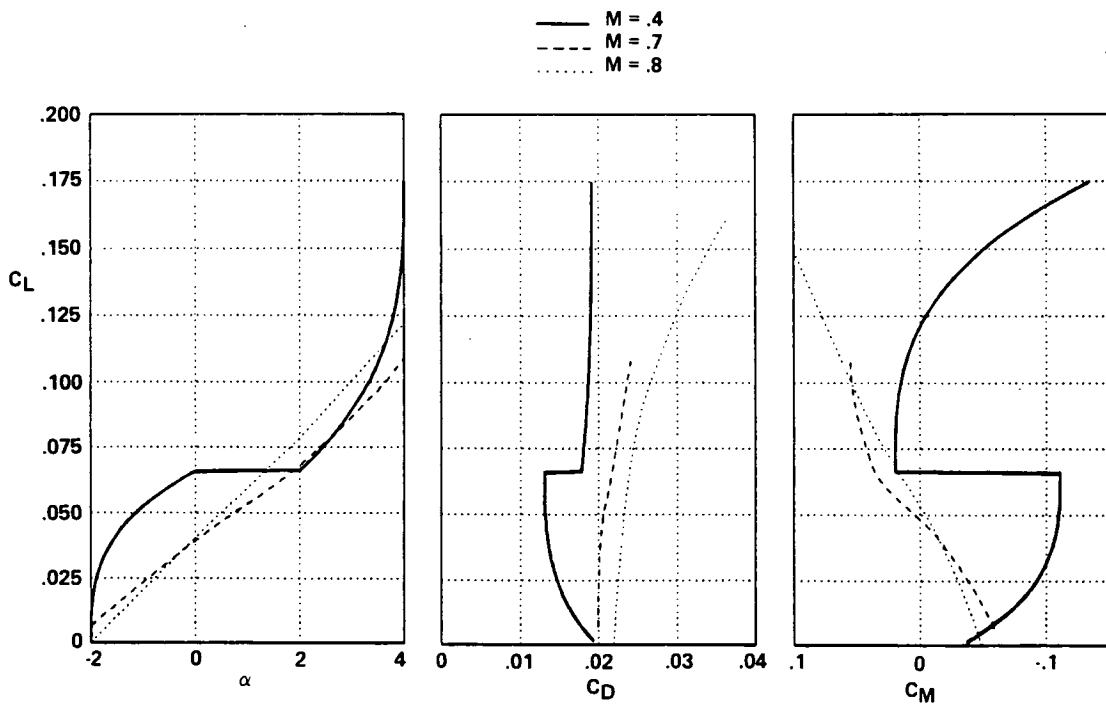
Fig. 21. Body forces and moments for Wing B, FLO57C.

84
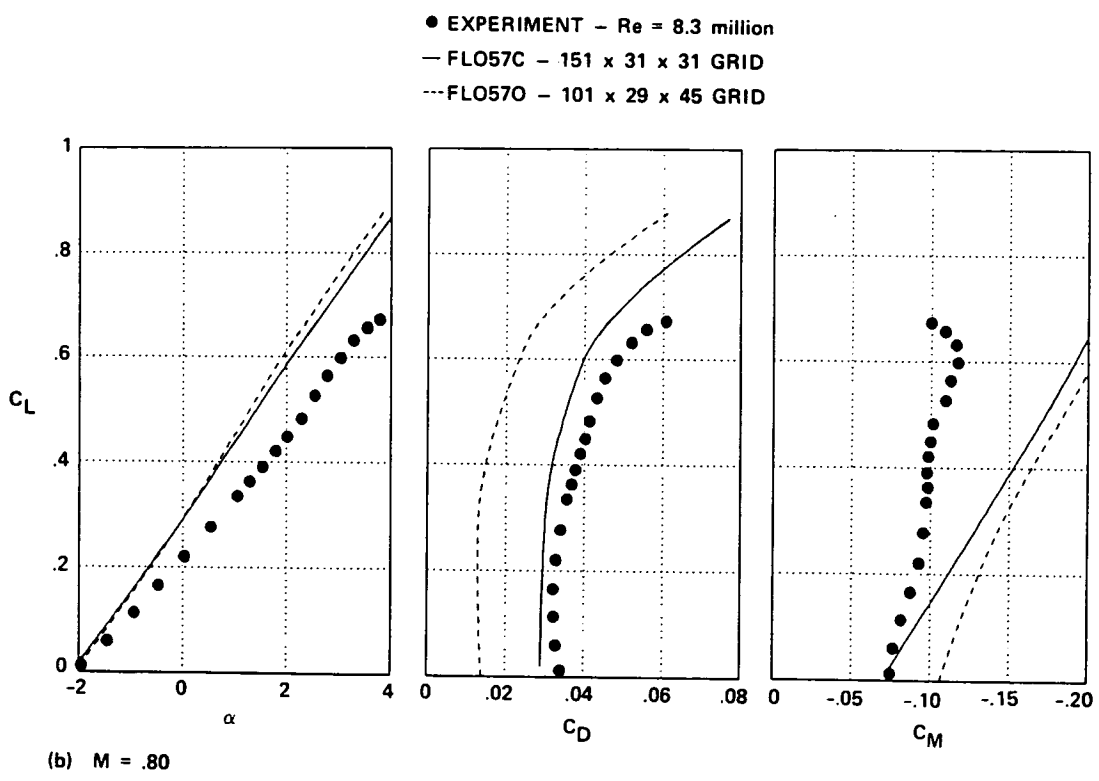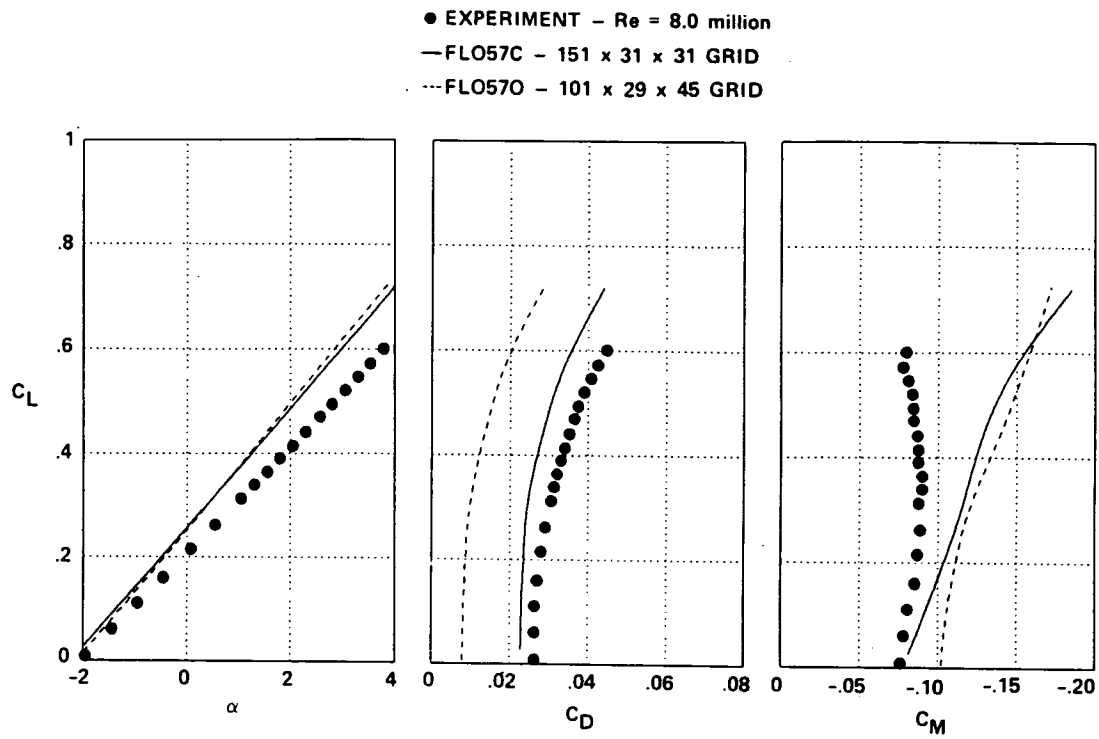
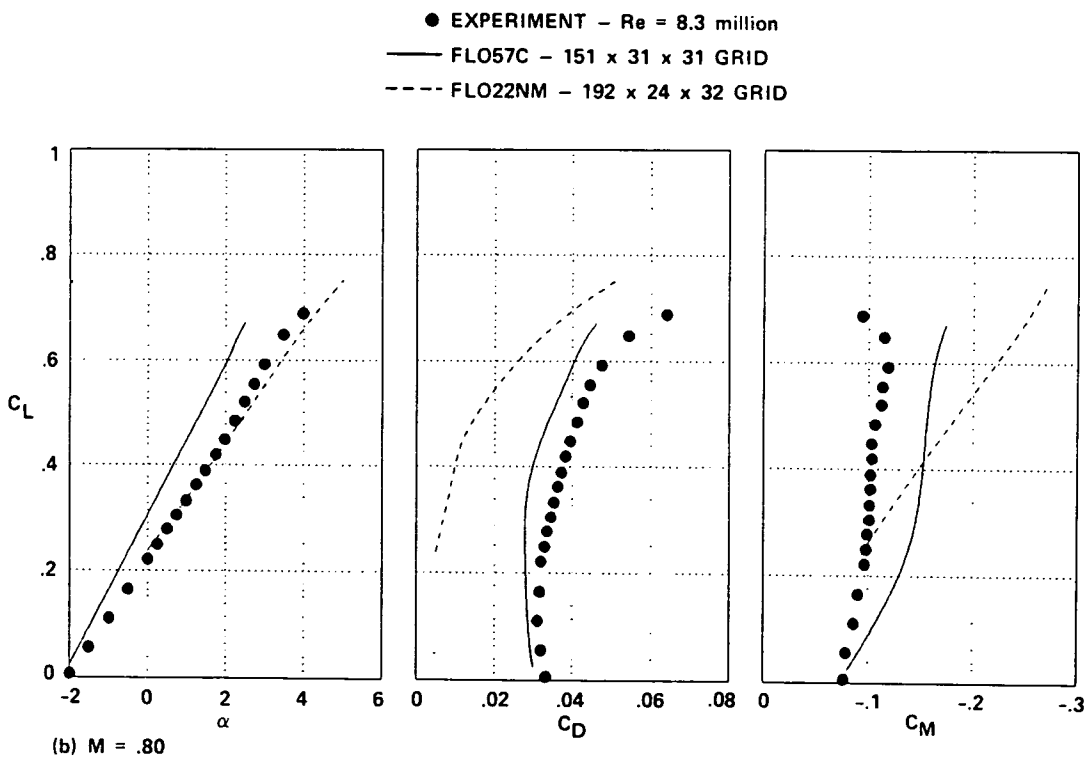Fig. 22. Experiment–CFD force-and-moment comparison for Wing B, FLO57C and FLO57O.

		M_∞	α	$Re \times 10^{-6}$	C_L	C_D	C_M
O, □	EXPERIMENT	0.401	-1.506	5.249	0.056	0.024	-0.072
——	FLO57C	0.400	-2.000	—	0.038	0.017	-0.107
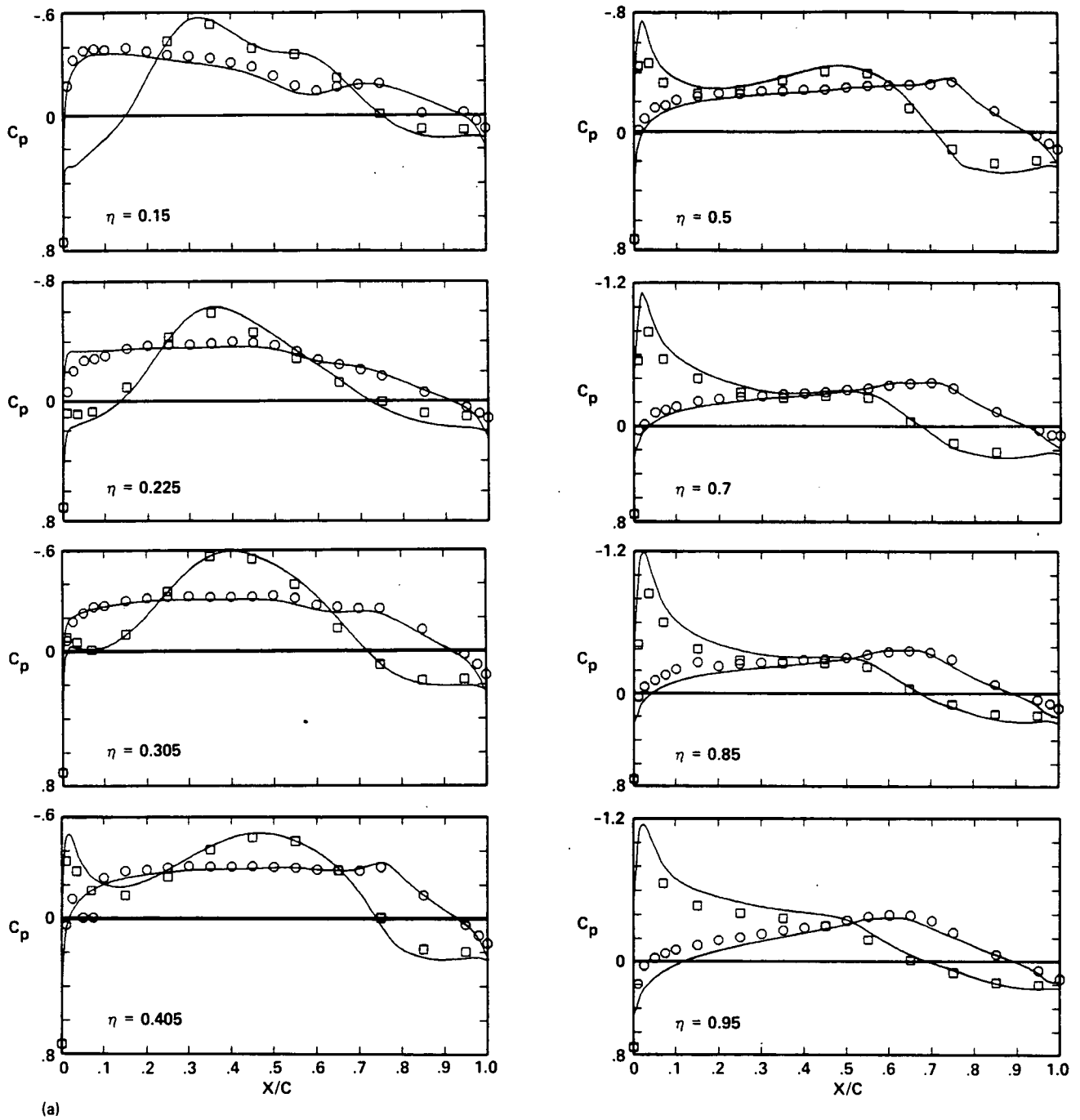
Fig. 23. Experiment–CFD pressure-distribution comparison for Wing C, FLO57C.

		M_∞	α	Re x 10^{-6}	C_L	C_D	C_M
O, □	EXPERIMENT	0.399	0.259	5.226	0.212	0.025	-0.074
——	FLO57C	0.400	0	—	0.239	0.018	-0.111
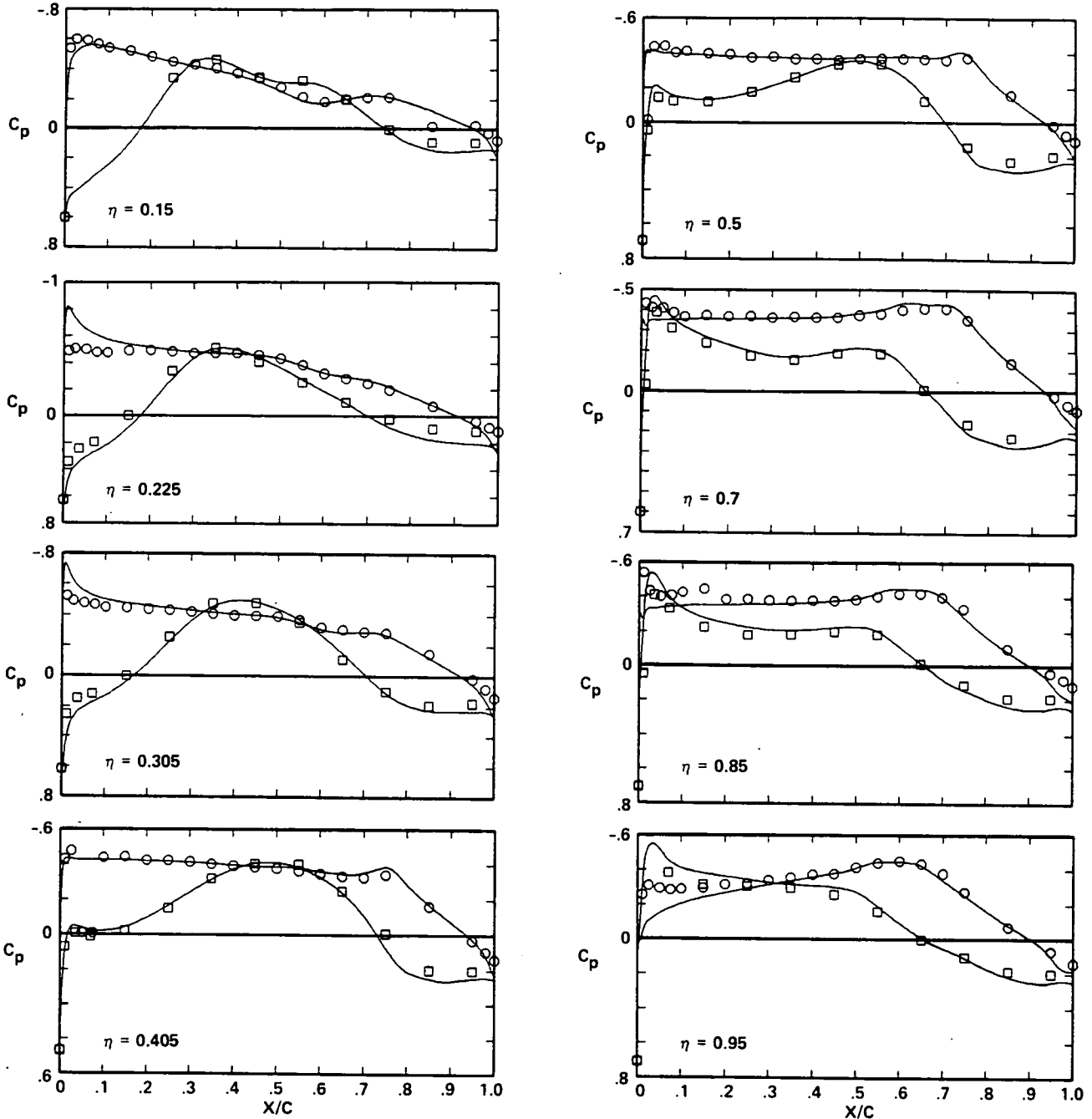
(b)

Fig. 23. Continued.

	M_∞	α	Re x 10^{-6}	C_L	C_D	C_M
O, □ EXPERIMENT	0.398	2.745	5.200	0.433	0.032	-0.067
—— FLO57C	0.400	2.000	—	0.433	0.021	-0.132
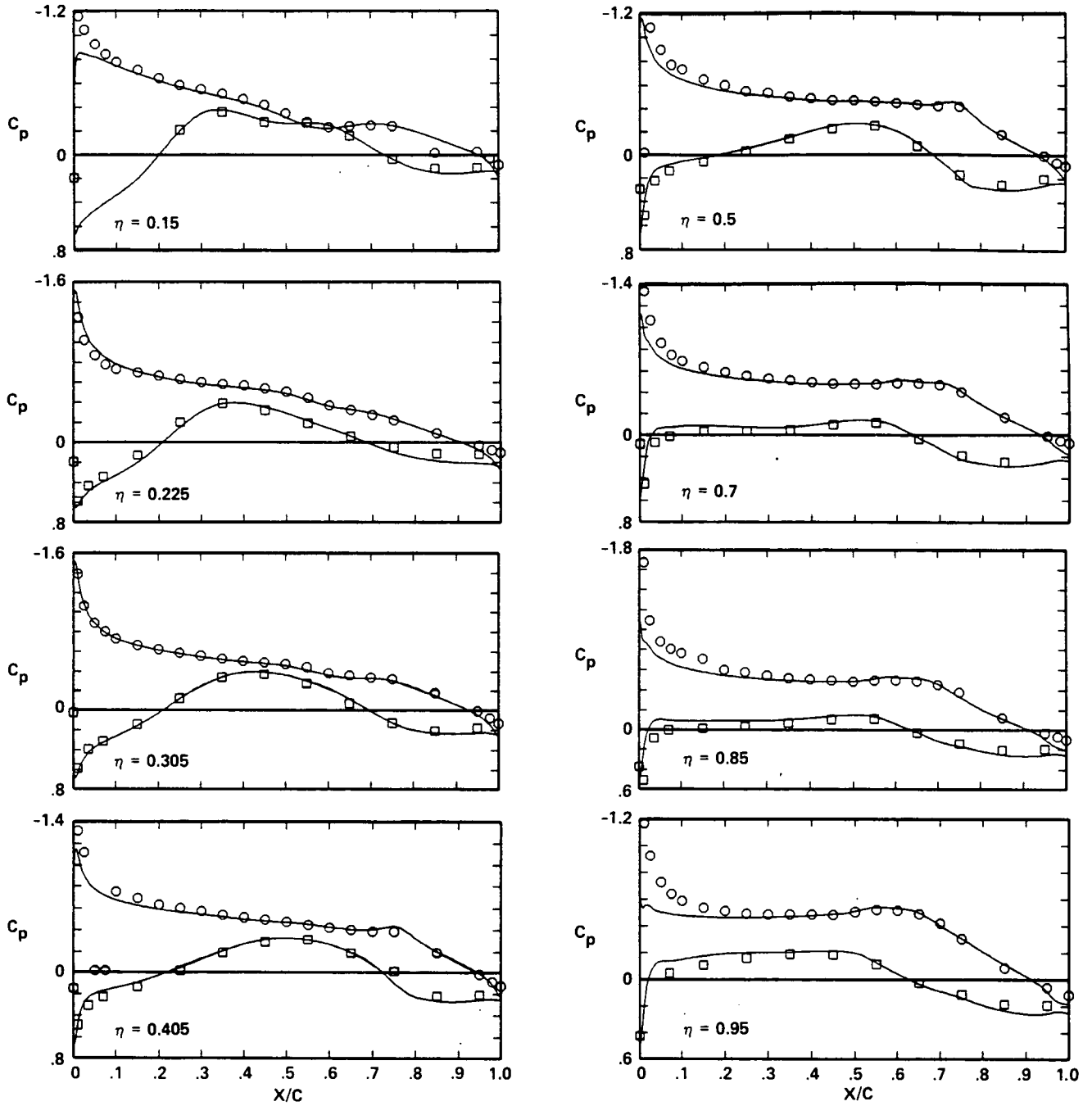
(c)

Fig. 23. Continued.

88
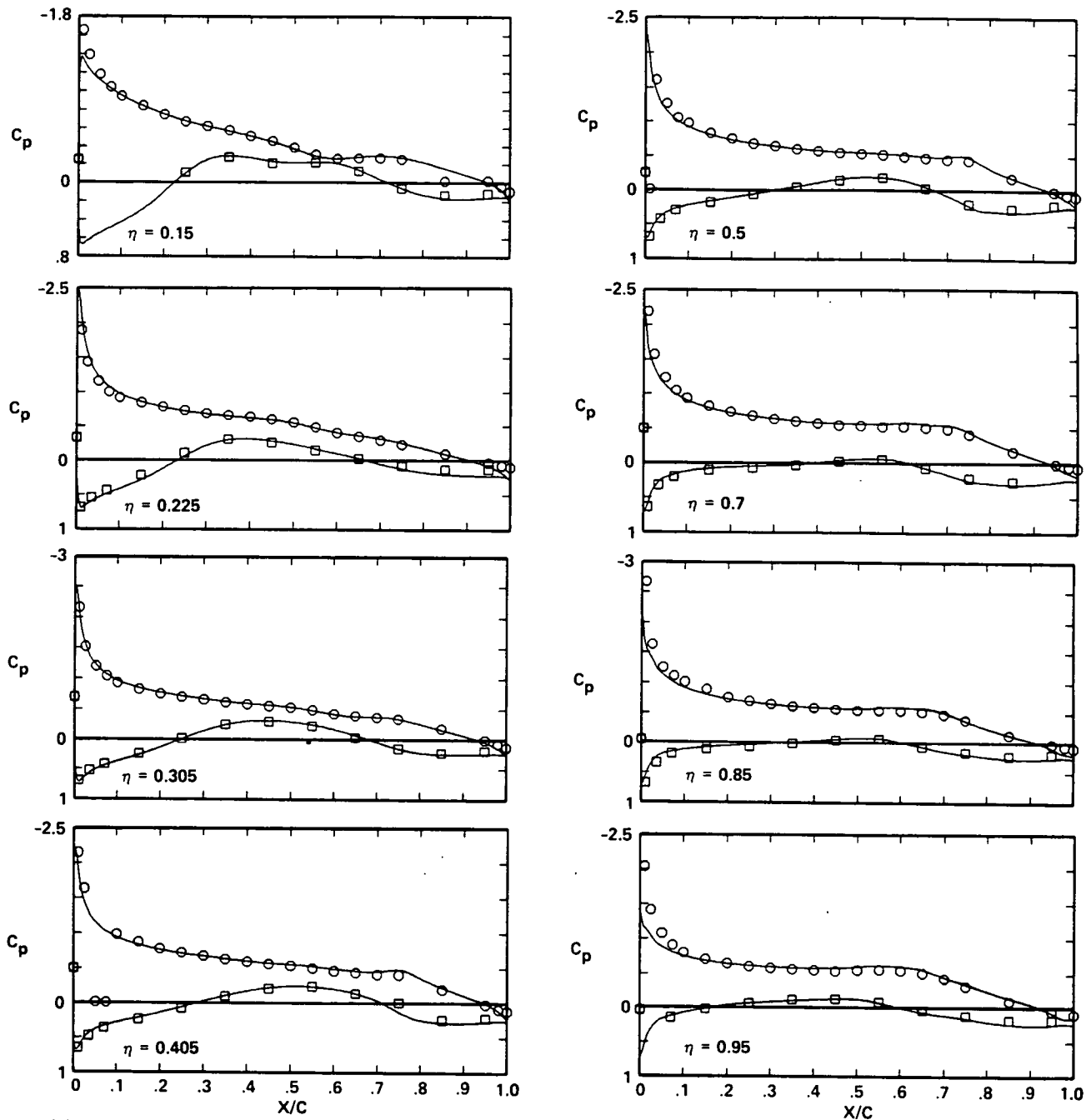
(d)

Fig. 23. Continued.

		M_∞	α	Re x 10^{-6}	C_L	C_D	C_M
o. □	EXPERIMENT	0.699	-2.019	2.089	0	0.029	-0.078
——	FLO57C	0.700	-2.000	——	0.021	0.020	-0.097
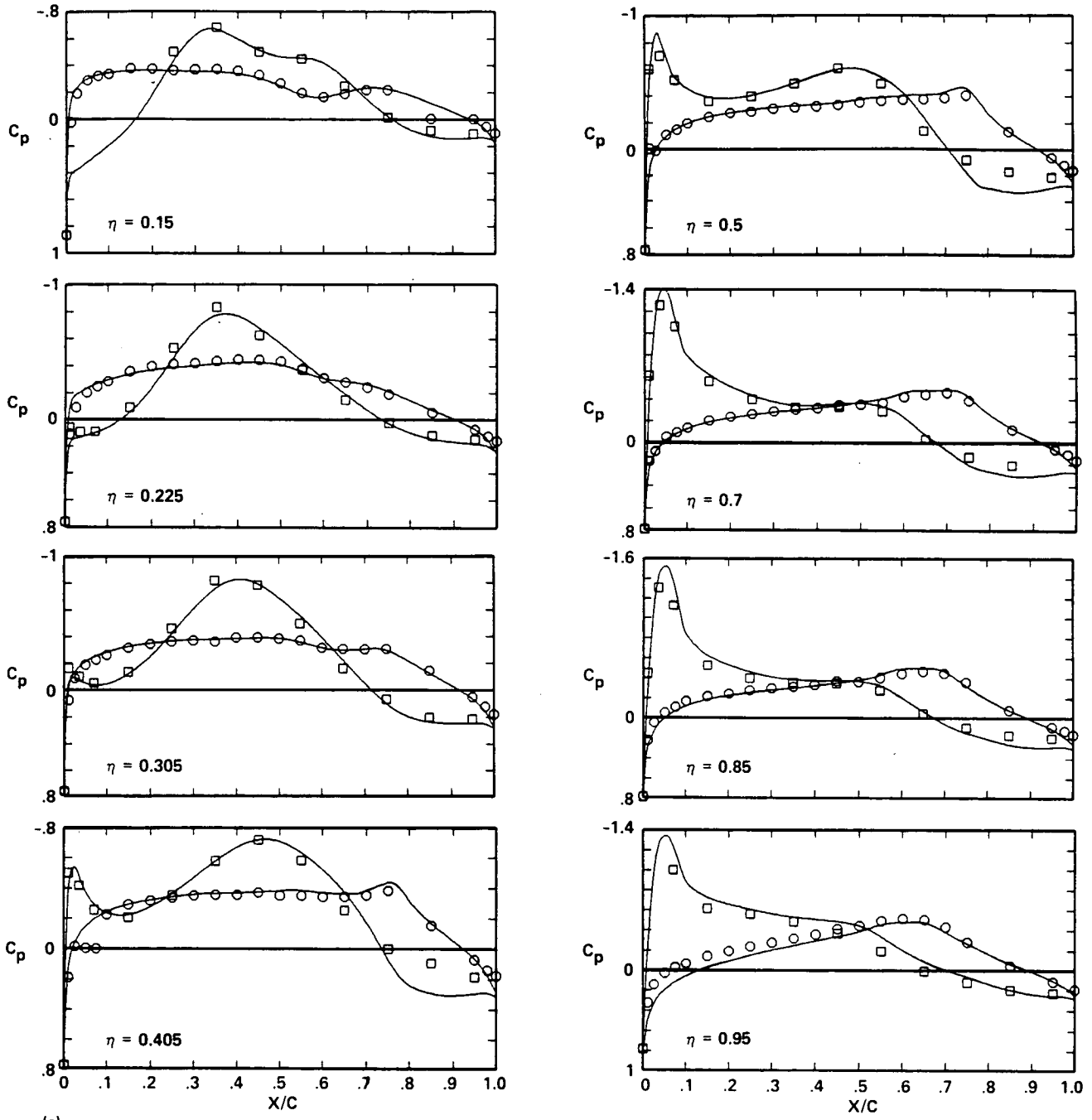
(e)

Fig. 23. Continued.

	M_∞	α	Re x 10^{-6}	C_L	C_D	C_M
○, □ EXPERIMENT	0.701	0.479	7.981	0.251	0.029	-0.090
—— FLO57C	0.700	0	—	0.243	0.024	-0.085

(f)
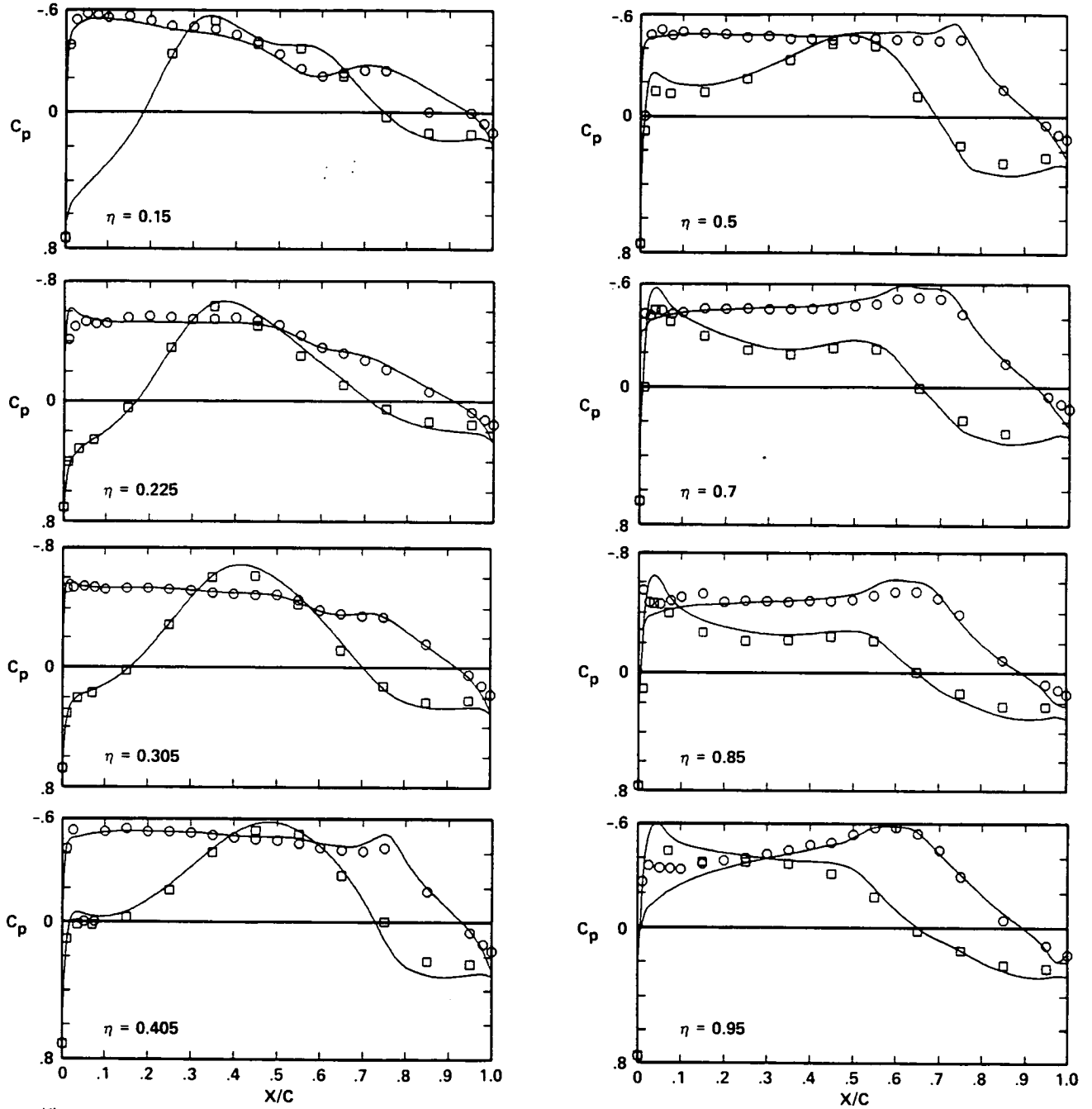
Fig. 23. Continued.

	M_∞	α	Re x 10^{-6}	C_L	C_D	C_M
EXPERIMENT	0.699	2.736	2.080	0.476	0.039	-0.087
FLO57C	0.700	2.000	—	0.480	0.029	-0.112

(g)

Fig. 23. Continued.

92
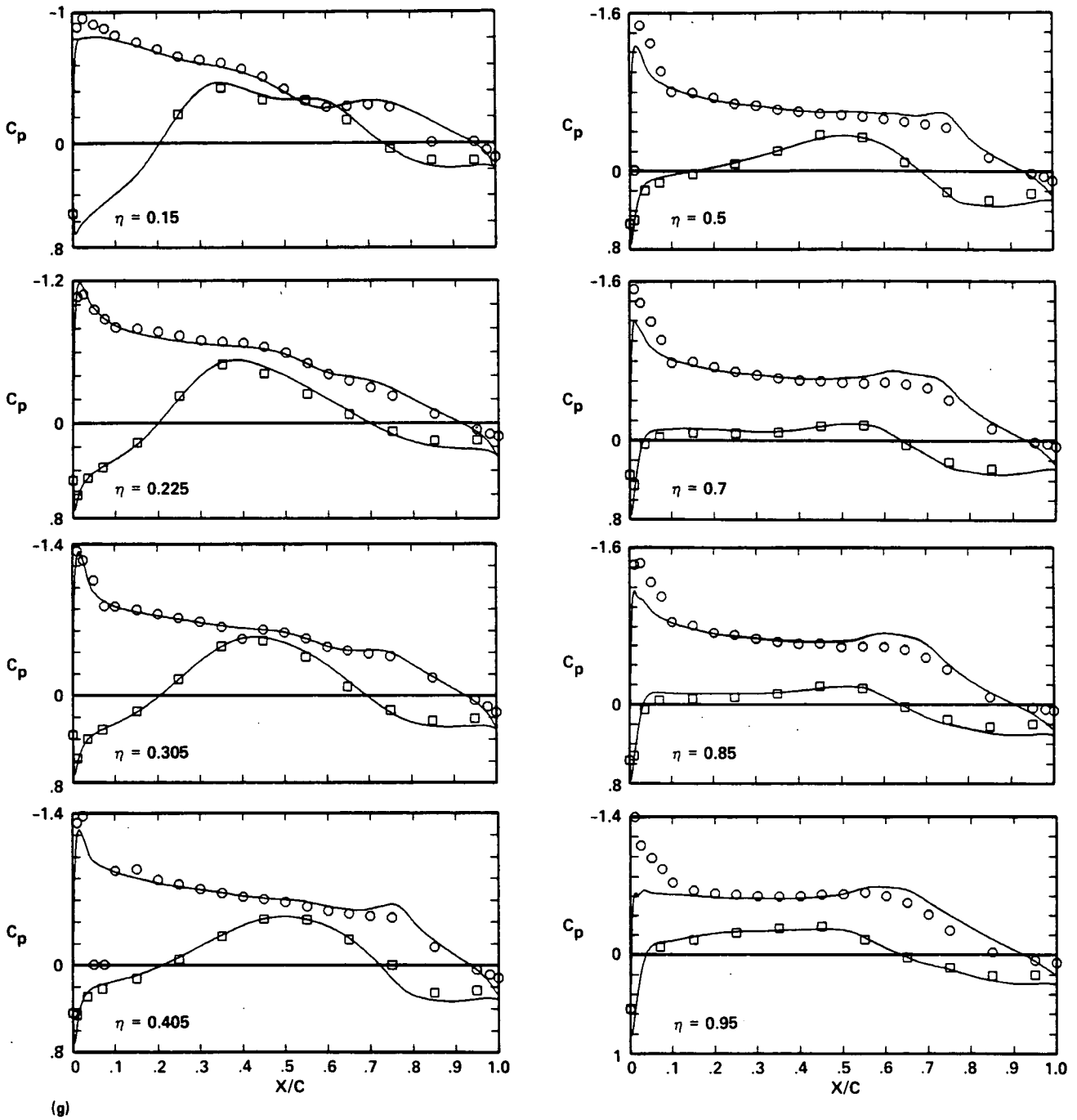
		M_∞	α	Re x 10^{-6}	C_L	C_D	C_M
○, □	EXPERIMENT	0.698	4.967	2.088	0.727	0.058	-0.079
——	FLO57C	0.700	4.000	——	0.723	0.041	-0.166

Fig. 23. Continued.

(i)

Fig. 23. Continued.

94
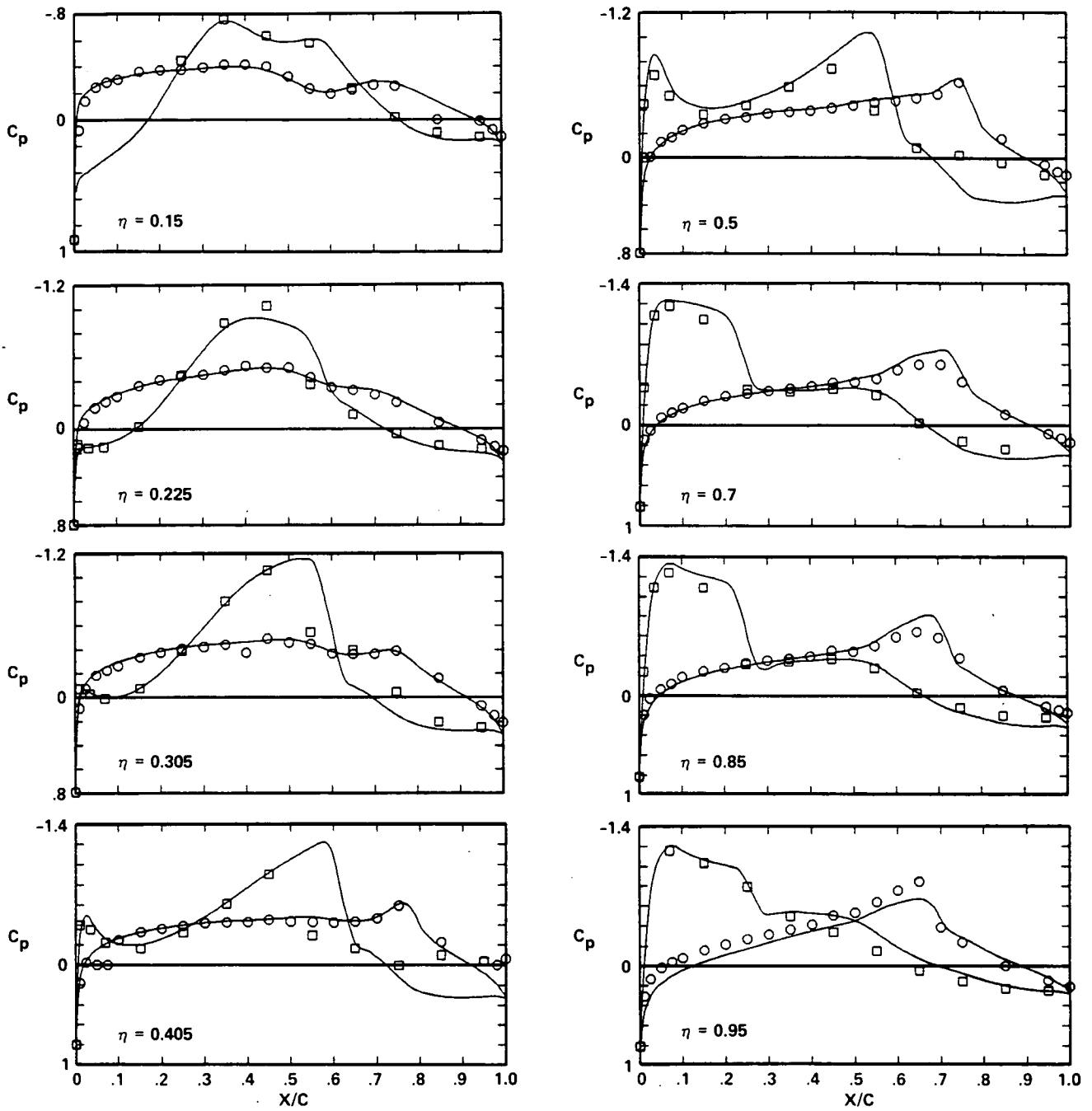
(j)

Fig. 23. Continued.

		M_∞	α	$Re \times 10^{-6}$	C_L	C_D	C_M
○, □	EXPERIMENT	0.801	2.730	2.215	0.591	0.050	-0.152
——	FLO57C	0.800	2.000	——	0.579	0.039	-0.163

Fig. 23. Continued.

96

C-2
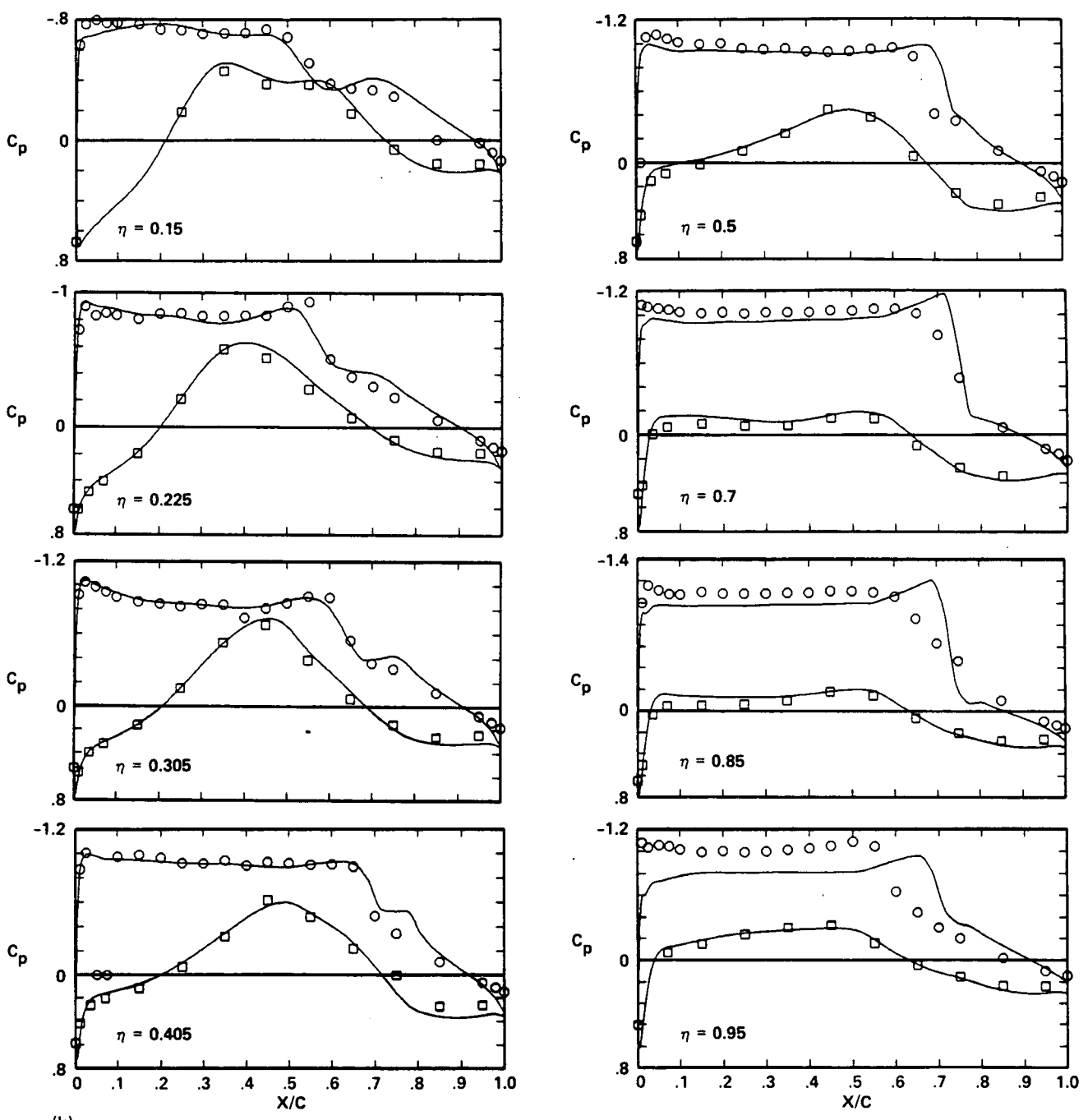
		M_∞	α	Re x 10^{-6}	C_L	C_D	C_M
○, □	EXPERIMENT	0.798	6.965	2.204	0.680	0.130	-0.044
——	FLO57C	0.800	4.000	—	0.869	0.075	-0.204

$\eta = 0.15$

$\eta = 0.5$

$\eta = 0.225$

$\eta = 0.7$

$\eta = 0.305$

$\eta = 0.85$

$\eta = 0.405$

$\eta = 0.95$

(l)

Fig. 23. Concluded.

(a)   M = .40

(b)   M = .70
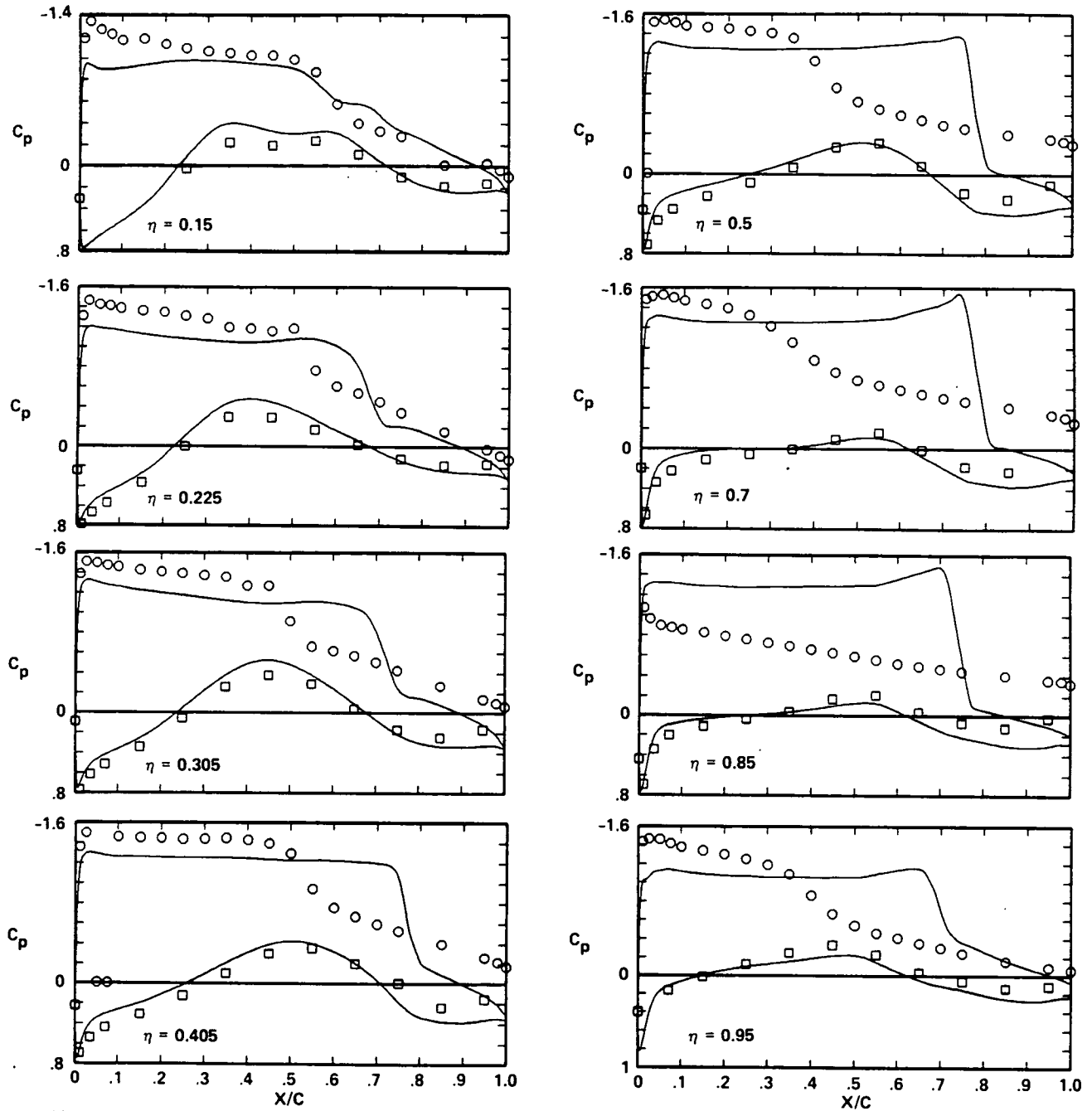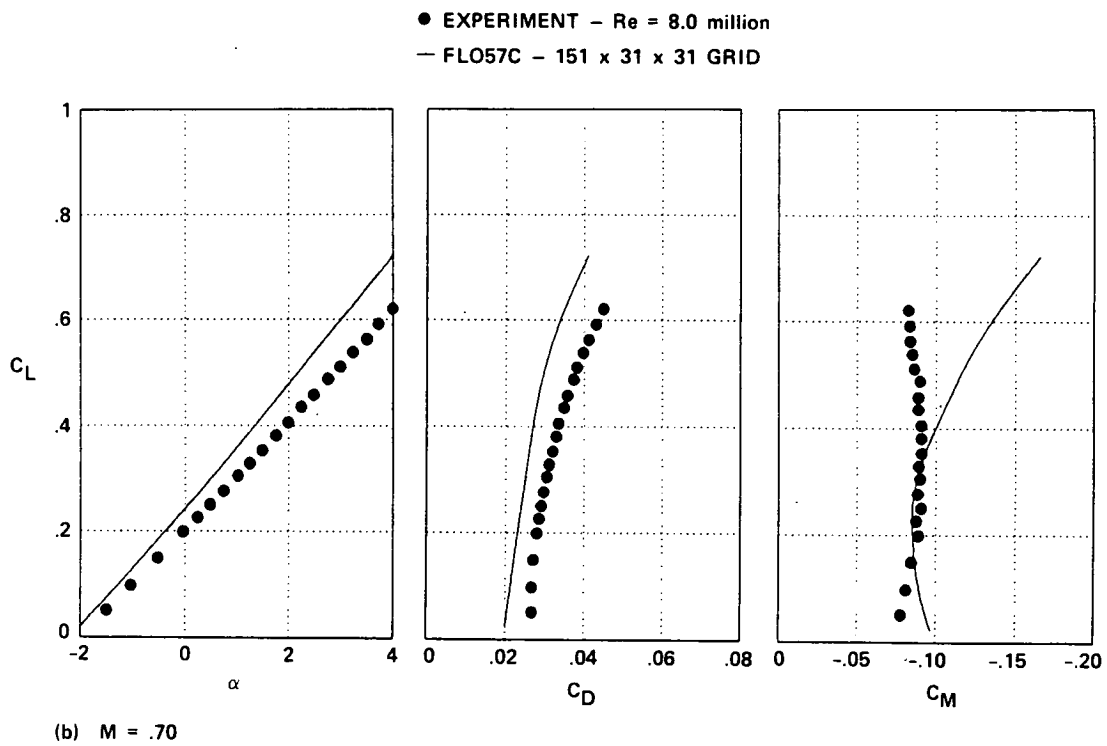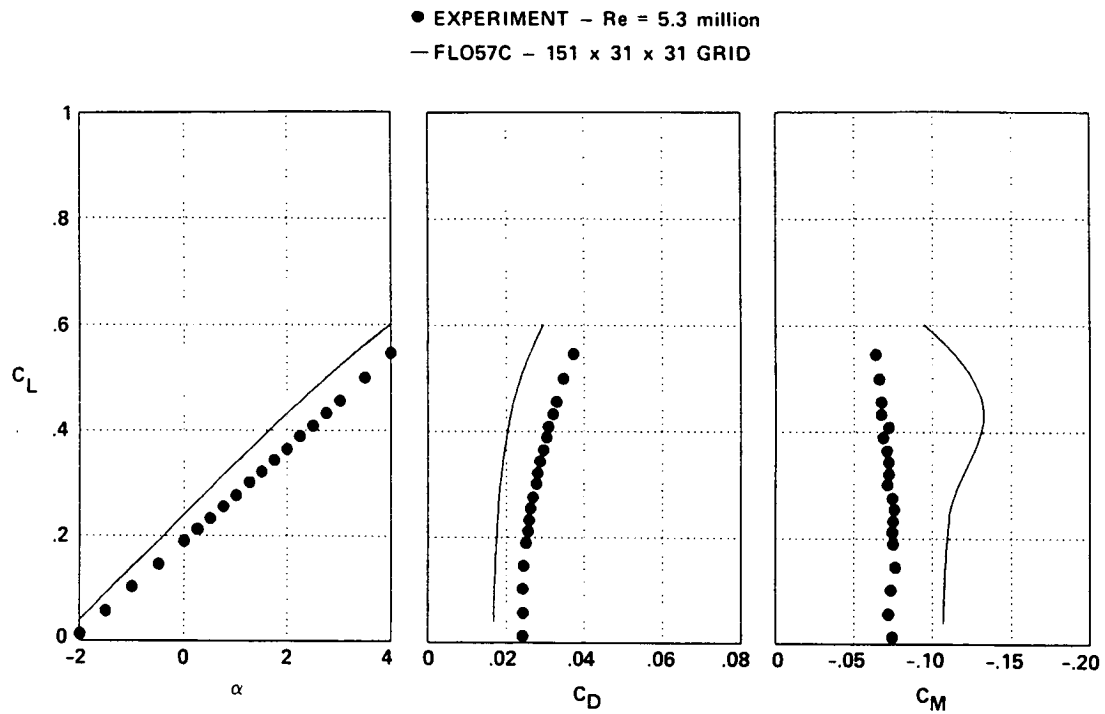
Fig. 24. Experiment–CFD force-and-moment comparison for Wing C, FLO57C.

(c)   M = .80

Fig. 24. Concluded.

(a)   M = .40
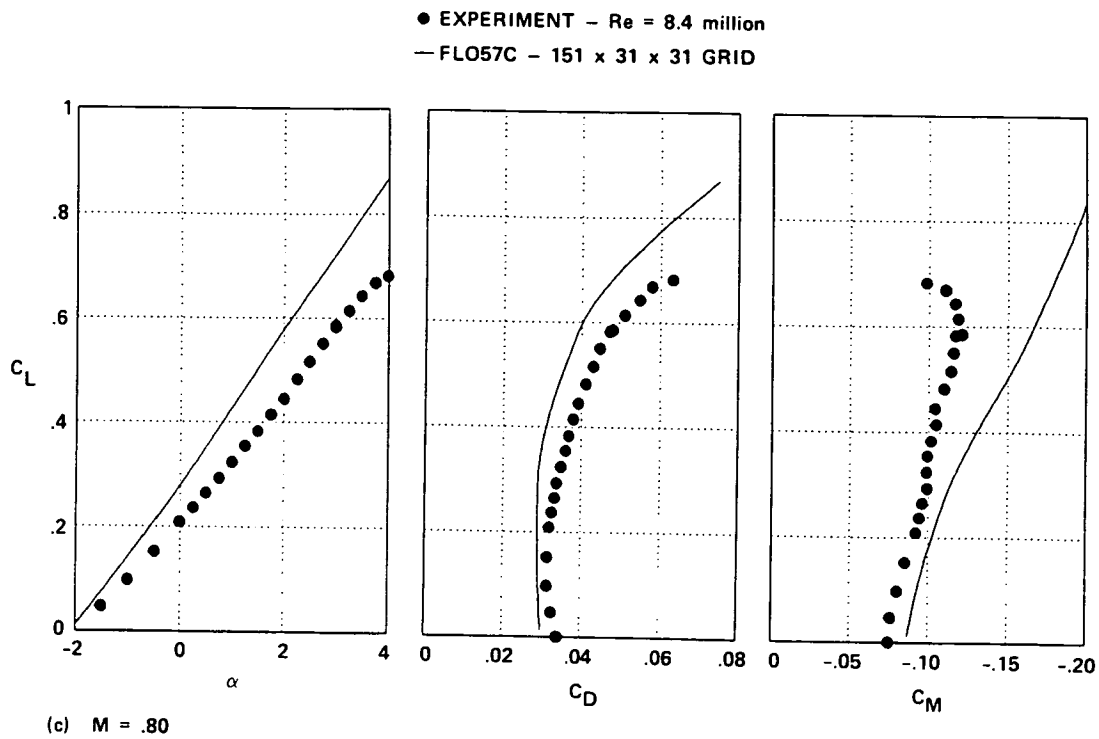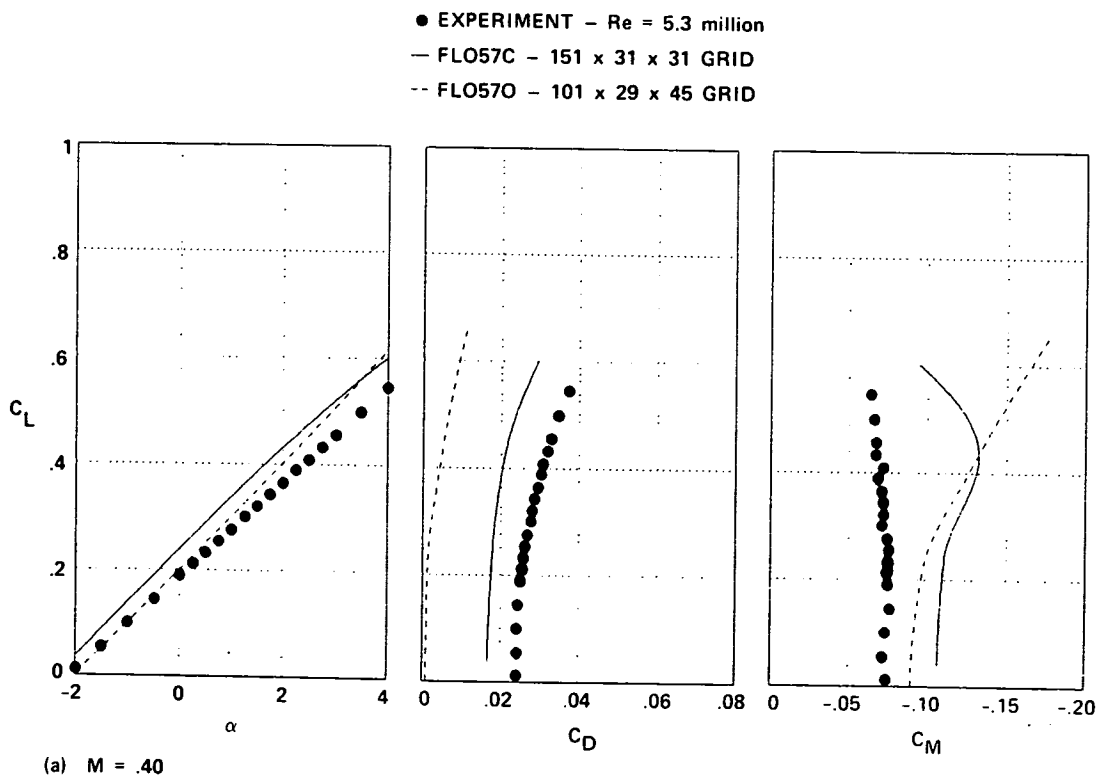
Fig. 25. Experiment–CFD force-and-moment comparison for Wing C, FLO57C and FLO57O.

● EXPERIMENT — Re = 8.0 million
— FLO57C — 151 x 31 x 31 GRID
-- FLO57O — 101 x 29 x 45 GRID

(b) M = .70
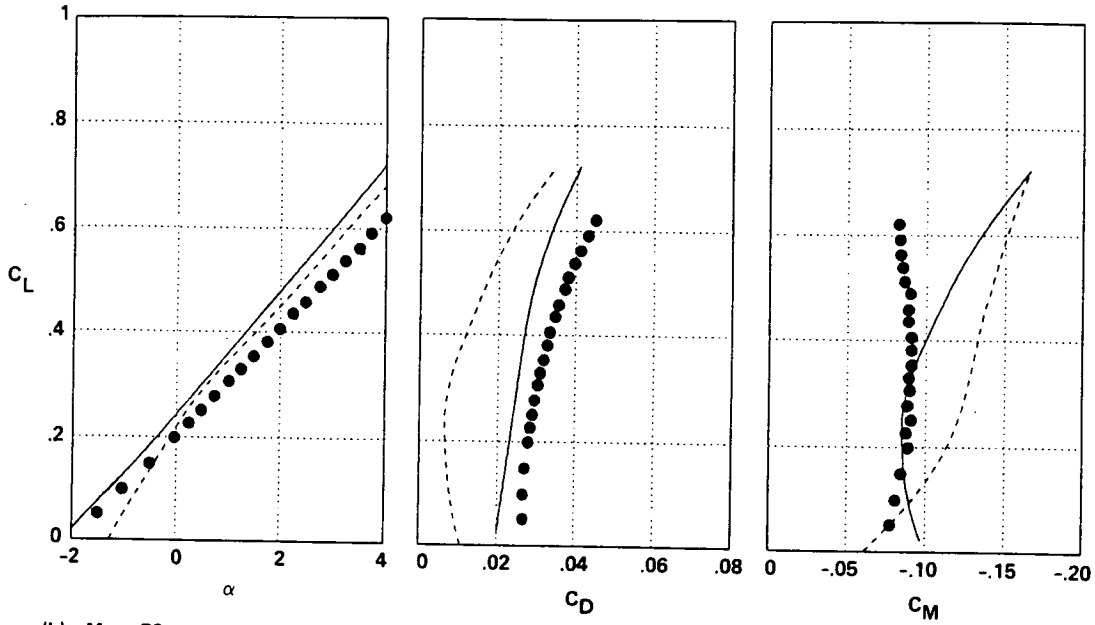
● EXPERIMENT — Re = 8.4 million
— FLO57C — 151 x 31 x 31 GRID
-- FLO57O — 101 x 29 x 45 GRID

(c) M = .80
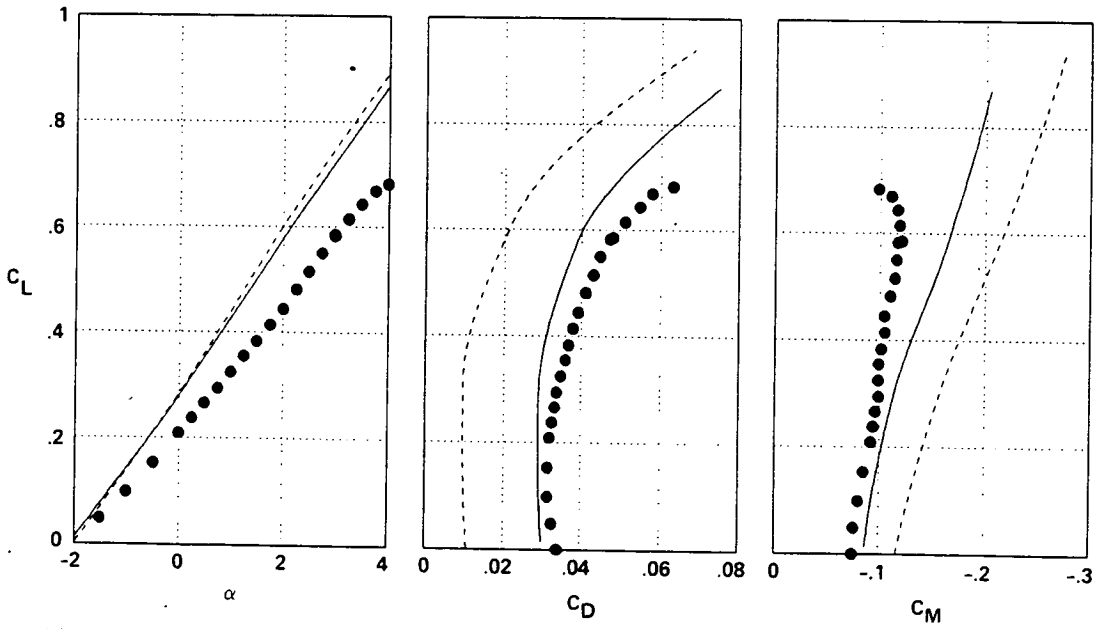
Fig. 25. Concluded.

	M_∞	α	Re x 10^{-6}	C_L	C_D	C_M
O, □ EXPERIMENT	0.401	-1.993	5.324	0.018	0.024	-0.075
—— FLO57C	0.400	-2.000	—	0.037	0.021	-0.078
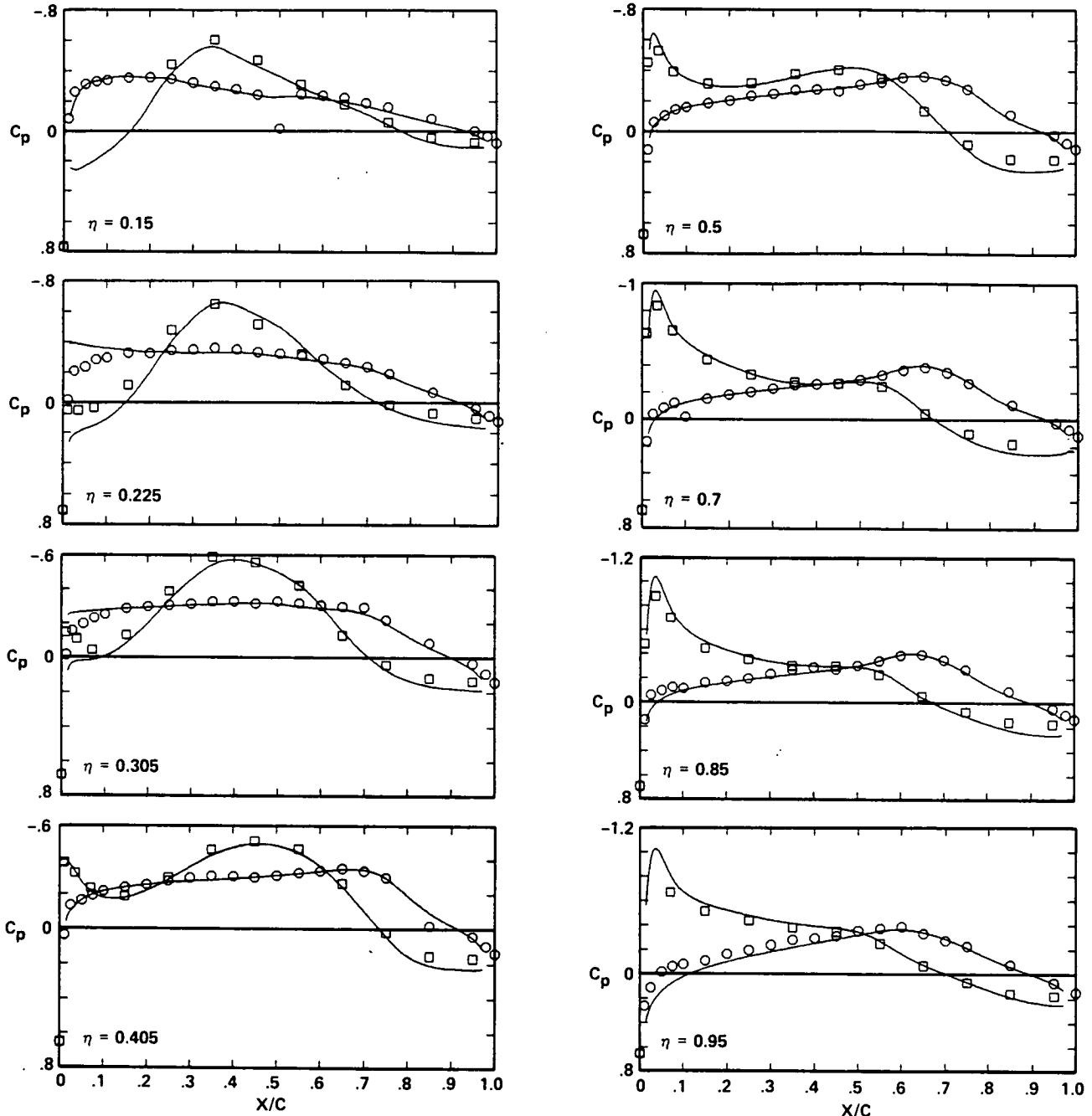
Fig. 26. Experiment–CFD pressure-distribution comparison for Wing D, FLO57C.

	M_∞	α	$Re \times 10^{-6}$	C_L	C_D	C_M
O, □ EXPERIMENT	0.400	0.758	5.307	0.261	0.026	−0.074
—— FLO57C	0.400	0.0	—	0.266	0.018	−0.142

$\eta = 0.15$

$\eta = 0.5$

$\eta = 0.225$

$\eta = 0.7$

$\eta = 0.305$

$\eta = 0.85$

$\eta = 0.405$

$\eta = 0.95$

C_p

X/C

X/C

(b)

Fig. 26. Continued.

102
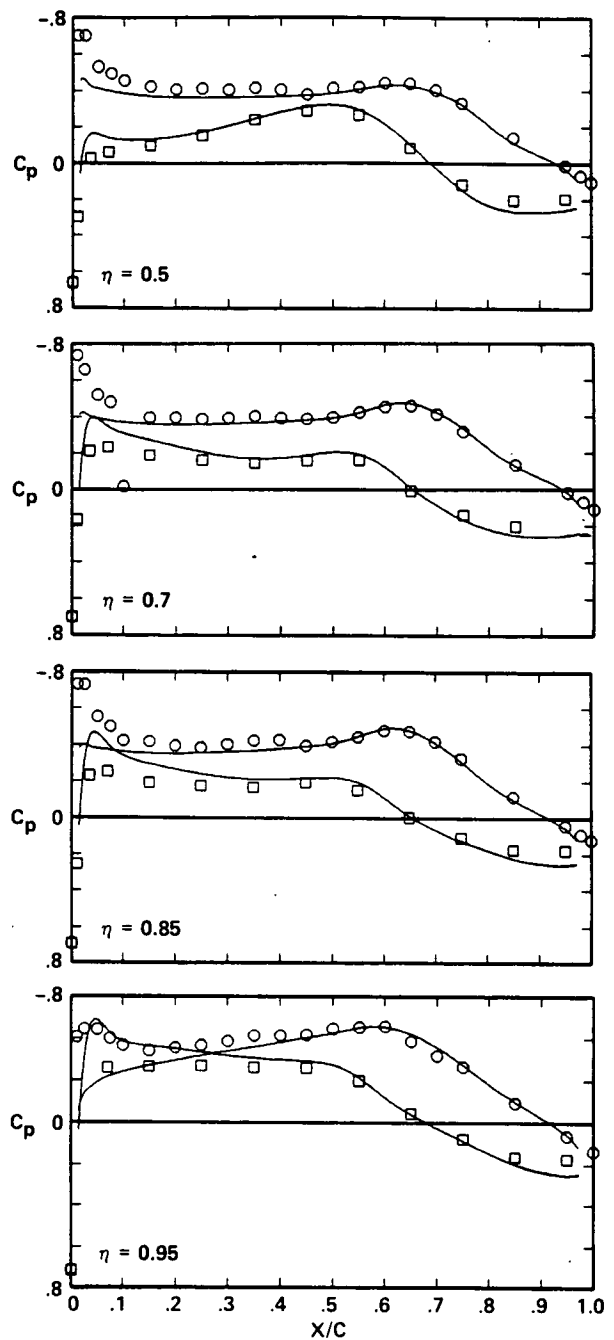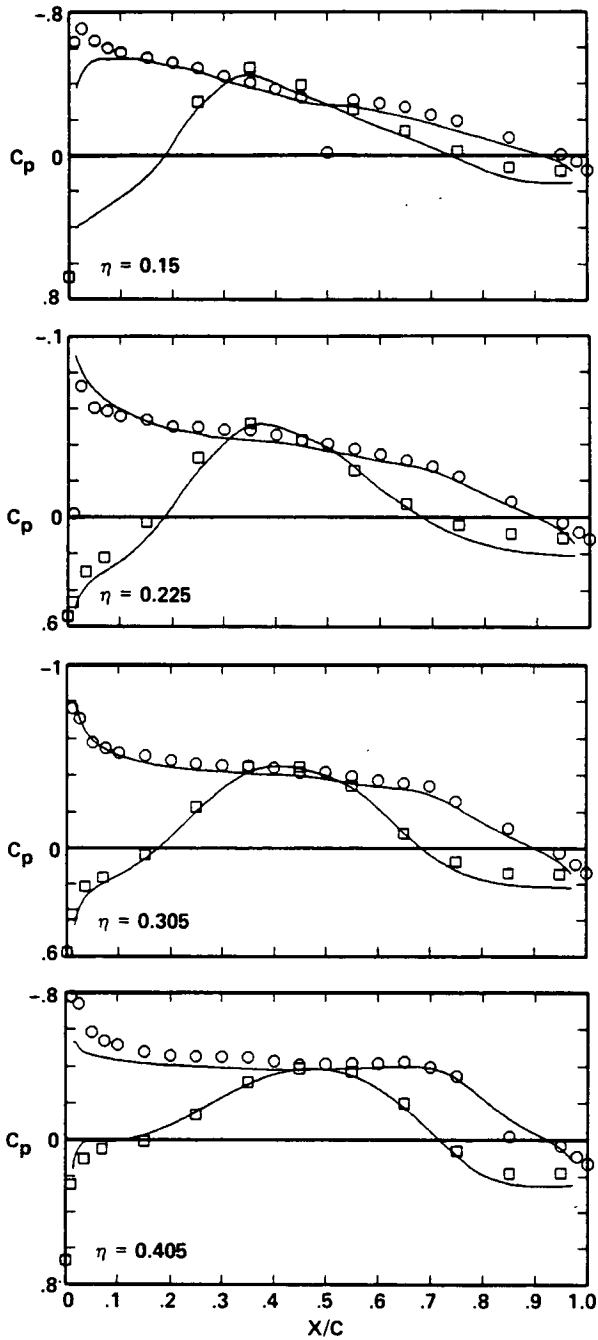
	M_∞	α	Re x 10^{-6}	C_L	C_D	C_M
O, □ EXPERIMENT	0.399	2.987	5.286	0.459	0.033	-0.065
—— FLO57C	0.400	2.000	—	0.455	0.023	-0.154
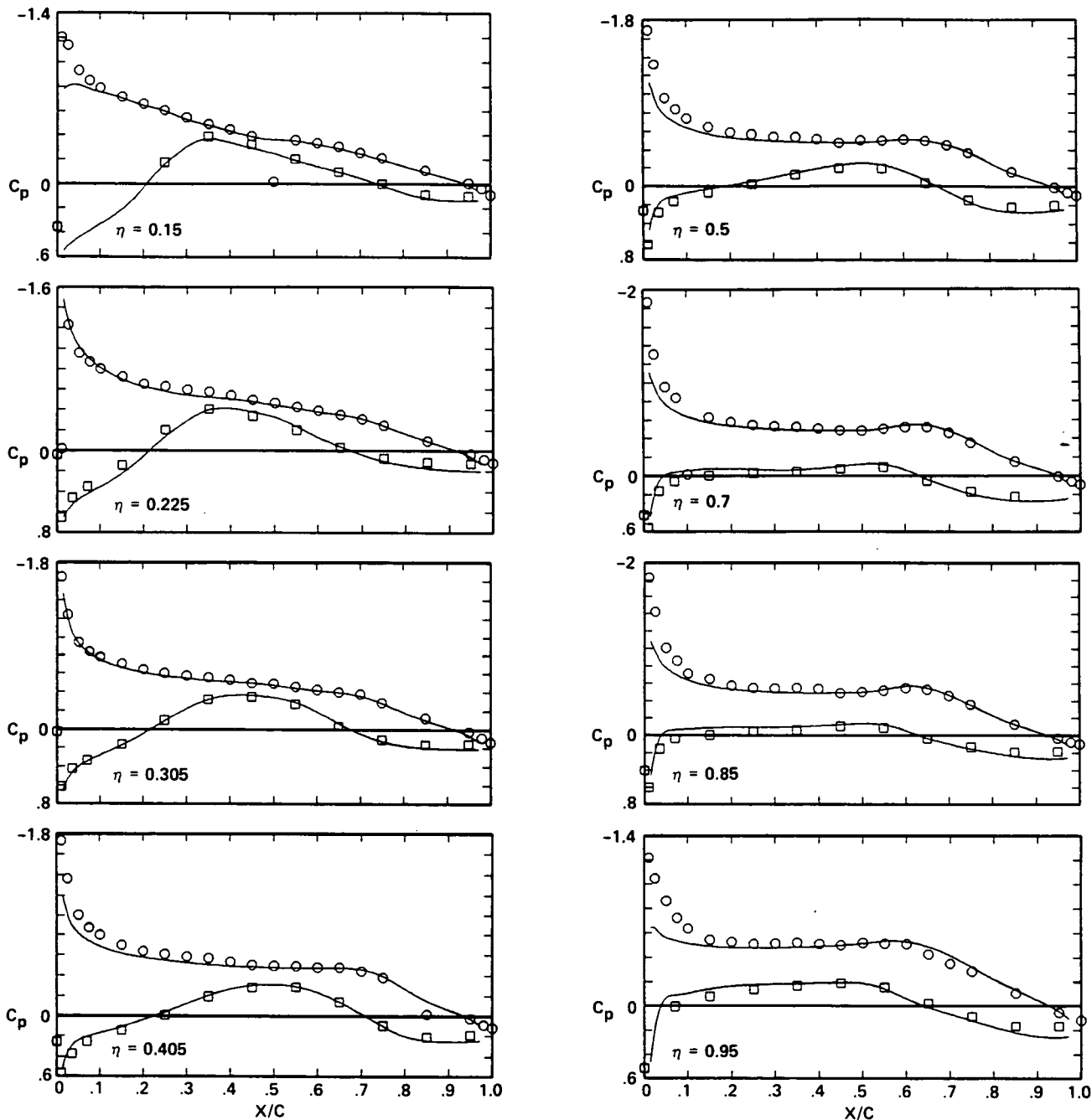
(c)

Fig. 26. Continued.

		M_∞	α	Re x 10^{-6}	C_L	C_D	C_M
O, □	EXPERIMENT	0.399	4.982	5.279	0.636	0.042	-0.054
——	FLO57C	0.400	4.000	—	0.625	0.030	-0.129

(d)
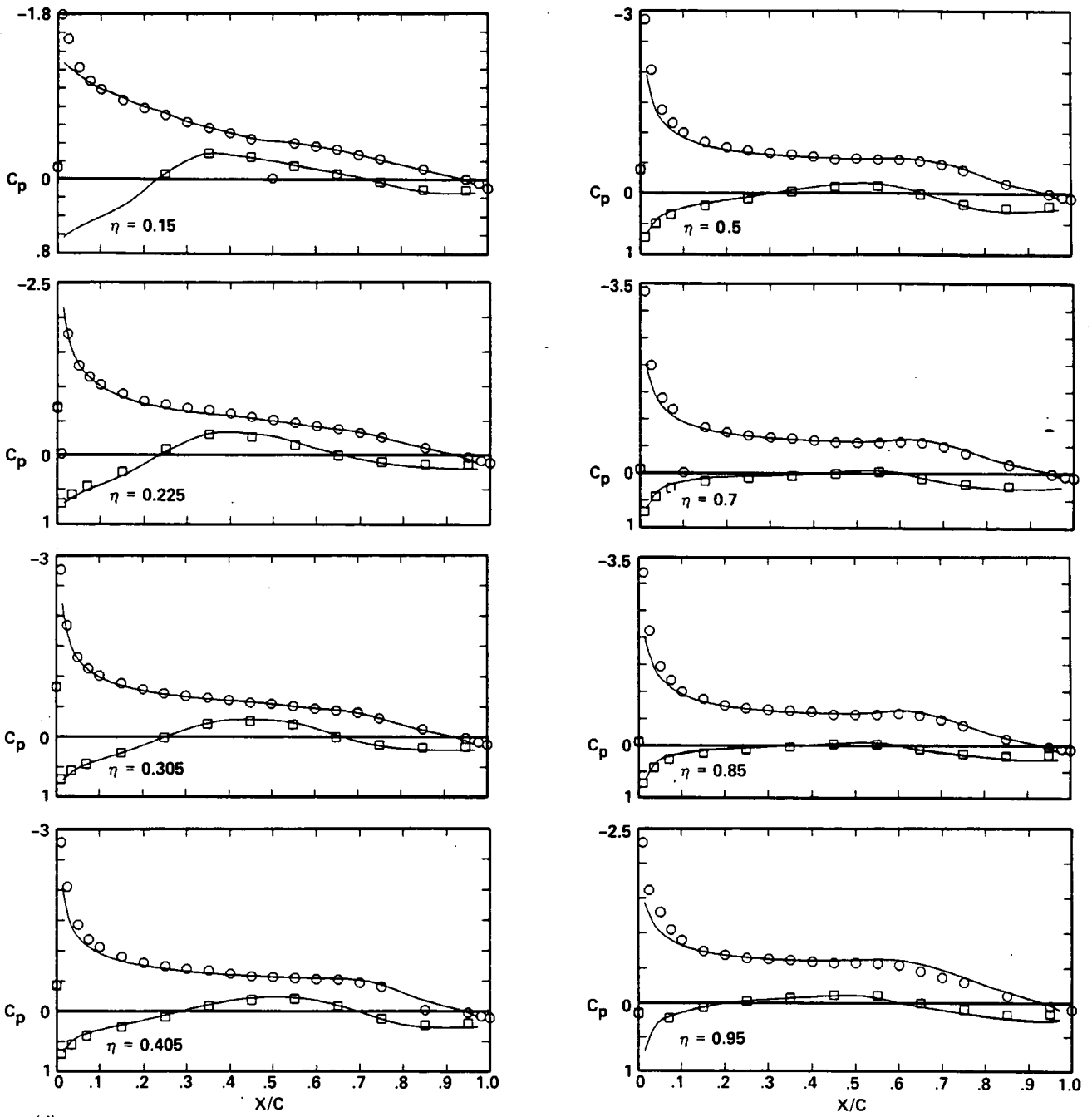
Fig. 26. Continued.

	M_∞	α	Re x 10^{-6}	C_L	C_D	C_M
o, □ EXPERIMENT	0.701	-2.002	8.170	0.011	0.026	-0.078
—— FLO57C	0.700	-2.000	—	0.025	0.023	-0.074
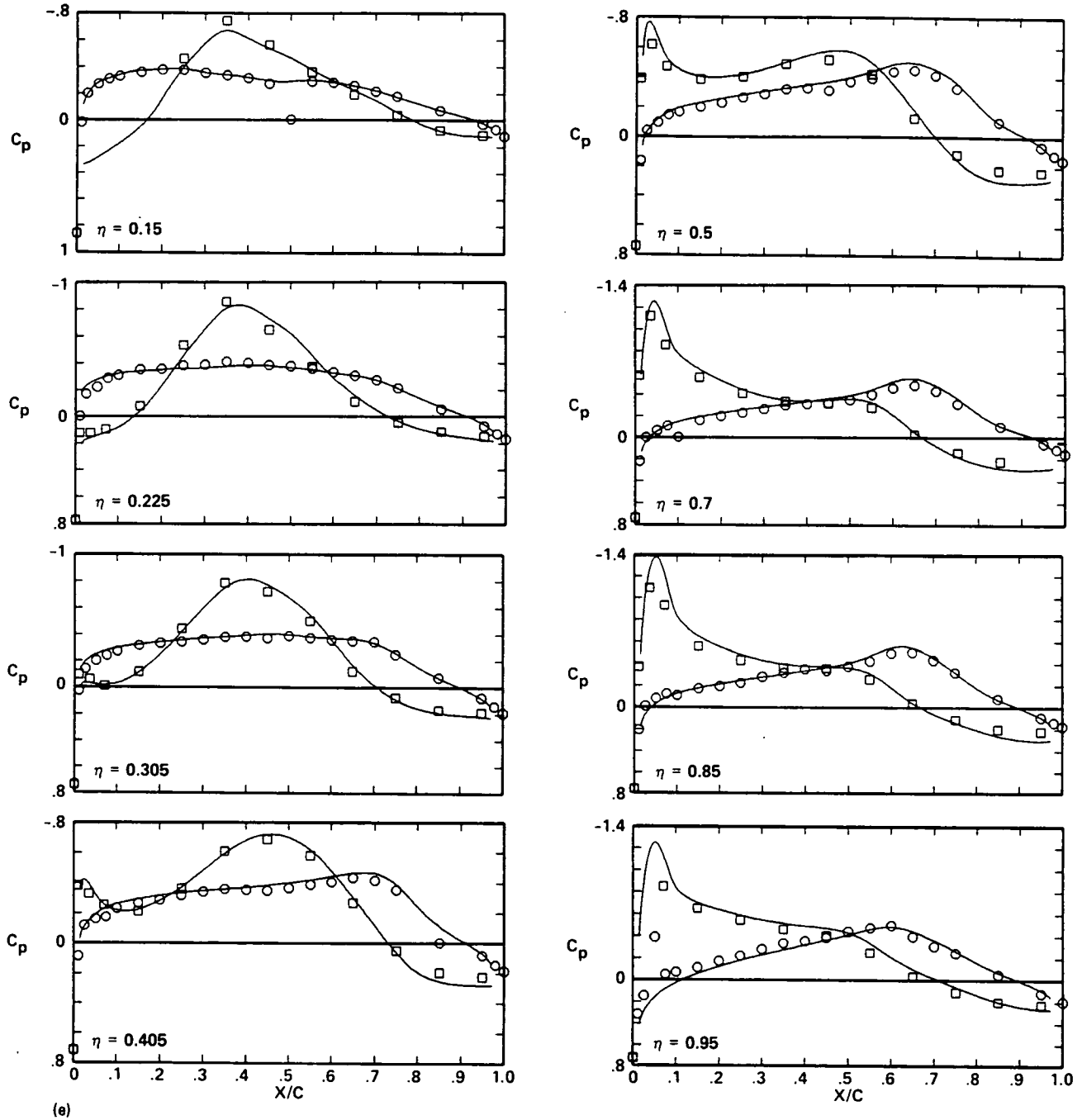
(e)

Fig. 26. Continued.

	M_∞	α	Re x 10^{-6}	C_L	C_D	C_M
O, □ EXPERIMENT	0.700	0.480	8.107	0.260	0.029	-0.088
—— FLO57C	0.700	0.0	—	0.260	0.023	-0.105
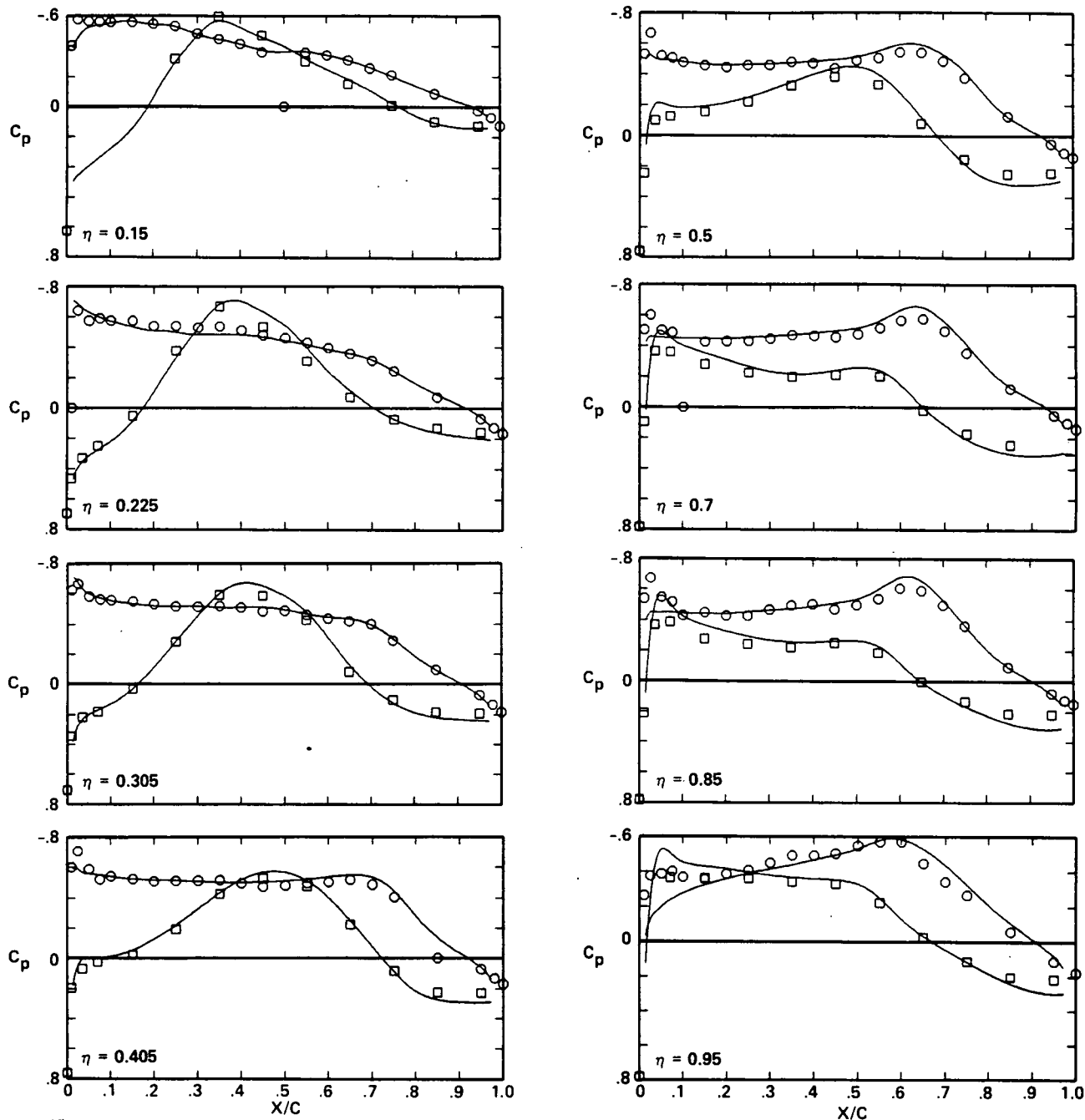
(f)

Fig. 26. Continued.

	M_∞	α	Re x 10^{-6}	C_L	C_D	C_M
O, □ EXPERIMENT	0.701	2.736	8.137	0.492	0.038	-0.085
—— FLO57C	0.700	2.000	—	0.491	0.030	-0.114
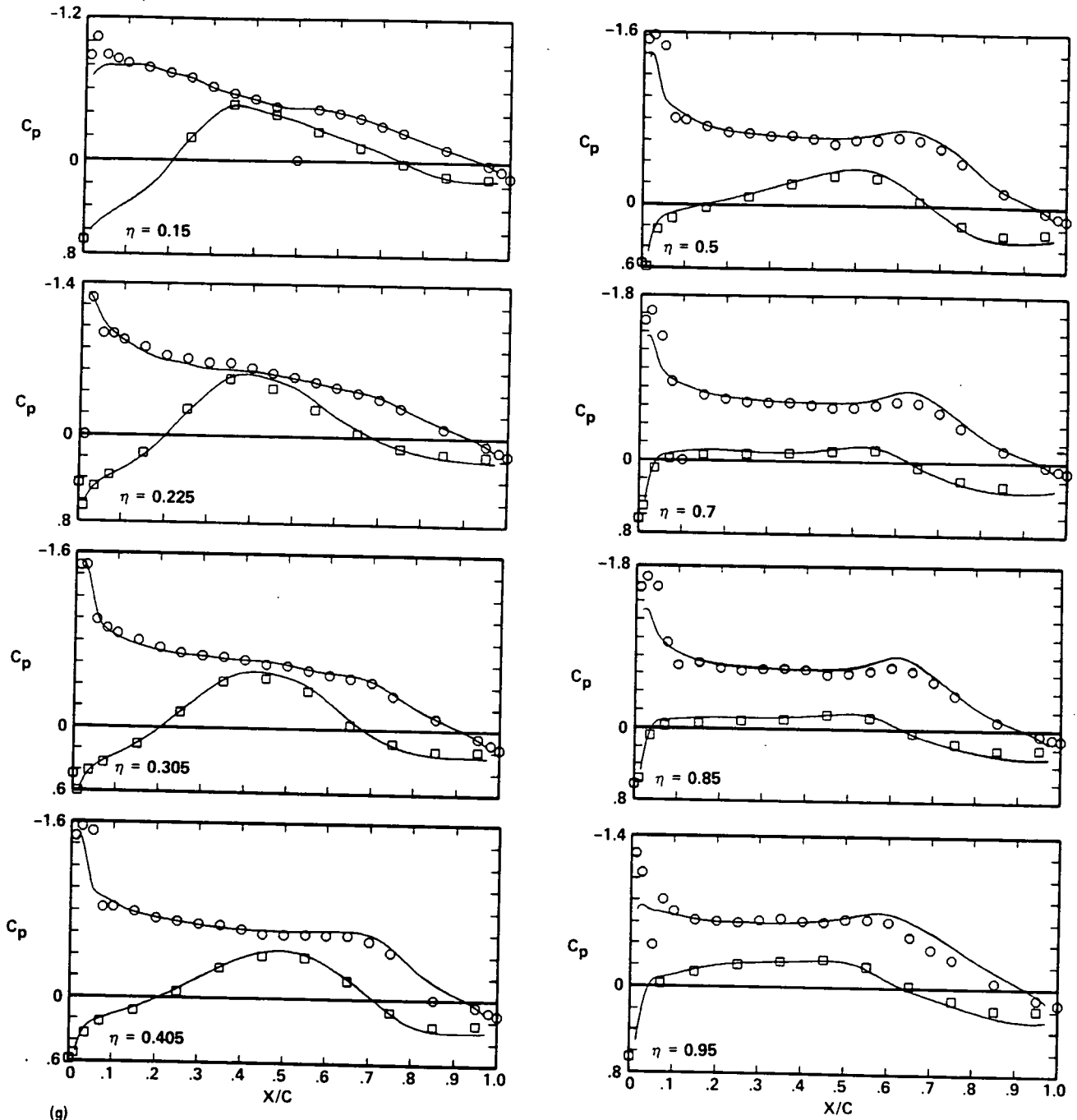
Fig. 26. Continued.

107
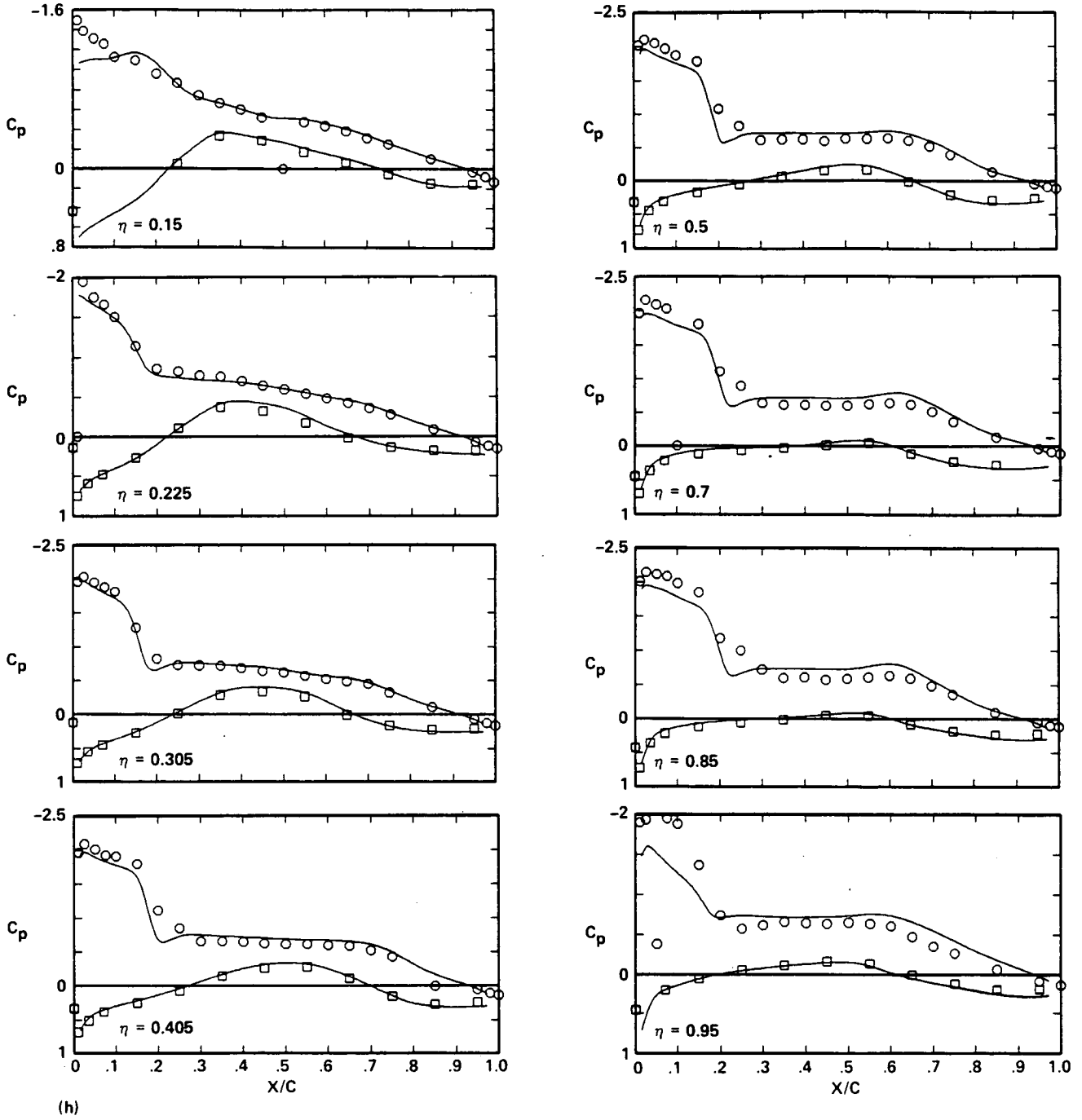
Fig. 26. Continued.

	M_∞	α	Re x 10^{-6}	C_L	C_D	C_M
o, □ EXPERIMENT	0.799	-1.513	8.292	0.056	0.032	-0.079
——FLO57C	0.800	-2.000	—	0.024	0.030	-0.080
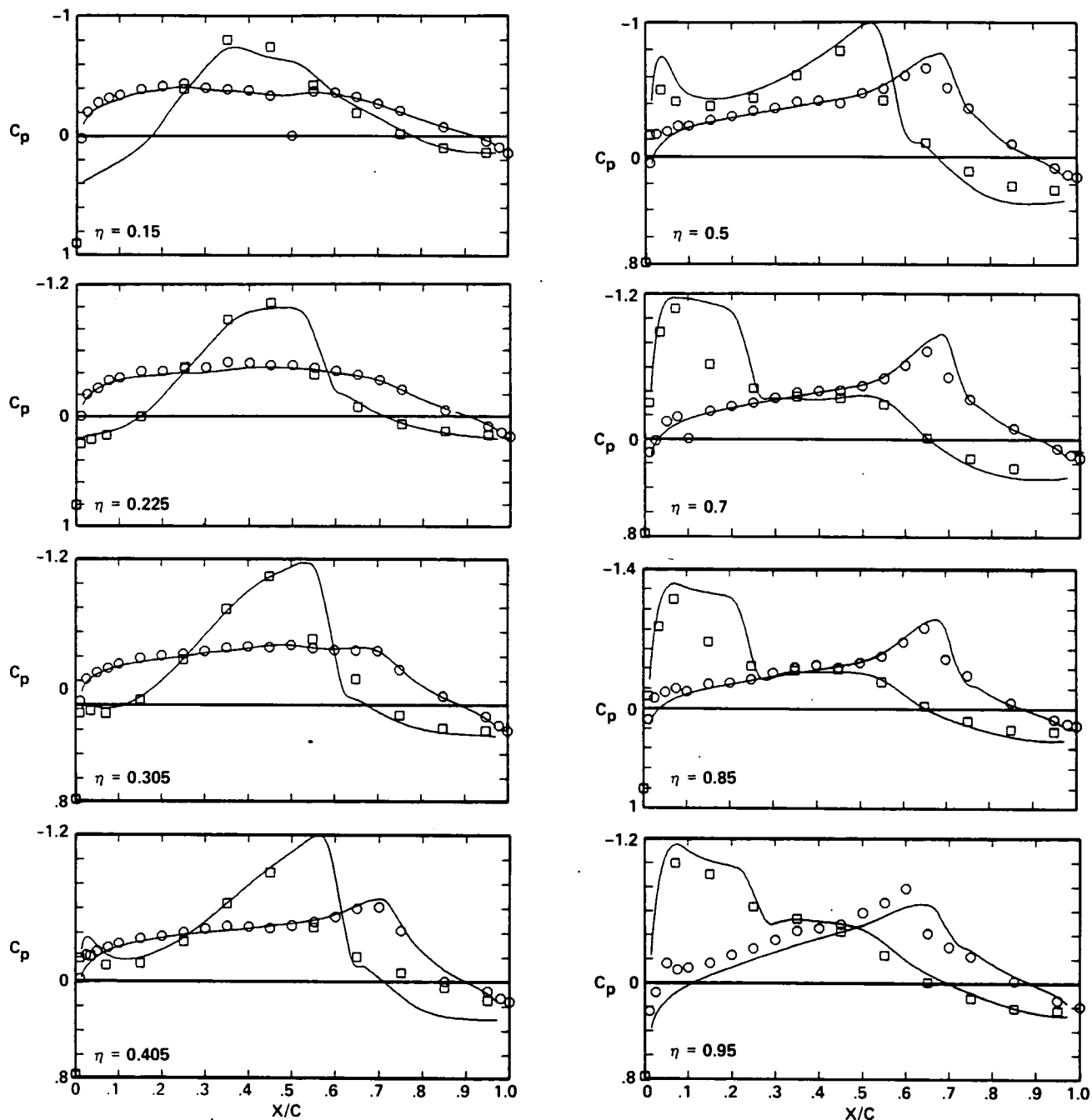
Fig. 26. Continued.

(j)

Fig. 26. Continued.

110
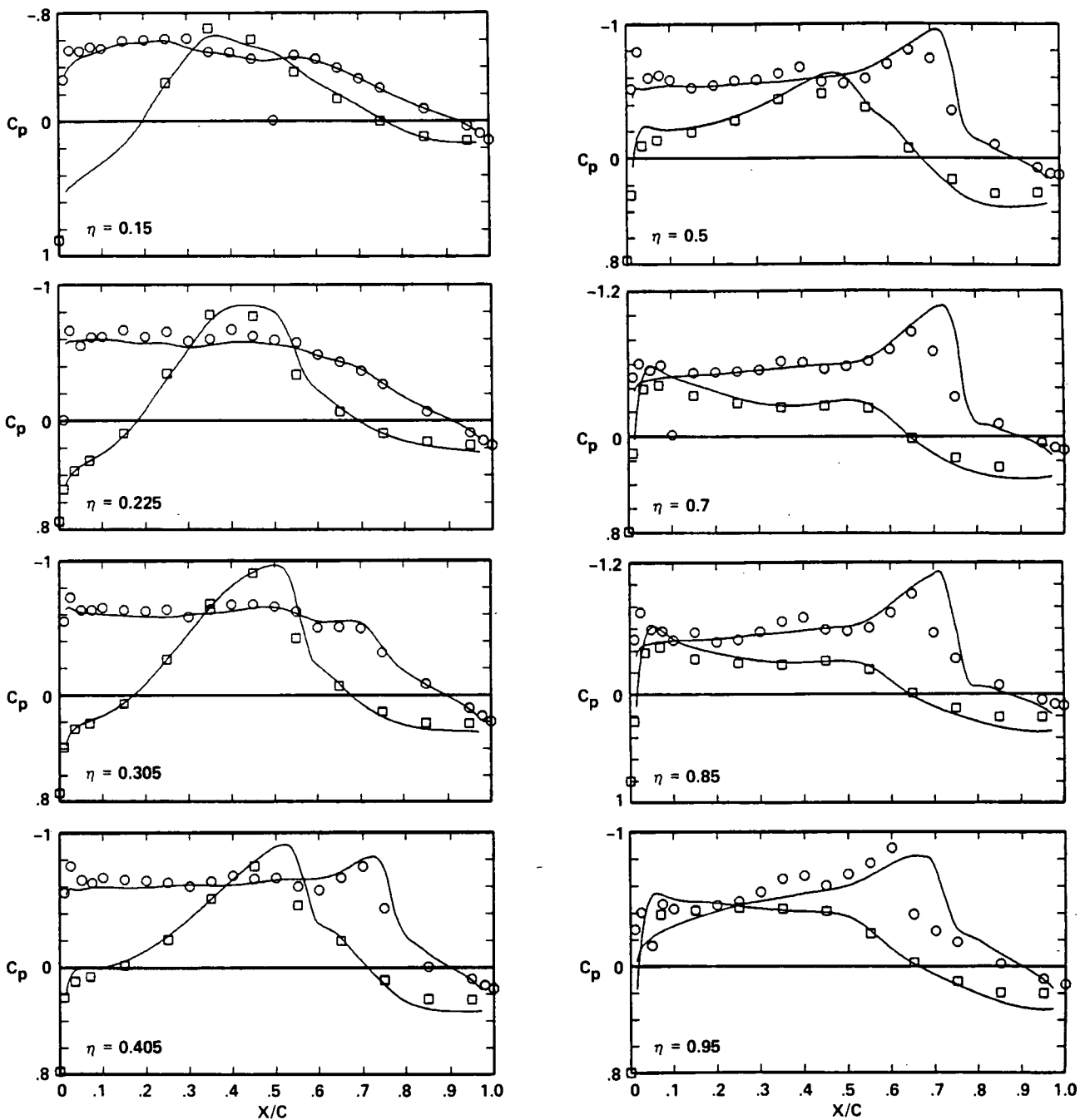
	M_∞	α	Re x 10^{-6}	c_L	c_D	c_M
○, □ EXPERIMENT	0.800	2.989	8.291	0.592	0.047	−0.118
—— FLO57C	0.800	2.000	—	0.593	0.040	−0.162

Fig. 26. Continued.

111
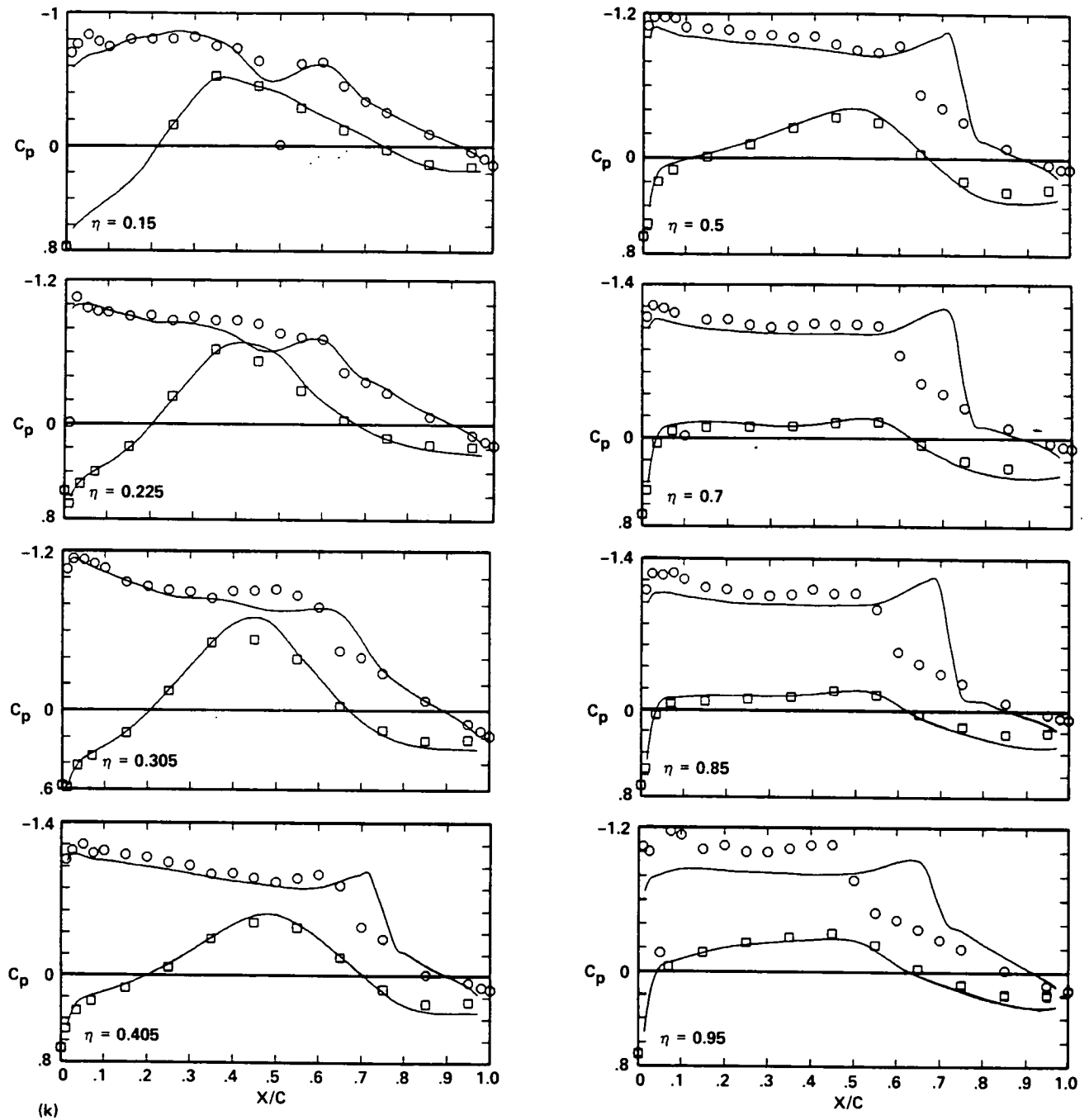
		M_∞	α	Re x 10^{-6}	C_L	C_D	C_M
○,□	EXPERIMENT	0.798	3.978	8.286	0.688	0.064	-0.094
—	FLO57C	0.800	2.500	—	0.671	0.046	-0.173

(l)
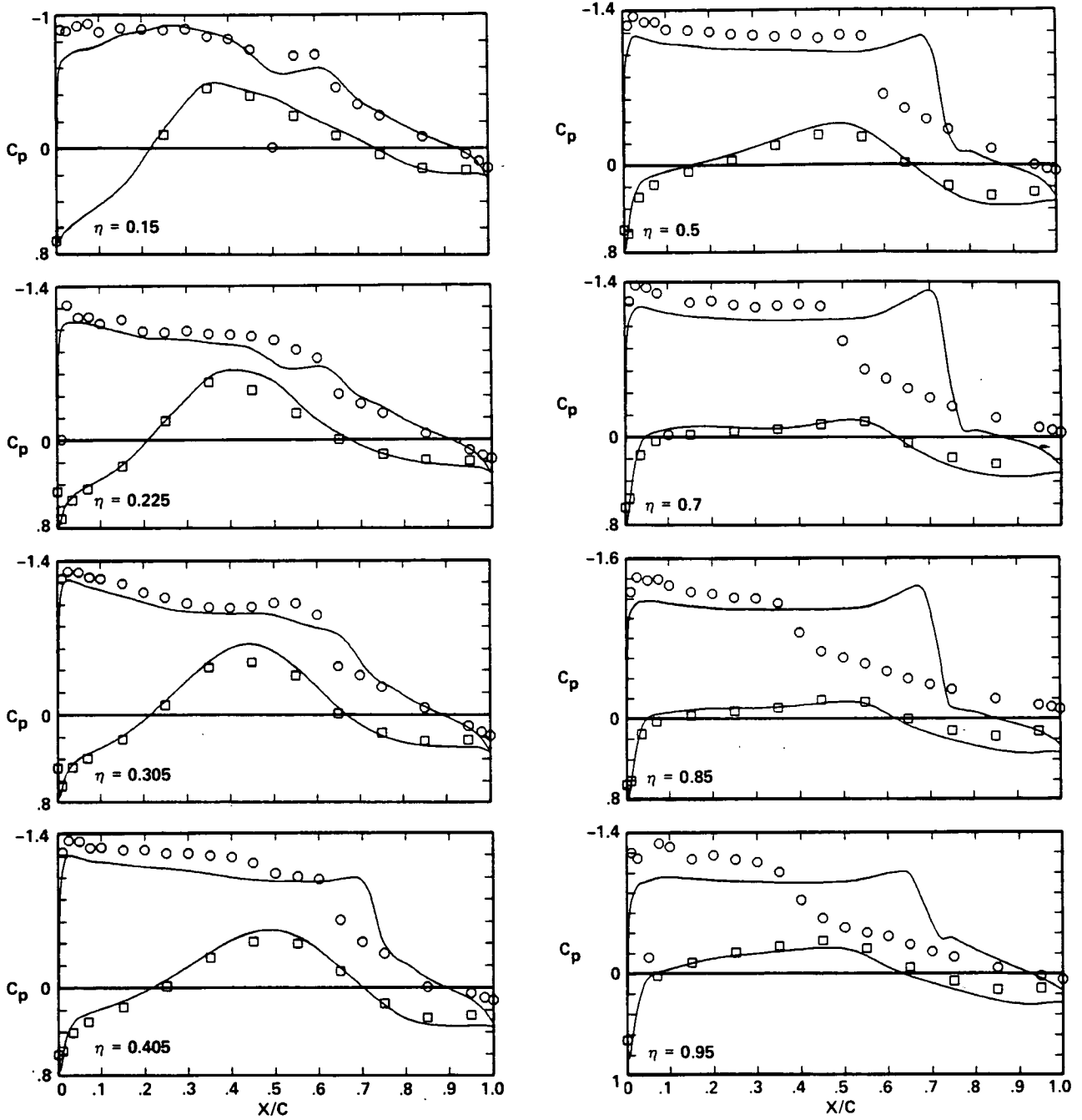
Fig. 26. Concluded.

	M_∞	α	$Re \times 10^{-6}$	C_L	C_D	C_M
O, □ EXPERIMENT	0.401	−0.489	5.321	0.152	0.0242	−0.074
—— FLO22NM	0.400	0.0	8.000	0.168	0.0042	−0.053
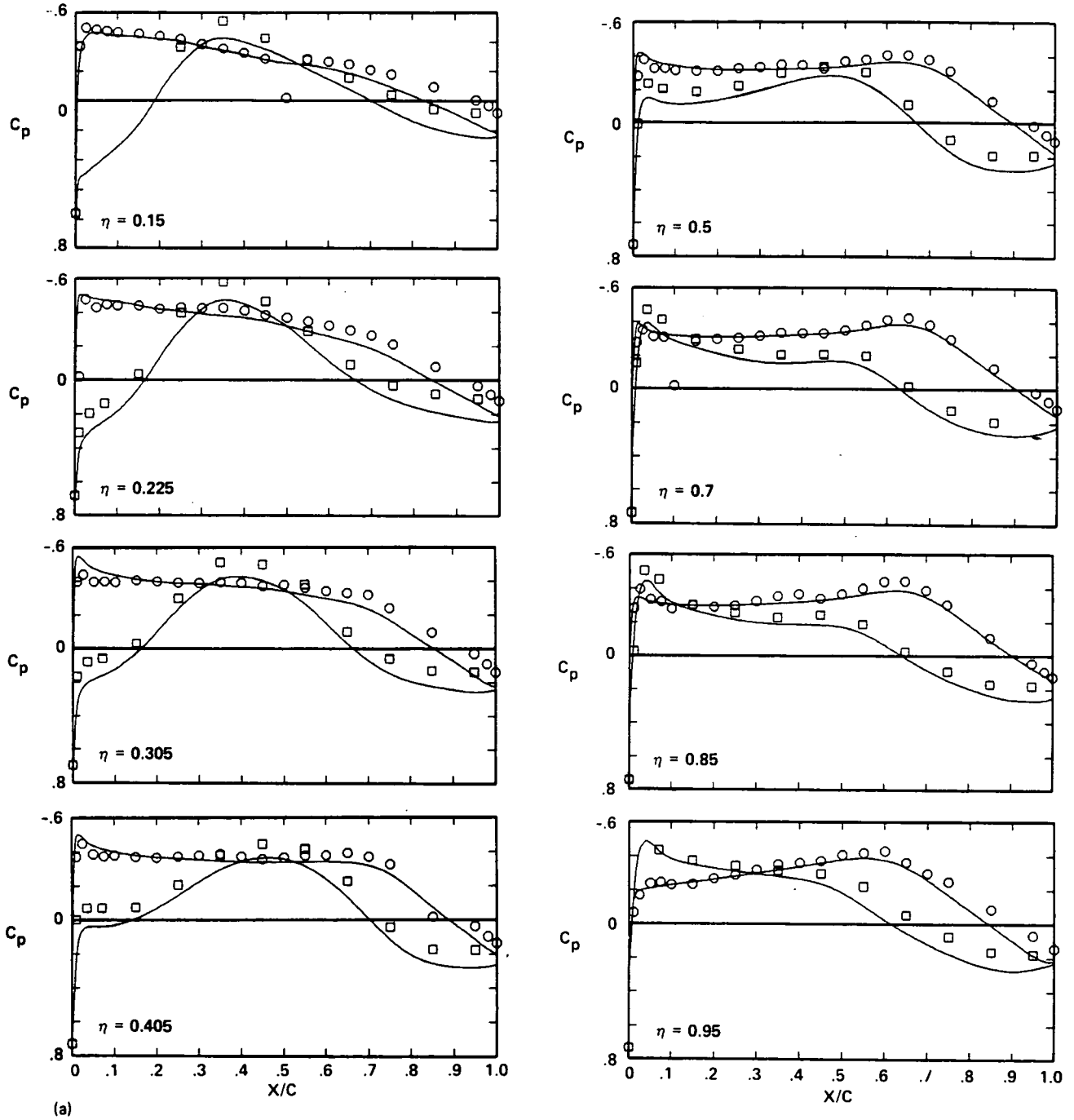
Fig. 27. Experiment–CFD pressure-distribution comparison for Wing D, FLO22NM.

113

	M_∞	α	Re x 10^{-6}	C_L	C_D	C_M
○, □ EXPERIMENT	0.400	0.497	5.312	0.238	0.0257	−0.073
—— FLO22NM	0.400	1.000	8.000	0.240	0.0055	−0.076

Fig. 27. Continued.

114
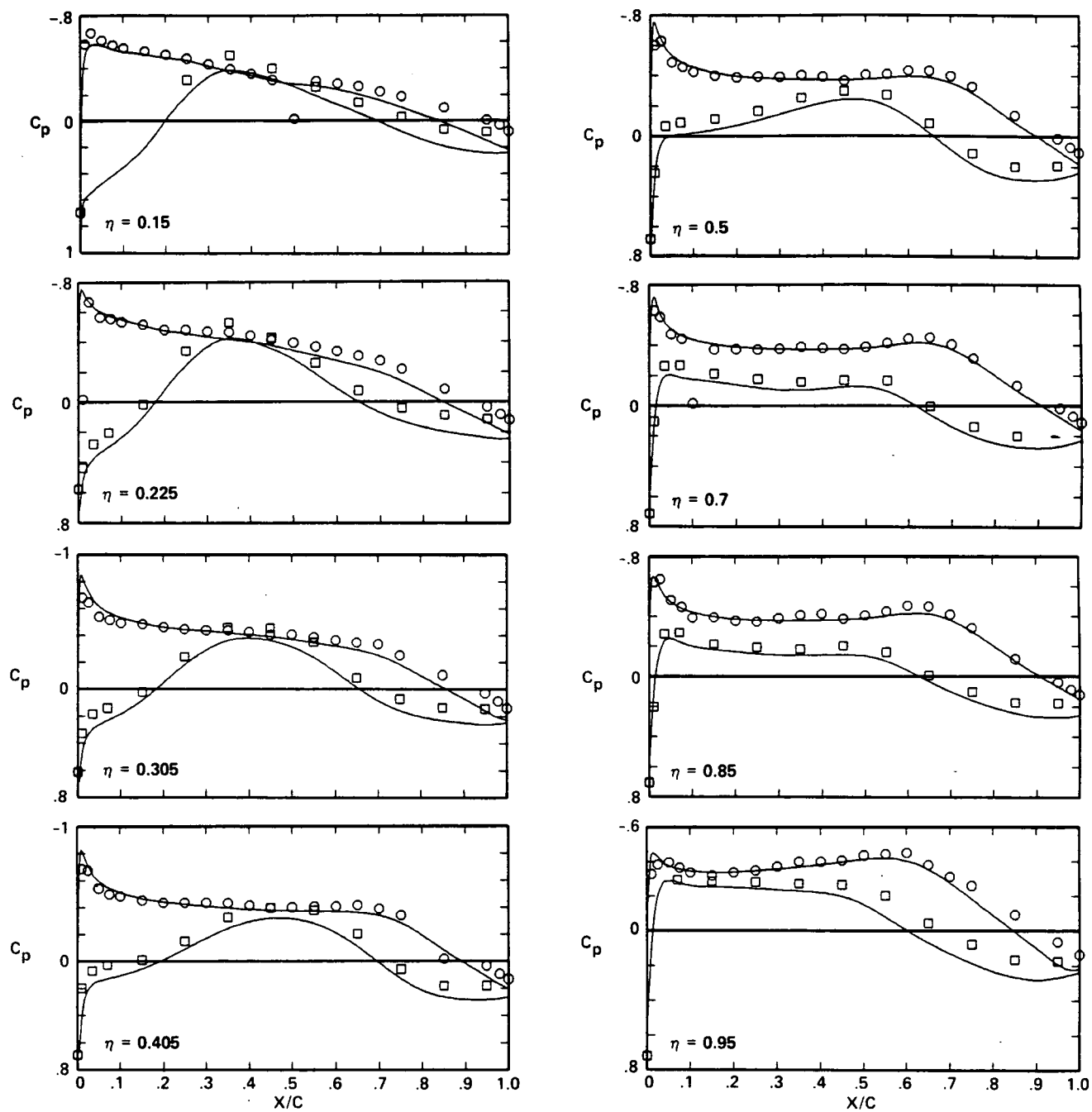
	M_∞	α	Re x 10^{-6}	C_L	C_D	C_M
O, □ EXPERIMENT	0.400	1.245	5.303	0.303	0.0273	-0.073
—— FLO22NM	0.400	2.000	8.000	0.312	0.0073	-0.102

(c)

Fig. 27. Continued.

115
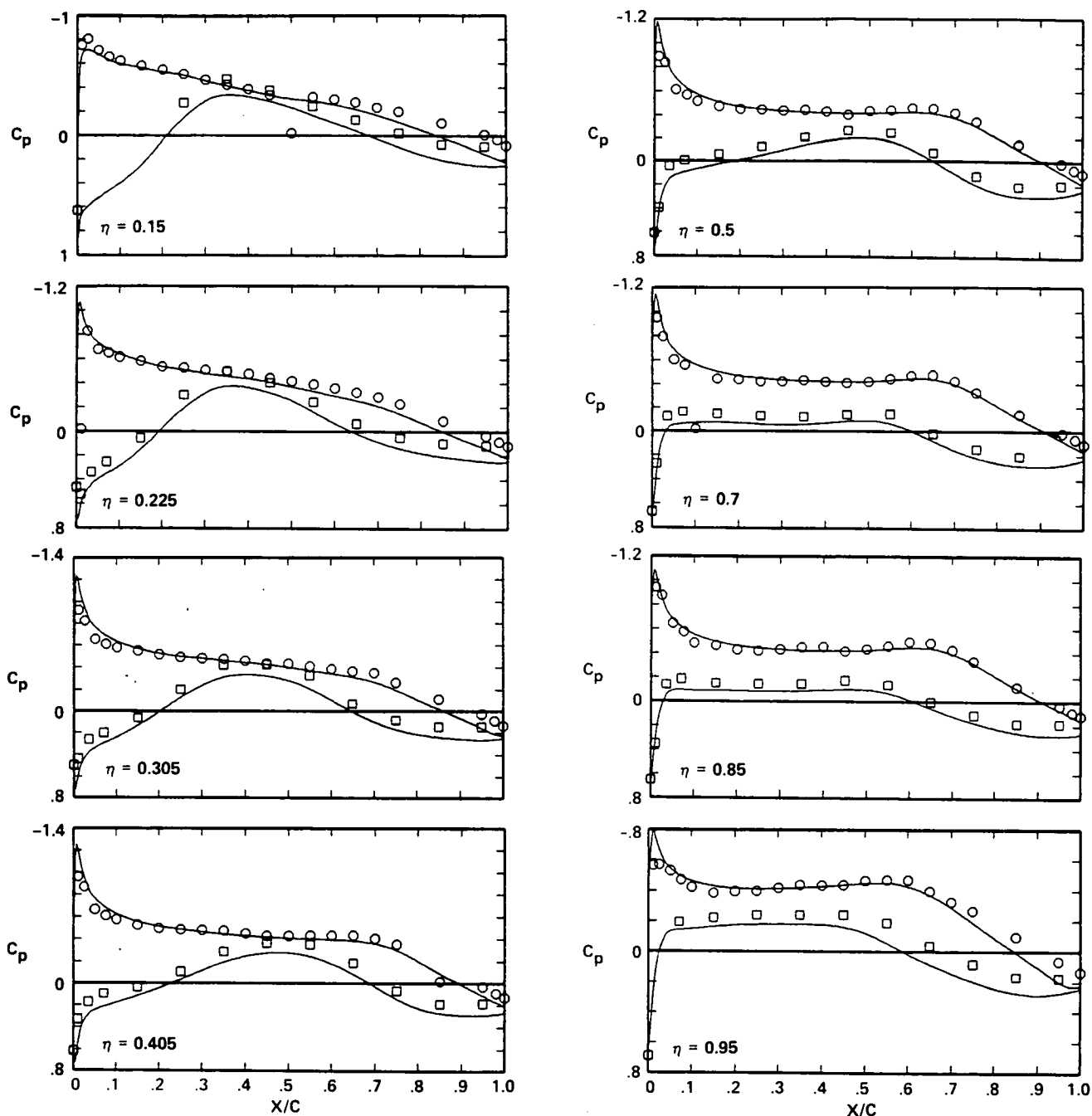
	M_∞	α	Re x 10^{-6}	C_L	C_D	C_M
○, □ EXPERIMENT	0.399	2.237	5.297	0.392	0.0301	−0.068
—— FLO22NM	0.400	3.000	8.000	0.384	0.0097	−0.130

(d)

Fig. 27. Continued.

116
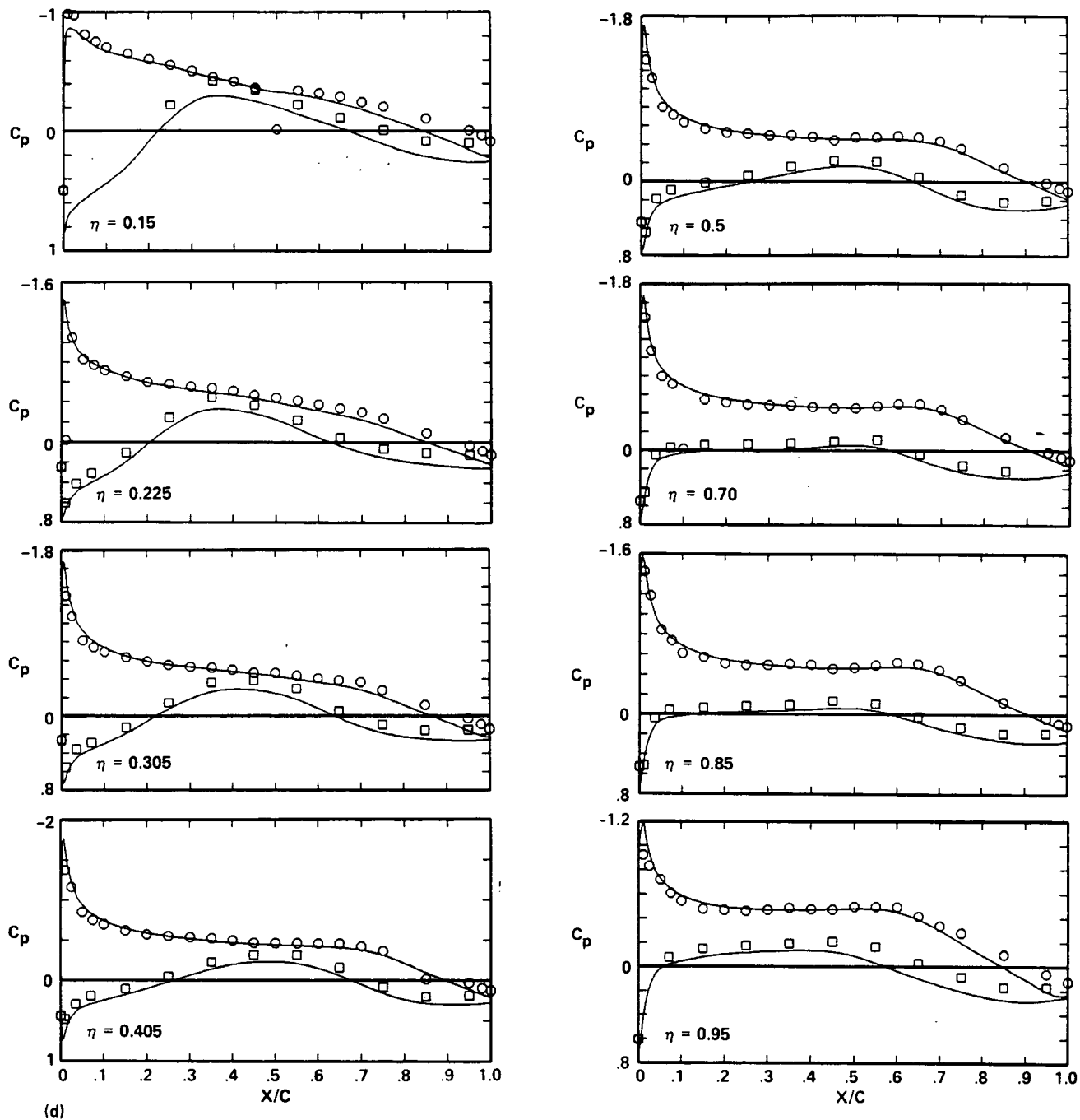
	M_∞	α	Re x 10^{-6}	C_L	C_D	C_M
O, □ EXPERIMENT	0.399	2.987	5.286	0.459	0.0328	-0.065
—— FLO22NM	0.400	4.000	8.000	0.454	0.0128	-0.159

(e)
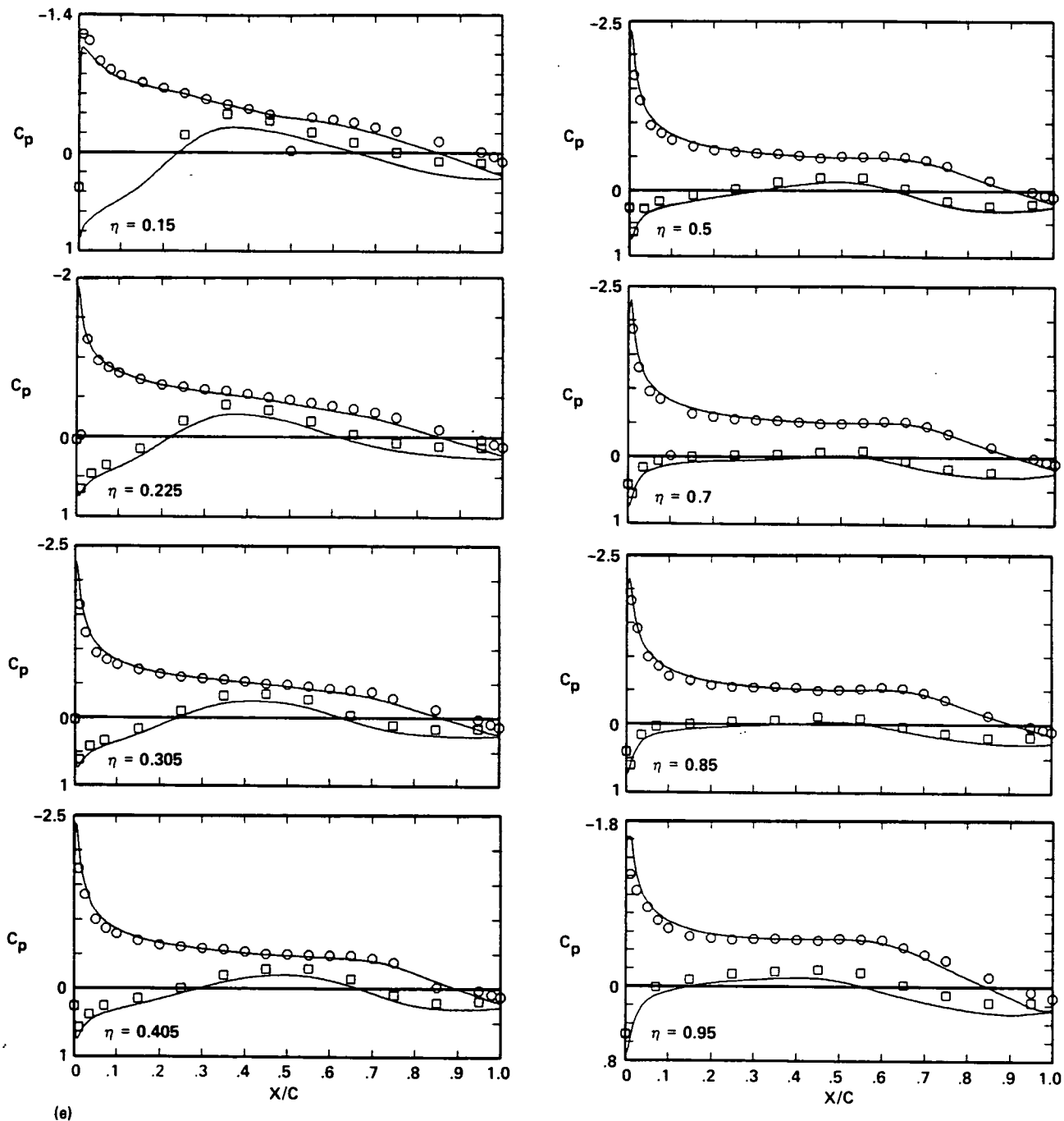
Fig. 27. Continued.

	M_∞	α	Re x 10^{-6}	C_L	C_D	C_M
○, □ EXPERIMENT	0.800	0.249	8.286	0.249	0.033	-0.098
—— FLO22NM	0.800	0.0	8.000	0.238	0.005	-0.093

(f)

Fig. 27. Continued.

118
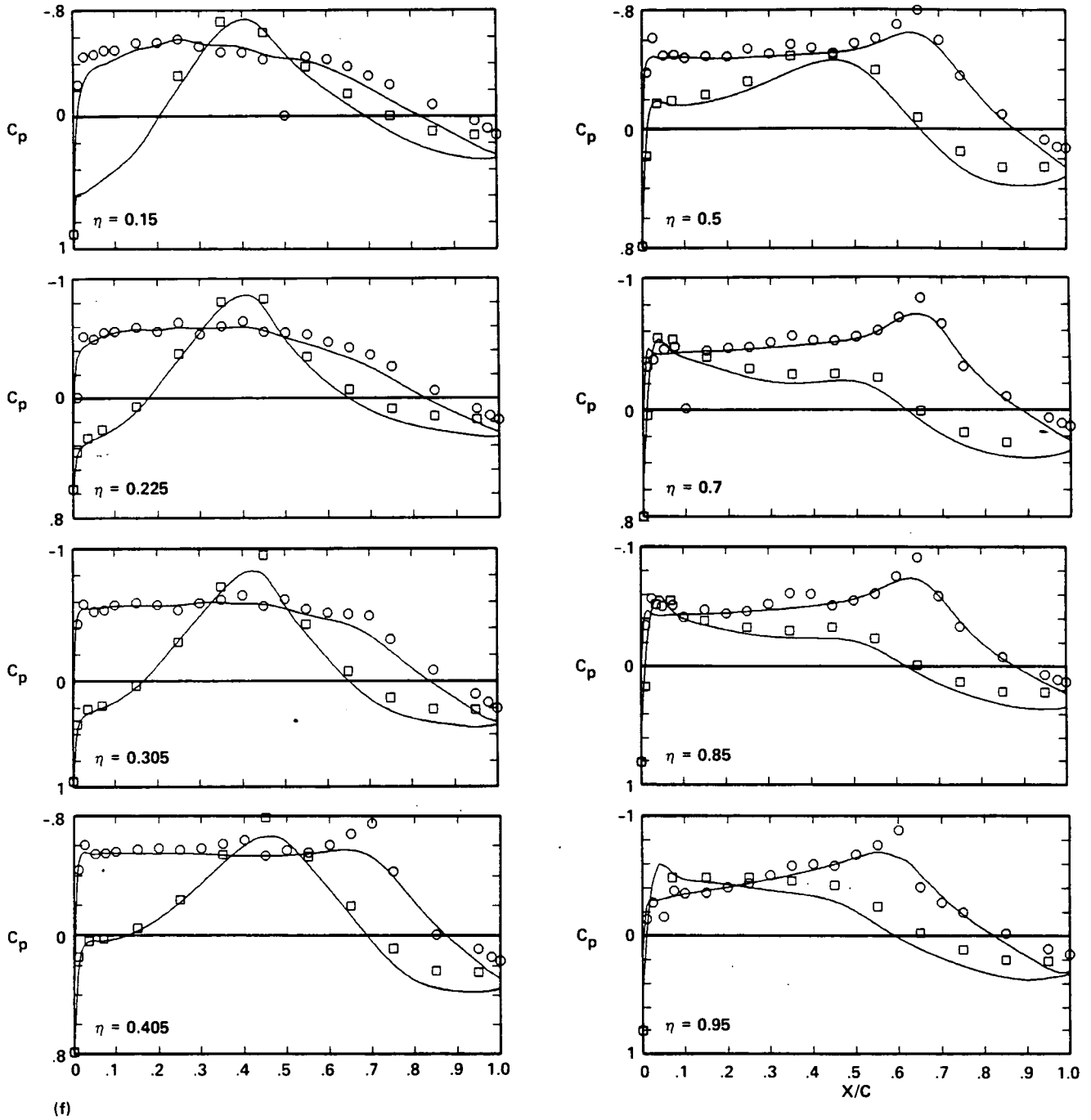
	M_∞	α	Re x 10⁻⁶	C_L	C_D	C_M
o, □ EXPERIMENT	0.798	0.992	8.268	0.332	0.035	–0.101
—— FLO22NM	0.800	1.000	8.000	0.335	0.008	–0.124

Fig. 27. Continued.

119
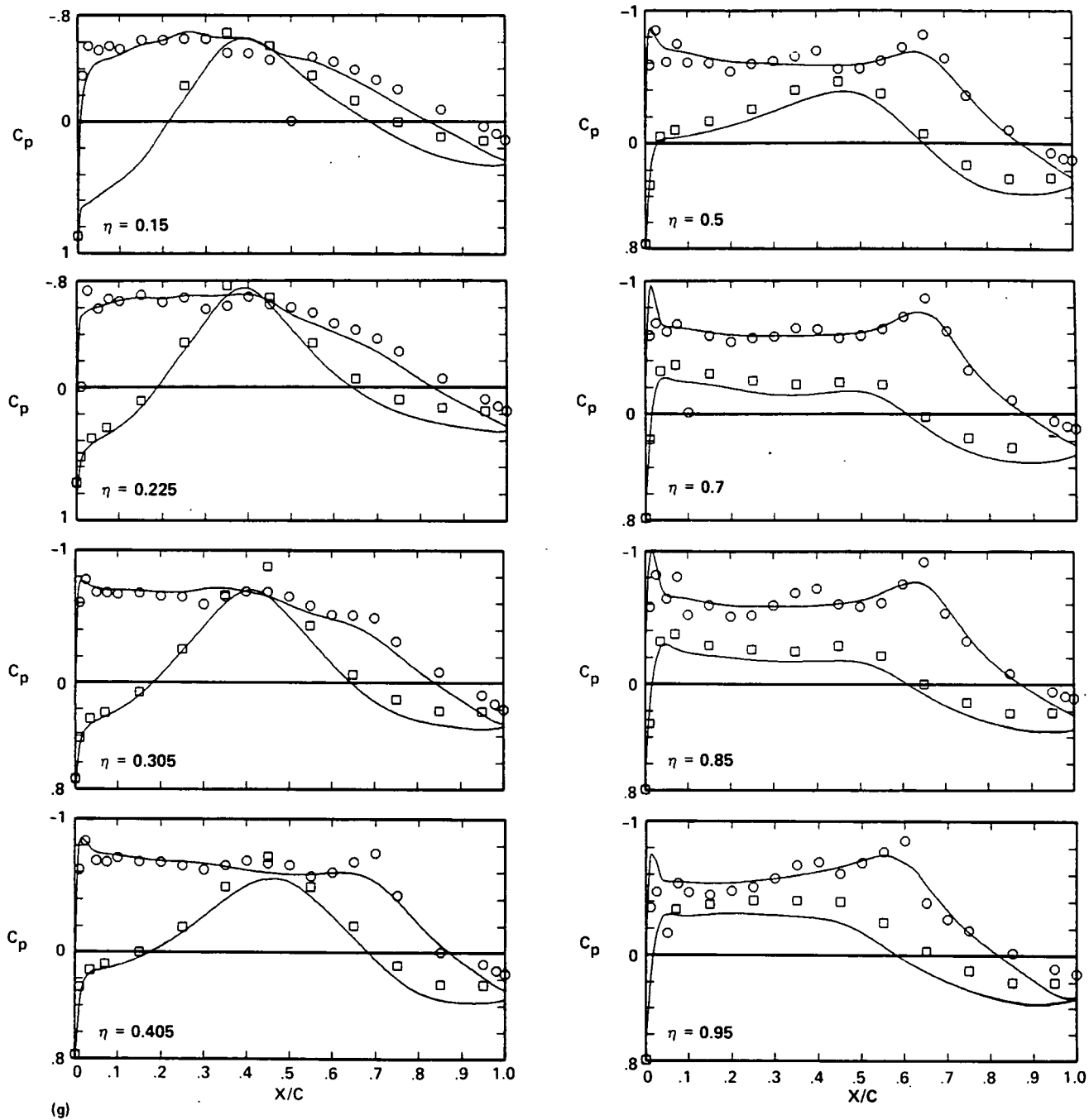
	M_∞	α	Re x 10^{-6}	C_L	C_D	C_M
○, □ EXPERIMENT	0.797	1.978	8.270	0.448	0.0393	−0.103
—— FLO22NM	0.800	2.000	8.000	0.441	0.0123	−0.162

(h)

Fig. 27. Continued.

120
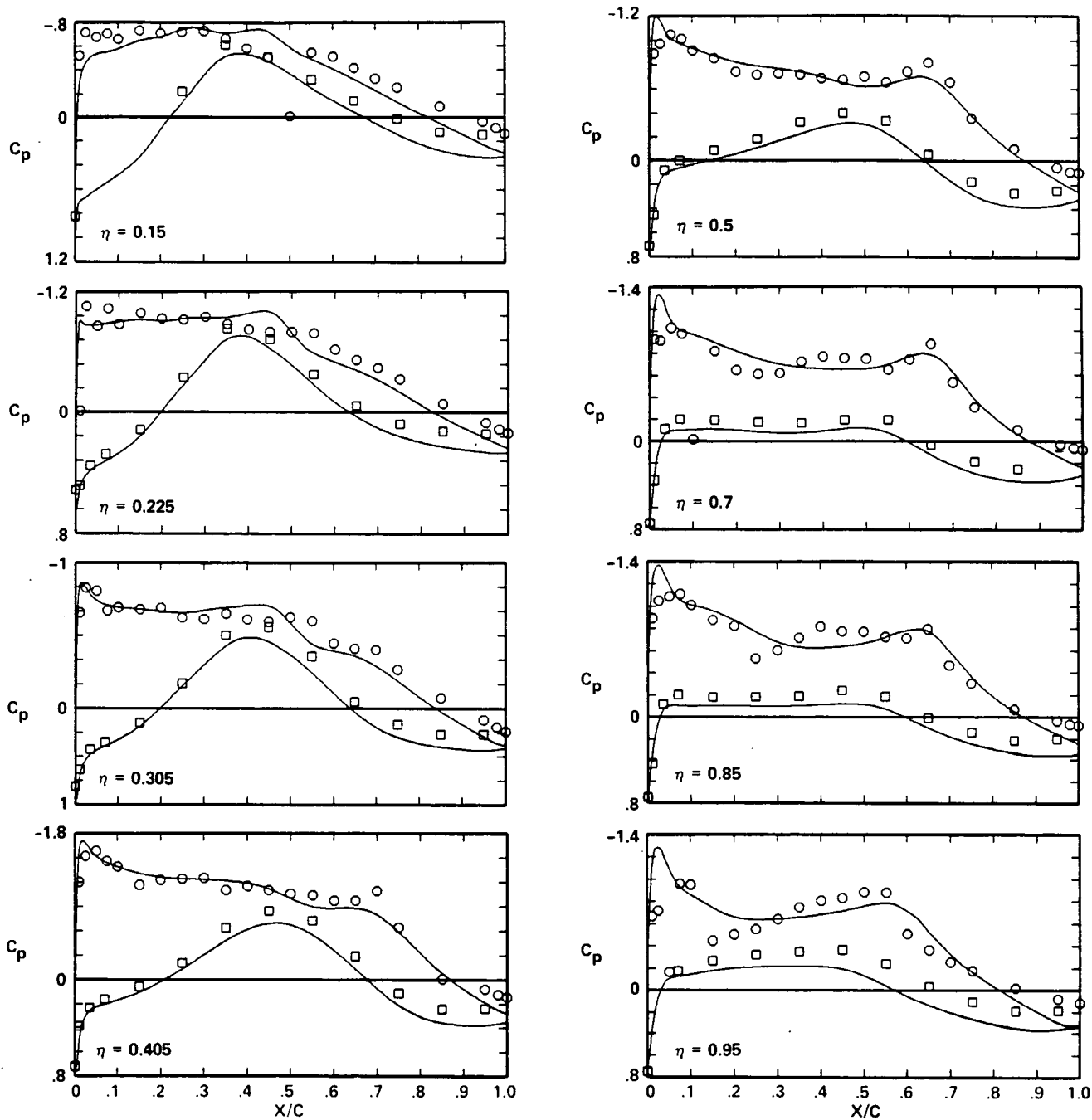
	M_∞	α	$Re \times 10^{-6}$	C_L	C_D	C_M
O, □ EXPERIMENT	0.799	2.479	8.270	0.521	0.043	-0.112
—— FLO22NM	0.800	3.000	8.000	0.553	0.021	-0.204
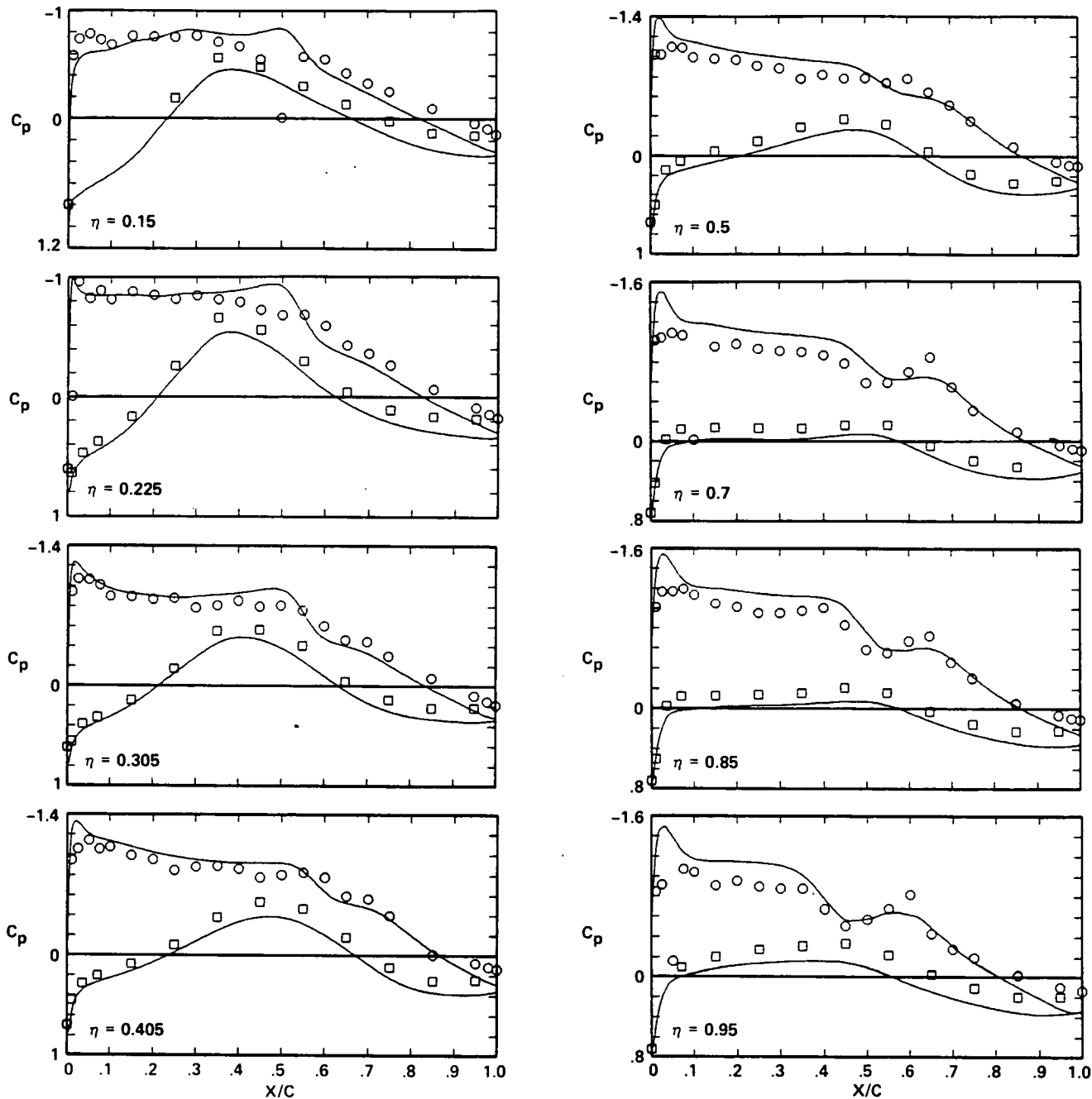
(i)

Fig. 27. Continued.

	M_∞	α	Re x 10^{-6}	C_L	C_D	C_M
O, □ EXPERIMENT	0.802	3.473	8.310	0.648	0.054	−0.114
—— FLO22NM	0.800	4.000	8.000	0.660	0.034	−0.244

(j)

Fig. 27. Continued.

122
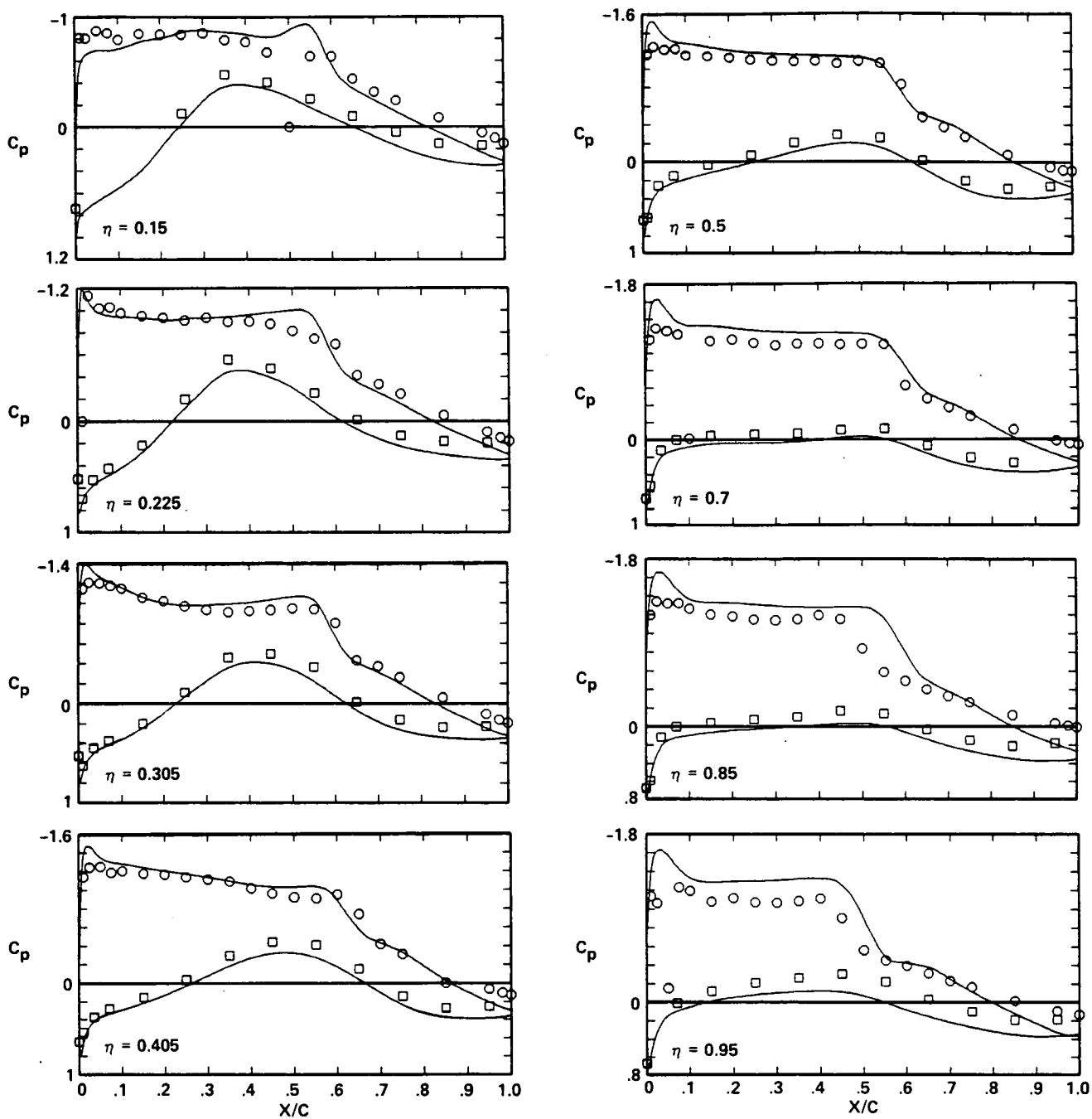
	M_∞	α	Re x 10^{-6}	C_L	C_D	C_M
O, □ EXPERIMENT	0.798	3.978	8.286	0.688	0.0640	-0.094
—— FLO22NM	0.800	5.000	8.000	0.751	0.0510	-0.272

Fig. 27. Concluded.

123

(a) M = .40

(b) M = .70
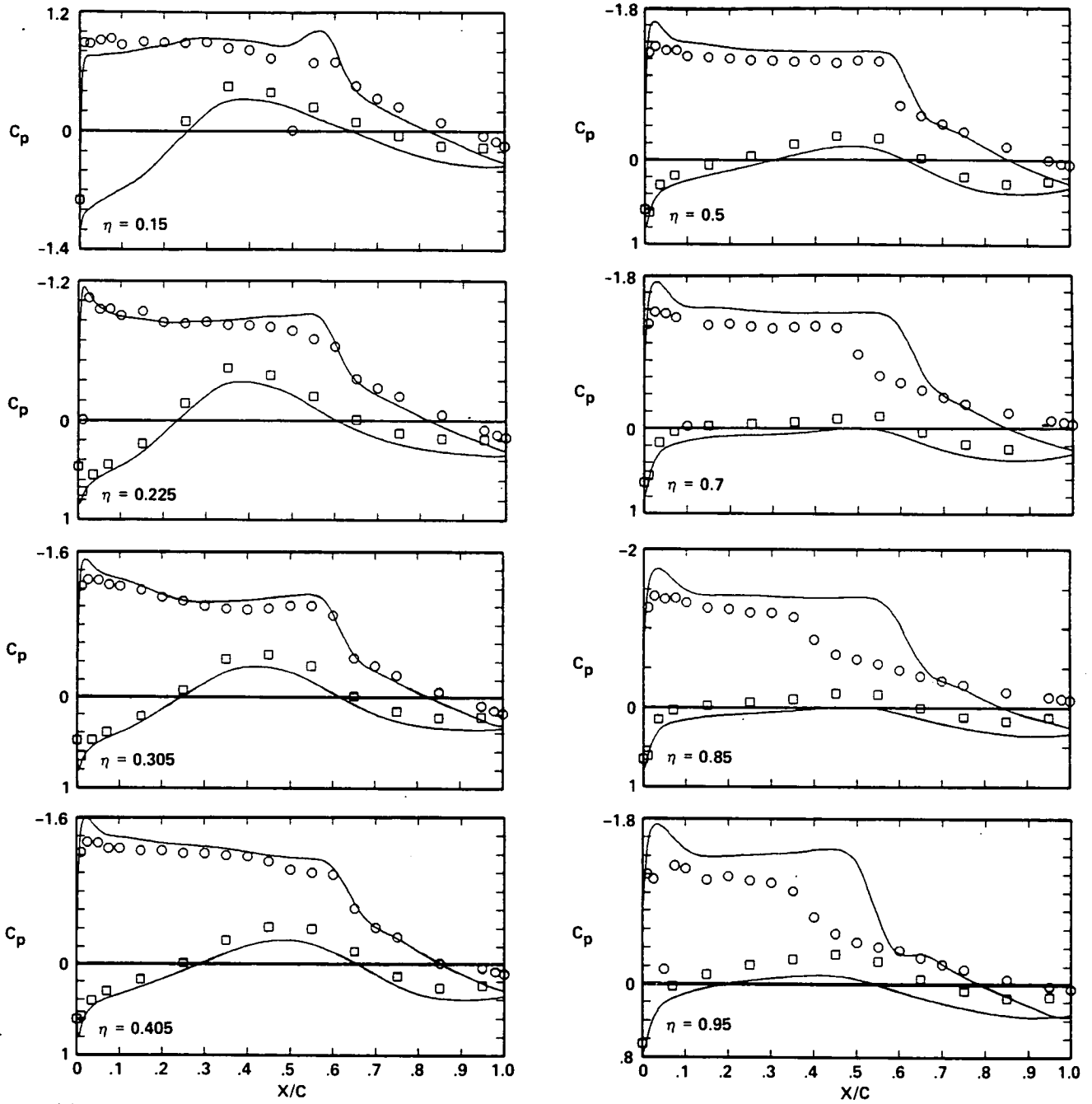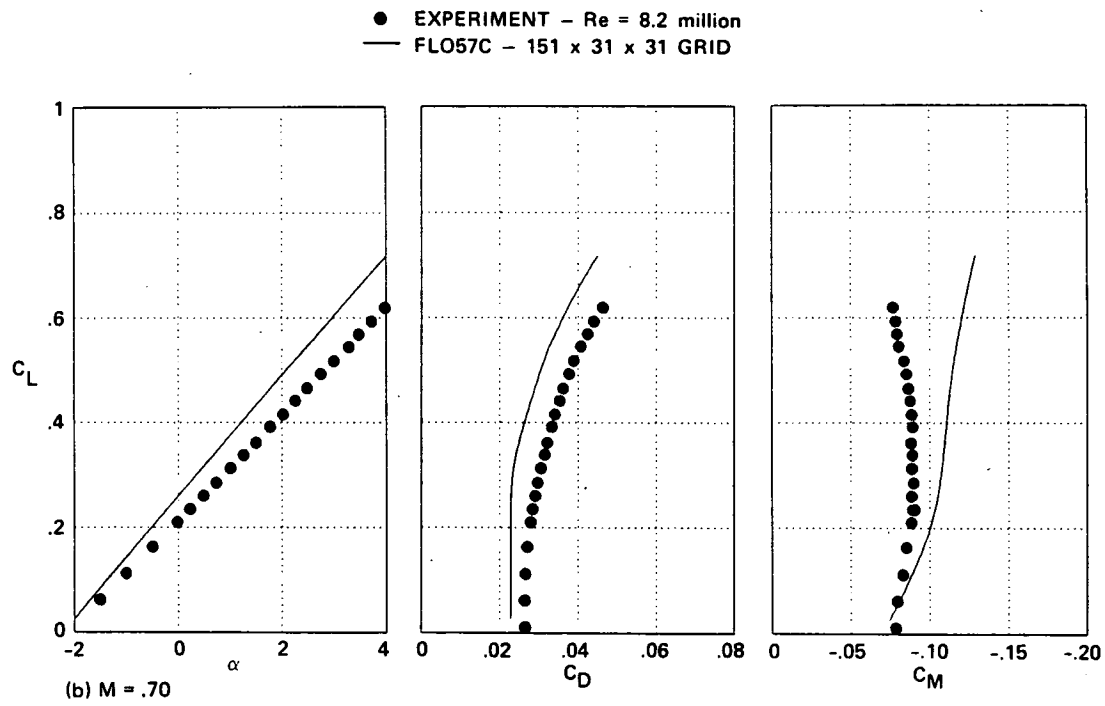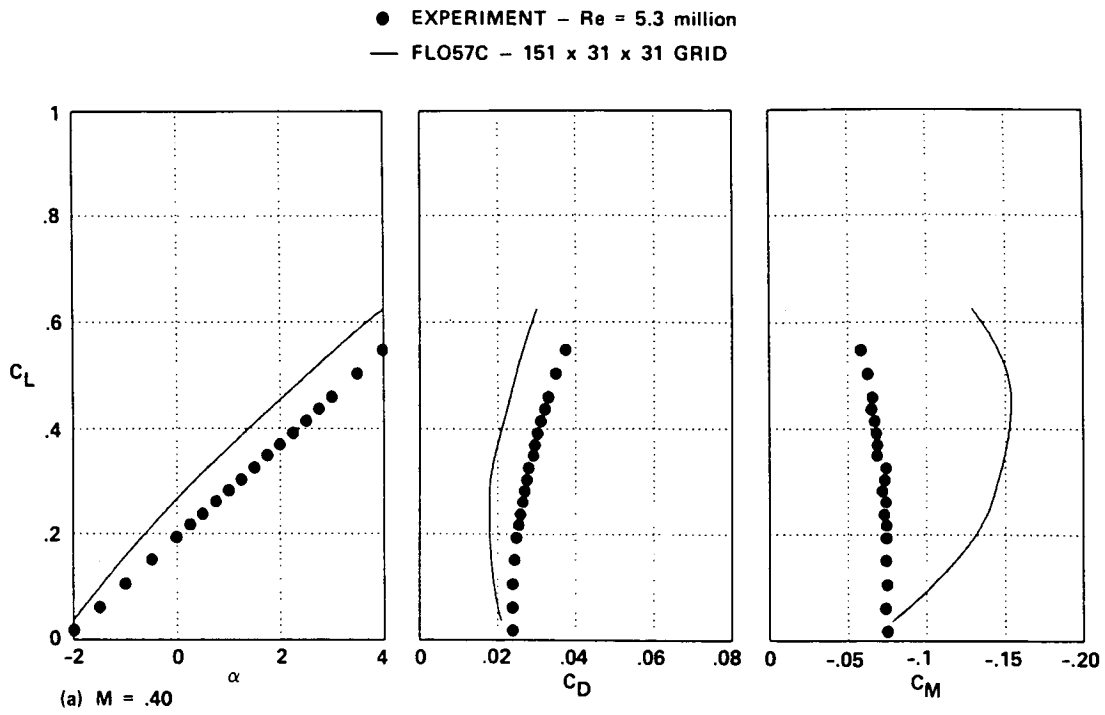
Fig. 28. Experiment–CFD force-and-moment comparison for Wing D, FLO57C.

(c) M = .80
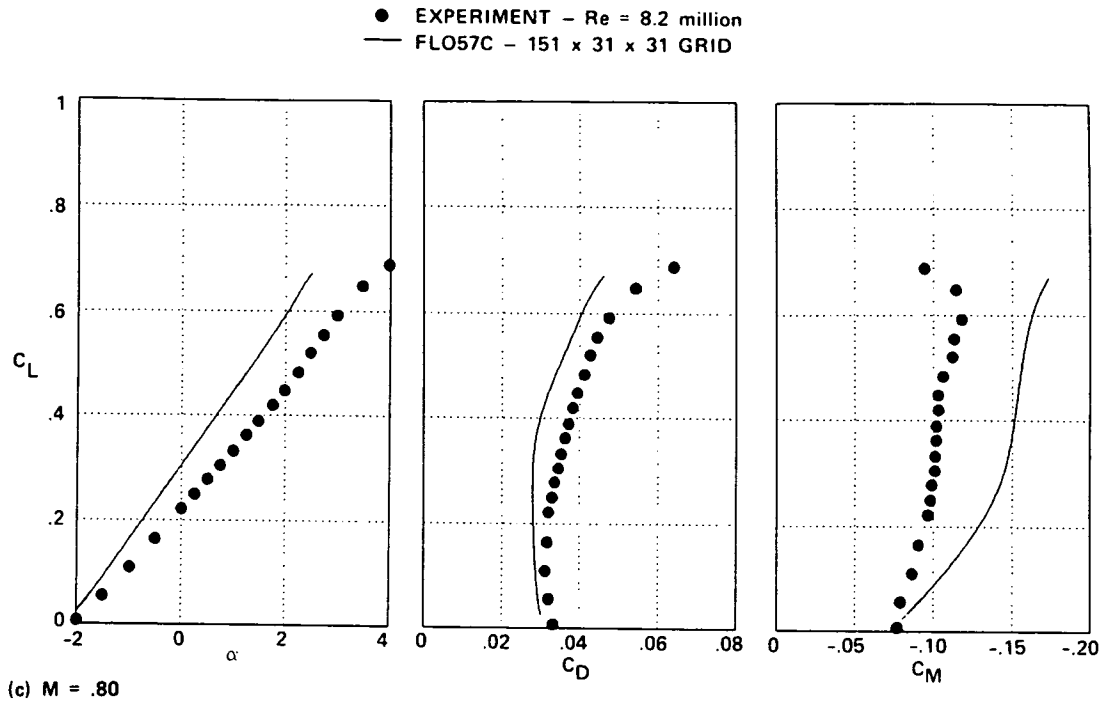
Fig. 28. Concluded.
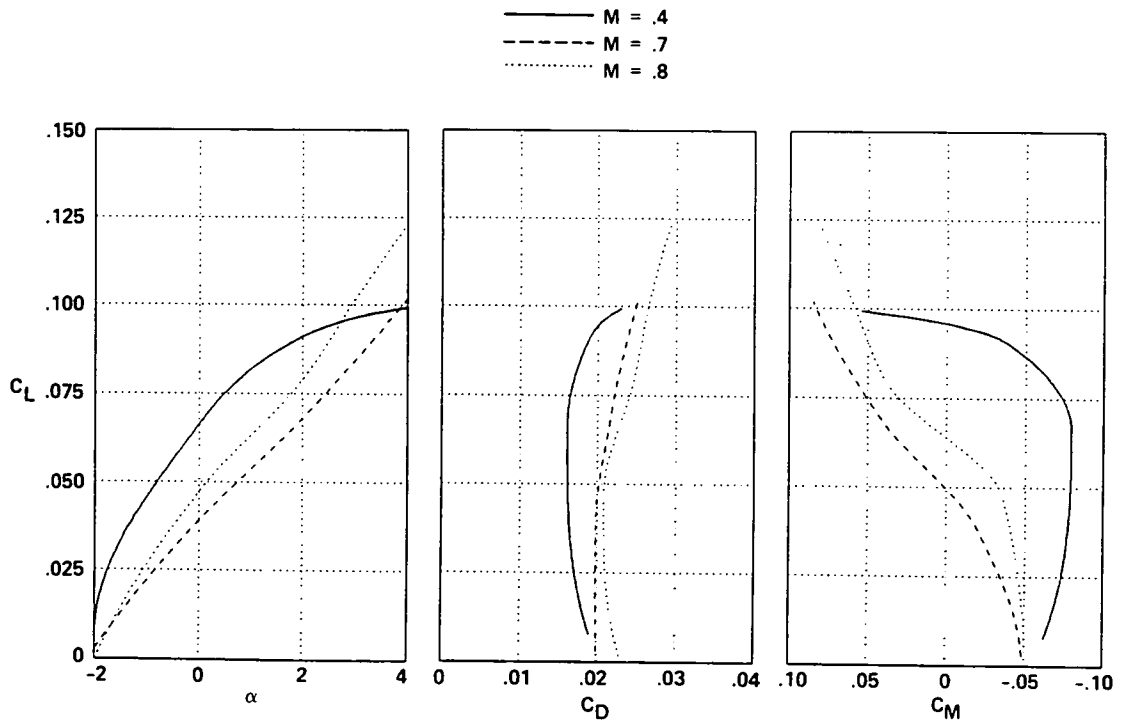
Fig. 29. Body forces and moments for Wing D, FLO57C.

125
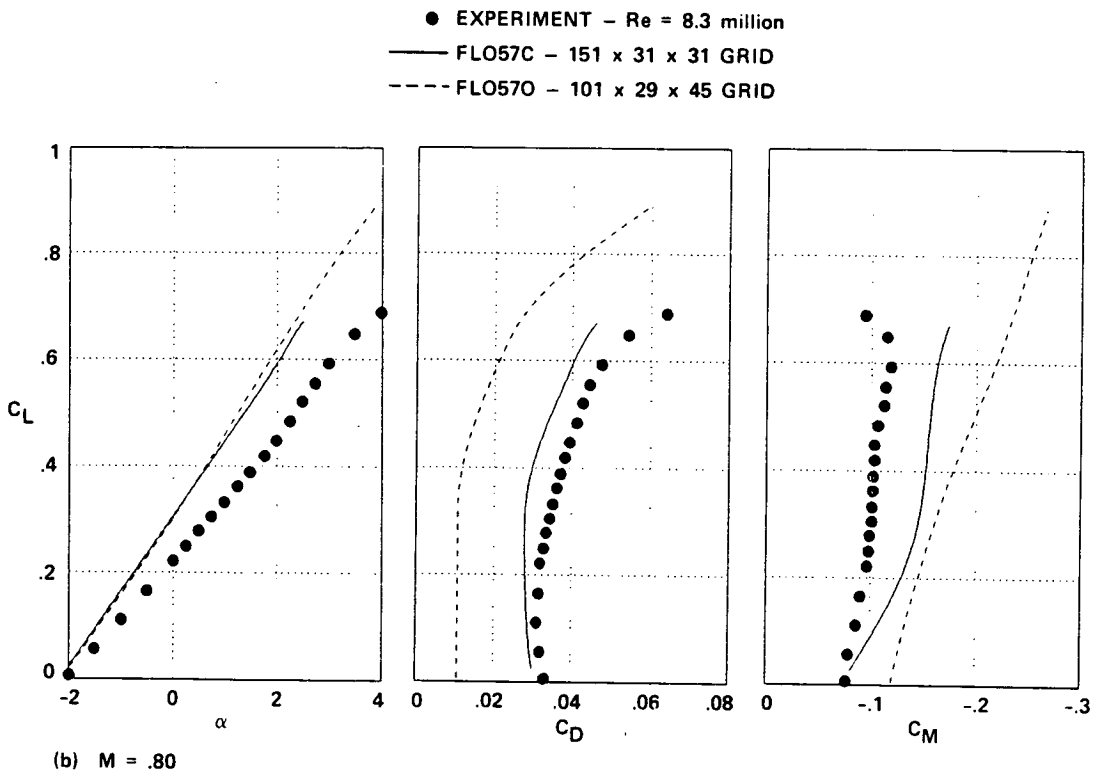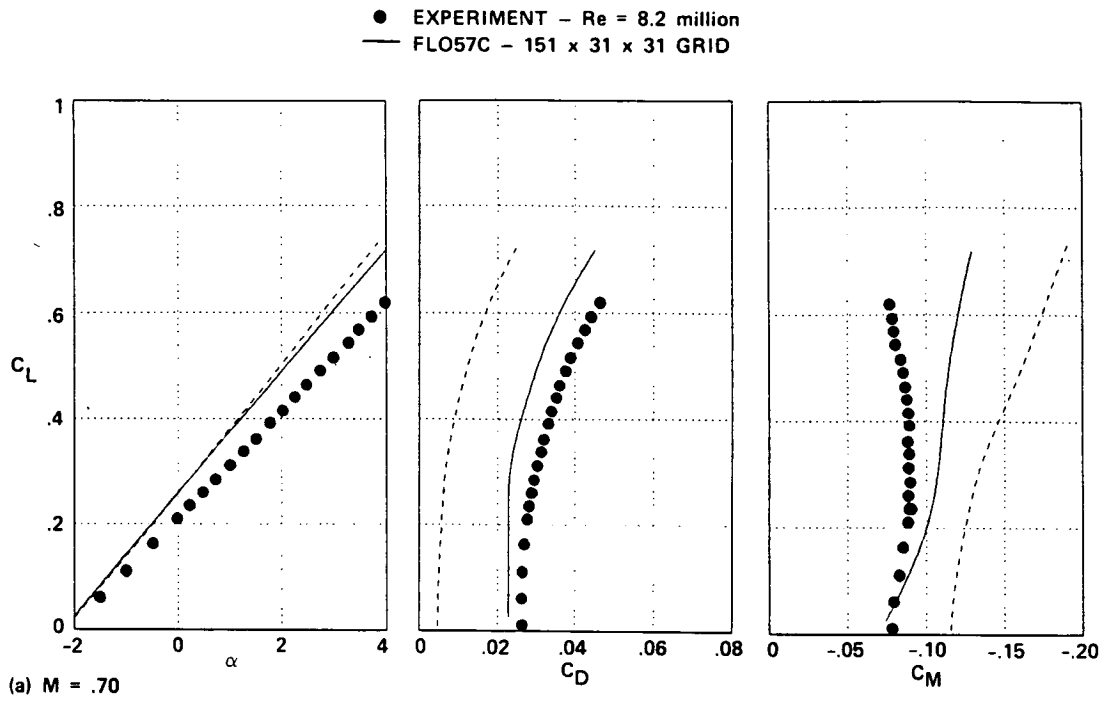
Fig. 30. Experiment–CFD force-and-moment comparison for Wing D, FLO57C and FLO57O.
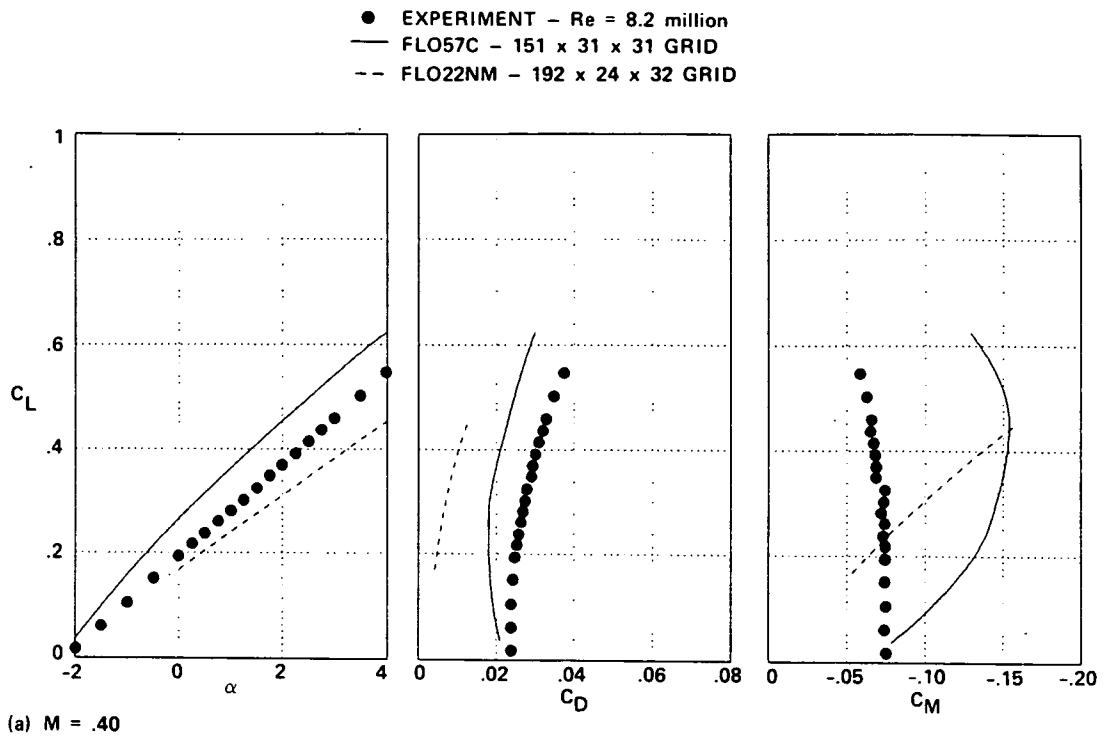
(a) M = .40

(b) M = .80

Fig. 31. Experiment–CFD force-and-moment comparison for Wing D, FLO22NM.
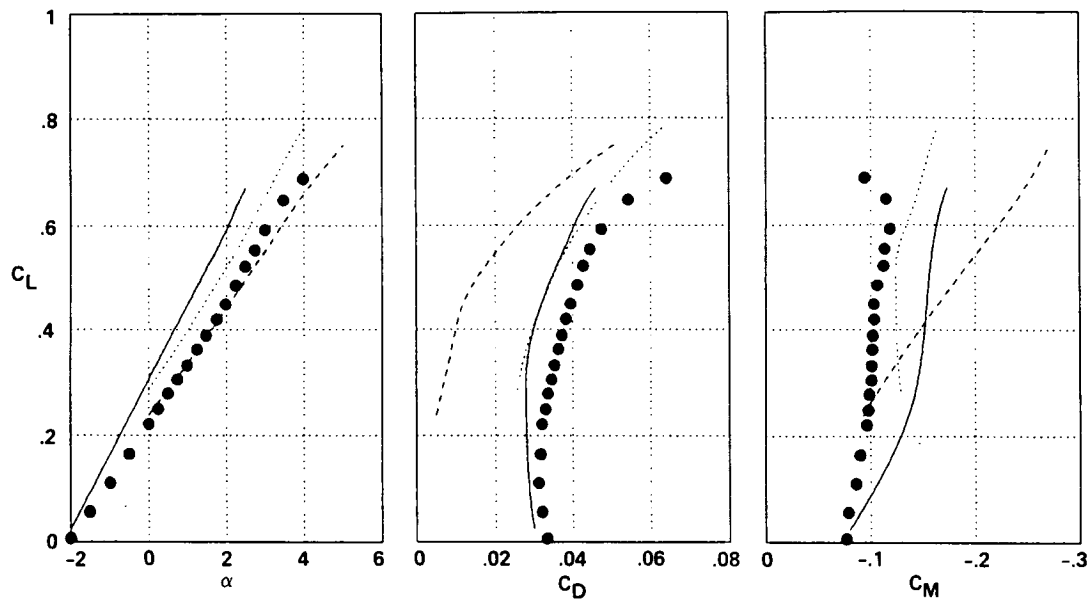
Fig. 32. Experiment–CFD force-and-moment comparison for Wing D, M = 0.80.
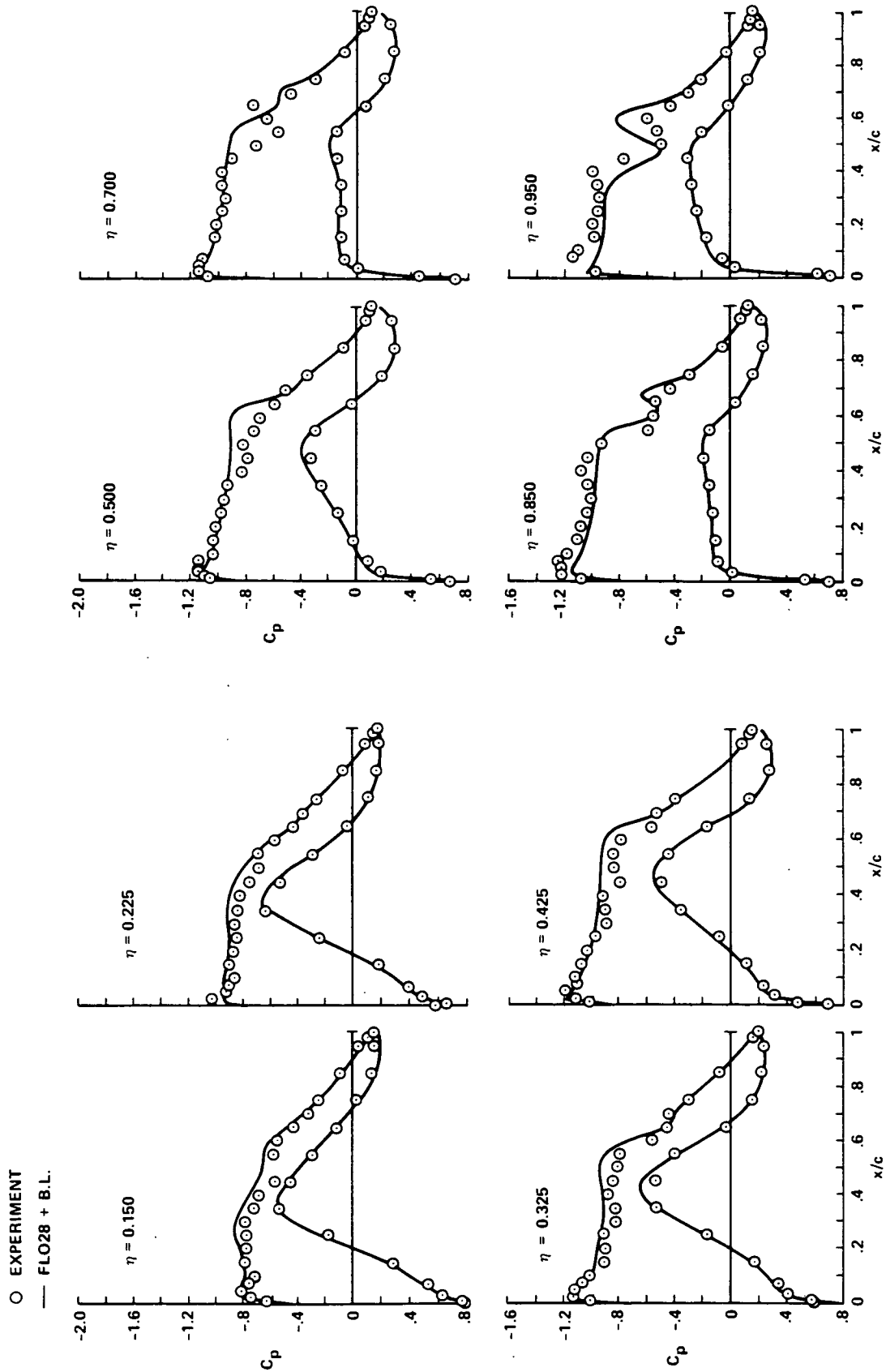
Fig. 33. Experiment–CFD pressure-distribution comparison for Wing D, M = 0.80, C_L = 0.55, FLO28 with boundary-layer correction.

129
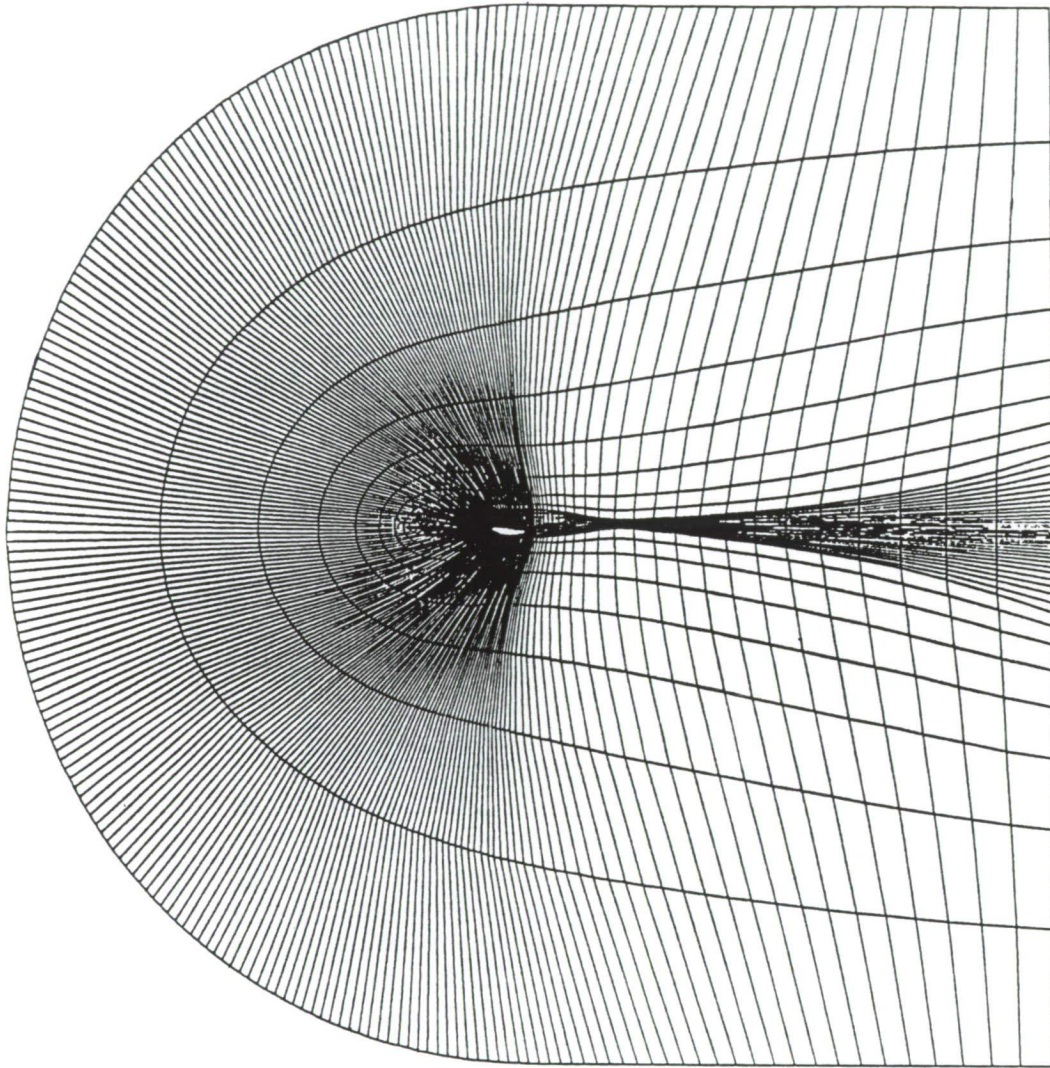
Fig. 34. C-H-grid distribution on centerplane, 217x25x33 points.
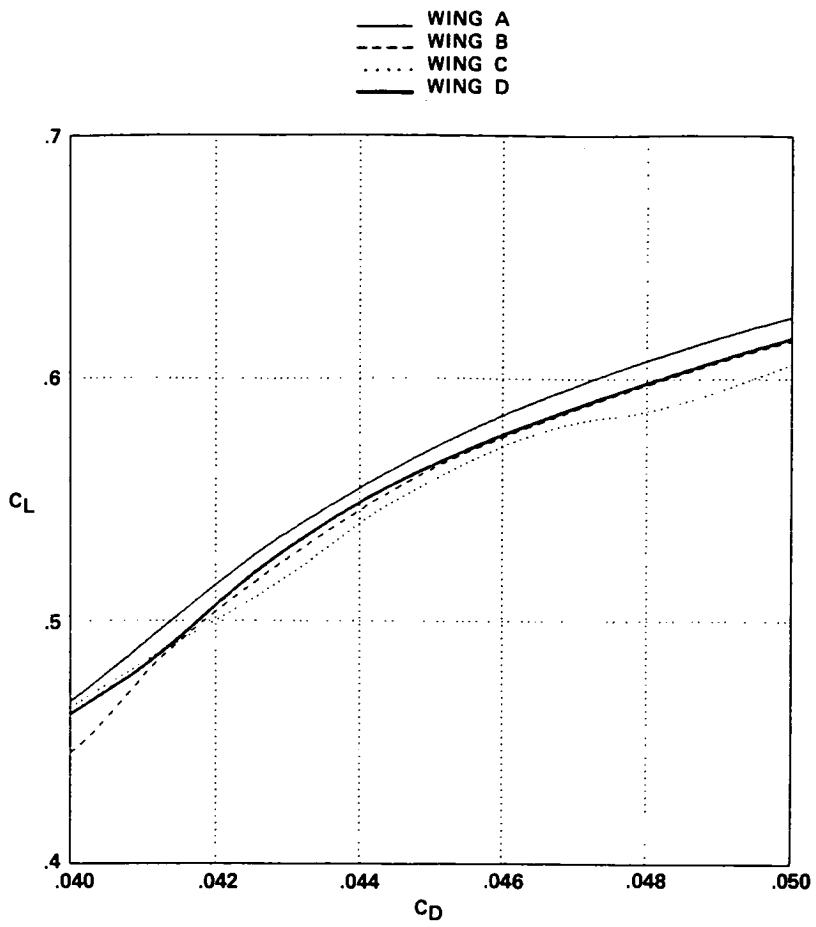
Fig. 35. Experimental drag comparison for transport wings, M = 0.80, Re = 8,300,000.
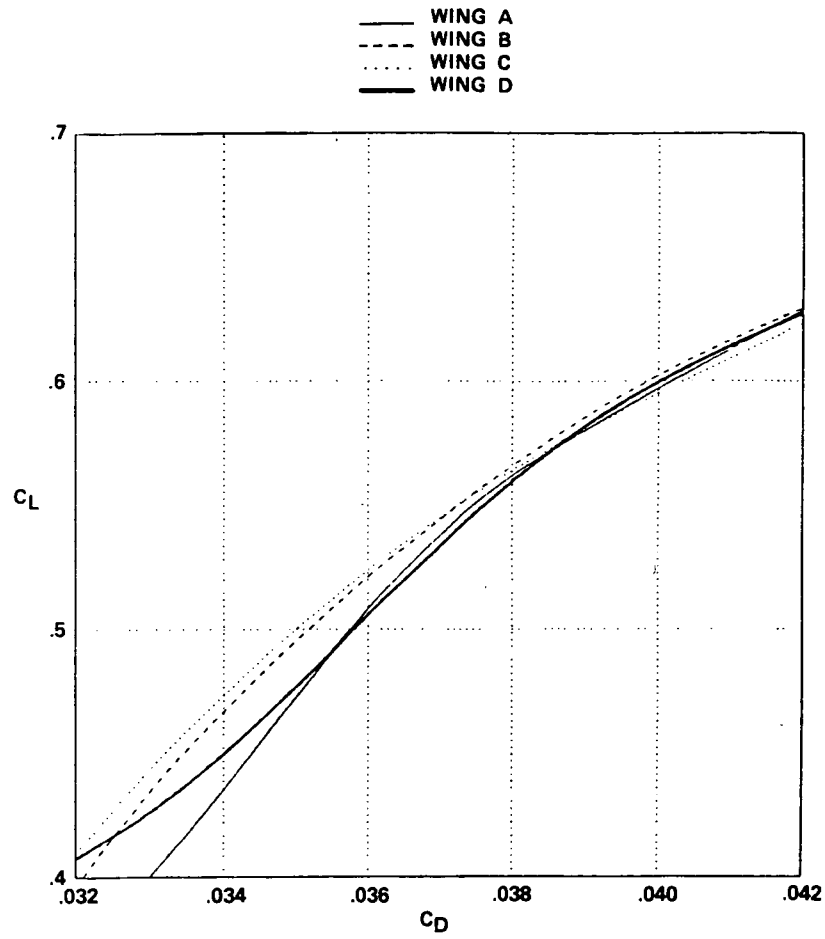
Fig. 36. Computational drag comparison for transport wings, M = 0.80, FLO57C.

WING D EXPERIMENT – Re = 8.3 million
WING D FLO22NM – 192 x 24 x 32 GRID
WING A EXPERIMENT – Re = 8.2 million
WING A FLO22NM – 192 x 24 x 32 GRID
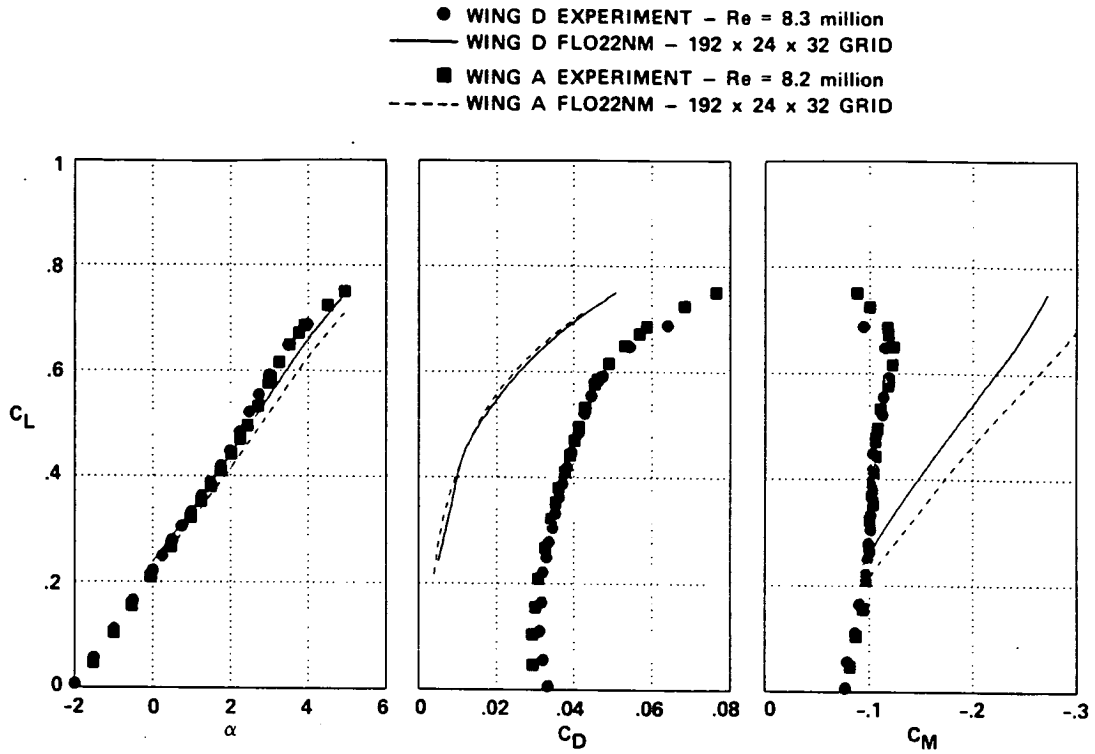
Fig. 37. Experiment–CFD force-and-moment comparison for Wing A and Wing D, FLO22NM.

PRESSURE TAP CHORD LOCATIONS

SECTION A–A

SECTION B–B
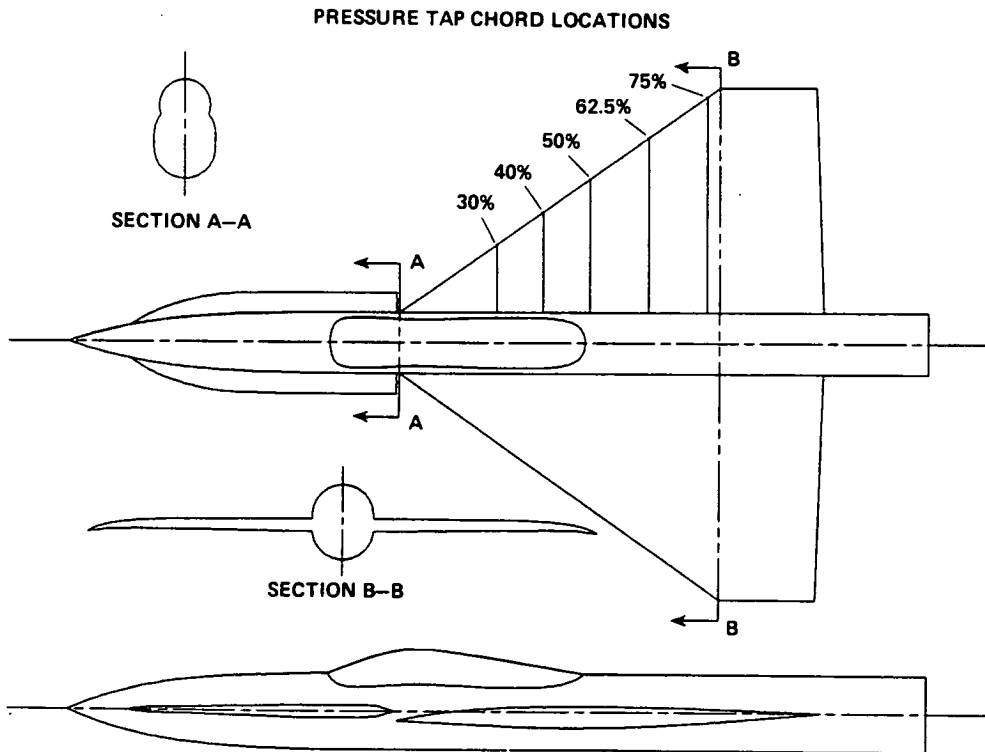
Fig. 38. Generic fighter with chine.

133
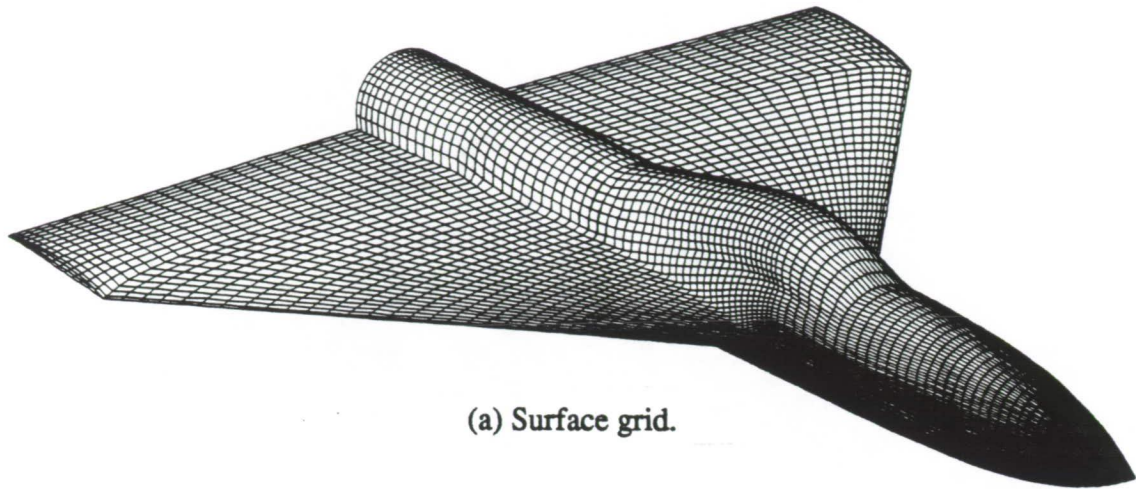
(a) Surface grid.
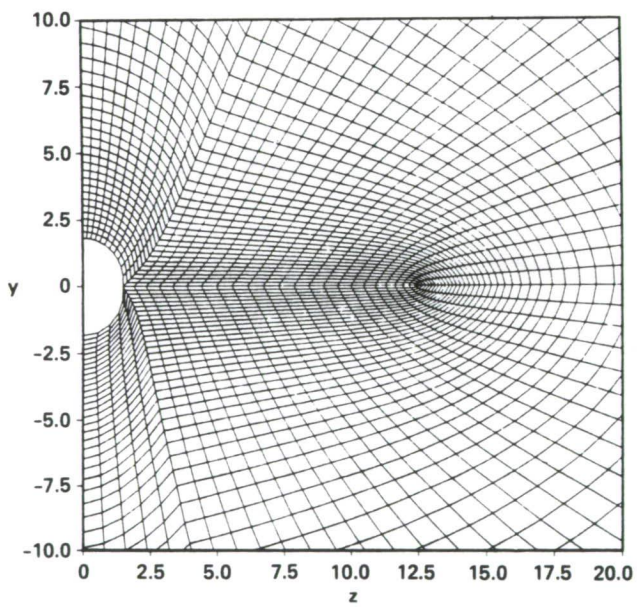
(b) Wing trailing-edge plane.
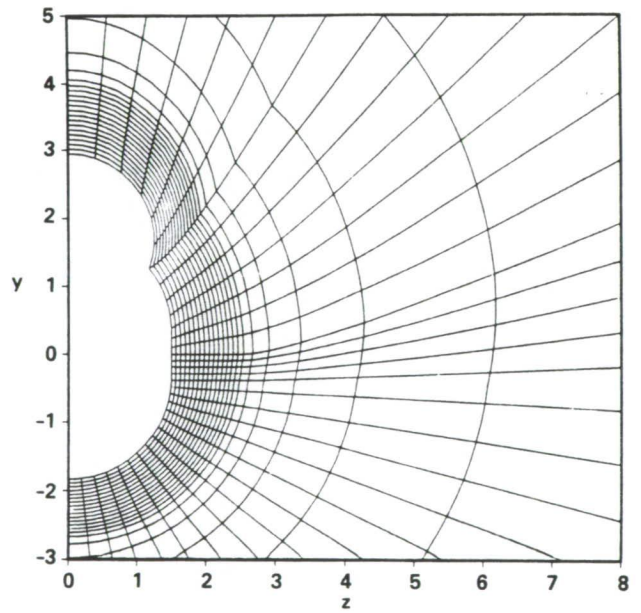
(c) Chine trailing-edge plane.

Fig. 39. Generic fighter wing/body grid, 134 x 49 x 65 points.
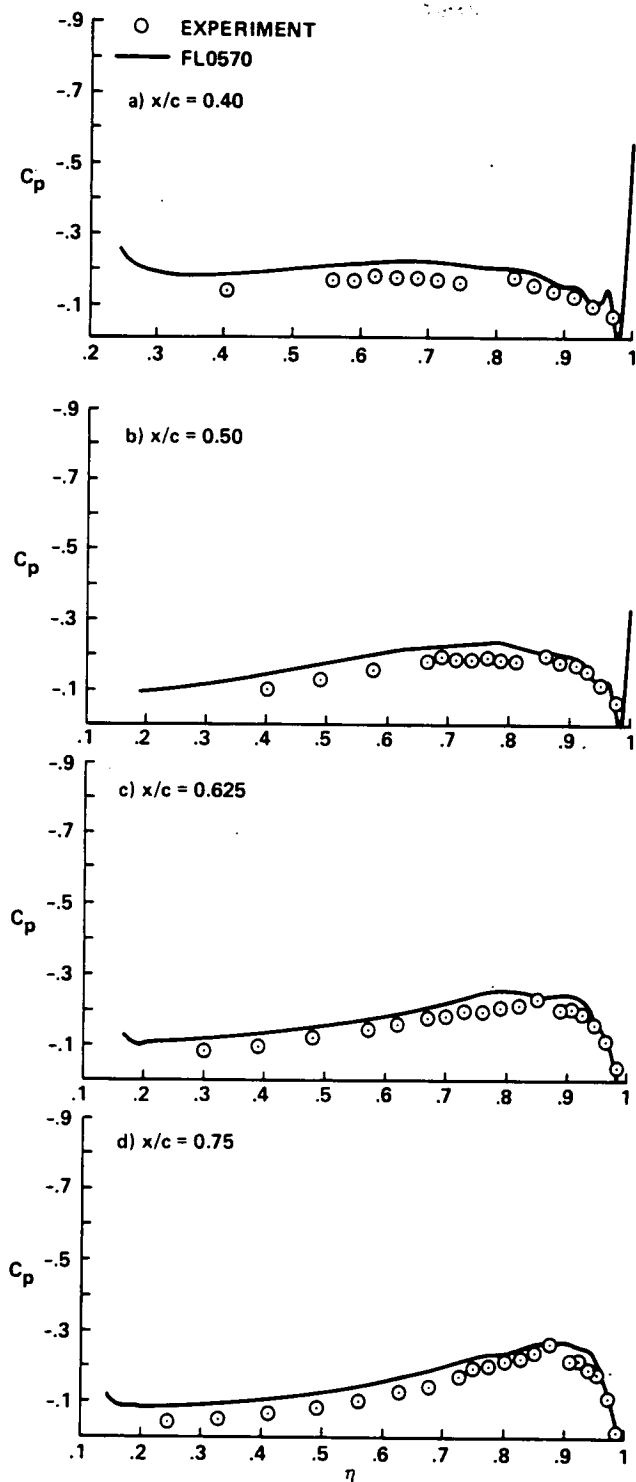
Fig. 40. Upper-surface pressure distributions for wing/body, $M = 0.6$, $\alpha = 4.0°$
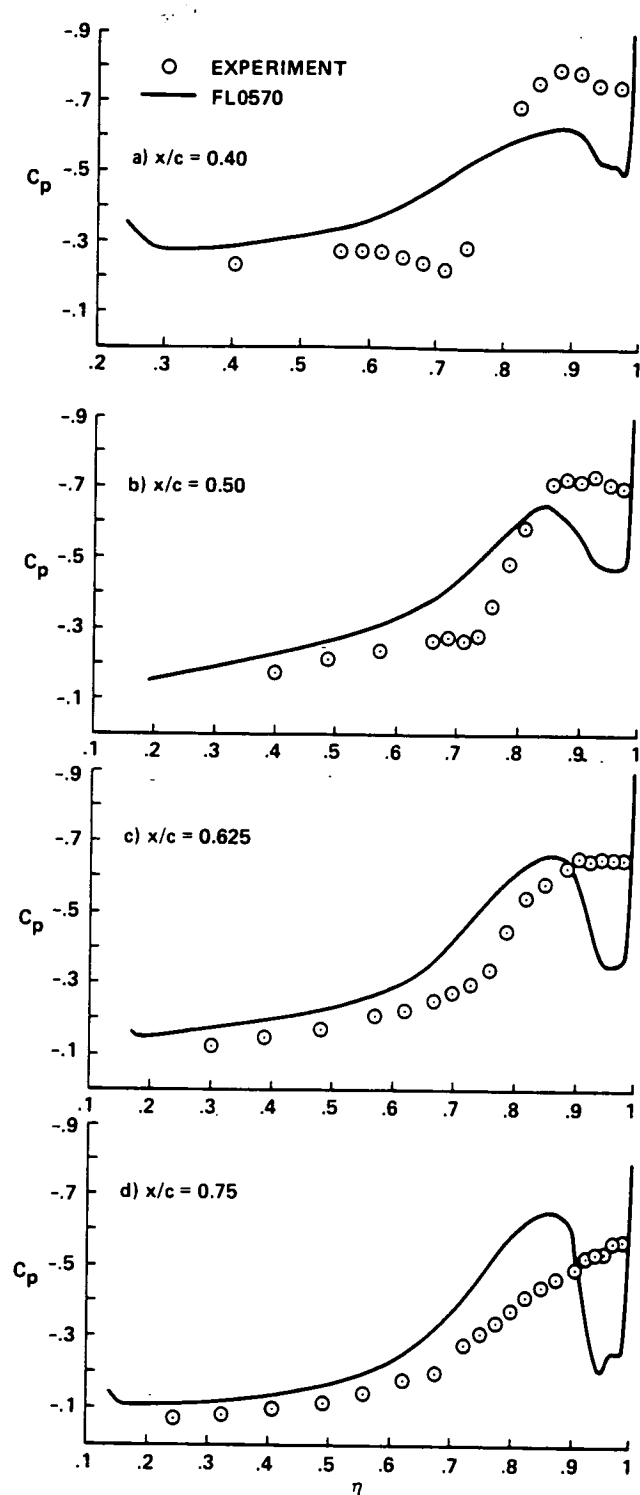
Fig. 41. Upper-surface pressure distributions for wing/body, $M = 0.6$, $\alpha = 8.0°$
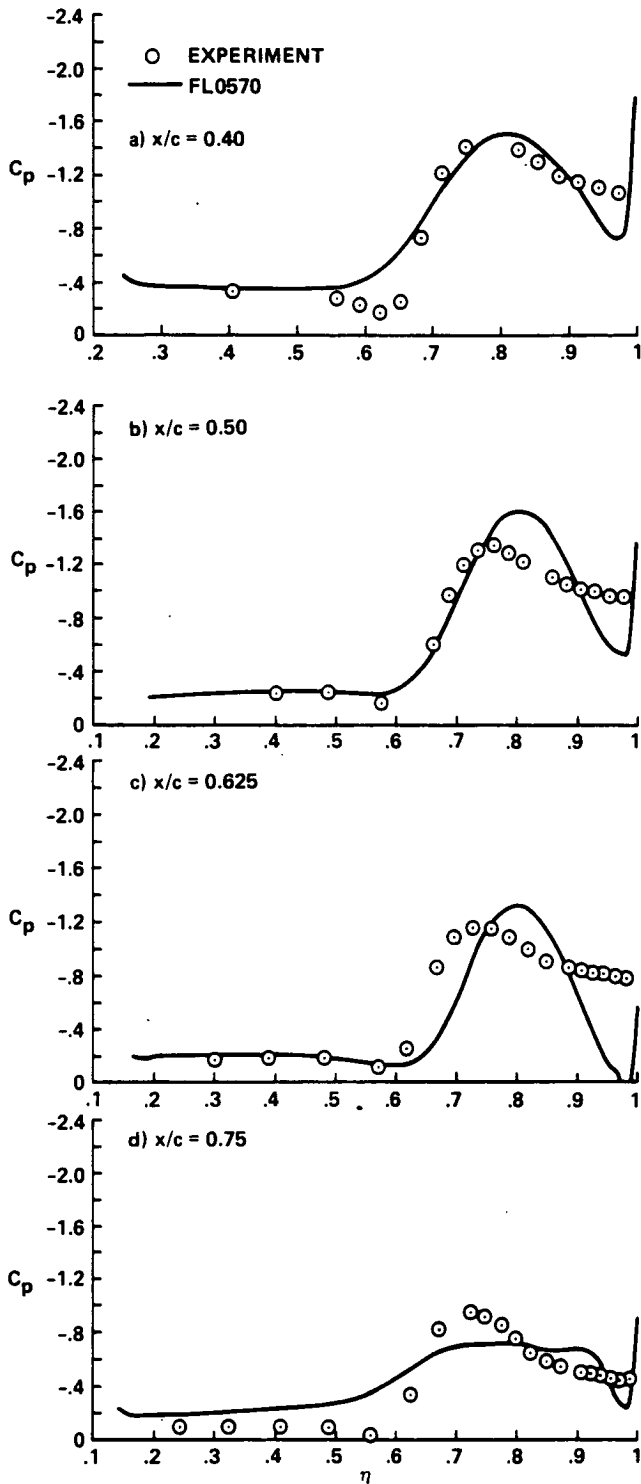
Fig. 42. Upper-surface pressure distributions for wing/body, $M = 0.6$, $\alpha = 12.0°$
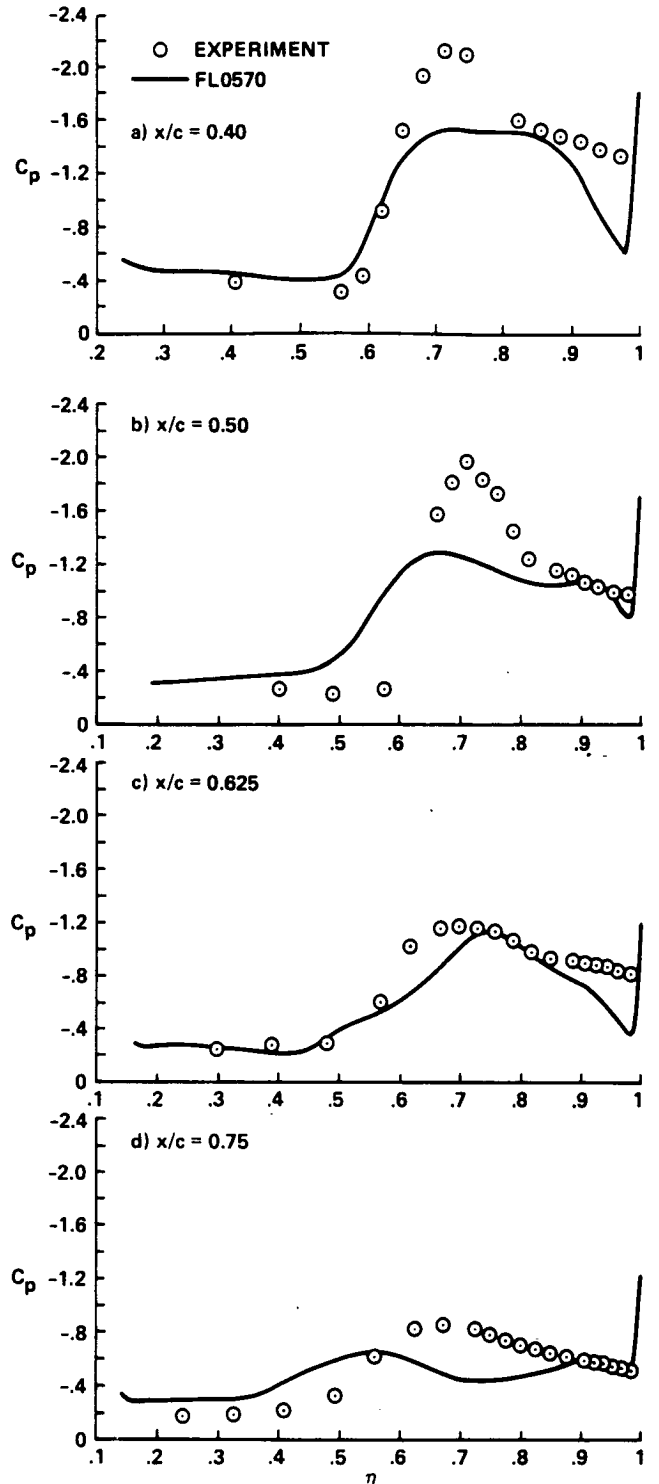
Fig. 43. Upper-surface pressure distributions for wing/body, $M = 0.6$, $\alpha = 16.0°$

136
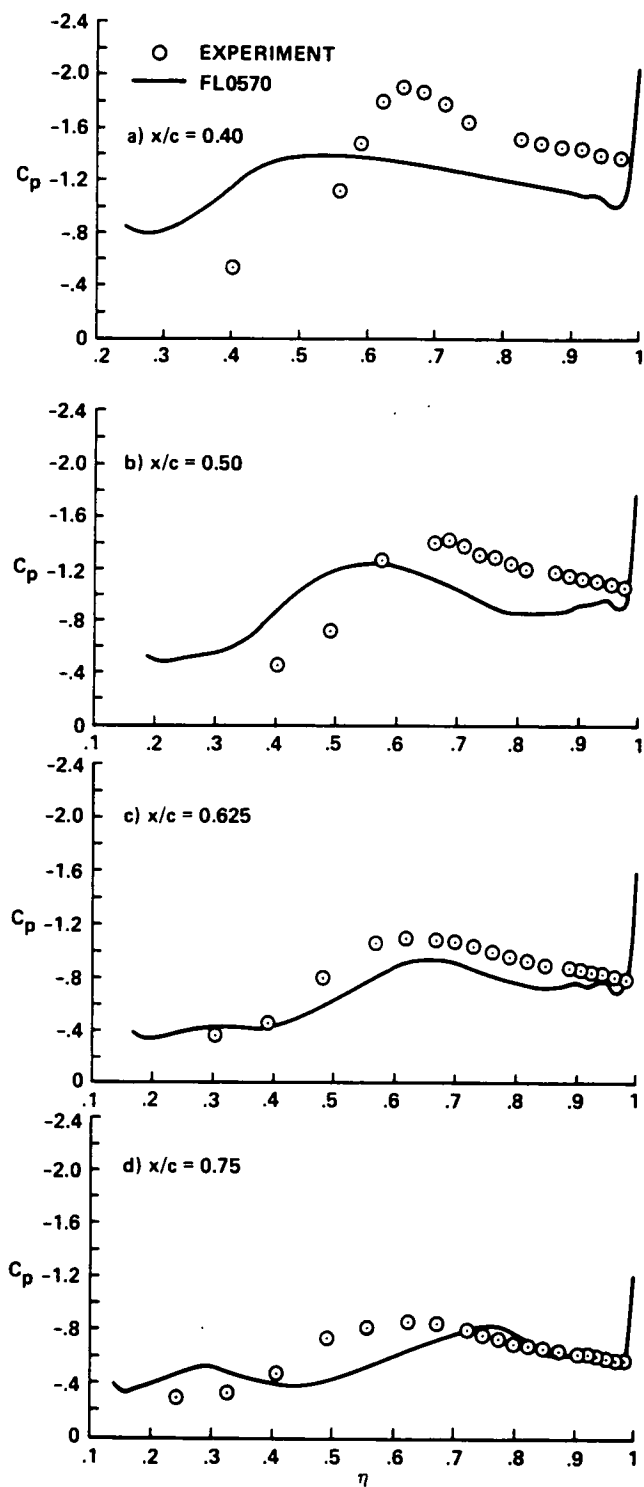
Fig. 44. Upper-surface pressure distributions for wing/body, M = 0.6, α = 20.0°
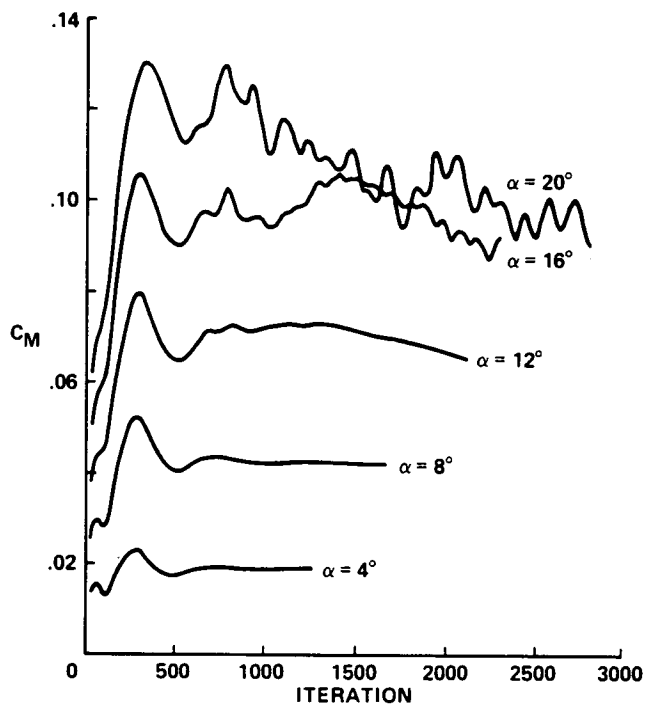
Fig. 45. Pitching-moment history for wing/body, M = 0.60.

137
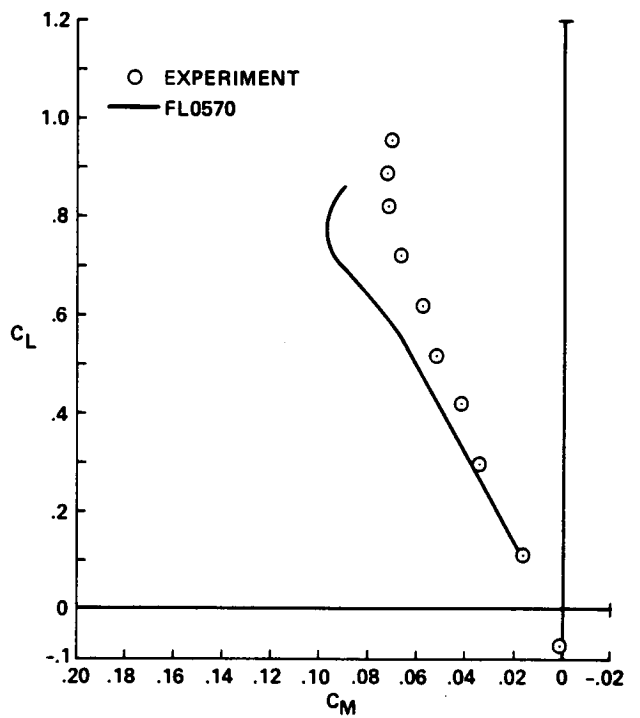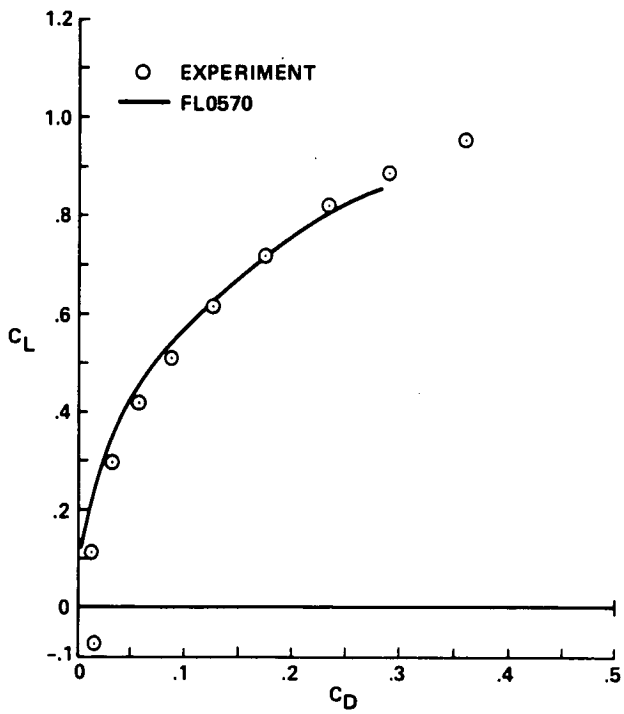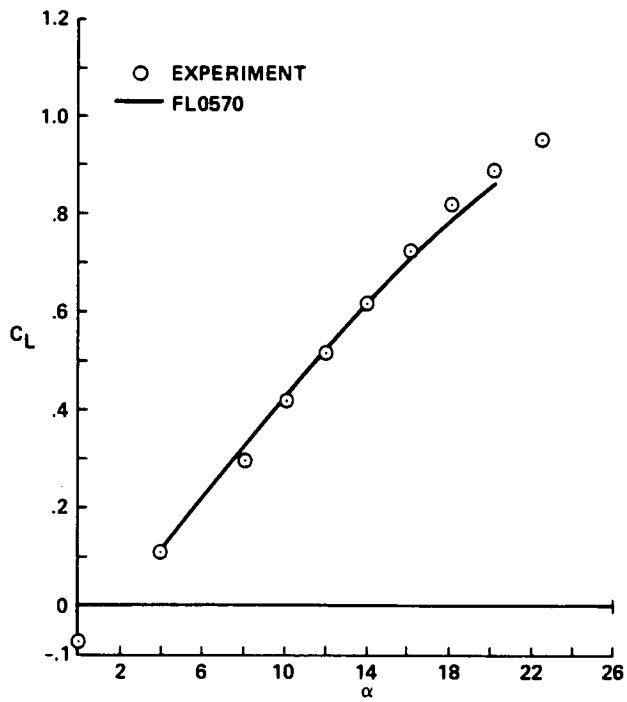
Fig. 46. Experiment–CFD forces and moments for wing/body, FLO570.
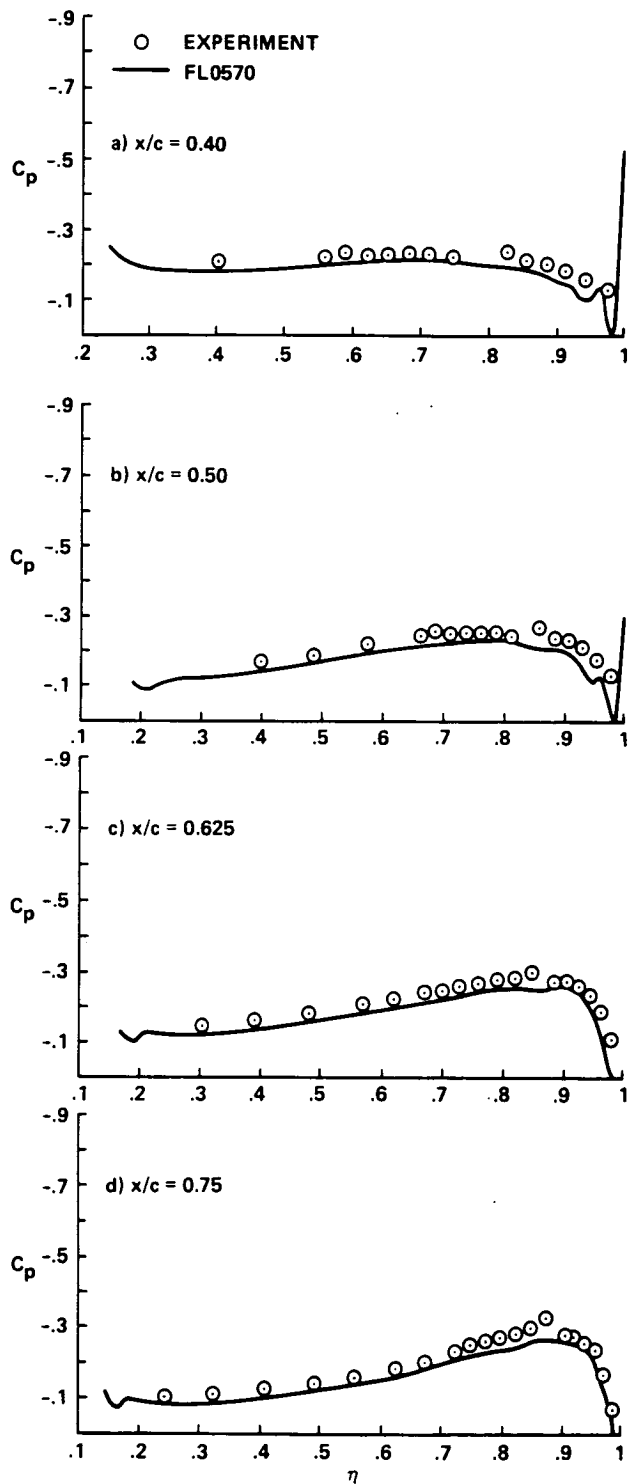
Fig. 47. Upper-surface pressure distributions for wing/body/chine, M = 0.6, $\alpha = 4.0°$
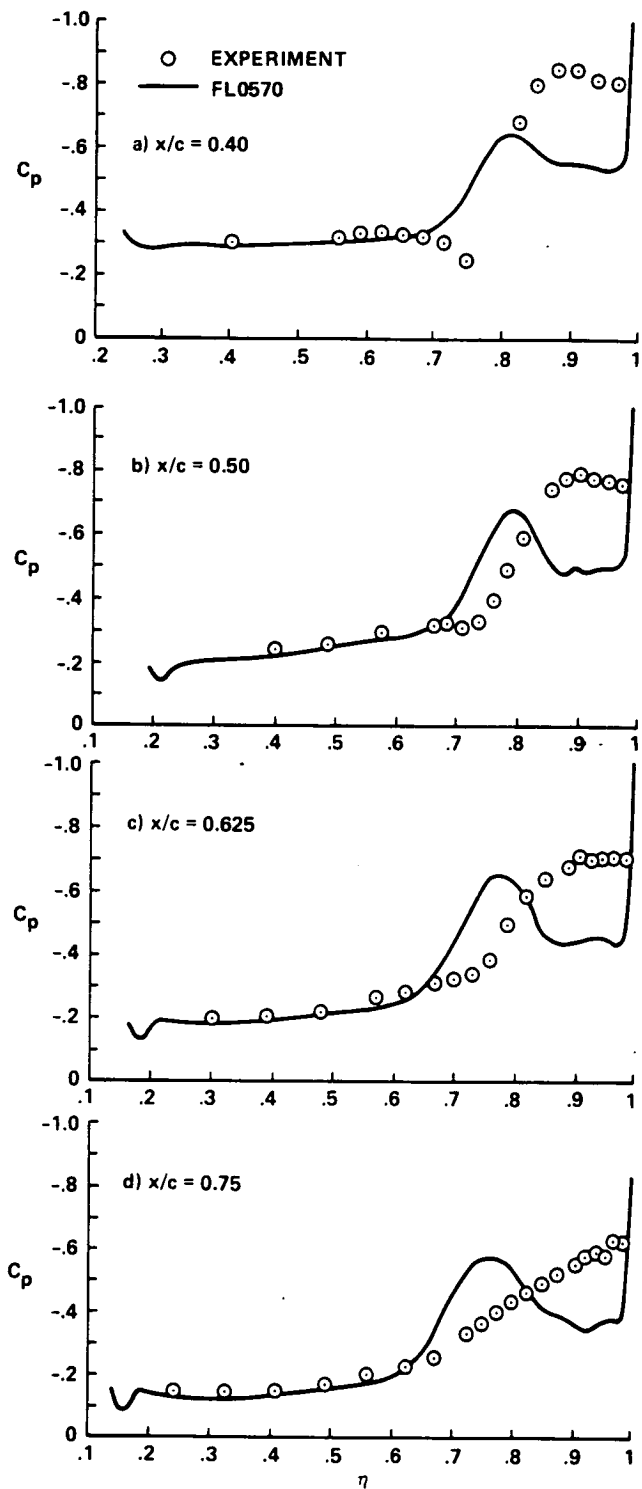
Fig. 48. Upper-surface pressure distributions for wing/body/chine, M = 0.6, $\alpha = 8.0°$
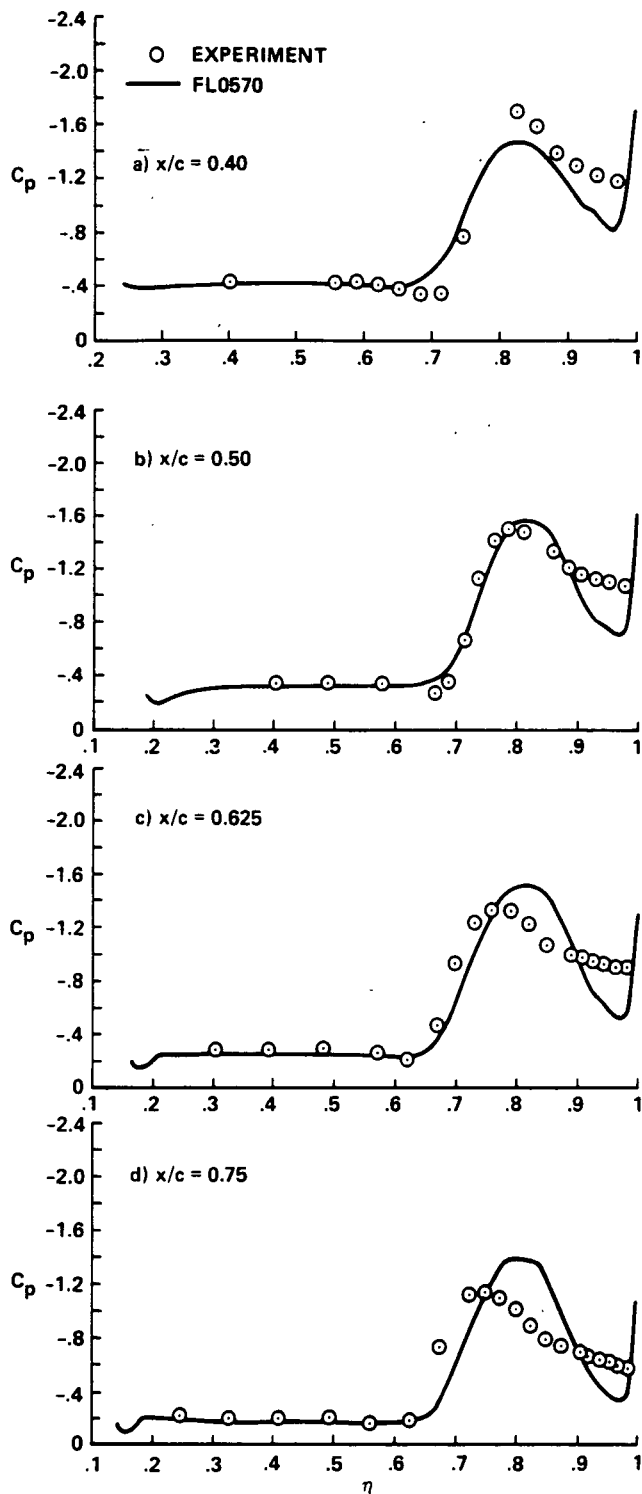
Fig. 49. Upper-surface pressure distributions for wing/body/chine, M = 0.6, α = 12.0°
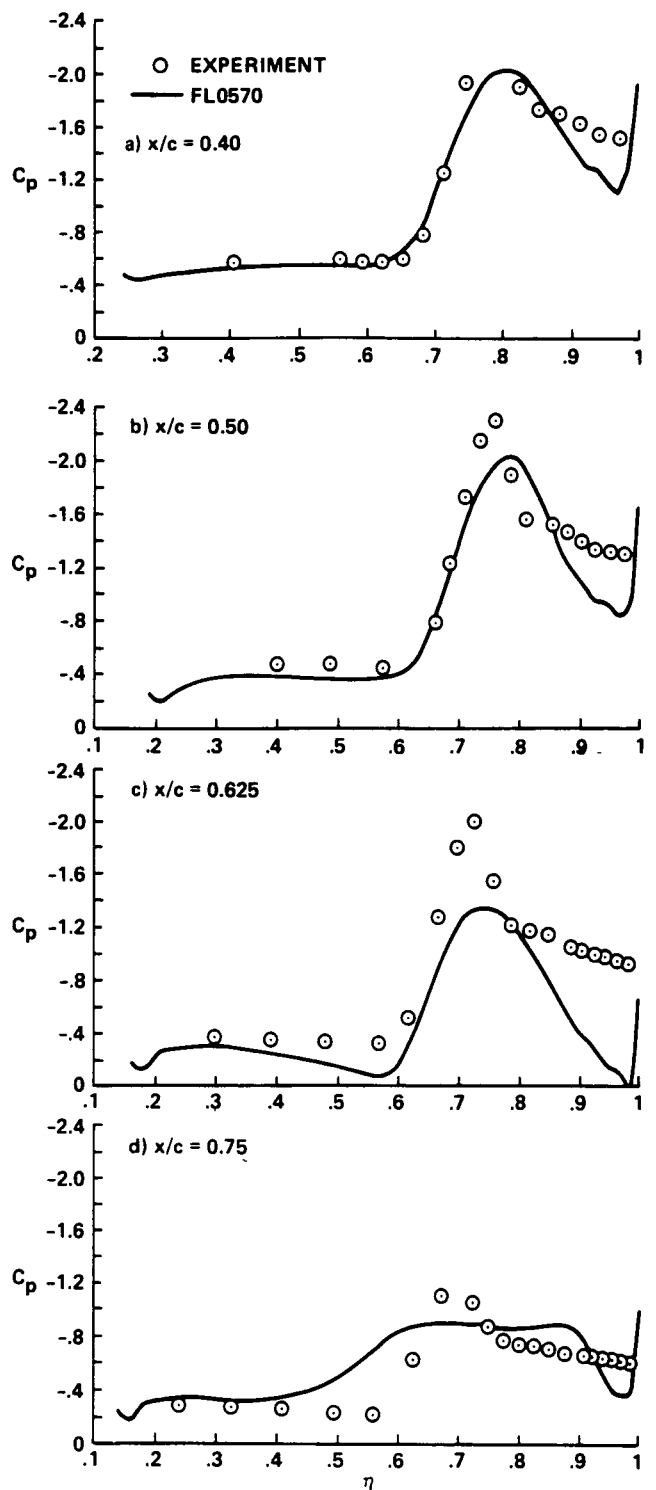
Fig. 50. Upper-surface pressure distributions for wing/body/chine, M = 0.6, α = 16.0°
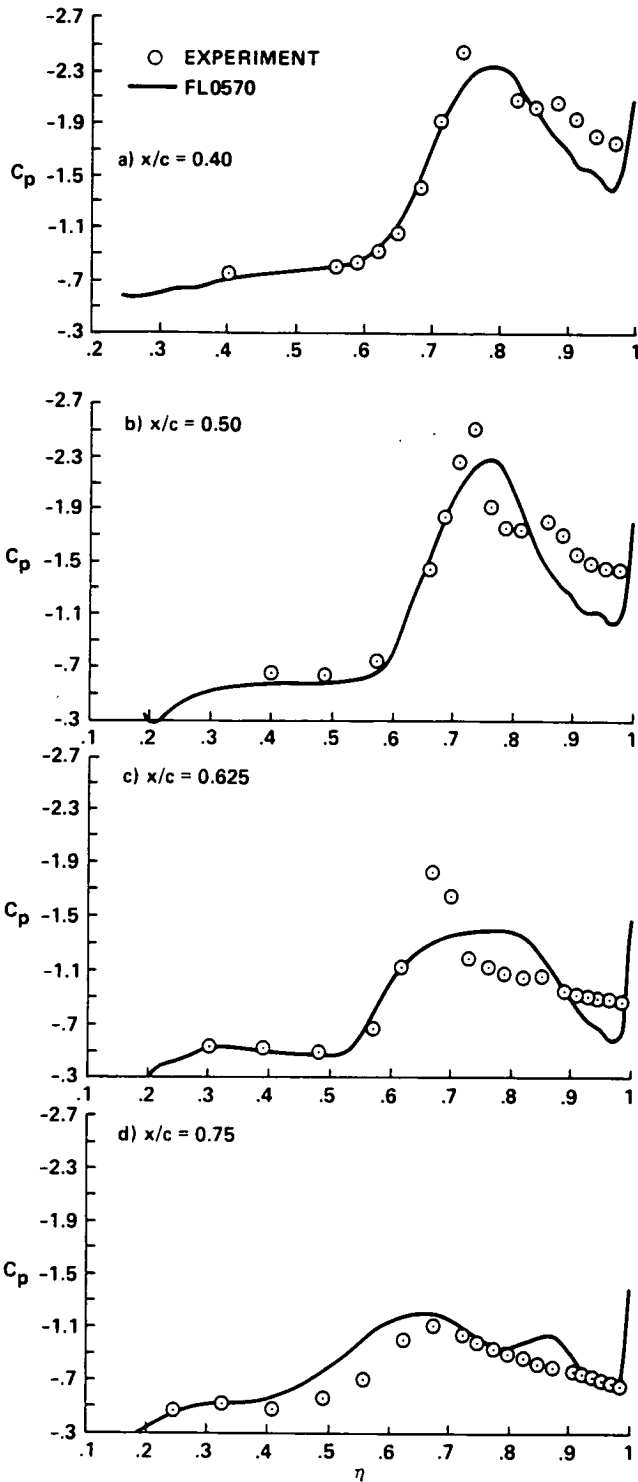
Fig. 51. Upper-surface pressure distributions for wing/body/chine, $M = 0.6$, $\alpha = 20.0°$
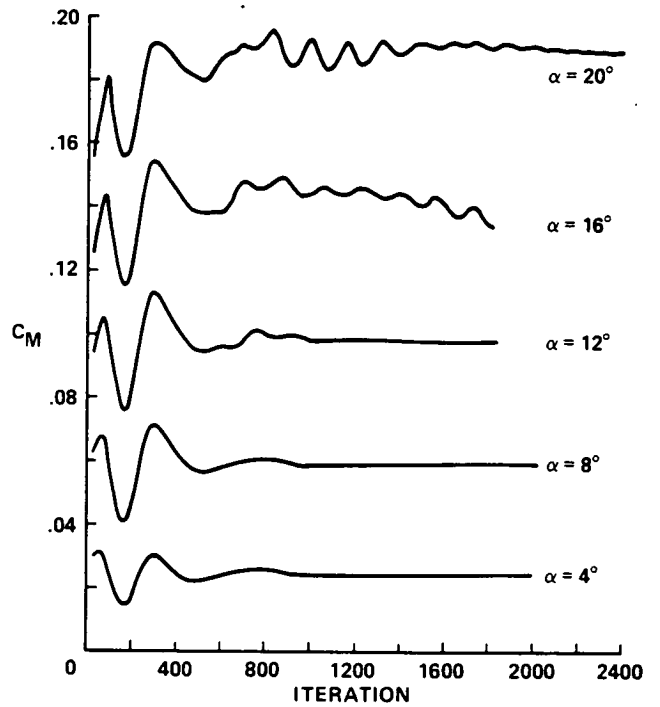
Fig. 52. Pitching-moment history for wing/body/chine, $M = 0.60$.

141
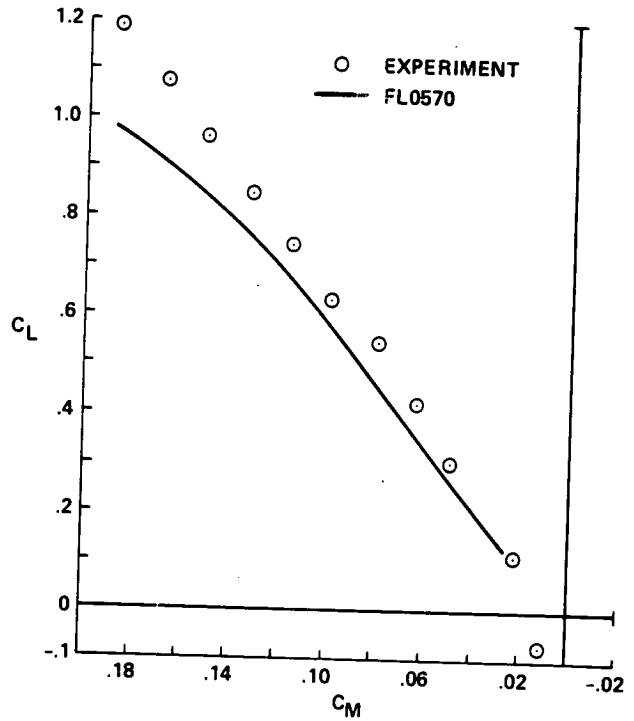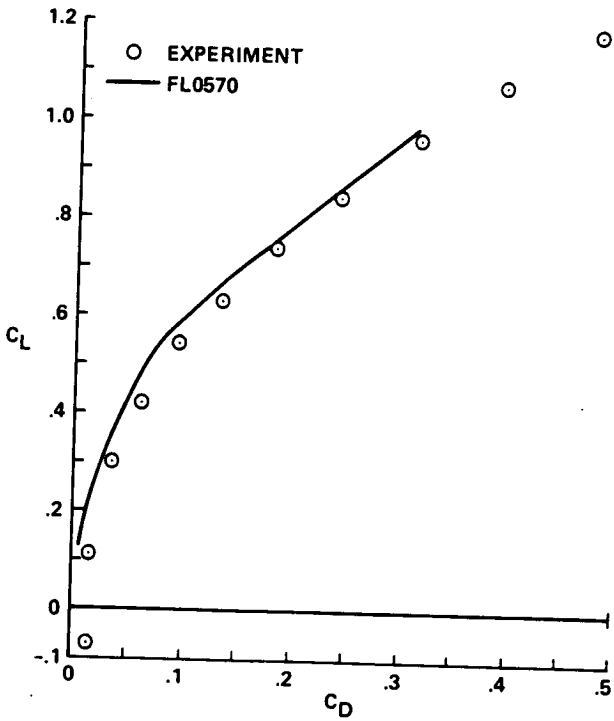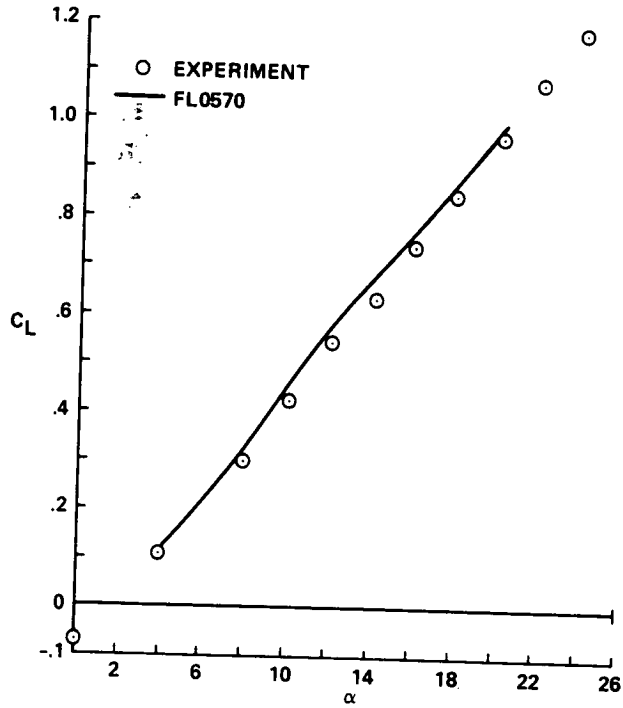
Fig. 53. Experiment–CFD forces and moments for wing/body/chine, M = 0.60.
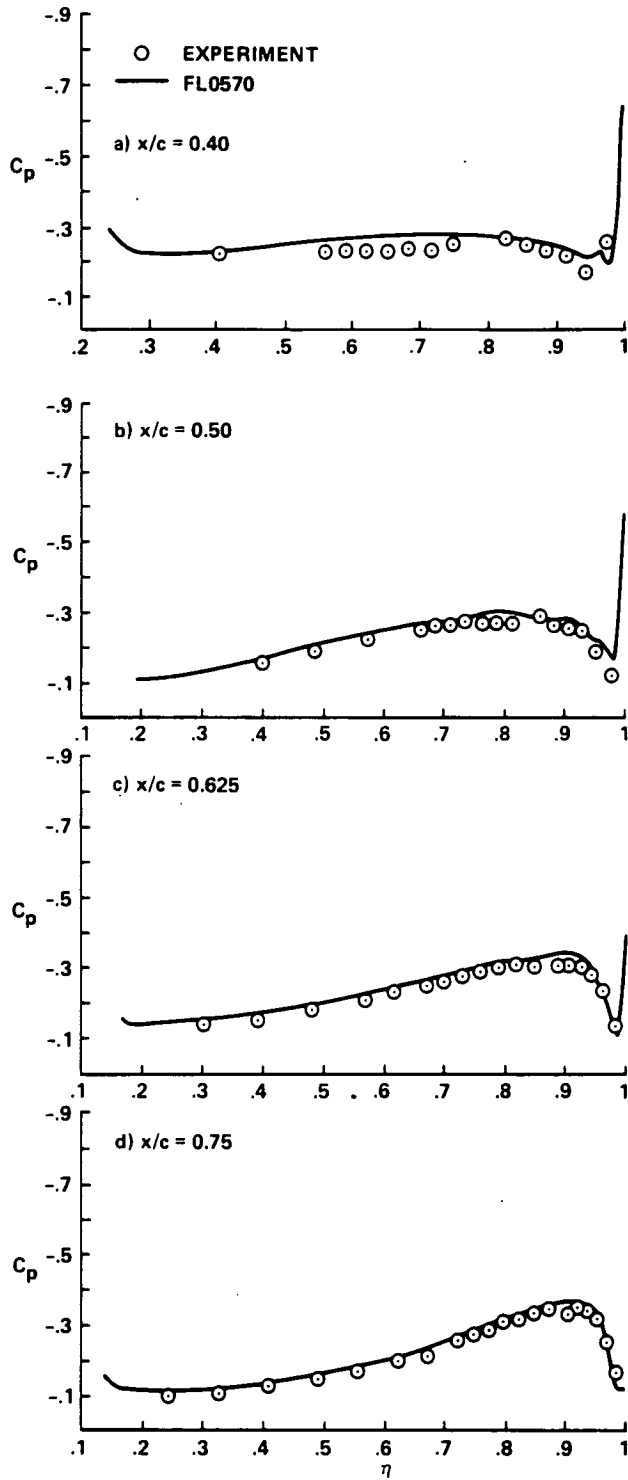
Fig. 54. Upper-surface pressure distributions for wing/body, $M = 0.80$, $\alpha = 5.0°$
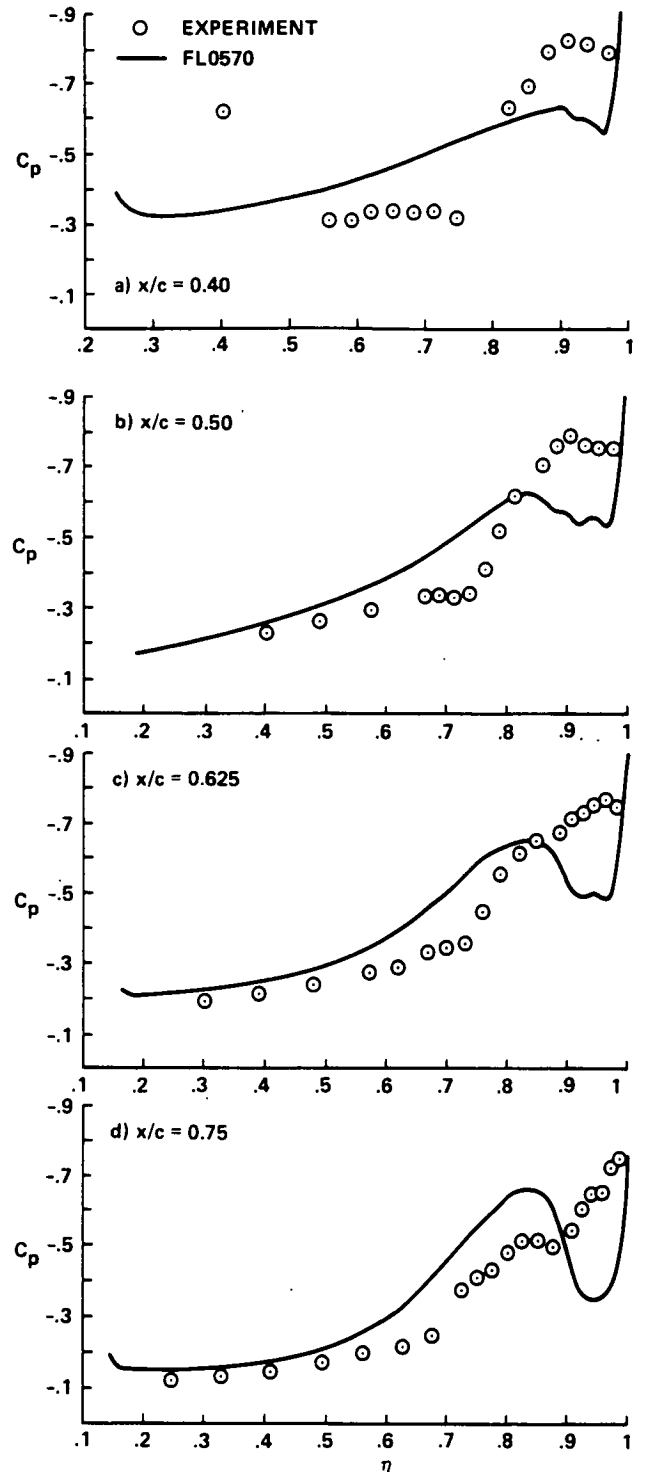
Fig. 55. Upper-surface pressure distributions for wing/body, $M = 0.80$, $\alpha = 8.0°$

143
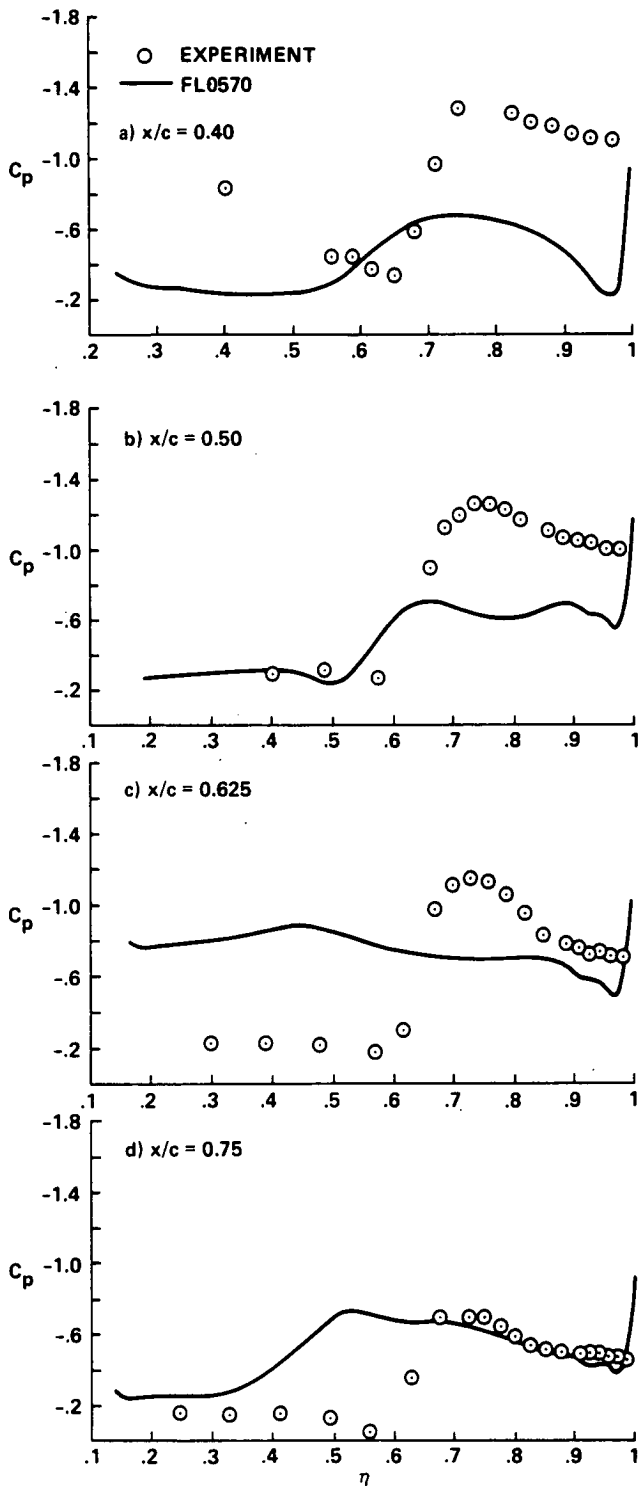
Fig. 56. Upper-surface pressure distributions for wing/body, M = 0.80, $\alpha = 12.0°$
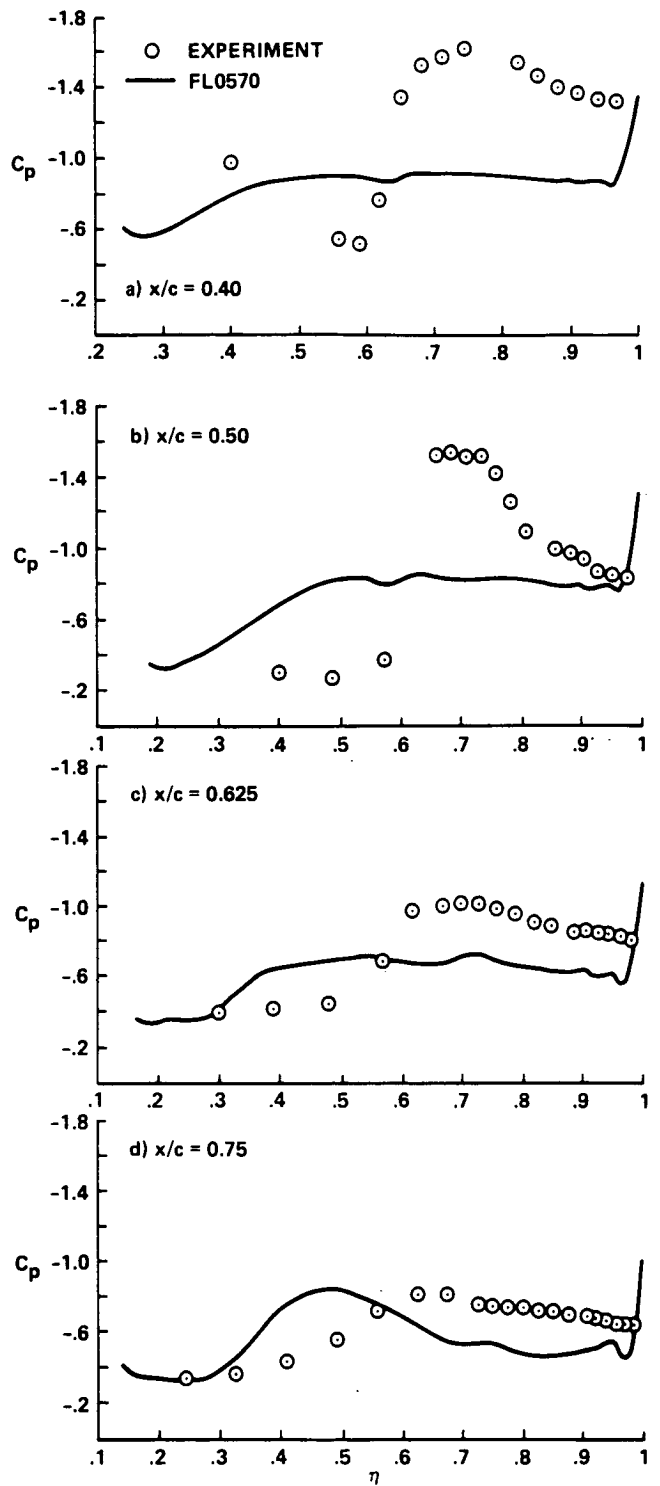
Fig. 57. Upper-surface pressure distributions for wing/body, M = 0.80, $\alpha = 16.0°$
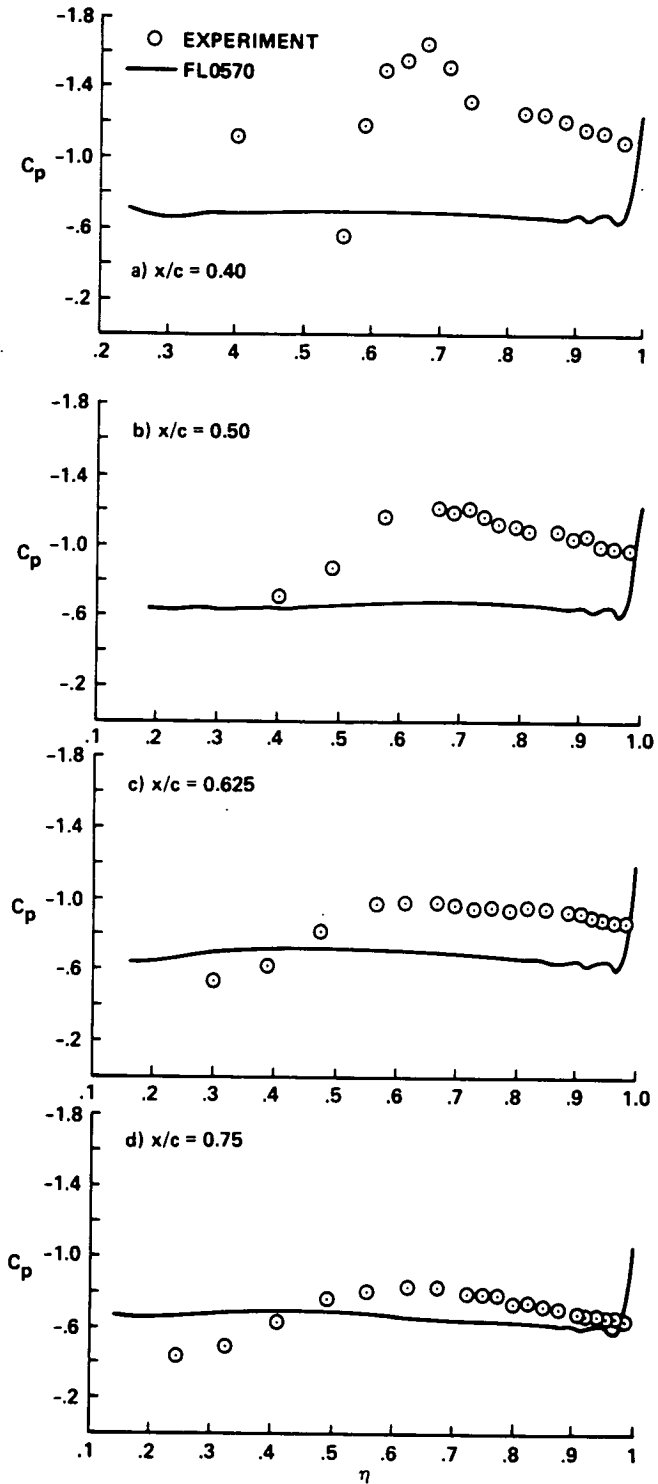
Fig. 58. Upper-surface pressure distributions for wing/body, M = 0.80, $\alpha = 20.0°$
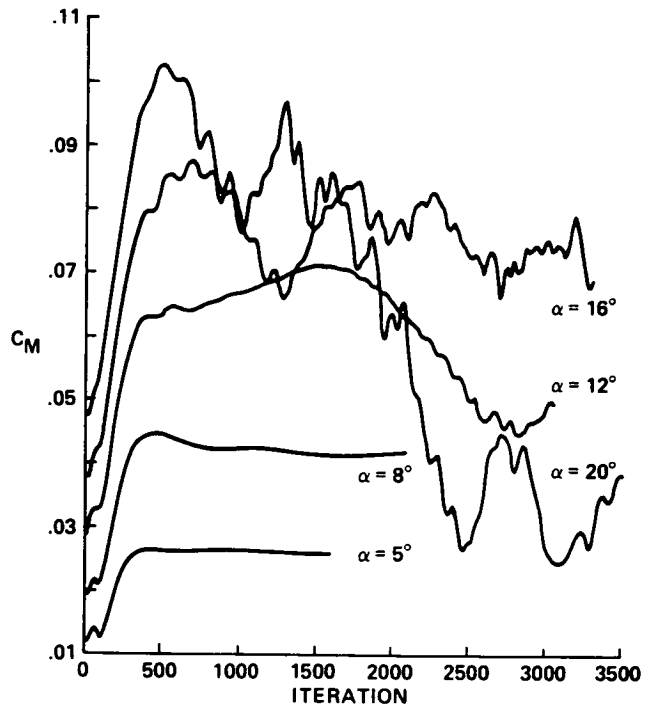
Fig. 59. Pitching-moment history for wing/body, M = 0.80.
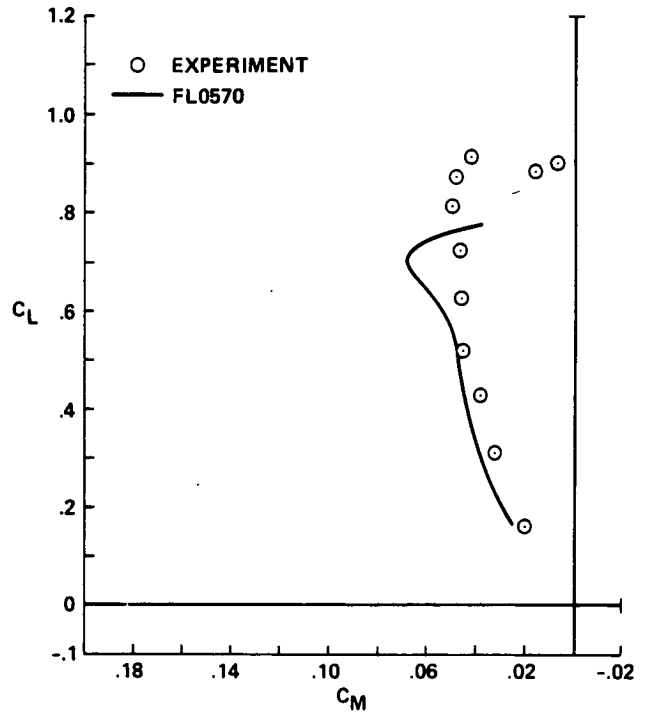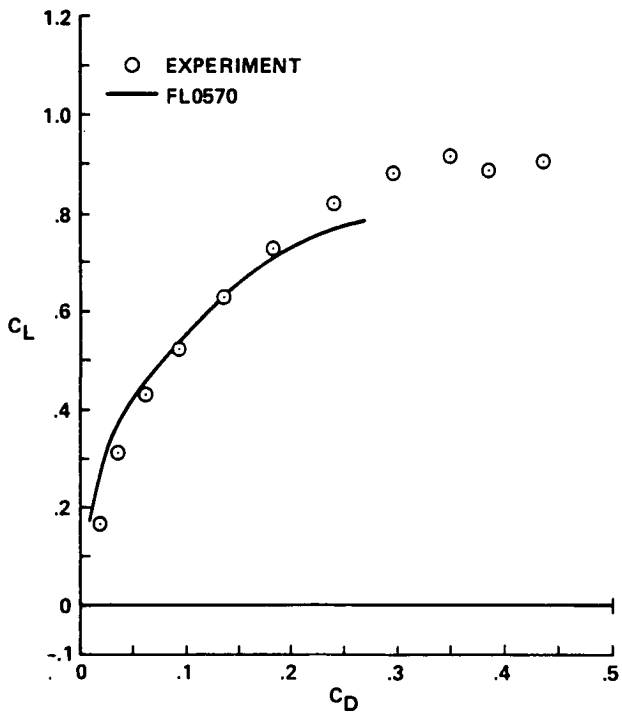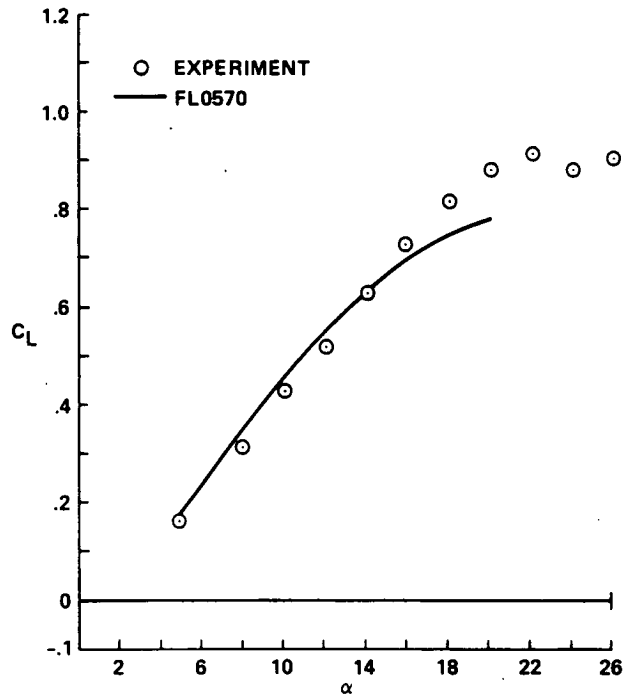
Fig. 60. Experiment–CFD forces and moments for wing/body, M = 0.80.
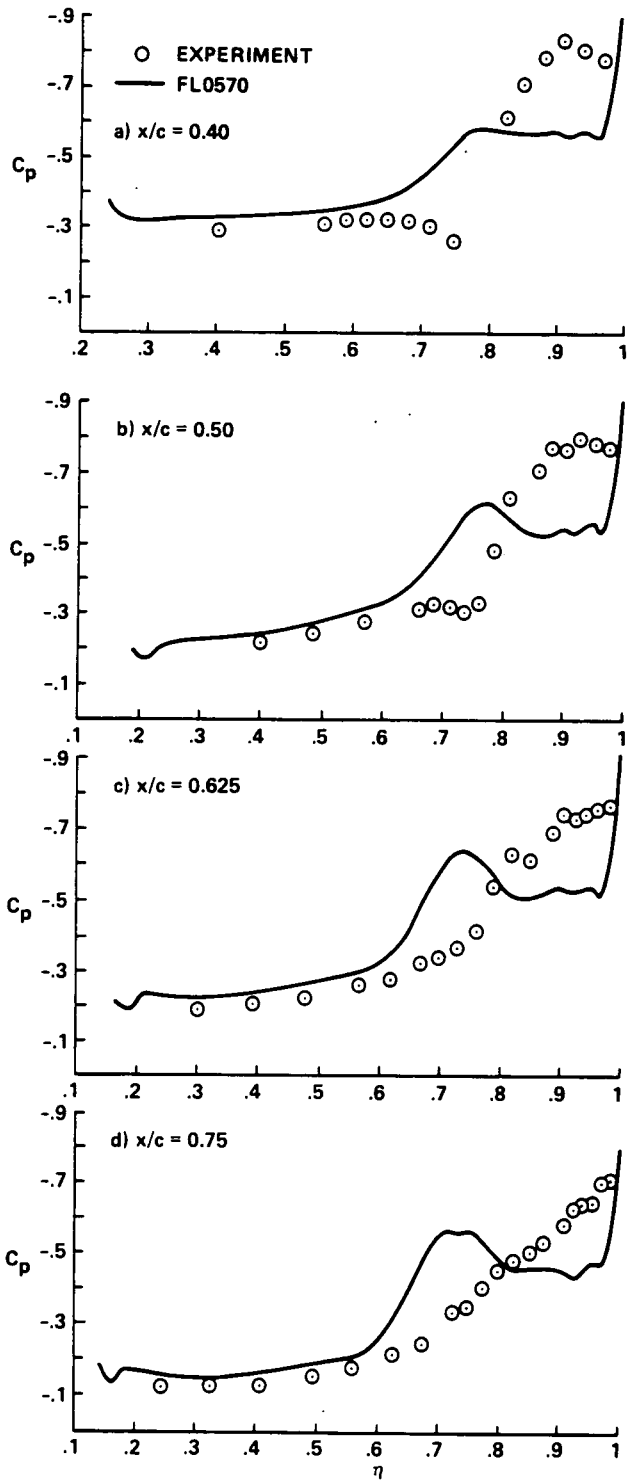
Fig. 61. Upper-surface pressure distributions for wing/body/chine, M = 0.80, α = 8.0°
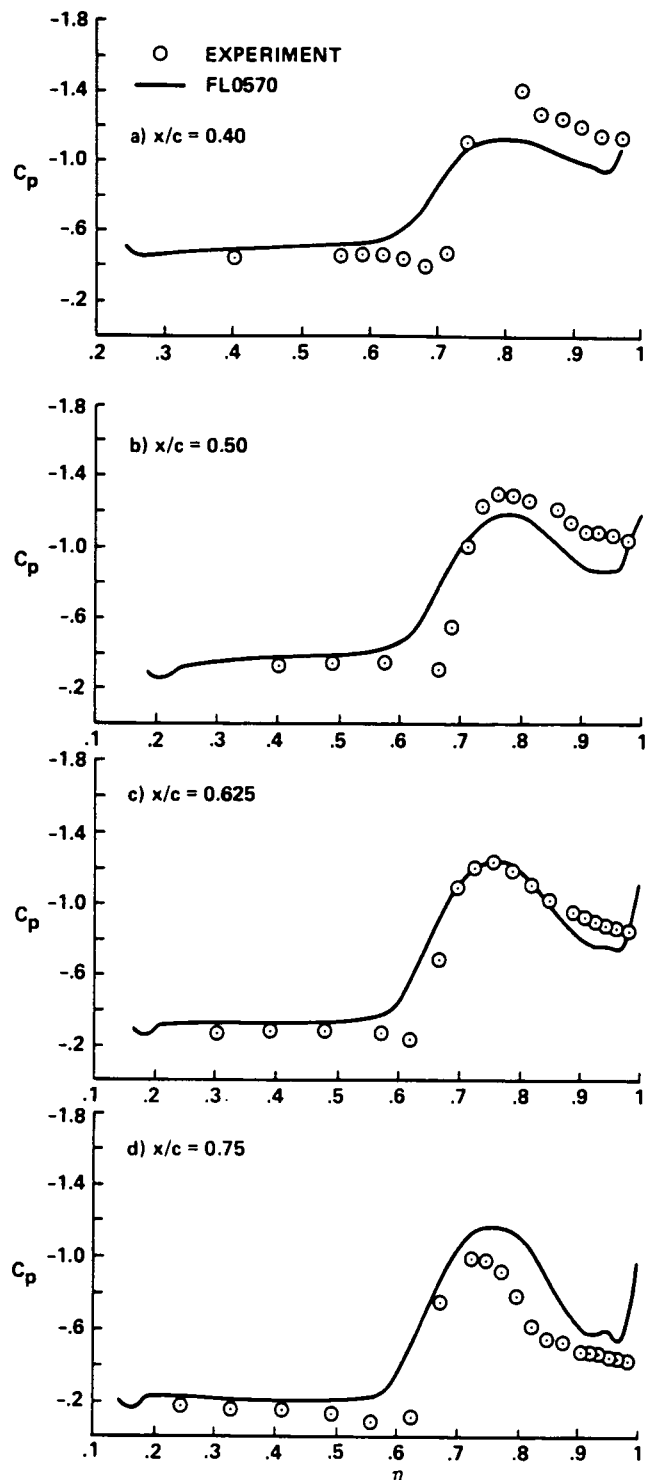
Fig. 62. Upper-surface pressure distributions for wing/body/chine, M = 0.80, α = 12.0°
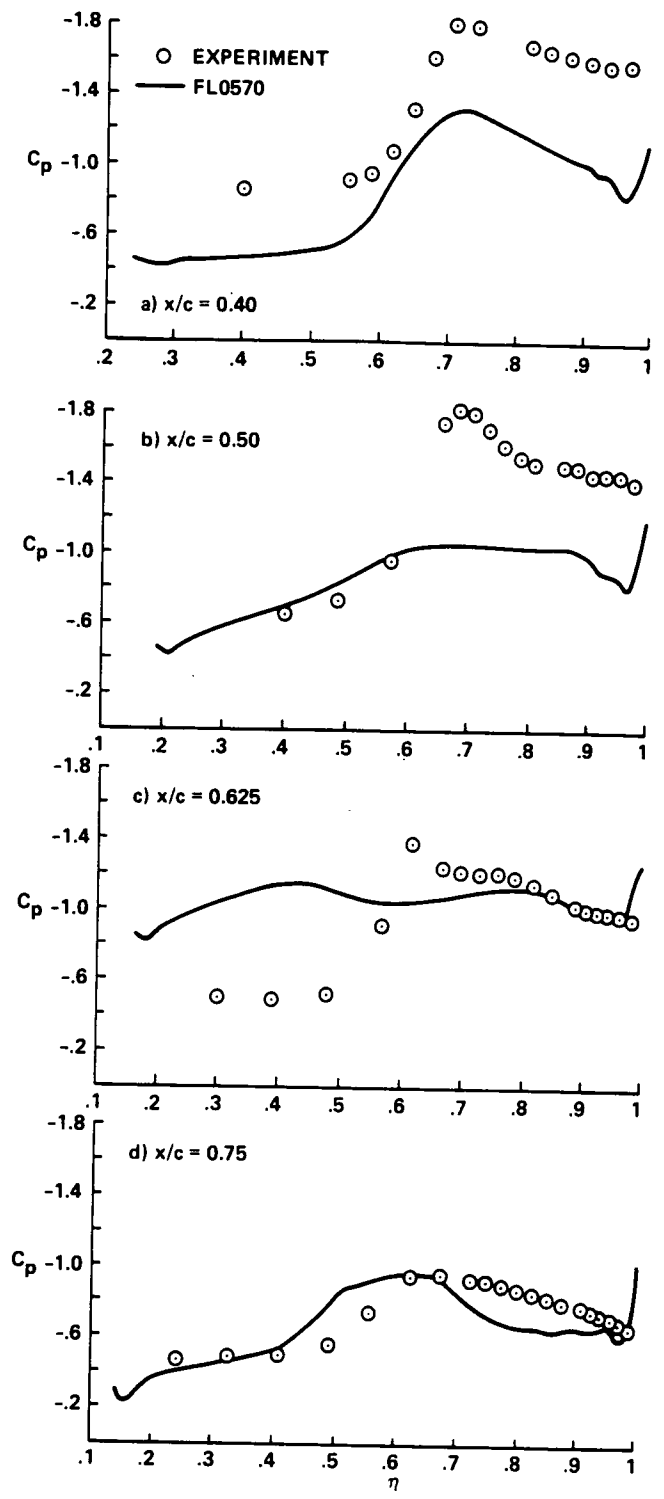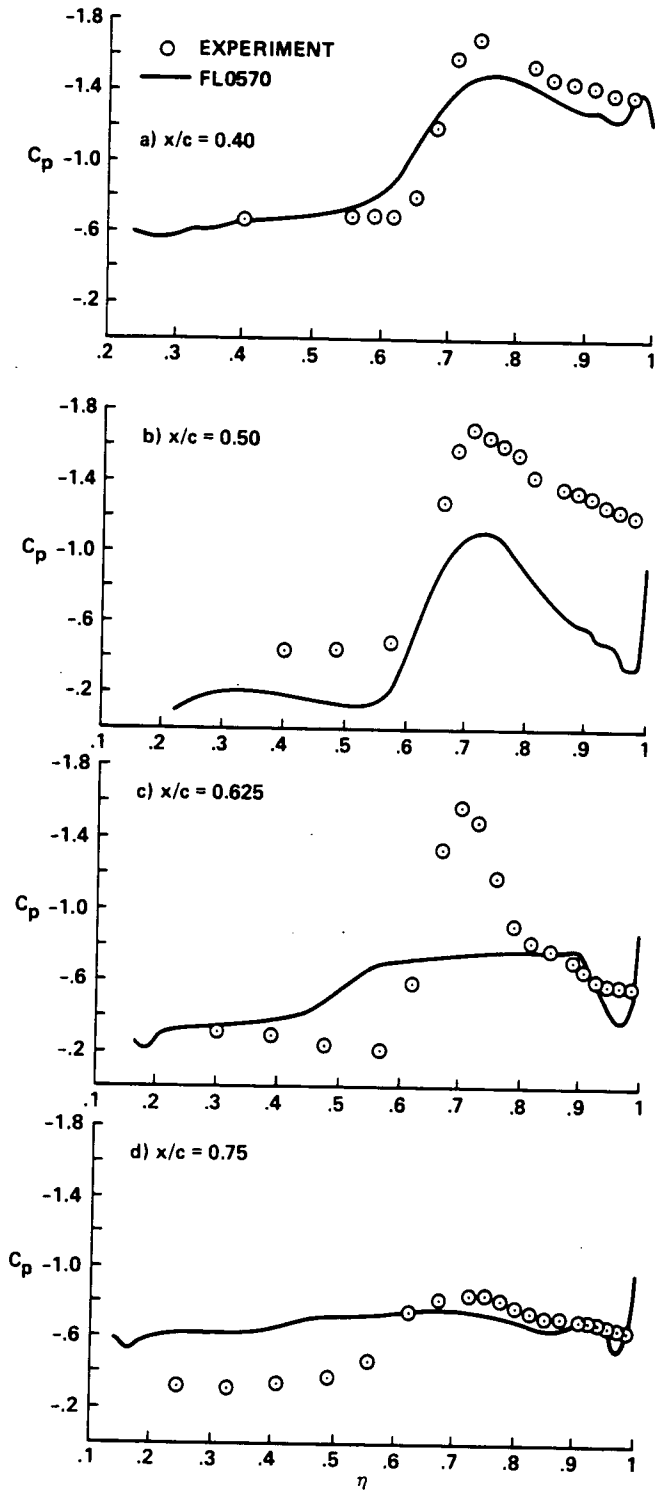
Fig. 63. Upper-surface pressure distributions for wing/body/chine, M = 0.80, α = 16.0°

Fig. 64. Upper-surface pressure distributions for wing/body/chine, M = 0.80, α = 20.0°

148
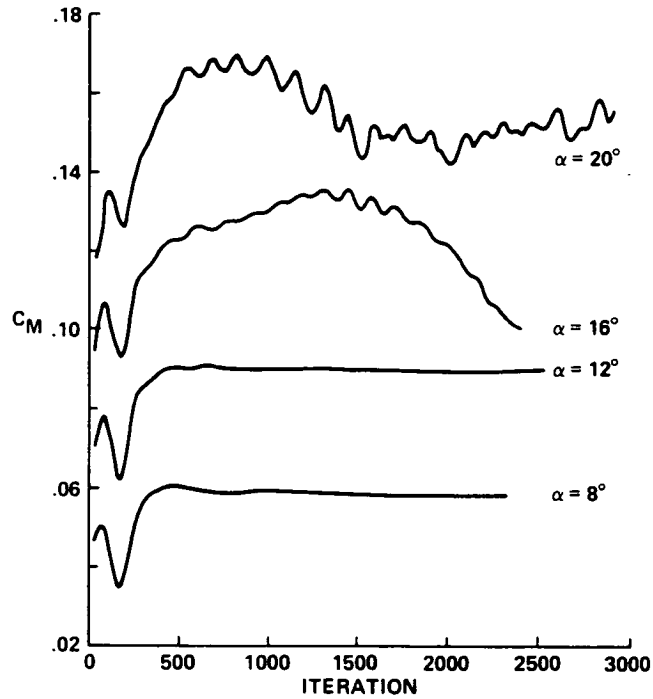
Fig. 65. Pitching-moment history for wing/body/chine, M = 0.80.
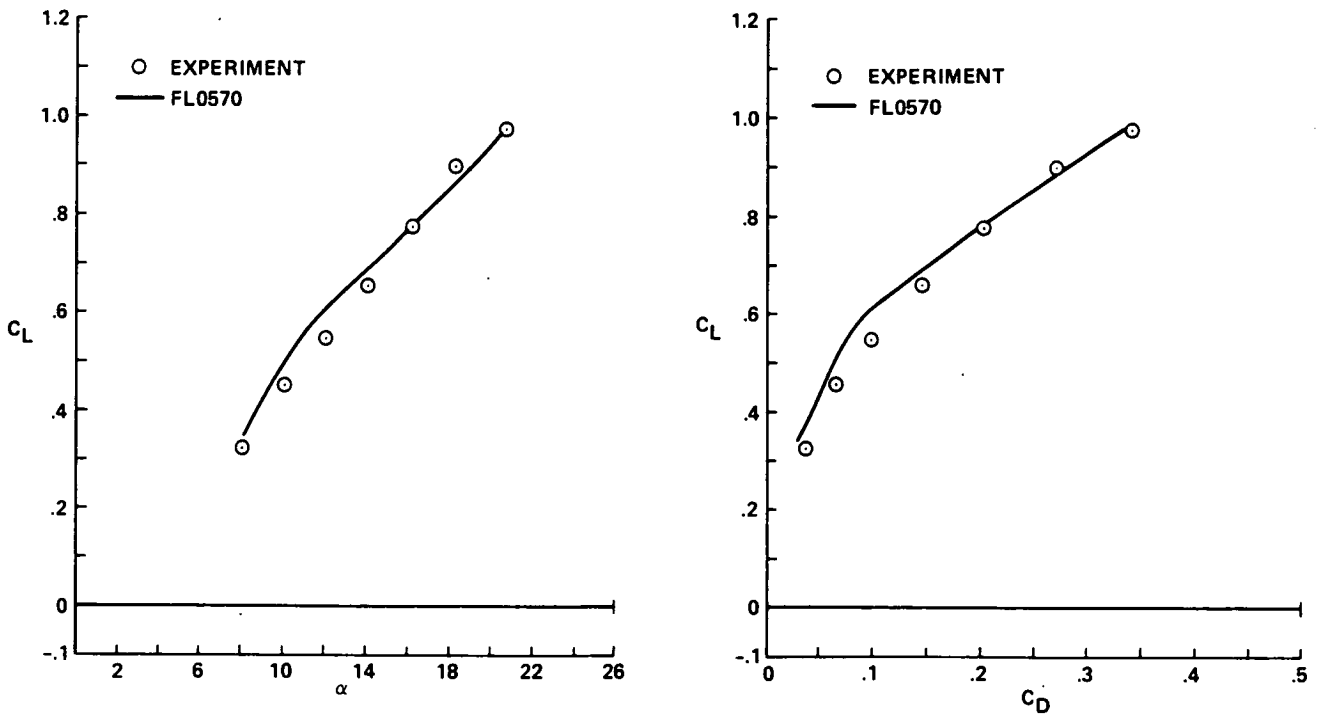
Fig. 66. Experiment–CFD forces and moments for wing/body/chine, M = 0.80.

149
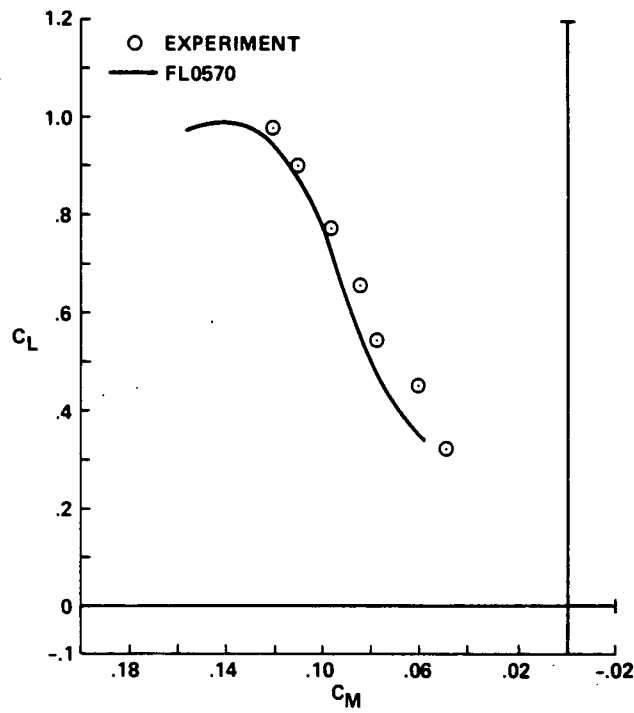
Fig. 66. Concluded.
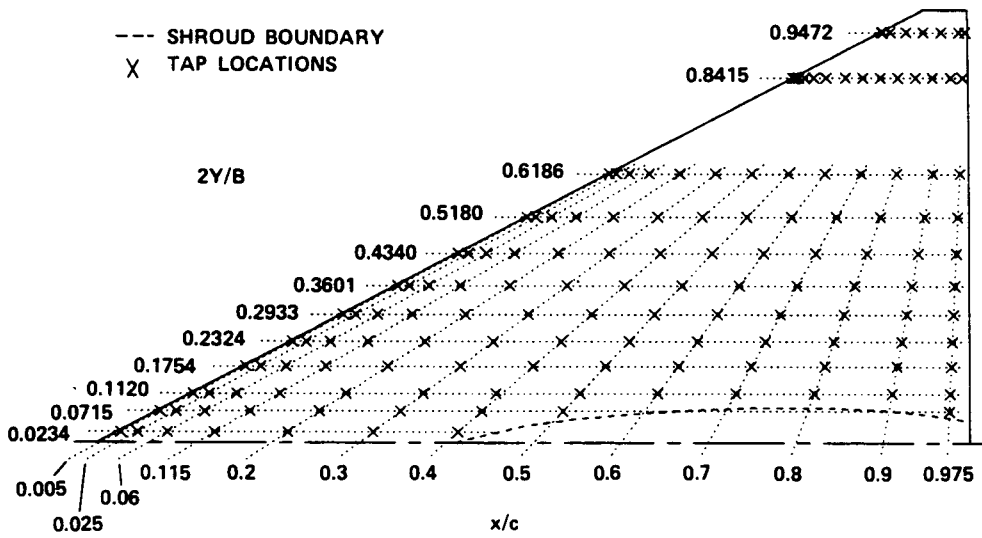
Fig. 67. Upper-surface plan view showing pressure tap locations.
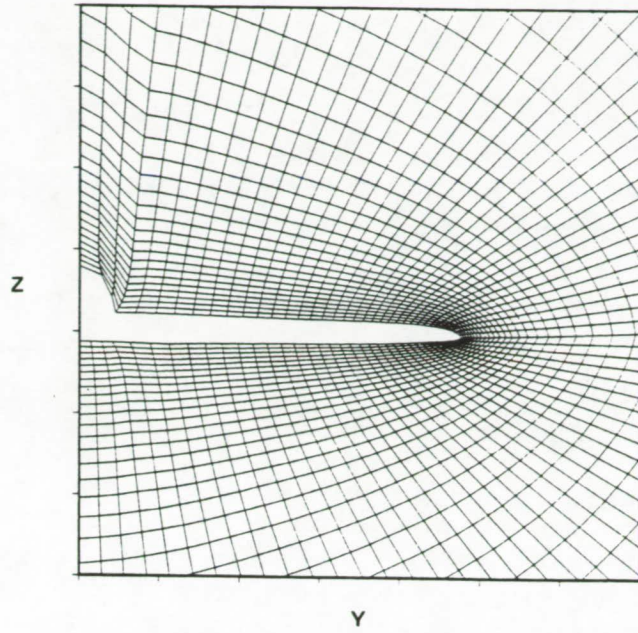
Fig. 68. Typical grid plane near trailing edge.

67 × 21 × 43

89 × 29 × 57

113 × 37 × 73

COARSE

MEDIUM

FINE
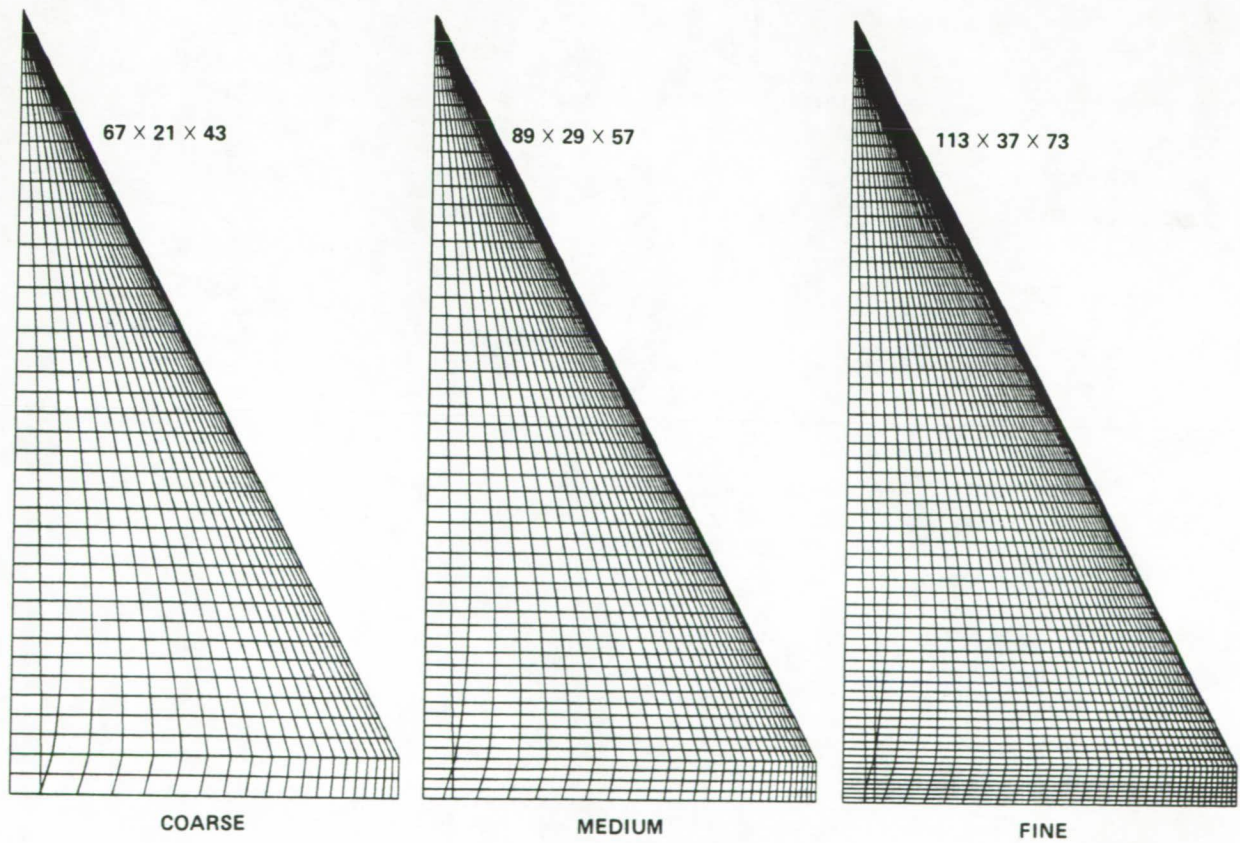
Fig. 69. Surface grid distributions, FLO57O.

151
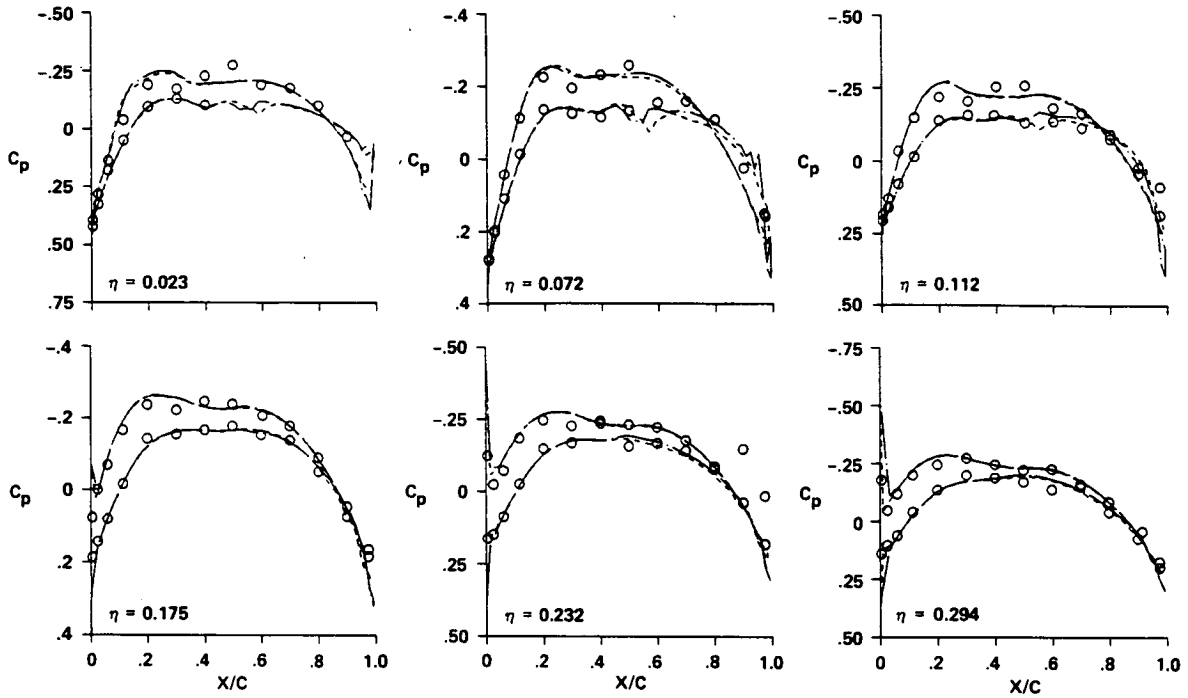
Fig. 70. Experiment–CFD pressure-distribution comparison for delta wing, M = 0.40.

152

$\eta = 0.023$

$\eta = 0.072$

$\eta = 0.112$

$\eta = 0.175$

$\eta = 0.232$

$\eta = 0.294$

(c)

	MACH	α	C_L	C_D	C_M
— · — FLO570 MEDIUM	0.401	0.029	0.0709	0.0012	-0.0025
- - - - FLO570 COARSE	0.401	0.029	0.0702	0.0017	-0.0025
O WIND TUNNEL	0.401	0.029	0.0631	0.0089	0.0005

$\eta = 0.360$

$\eta = 0.434$

$\eta = 0.518$

$\eta = 0.619$

$\eta = 0.842$

$\eta = 0.947$

(d)

Fig. 70. Continued.

153

(e)
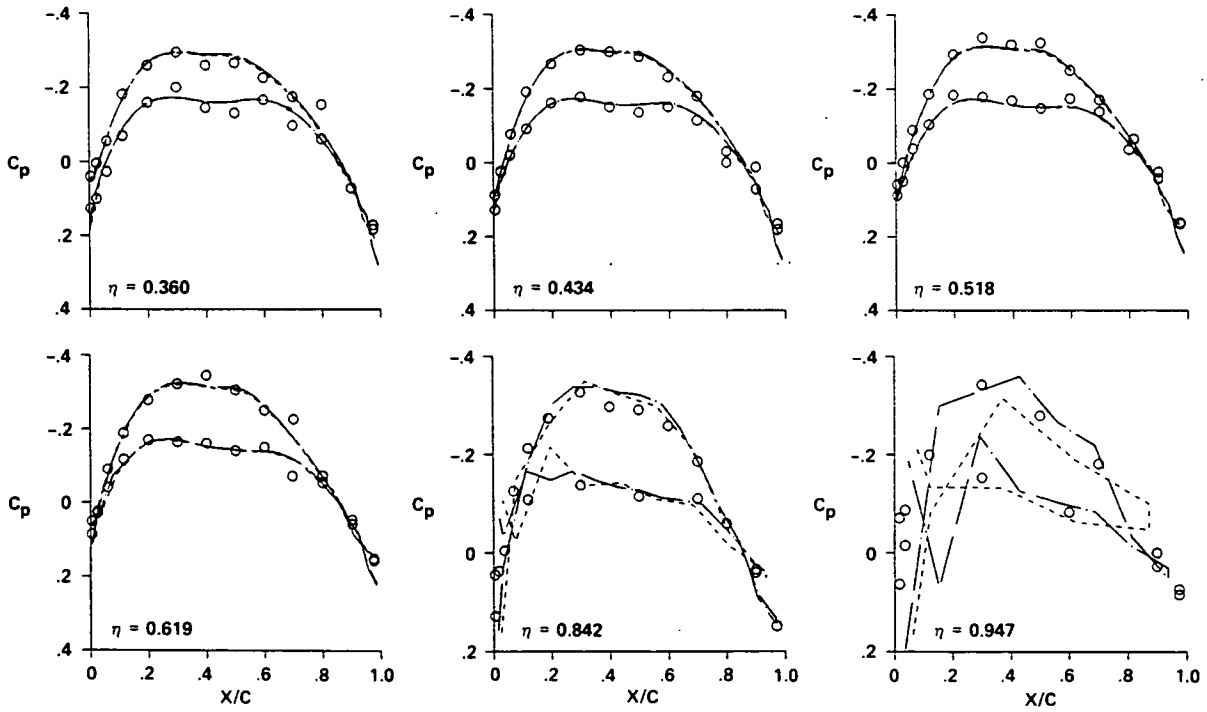
	MACH	α	C_L	C_D	C_M
—··— FLO570 MEDIUM	0.400	3.964	0.2358	0.0123	-0.0029
- - - - FLO570 COARSE	0.400	3.964	0.2368	0.0132	-0.0028
O WIND TUNNEL	0.400	3.964	0.2162	0.0175	0.0025

(f)

Fig. 70. Continued.

154

(g)

(h)

Fig. 70. Concluded.

155
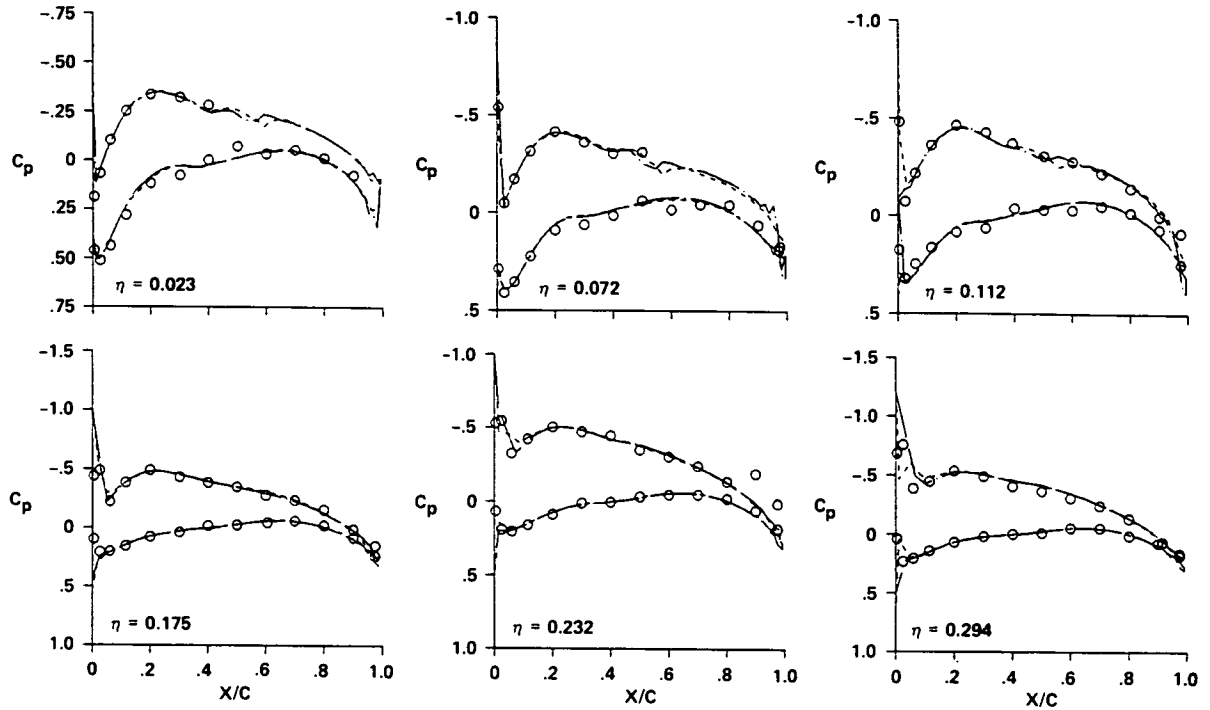
Fig. 71. Experiment–CFD pressure-distribution comparison for delta wing, M = 0.70.

	MACH	α	C_L	C_D	C_M
—·— FLO570 MEDIUM	0.700	0.155	0.0838	0.0014	-0.0042
----- FLO570 COARSE	0.700	0.155	0.0815	0.0020	-0.0039
O WIND TUNNEL	0.700	0.155	0.0661	0.0090	0.0006
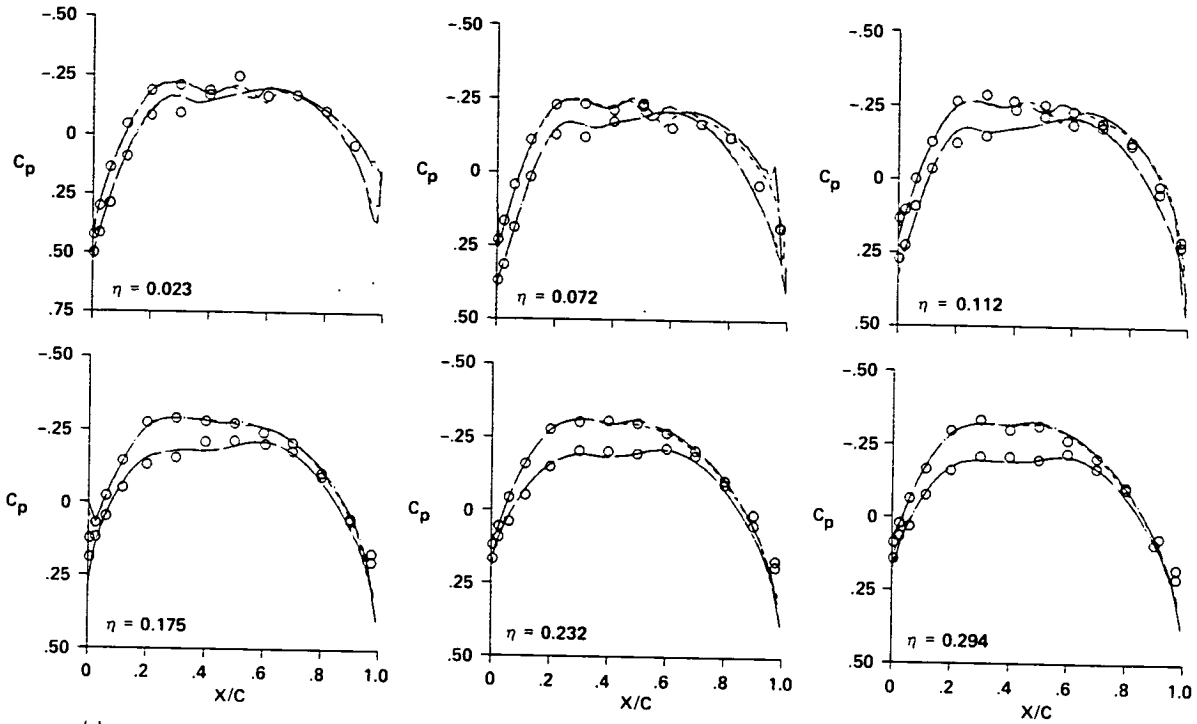
(c)

	MACH	α	C_L	C_D	C_M
—·— FLO570 MEDIUM	0.700	0.155	0.0838	0.0014	-0.0042
----- FLO570 COARSE	0.700	0.155	0.0815	0.0020	-0.0039
O WIND TUNNEL	0.700	0.155	0.0661	0.0090	0.0005
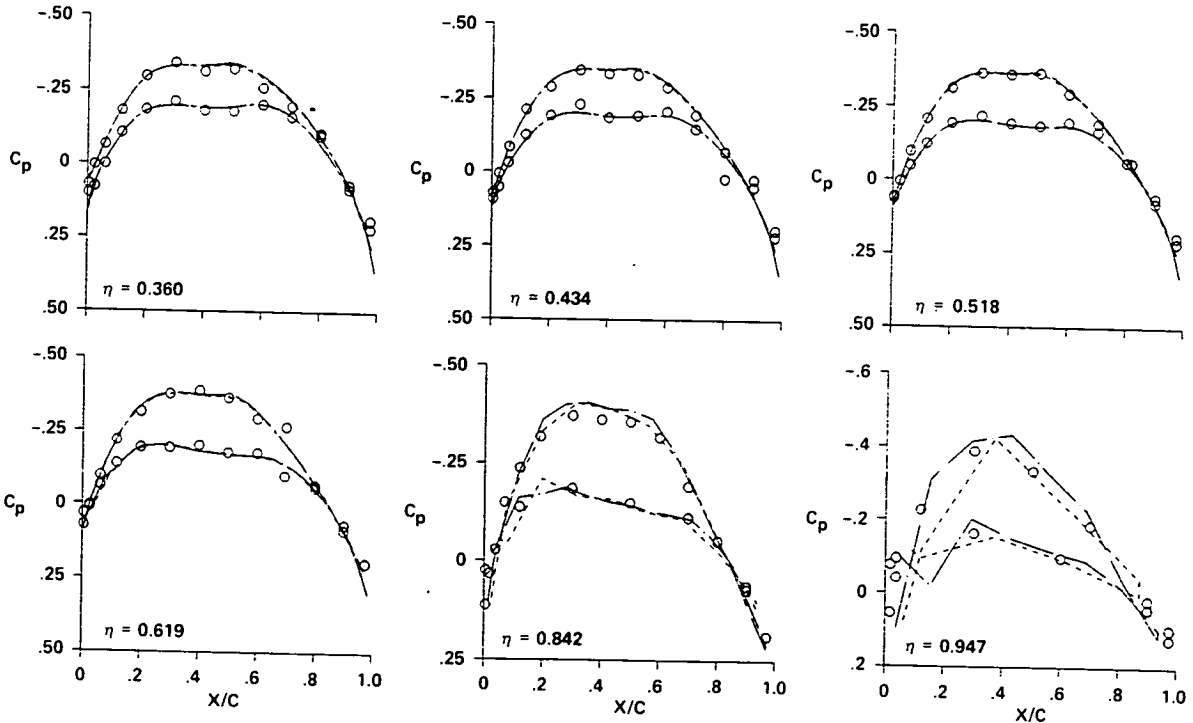
(d)

Fig. 71. Continued.

157

	MACH	α	C_L	C_D	C_M
FLO570 MEDIUM	0.699	4.322	0.2681	0.0160	−0.0050
FLO570 COARSE	0.699	4.332	0.2672	0.0171	−0.0049
WIND TUNNEL	0.699	4.322	0.2391	0.0201	0.0030
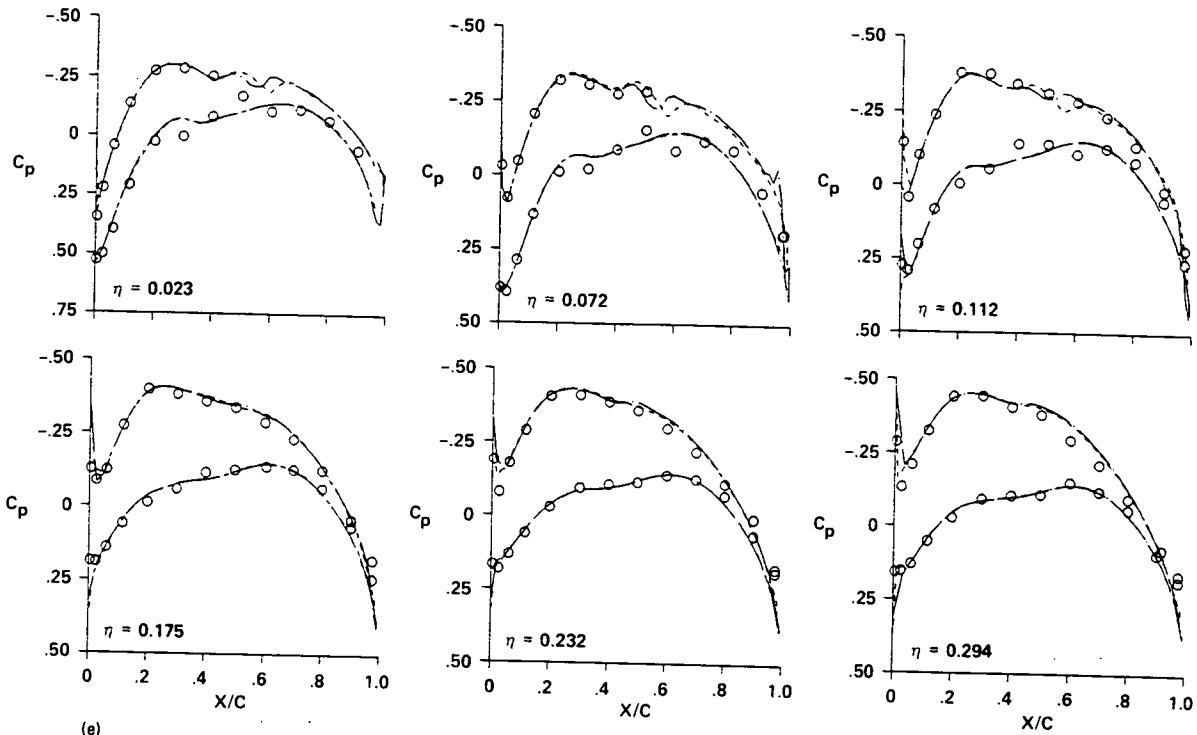
	MACH	α	C_L	C_D	C_M
FLO570 MEDIUM	0.699	4.322	0.2681	0.0160	−0.0050
FLO570 COARSE	0.699	4.322	0.2672	0.0171	−0.0049
WIND TUNNEL	0.699	4.322	0.2391	0.0201	0.0030

Fig. 71. Continued.

158

	MACH	α	C_L	C_D	C_M
—·—— FLO570 MEDIUM	0.701	8.531	0.4652	0.0565	-0.0039
– – – – FLO570 COARSE	0.701	8.531	0.4735	0.0610	-0.0082
O WIND TUNNEL	0.701	8.531	0.4249	0.0540	0.0047

(g)

	MACH	α	C_L	C_D	C_M
—·—— FLO570 MEDIUM	0.701	8.531	0.4652	0.0565	-0.0039
–·– – – FLO570 COARSE	0.701	8.531	0.4735	0.0610	-0.0082
O WIND TUNNEL	0.701	8.531	0.4249	0.0540	0.0047

(h)

Fig. 71. Concluded.

159

	MACH	α	C_L	C_D	C_M
——·—— FLO570 FINE	0.800	0.000	0.0771	0.0008	-0.0043
————— FLO570 MEDIUM	0.800	0.000	0.0809	0.0011	-0.0053
·········· FLO570 COARSE	0.800	0.000	0.0784	0.0020	-0.0049
✕ PANAIR	0.800	-0.120	0.0751	0.0007	-0.0047
○ WIND TUNNEL	0.801	0.399	0.0773	0.0099	0.0018

(a)

Fig. 72. Experiment-CFD pressure-distribution comparison for delta wing, M = 0.80.

	MACH	α	C_L	C_D	C_M
—·— FLO570 FINE	0.800	0.000	0.0771	0.0008	−0.0043
— — — FLO570 MEDIUM	0.800	0.000	0.0809	0.0011	−0.0053
········· FLO570 COARSE	0.800	0.000	0.0784	0.0020	−0.0049
✕ PANAIR	0.800	−0.120	0.0751	0.0007	−0.0047
○ WIND TUNNEL	0.801	0.399	0.0773	0.0099	0.0018

(b)
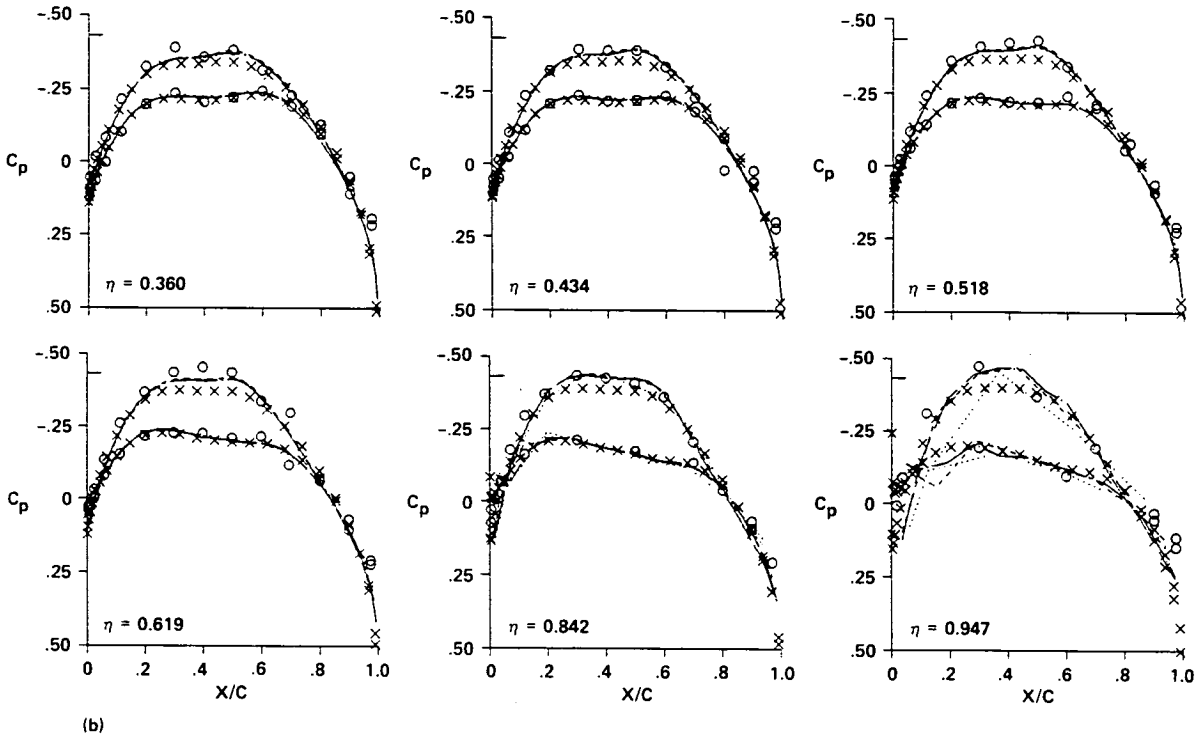
Fig. 72. Continued.

	MACH	α	C_L	C_D	C_M
—·— FLO570 FINE	0.800	4.000	0.2597	0.0145	-0.0051
----- FLO570 MEDIUM	0.800	4.000	0.2663	0.0153	-0.0073
·········· FLO570 COARSE	0.800	4.000	0.2646	0.0167	-0.0072
✕ PANAIR	0.800	4.110	0.2601	0.0126	-0.0083
○ WIND TUNNEL	0.802	4.685	0.2600	0.0230	0.0042
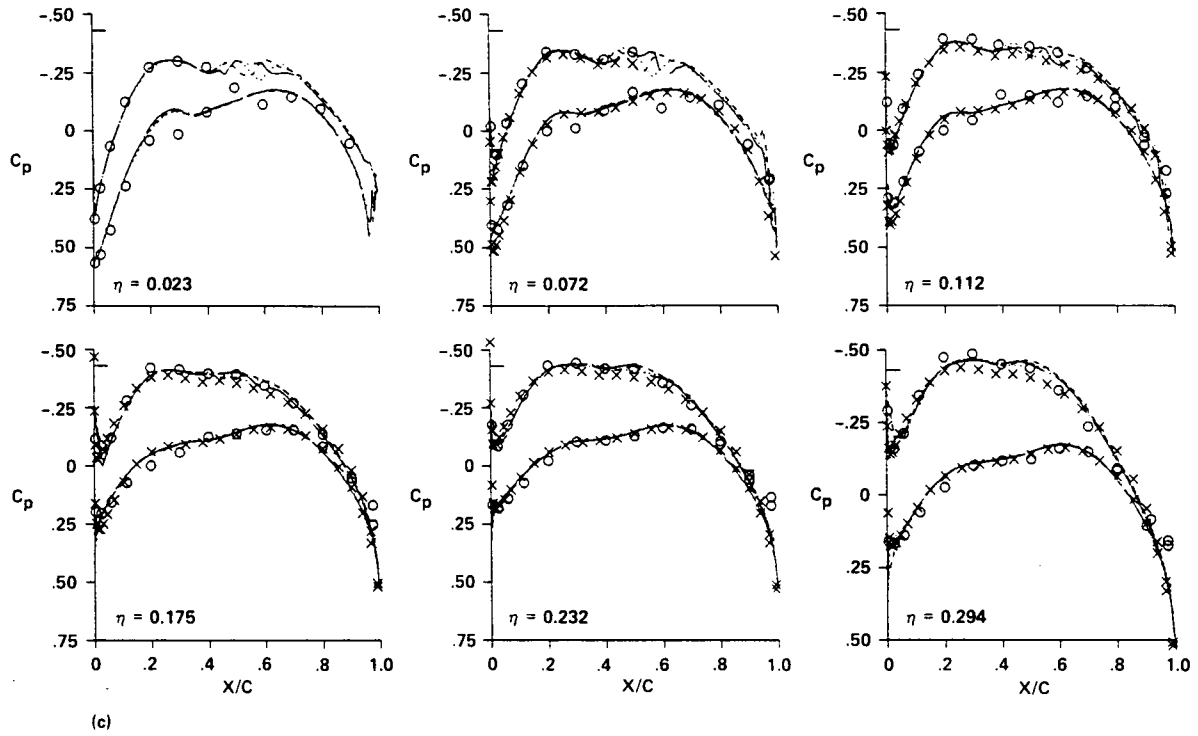
(c)

Fig. 72. Continued.

162

	MACH	α	C_L	C_D	C_M
—·— FLO570 FINE	0.800	4.000	0.2597	0.0145	−0.0051
— — — FLO570 MEDIUM	0.800	4.000	0.2663	0.0153	−0.0073
·········· FLO570 COARSE	0.800	4.000	0.2646	0.0167	−0.0072
✕ PANAIR	0.800	4.110	0.2601	0.0126	−0.0083
O WIND TUNNEL	0.802	4.685	0.2600	0.0230	0.0042
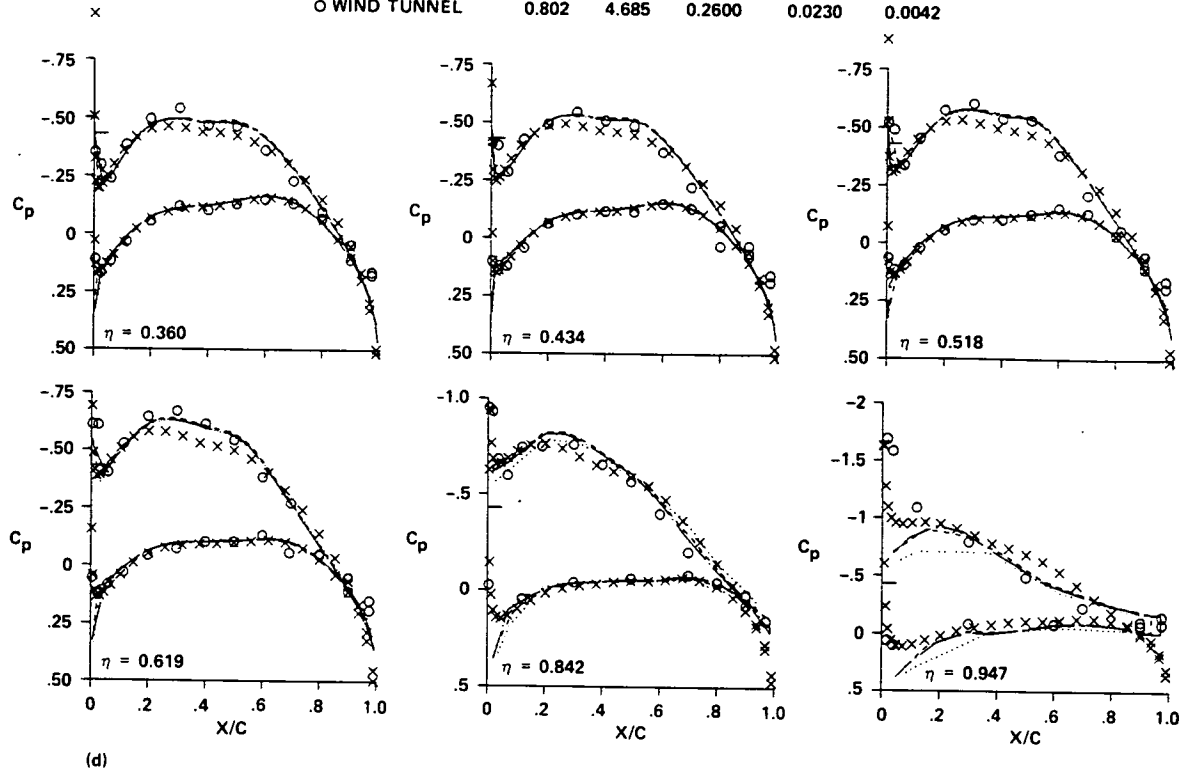
(d)

Fig. 72. Continued.

	MACH	α	C_L	C_D	C_M
—·— FLO570 FINE	0.800	7.700	0.4446	0.0504	-0.0079
----- FLO570 MEDIUM	0.800	7.700	0.4551	0.0529	-0.0122
········· FLO570 COARSE	0.800	7.700	0.4475	0.0548	-0.0107
× PANAIR	0.800	8.770	0.4598	0.0464	-0.0120
O WIND TUNNEL	0.801	9.167	0.4600	0.0684	0.0059

Fig. 72. Continued.

164

	MACH	α	C_L	C_D	C_M
—·— FLO570 FINE	0.800	7.700	0.4446	0.0504	-0.0079
– – – FLO570 MEDIUM	0.800	7.700	0.4551	0.0529	-0.0122
·········· FLO570 COARSE	0.800	7.700	0.4475	0.0548	-0.0107
✕ PANAIR	0.800	8.770	0.4598	0.0464	-0.0120
○ WIND TUNNEL	0.801	9.167	0.4600	0.0684	0.0059

Fig. 72. Concluded.

165

Fig. 73. Experiment–CFD force-and-moment comparisons for delta wing, M = 0.40.
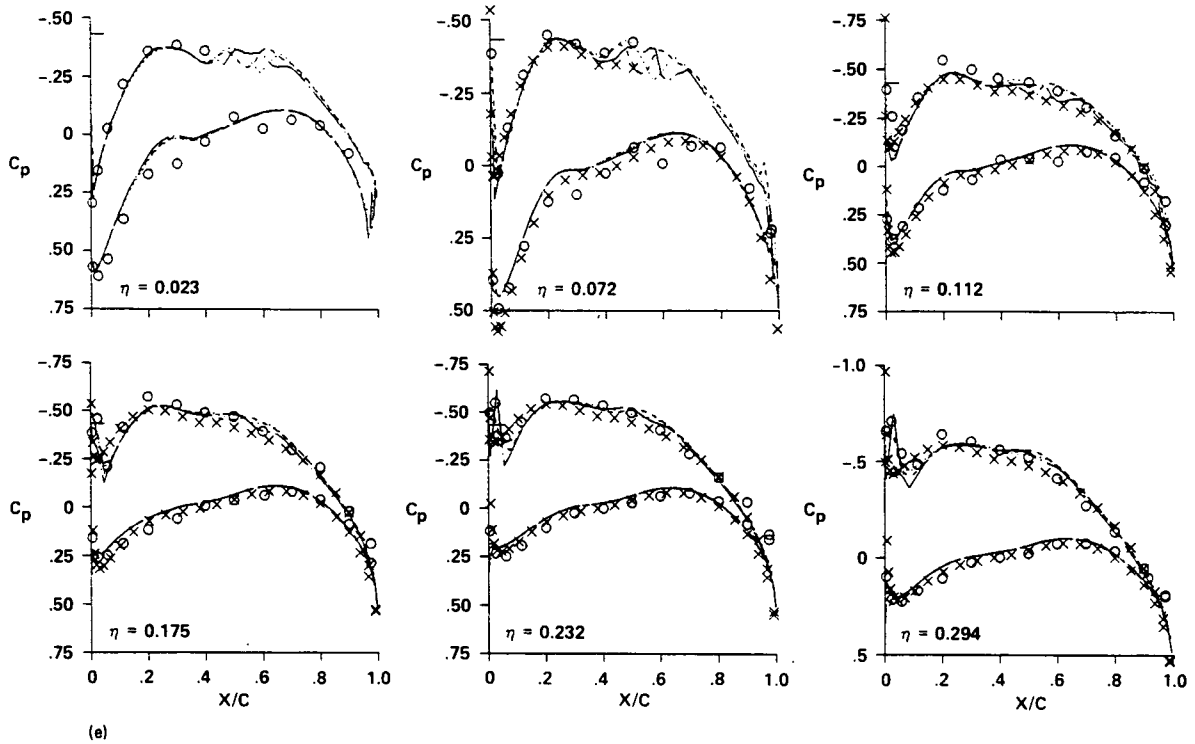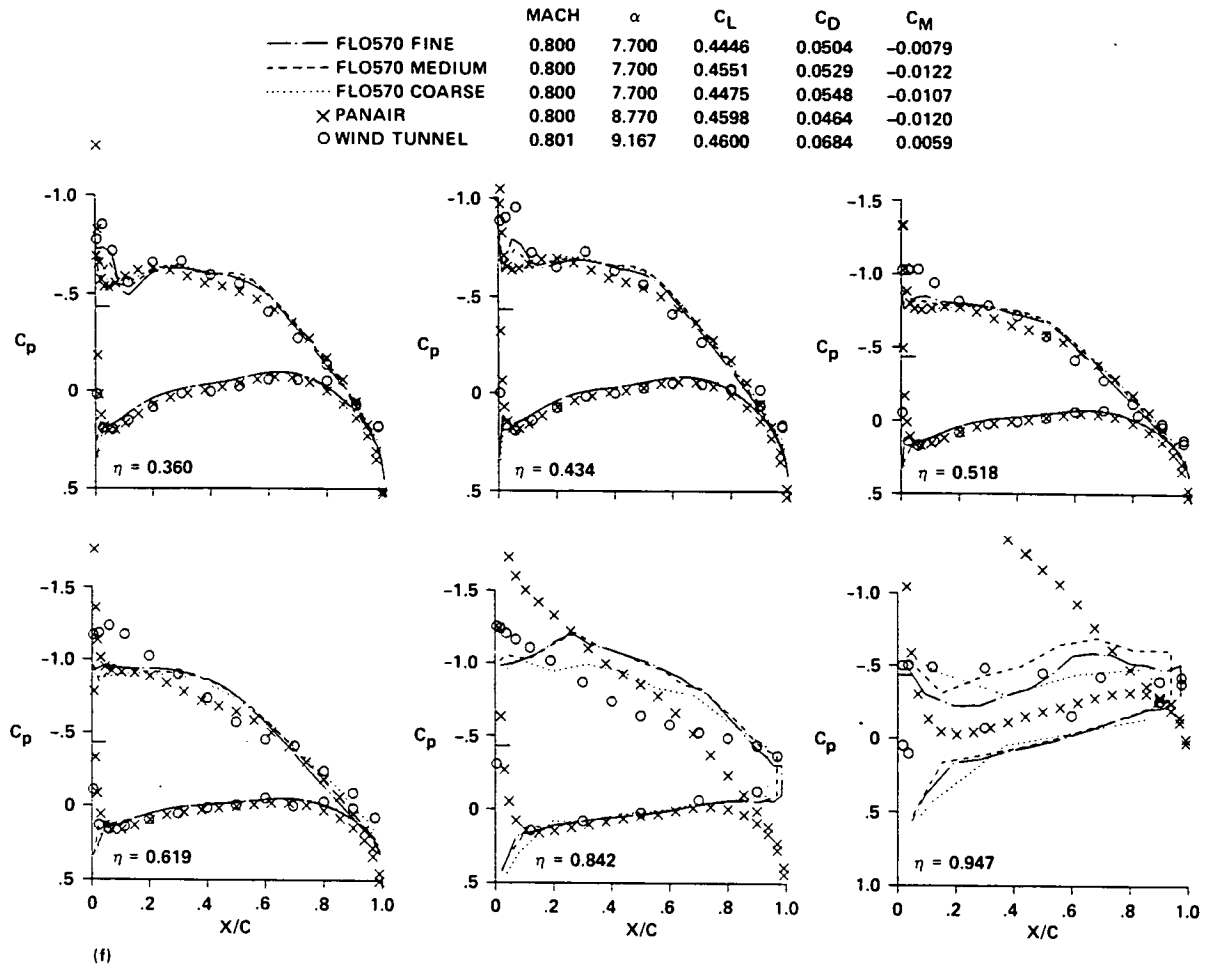
GRID
∇ = FLO570   89 x 29 x 57
□ = FLO570   67 x 21 x 43
x = PANAIR
■ = WIND TUNNEL
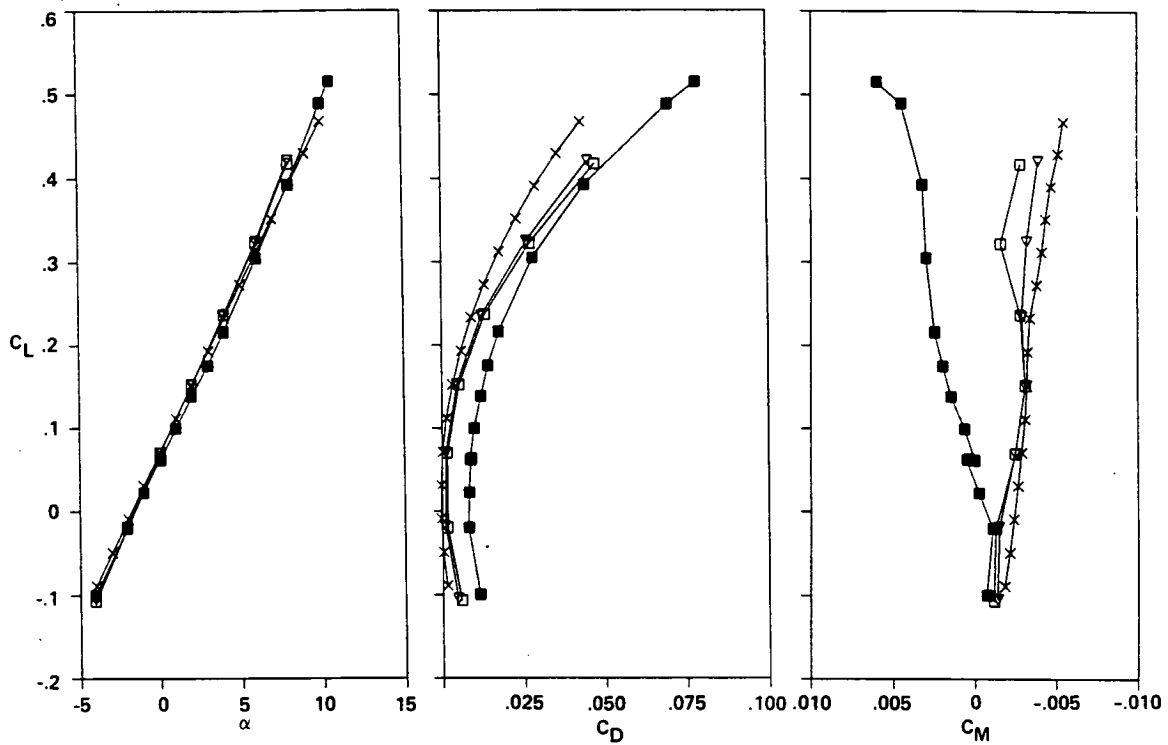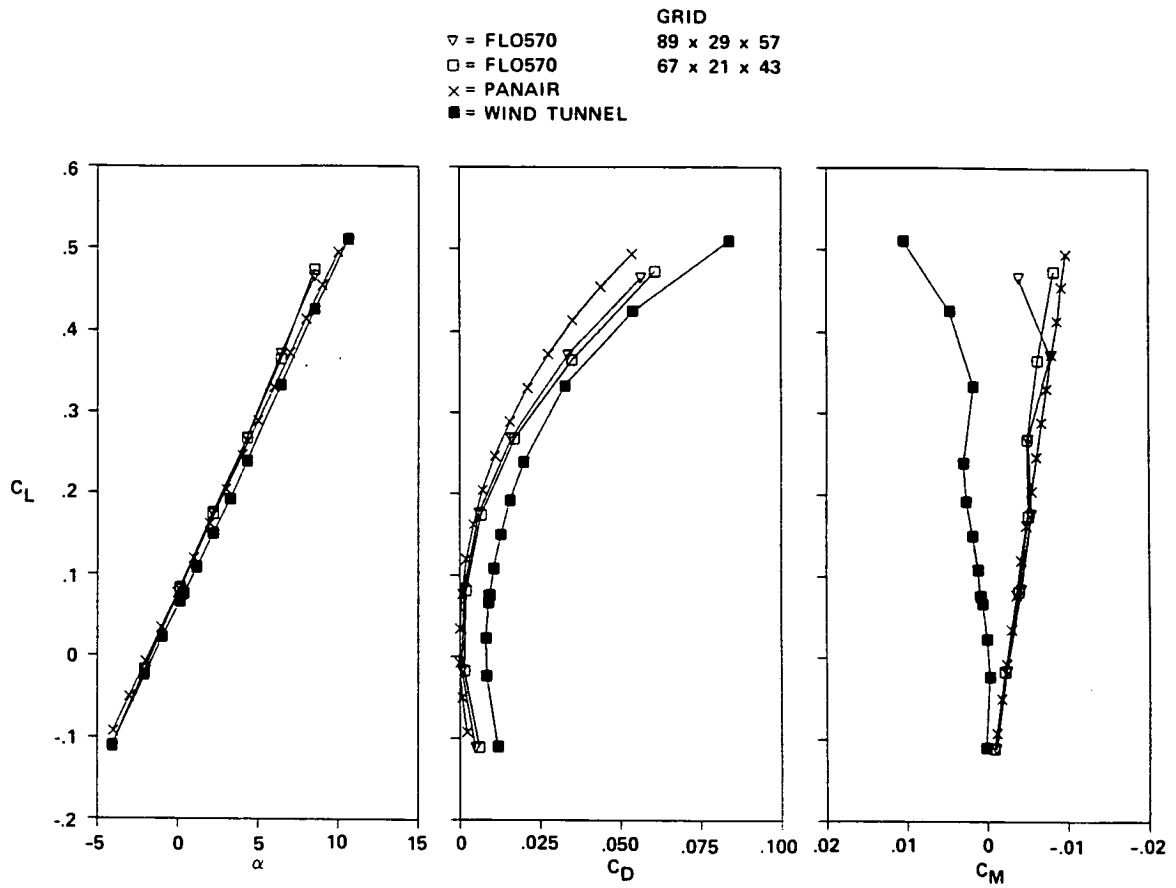
Fig. 74. Experiment–CFD force-and-moment comparisons for delta wing, M = 0.70.
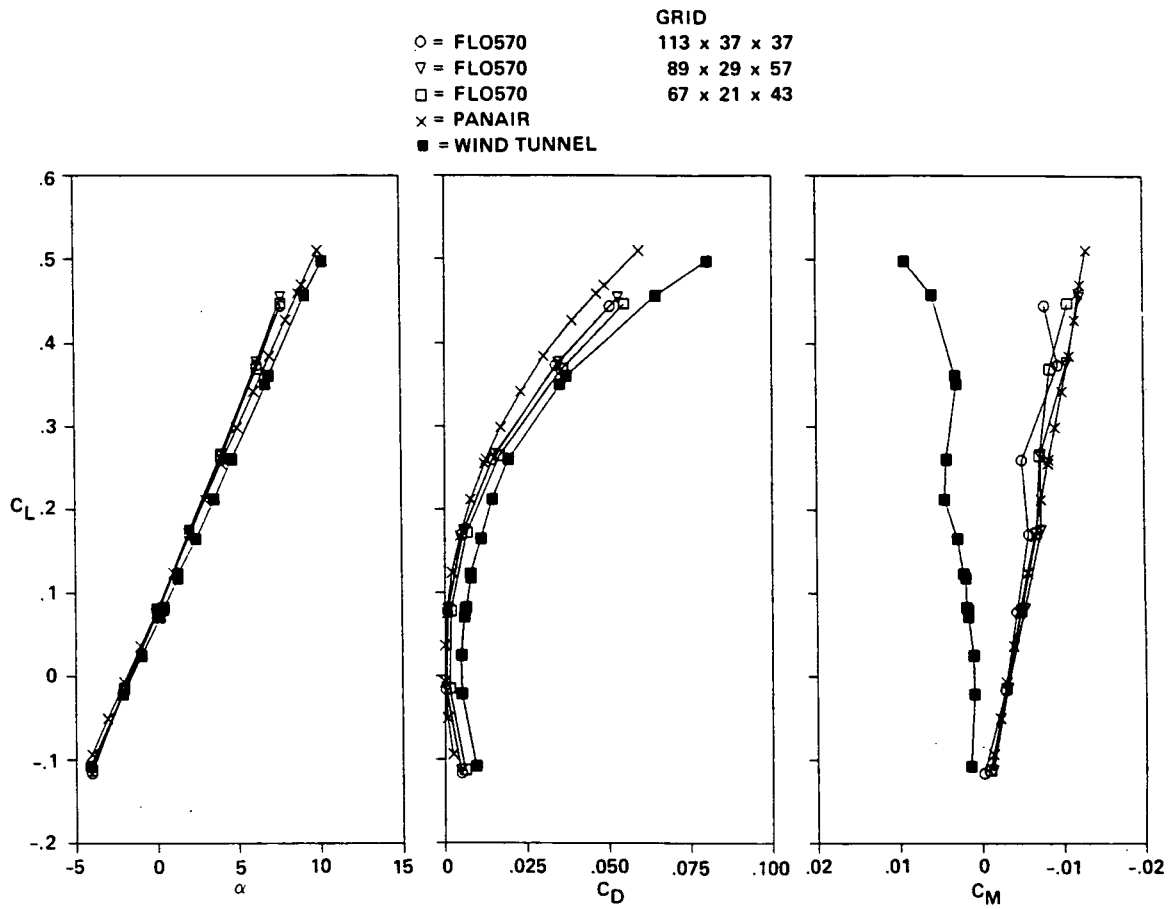
Fig. 75. Experiment–CFD force-and-moment comparisons for delta wing, M = 0.80.
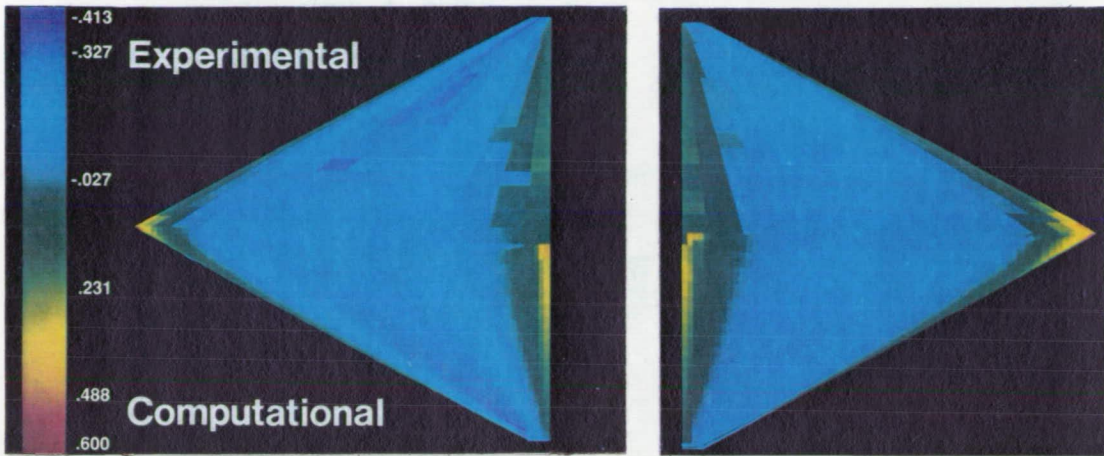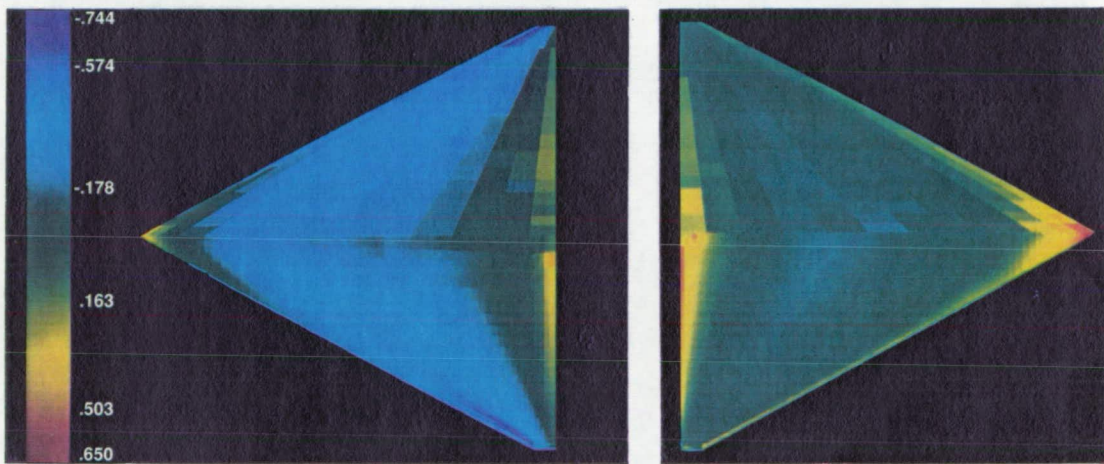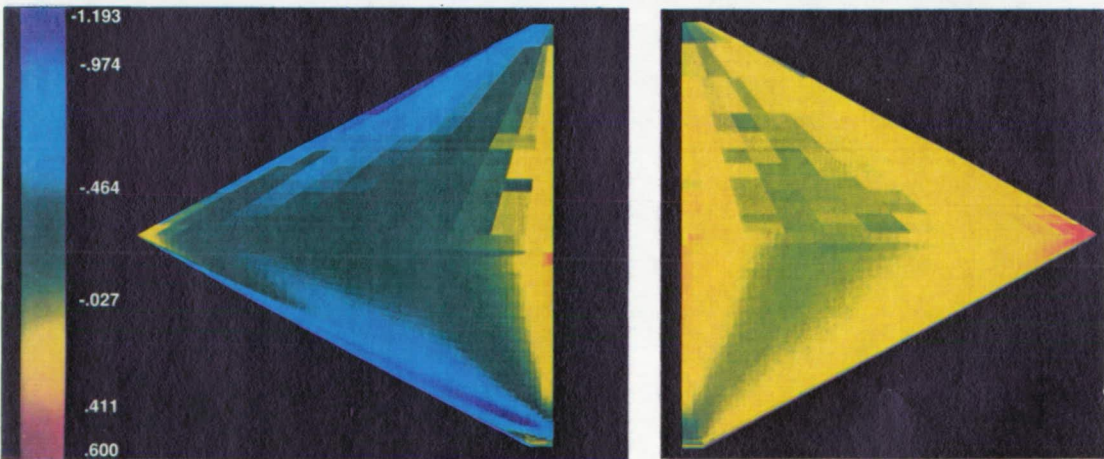
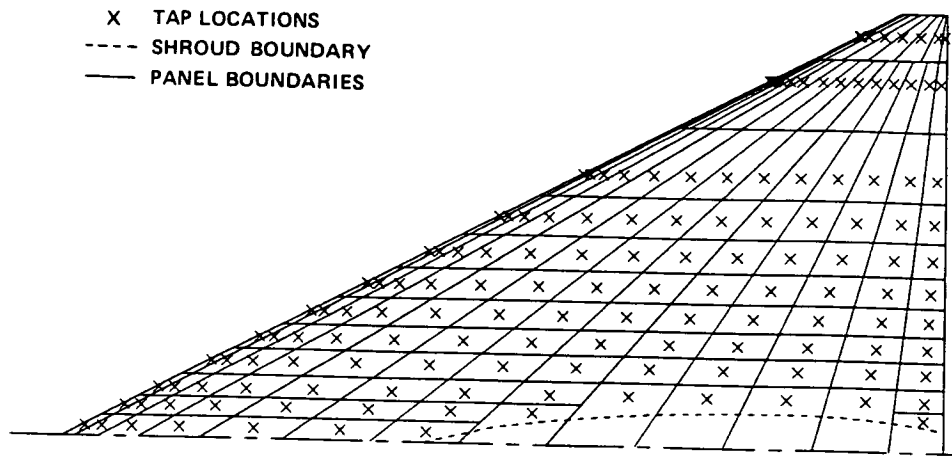Figure 76.– Surface pressure distributions for Mach = 0.4 (upper surface on the right; lower surface on the left).
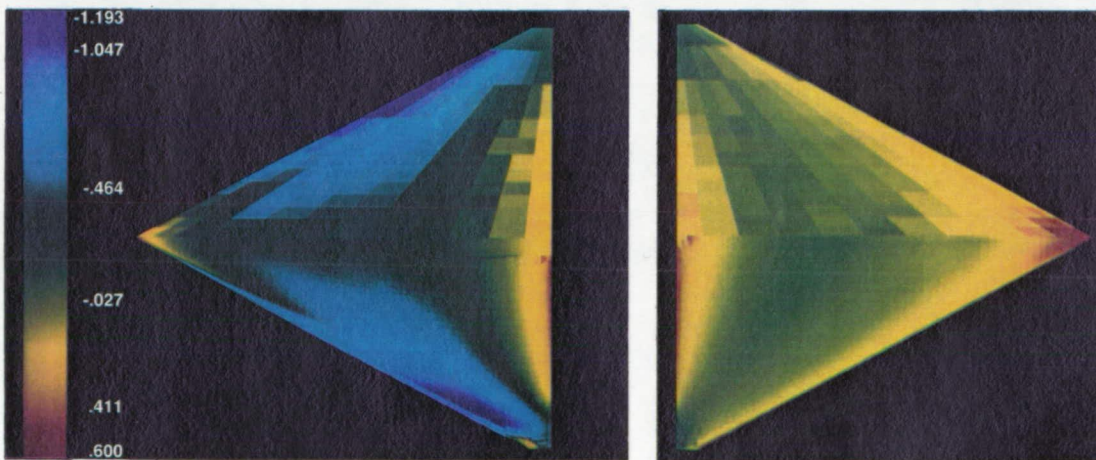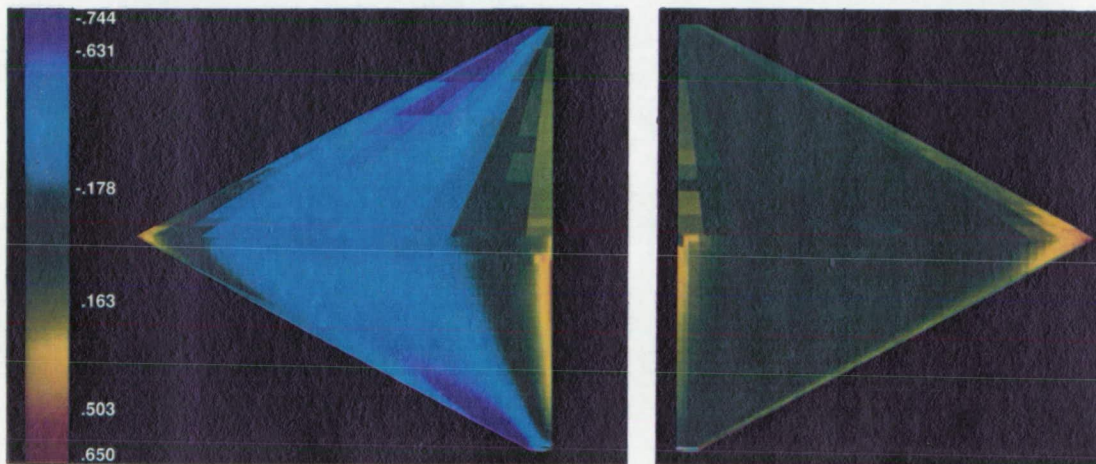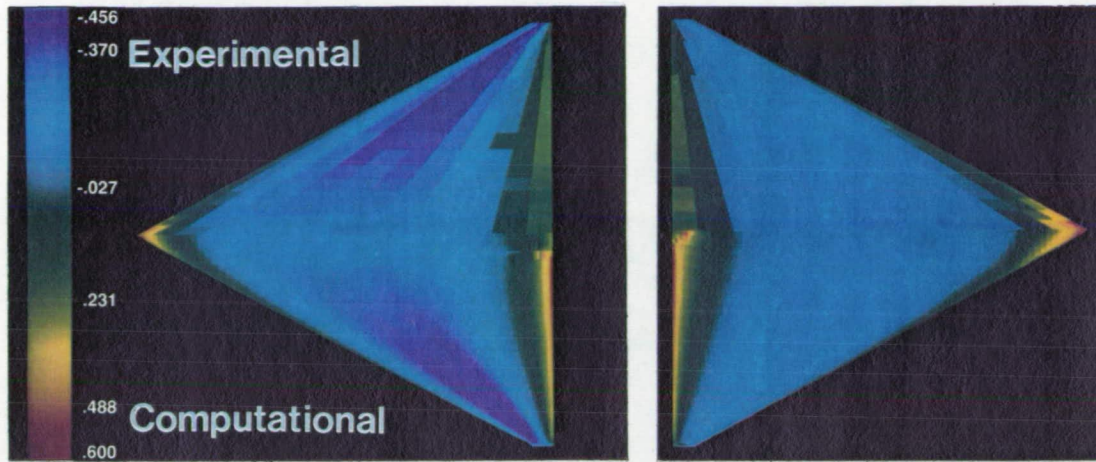
Figure 77.– Surface pressure distributions for Mach = 0.8 (upper surface on the right; lower surface on the left).

171

Fig. 78. Tap locations and paneling for experimental pressure integration.

Fig. 79. Experimental forces and moments for delta wing, M = 0.40.

173

■ = BALANCE
▽ = INTEGRATED FROM WIND
    TUNNEL TAPS
◇ = INTEGRATED + SKIN FRICTION
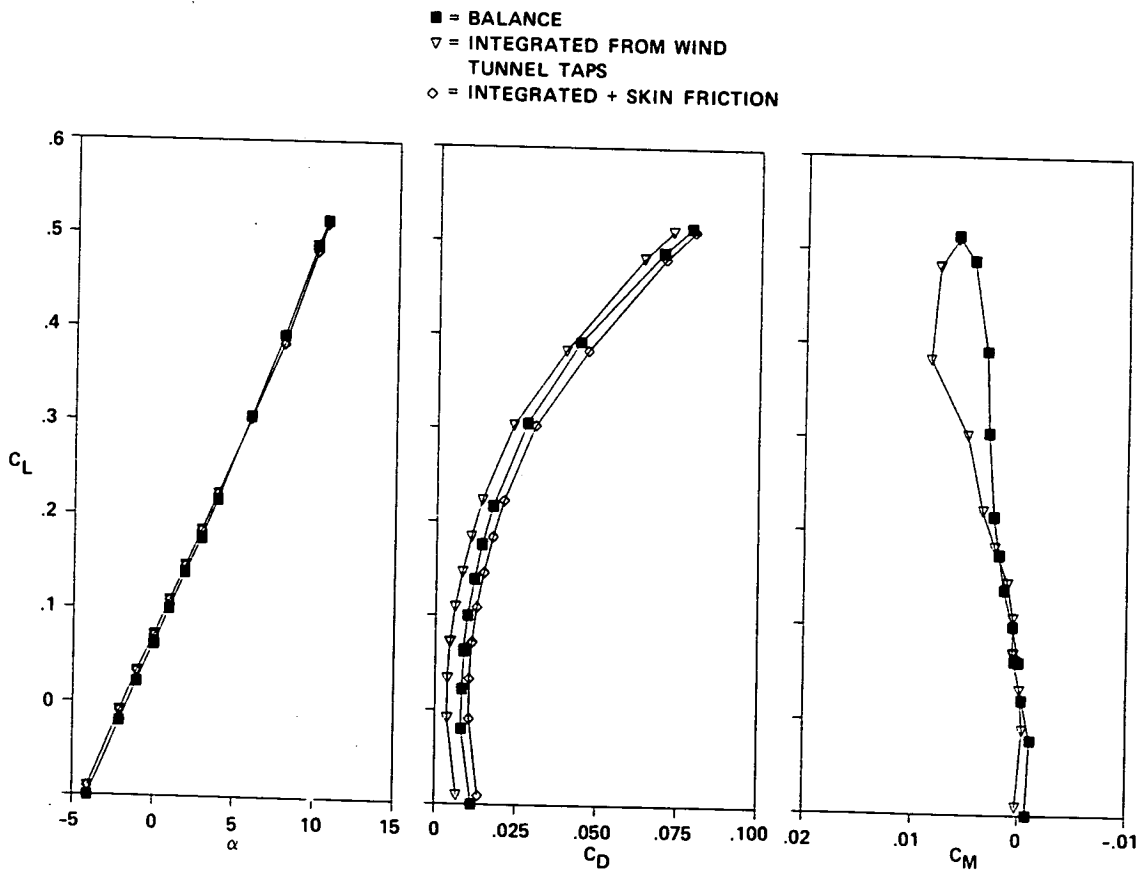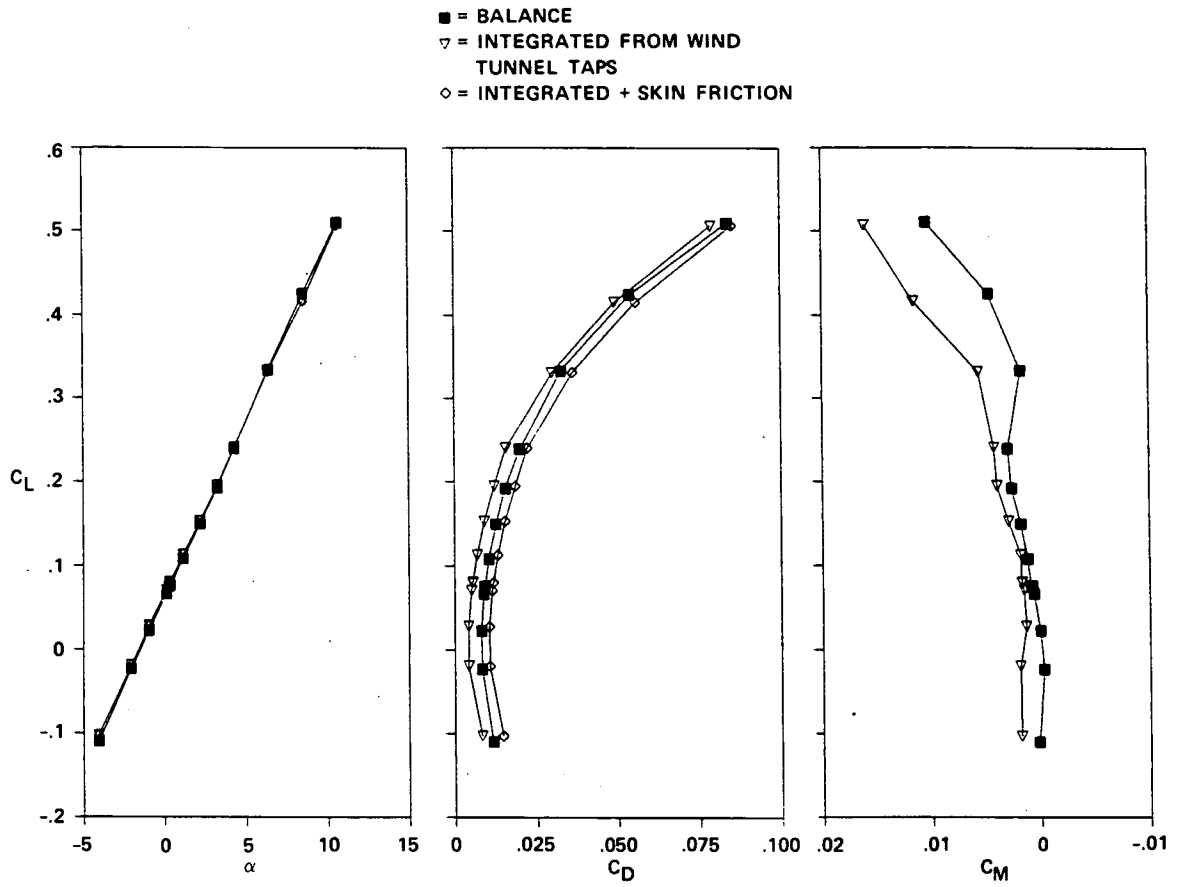
Fig. 80. Experimental forces and moments for delta wing, M = 0.70.
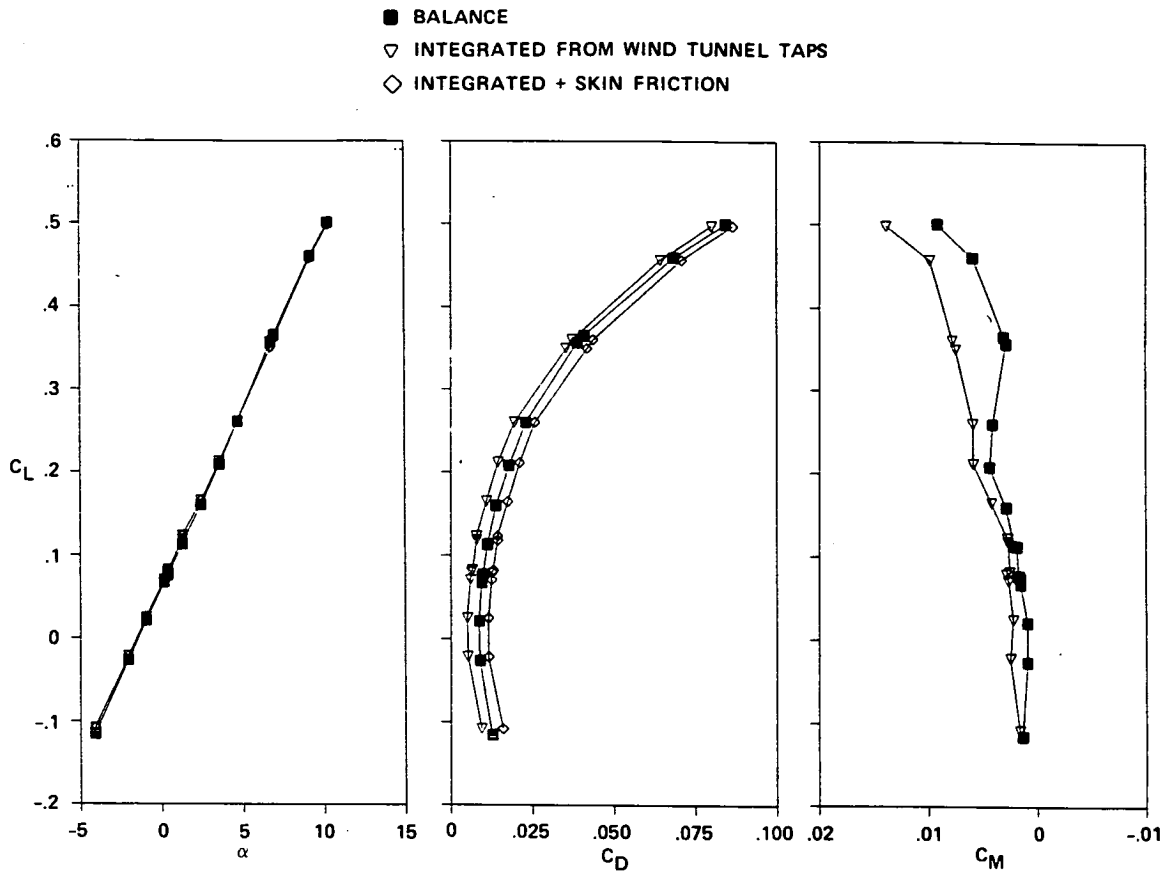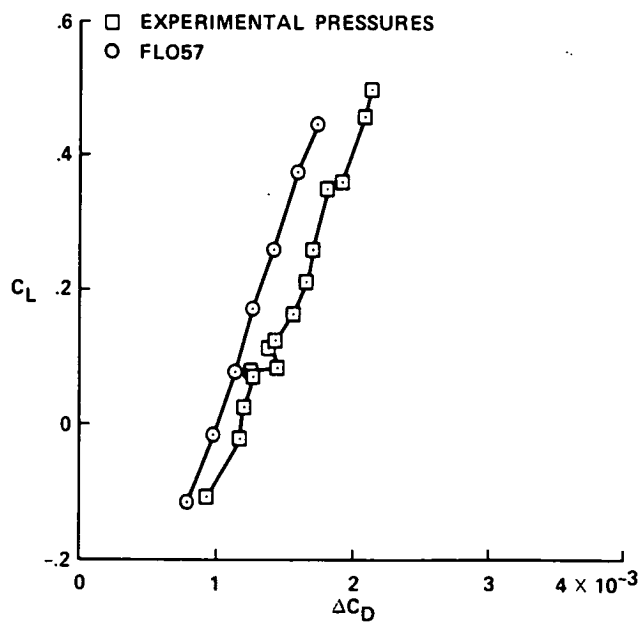
Fig. 81. Experimental forces and moments for delta wing, M = 0.80.

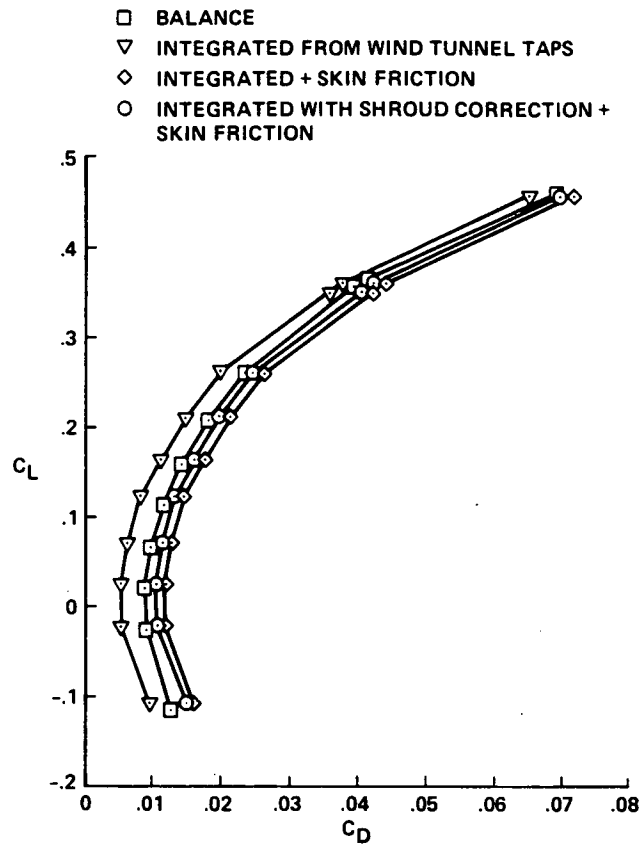Fig. 82. Effect of removing the sting shroud on integrated drag, M = 0.80.

175

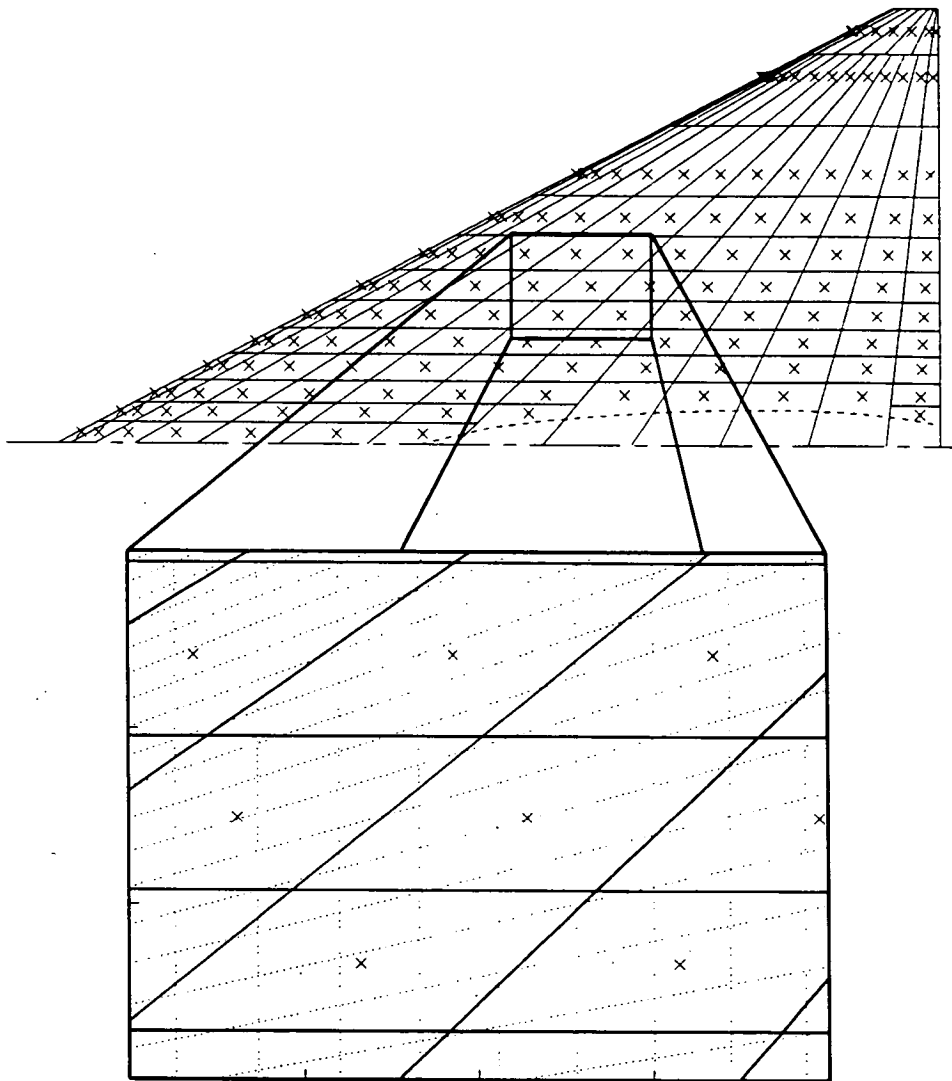Fig. 83. Shroud increment removed from the M = 0.80 drag polar.

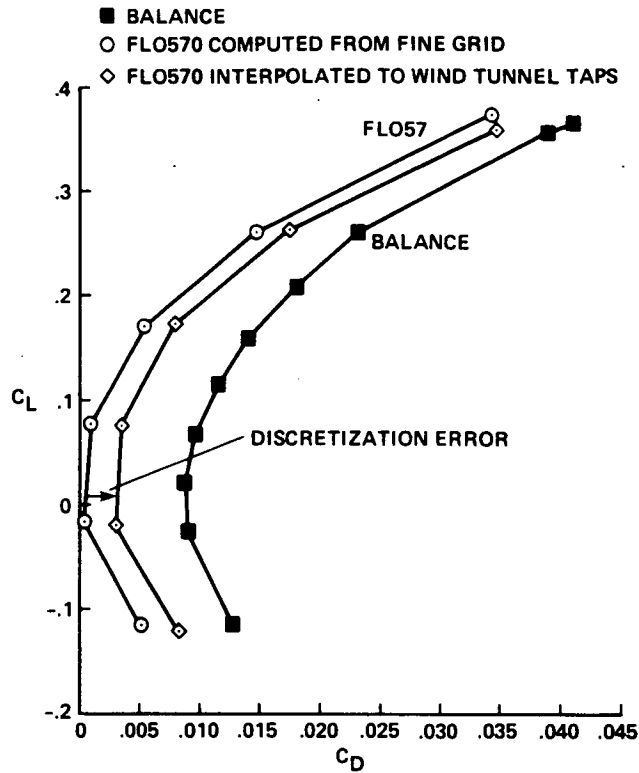Fig. 84. Computational and experimental grid comparison, FLO570.

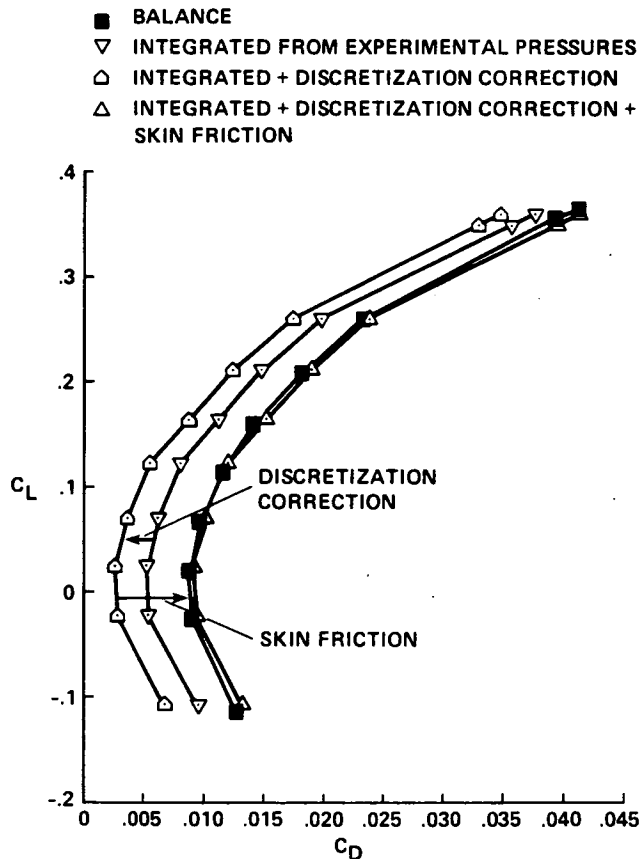Fig. 85. Discretization effect of drag calculated from FLO57O, M = 0.80.

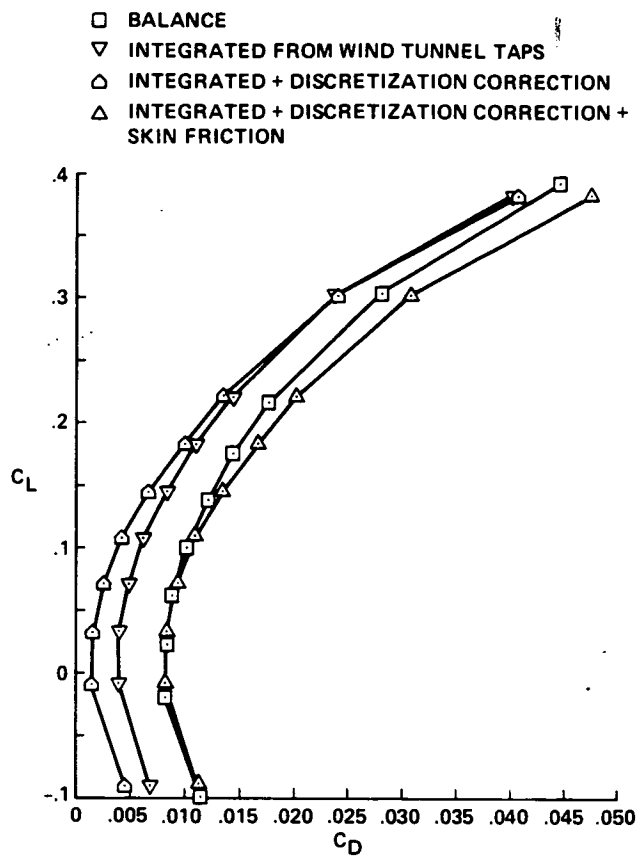Fig. 86. Discretization correction determined from FLO57O applied to experimental data, M = 0.80.

Fig. 87. Discretization correction determined from FLO570 applied to experimental data, M = 0.40.

Report Documentation Page

1. Report No. NASA TM-102208	2. Government Accession No.	3. Recipient's Catalog No.

4. Title and Subtitle	5. Report Date
Euler and Potential Experiment/CFD Correlations for a Transport and Two Delta-Wing Configurations	August 1990
	6. Performing Organization Code

7. Author(s)	8. Performing Organization Report No.
R. M. Hicks, S. E. Cliff, J. E. Melton, R. G. Langhi, A. M. Goodsell, D. D. Robertson, and S. A. Moyer	A-89197
	10. Work Unit No. 505-61-21

9. Performing Organization Name and Address	11. Contract or Grant No.
Ames Research Center Moffett Field, CA 94035-1000	
	13. Type of Report and Period Covered

12. Sponsoring Agency Name and Address	Technical Memorandum
National Aeronautics and Space Administration Washington, DC 20546-0001	14. Sponsoring Agency Code

16. Abstract

This report discusses a selection of successes and failures of CFD. Experiment/CFD correlations involving full potential and Euler computations of the aerodynamic characteristics of four commercial transport wings and two low-aspect-ratio, delta-wing configurations are shown. The examples consist of experiment/CFD comparisons for aerodynamic forces, moments, and pressures. Navier-Stokes calculations are not considered.

17. Key Words (Suggested by Author(s))	18. Distribution Statement
Wing design CFD Wind tunnel testing	Unclassified-Unlimited Subject Category - 02

19. Security Classif. (of this report) Unclassified	20. Security Classif. (of this page) Unclassified	21. No. of Pages 180	22. Price A09